UNIVERSITÀ DEGLI STUDI DI MILANO

SCUOLA DI DOTTORATO
FISICA, ASTROFISICA E FISICA APPLICATA

DIPARTIMENTO DI FISICA

CORSO DI DOTTORATO DI RICERCA IN
FISICA, ASTROFISICA E FISICA APPLICATA

CICLO XXV

Measurement of high-energy γ rays to study the dynamical dipole emission and the isospin mixing

Settore Scientifico disciplinare FIS/04

Tesi di Dottorato di:
Agnese Giaz

Supervisore: Prof. Franco Camera

Coordinatore: Prof. Marco Bersanelli

Anno Accademico 2011-2012

Contents

Introduction

The study of the collective properties of a nuclear system is a powerful tool to understand the structure which lies inside the nucleus. A successful technique which was used in this field is the measurement of the decay of the collective Giant Dipole Resonance (GDR) as a probe to understand structural or dynamical aspects of the nucleus [1], [2].

The use of fusion-evaporation reactions made recently possible the study of, for example, i) the yield of the high-energy gamma-ray emission of the Dynamical Dipole (DD) which takes place during the compound nucleus formation process if there an N/Z asymmetry and ii) the degree of isospin mixing at finite temperature in the decay of N=Z nuclei. In this thesis two experiments will be presented, the first one aims to measure the dynamical dipole contribution for the system ^{16}O + ^{116}Sn at 12 MeV/u and the second aims to measure the degree of the isospin mixing in ^{80}Zr at T=2.4 MeV. In the first experiment the DD contribution has to be separated from the GDR decay, instead in the second one the GDR itself constitute a tool to measure the isospin mixing probability. The results of the data analysis of the DD experiment will be presented, whereas the preliminary analysis (detector calibration, in-beam detector performance and data reduction) will be described for the isospin mixing experiment. In order to measure GDR γ decay, the best detectors are $LaBr_3$:Ce scintillators, due to the good energy and time resolution. A study of the performances of these detectors at high energy (up to 22 MeV)will be described.

If there is an N/Z asymmetry between the projectile and the target ($N_p/Z_p \neq N_t/Z_t$) in heavy ion fusion reactions, it is possible to form a time dependent dipole moment which is associated to a gamma radiation emission, called dynamical dipole. The DD γ emission has the same energy and the same dipolar nature of GDR γ decay but it is not of statistical nature and therefore the DD carries information on the nuclear state before equilibration is achieved and on the dynamics fusion process. To obtain the DD contribution it is necessary to compare the experimental high-energy γ-

rays spectrum from an N/Z asymmetric reaction with the spectrum from a N/Z symmetric reaction (in which there is only the contribution of the GDR), or a spectrum from a theoretical model that includes only the statistical decay).

The existing experimental data are still rather scarce, although some data exist in the A=132 mass region. The data, moreover, do not seem to follow the theoretical predictions concerning the dependence of the DD yield emission with beam energy [3]–[5]. Experimentally, it was observed that dynamical dipole emission increases with beam energy up to ≈ 10 MeV/u, then the yield significantly decreases. The dependence of DD with beam energy is the main topic of this thesis, in particular is the study of the dynamical dipole contribution for the system $^{16}O + ^{116}Sn$ at 12 MeV/u that is an intermediate point respect the two already existing data points (8.1 and 15.6 MeV/u) [6].

The model which better describes the dynamical dipole emission studies the dynamical evolution of the dipole in the framework of the Boltzmann-Nordheim-Vlasov (BNV) prescription and employs the bremsstrahlung expression for the calculation of the photon yield [7]. It is important to point out that the model critically depends on the nuclear equation of state with its symmetry term and on its density dependence. In the case of $^{16}O + ^{116}Sn$ the dependence on the nuclear Equation Of State (EOS) with its symmetry term is not so strong, instead this dependence become significant with neutron rich exotic beams (highly asymmetric) such as ^{132}Sn. The theoretical model predicts that the dependence on the symmetry term of the EOS should be clearly visible for $^{132}Sn + ^{58}Ni$ reaction [8]. The understanding of this mechanism is relevant for the study of exotic nuclear matter, especially in view of the future availability of intense radioactive beams that are expected to give a boost to this kind of measurements.

An experimental campaign on the DD yield was performed at Laboratori Nazionali di Legnaro (LNL), using the GARFILED-HECTOR set up. During this campaign the DD emission in the fusion reaction $^{16}O + ^{116}Sn$ was measured as a function of the beam energy (in particular at 8.1, at 12 and at 15.6 MeV/u).

The experimental set up was composed of the GARFIELD array (for the measurement of light charged particles); an array of PHOSWICH detectors from FIASCO array (for the measurement of fusion residues); and the HECTOR and HELENA arrays of BaF_2 detectors (the first for the measurement of high-energy gamma rays, the second to discriminate pre-equilibrium neutrons and as time reference).

The second experiment discussed in this thesis was focused on the measurement of the isospin mixing in nuclei in the mass region A = 80, populated using a fusion-evaporation reaction at an average temperature of 2.4 MeV. This is the follow up of a 2008 GARFIELD-HECTOR experiment in which the isospin mixing was measured at higher temperature, namely ~3 MeV. This new experiment will integrate and complete the previous dataset and, in addition, it will allow to extract "experimentally" the value of isospin mixing of ^{80}Zr at zero temperature from the one measured at T>0.

The problem of the isospin symmetry in N ≈ Z nuclei and its breaking, mainly by Coulomb interaction, is a topic which goes beyond nuclear structure [9]. The restoration of the isospin symmetry, observed as the excitation energy of the nucleus increases, can be understood in terms of simple arguments. If the compound nucleus decays on a time scale which is shorter than the time needed for a well-defined isospin state to mix with states with different isospin values, then the isospin symmetry is partially or totally restored [10], [11]. Theoretically, the isospin mixing probability is related to the ratio of the spreading width of the Isobaric Analog State (IAS) with the statistical decay width of the compound nucleus. As the spreading width of IAS is expected to weakly depend on temperature and the decay width of the compound is known to increase with temperature, the interplay of these two effects results in a decrease of the isospin mixing probability as the temperature increases and on the restoration of the symmetry.

Experimentally, if we restrict the comparison to the results obtained using the same experimental technique for systems with Z = 16-40 at T = 2-3 MeV, there is an increase of the degree of isospin mixing with increasing Z and a decrease with increasing temperature. However, the fact that both T and Z are different for each measurement does not allow to completely separate the two effects.

We used the two fusion-evaporation reactions $^{40}Ca + ^{40}Ca$ (entrance channel with isospin I = 0) and $^{37}Cl + ^{44}Ca$ (isospin I ≠ 0) to form the ^{80}Zr and ^{81}Rb nuclei in order to extract the isospin mixing probability from the comparison of the high-energy γ-rays yield from the giant dipole resonance decay measured in the two reactions.

The experiment was performed in may 2011 at LNL (Laboratori Nazionali di Legnaro) using the AGATA Demonstrator coupled to HECTOR+ array. The AGATA Demonstrator consists of an array of segmented HPGe detector used, in this experiment, for the identification of the fusion-evaporation residues and for the measurement of GDR γ-decay. HECTOR+ is composed of 7 large volume $LaBr_3$:Ce scintillators (6 detectors are 3.5″ x 8″ and 1 detector is 3″x 3″) $LaBr_3$:Ce scintillators and it is was used for the measurement of both high and low energy γ-rays with excellent time resolution.

In this work, the preliminary analysis of the isospin mixing experiment will be presented. In particular the performances of HECTOR+ array were compared with the ones of the AGATA Demonstrator.

Large volume $LaBr_3$:Ce crystals are particular suited to measure high-energy gamma rays, as an example, for the measurements of the Giant or Pygmy Dipole resonances. Since a few years, large volume crystals are also available; in Milan, it was built an array of 10 $LaBr_3$:Ce scintillators with a size of 3.5″ x 8″. This array is named HECTOR+ and these crystals are, as far as we know, the largest produced till now. The HECTOR+ array has already been used in several experimental campaigns (Legnaro National Laboratories, Italy, ATOMKI, Hungary, GSI Laboratories, Germany, Oslo University, Norway, and Riken Laboratory, Japan).

$LaBr_3$:Ce scintillators are excellent detectors for γ-rays measurement and spectroscopy, providing an energy resolution of 2.7-3.3% at 662 keV, a sub-nanosecond time resolution and good efficiency due to the density of 5.1 g/cm^3 [12], [13]. The study of signal line-shape allows also the possibility to discriminate between alpha and gamma-rays, using Pulse Shape Analysis techniques [14].

In chapter 1 the properties of the giant dipole resonances will be described, in chapters 2 and 7 the DD and the isospin mixing physics cases

will be, respectively, discussed. In chapters 3 and 8 the GARFIELD-HECTOR array and the experimental set up of isospin mixing experiment will be described. In chapter 4 the data analysis of DD experiment will be presented and in chapter 5 the theoretical calculations and the data interpretation will be discussed. In chapter 6, the performances of large volume $LaBr_3$:Ce detectors will be described. The preliminary analysis of the isospin mixing experiment will be presented in chapter 9.

1. Giant dipole resonances

Giant resonances are fundamental modes of excitation of nuclei, described as collective vibrations involving many if not all nucleons. Section 1.1 will detail the general properties of such states and their classification. Out of all giant resonances, the giant dipole resonance holds particular importance as it is the most easily populated and studied. In section 1.2 a description of its properties at a nuclear temperature equal to zero will be given, while in section 1.3 its behavior with increasing temperature will be described.

1.1. Giant resonances

Giant resonances are basic modes of excitation of nuclei, corresponding to a collective vibrational motion involving many if not all the nucleons. They are a well known example of the common feature of many-body quantum systems to form collective modes [1], [2].

Giant resonances are studied to provide useful information on nuclear structure and on the effective nucleon-nucleon interaction, as well as on the bulk properties of nuclear matter such as the compression modulus, the viscosity or the symmetry energy.

Giant resonances can be seen as high-frequency, damped, nearly elastic vibrations of the density or shape of the nuclear system around an equilibrium value. The vibration amplitude is small, only a few per cent of the nuclear radius. Giant resonances can be described with a Lorentzian curve with 3 parameters: the energy E_R, the width Γ_R, and the strength S_R:

$$\sigma(E) = \frac{\sigma_m(S_R)\,\Gamma_R^2 E^2}{(E^2 - E_R^2) + \Gamma_R E^2} \qquad (1.1)$$

where σ_m is the cross-section value at the maximum, related to the strength via a normalization factor.

Typically, the centroid energy of a giant resonance lies well above the neutron separation energy (8-10 MeV), with a corresponding vibration frequency of the order of 10^{21} Hz. The width of a giant resonance is of the order of 2-5 MeV, meaning that after only a few vibrations the resonance is completely damped. The strength of a giant resonance is limited by and generally close to the maximum allowed by sum rule considerations. It can be shown that in many quantum systems the sum of all transition strengths for a given set of quantum numbers is limited by basic properties of the system, which would be for example the number of nucleons A and the atomic number Z in the case of a nuclear system.

Since a giant resonance is a collective motion of all nucleons, it is to be expected that its gross features do not depend on the detailed structure of the nucleus, but rather on its bulk structure. Giant resonances of various nature were observed over the years throughout the mass table, and the parameters of a given resonance were shown to vary smoothly with the number of nucleons A. It should be noted, though, that the width of a giant resonance depends on the microscopic structure of the nucleus, due to direct particle emission and to the coupling to more complex configurations.

1.1.1. Classification of giant resonances

It is known that there are many types of giant resonance, classified according to the multipolarity L (L=0 monopole resonance, L=1 dipole resonances, L=2 quadruple resonances), the spin S and the isospin T quantum numbers.

The electric oscillations ($\Delta S=0$) are divided in isoscalar ($\Delta T=0$) in which neutrons and protons oscillate in phase and isovector ($\Delta T=1$) in which protons oscillate against neutrons. The magnetic oscillations ($\Delta S=1$) are divided in isoscalar ($\Delta T=0$) in which nucleons with spin up oscillate against nucleons with spin down and isovector in which protons with spin up oscillate against neutrons with spin down and vice versa. In Fig. 1.1 there is a schematic view of this giant resonances classification.

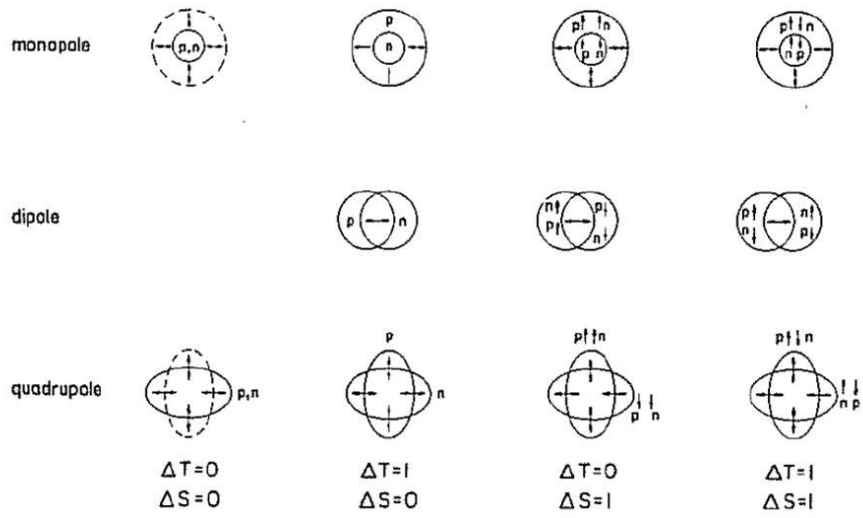

Fig. 1.1: Giant resonances classification as a function of the quantum number L, S, T [1].

1.2.Giant dipole resonance at zero temperature

The Giant Dipole Resonance (GDR) corresponds to a vibration out of phase of protons against neutrons. These collective vibrations were first observed in the 1940s, when was discovered a strong resonant behavior of the nuclear photoabsorption cross section around 15MeV when the stable nuclei were bombarded with high-energy gamma rays. Such vibration can be generated by the oscillating electric field of the incident photons, which generates a force acting on protons causing then to move. Since the center of mass must remain at rest, the neutrons move in the opposite direction. The restoring force of the resulting vibration is ultimately generated by the attractive nuclear force acting between the nucleons [15].

The shape of the resonance is well defined by a Lorentzian distribution and the centroid and the width of the distribution vary smoothly with the nuclear mass A, for the centroid this smooth variation is shown in Fig. 1.2. The systematic of the GDR centroid indicate that the energy varies as:

$$E_{GDR} = 31.2\ A^{-1/3} + \ 20.6\ A^{-1/6} \tag{1.2}$$

and for the nuclei with $A > 100$ the GDR energy as a function of the mass (A) could by approximate by:

$$E_{GDR} = 79\ A^{-1/3} \tag{1.3}$$

as show in Fig. 1.2.

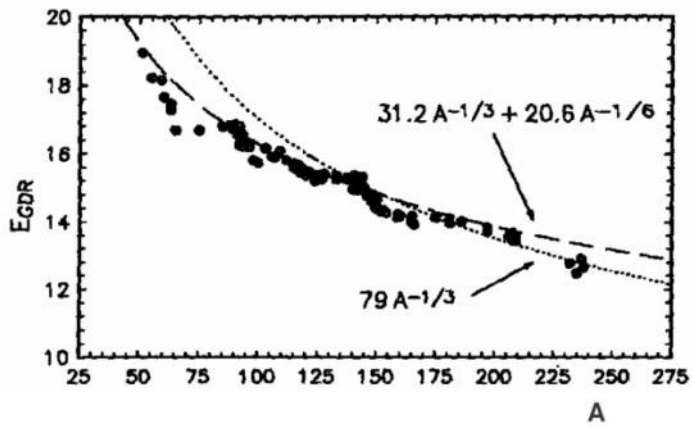

Fig. 1.2: The GDR centroid as a function of mass A [15].

The strength is related to the energy weighted sum rule for the dipole operator. In general for an operator F_λ of a multipolarity λ the sum rule is defined as:

$$S(F_\lambda) = \sum_e (E_e - \ E_0)|\langle e|F_\lambda|0\rangle|^2 \tag{1.4}$$

where $|e\rangle$ and $|0\rangle$ denote an excited state and the ground state respectively. In the case of dipole operator E_1, the strength has the following expression:

$$S(E_1) = \frac{9}{4\pi}\frac{\hbar^2}{2m}\frac{NZ}{A}\ e^2 \sim 14.8\ \frac{NZ}{A}\ e^2\ fm^2\ MeV \tag{1.5}$$

It is found that the experimental data are in agreement, in the 90% of the cases, with the calculated value.

From a microscopic point of view, giant resonances are commonly described as a coherent superposition of particle-hole excitations coupled to the same angular momentum, spin and isospin of the resonance. Instead, to

describe the GDR, from a macroscopic point of view, hydrodynamic collective models are used; these models yield an inverse volume dependence of the centroid energy and an inverse surface one.

The width of the GDR built of a ground state of a nucleus varies from 4 to 8 MeV; the narrowest widths are found in magic nuclei. These widths are given from the sum of the decay width of the resonance $\Gamma^{\uparrow}$ associated to the direct decay of GDR and the spreading width $\Gamma^{\downarrow}$ that is given by a complicate mixing of state n-particle – n holes (with $n \geq 2$) which describes the coupling with the coupled of nucleons; for this reason the GDR width could by write as:

$$\Gamma = \Gamma^{\downarrow} + \Gamma^{\uparrow}. \qquad (1.6)$$

1.3. Giant dipole resonance at finite temperature

The first evidence for the existence of the giant dipole oscillations in excited nuclei was found in the early 1980s in measurement of spectra of γ-rays with transition energies between 5 to 25 MeV emitted by compound nuclei following fusion reactions induced in heavy ion collisions.

Most of the knowledge on giant resonances, was obtained from the study of the gamma decay of the compound nucleus (CN) obtained by collisions between heavy ions. In case of CN, the excitation energy is equally divided between all the single particle degree of freedom. The system is well described in a thermodynamical approach with the formalism of the Micro-canonical ensemble, as consequence it is possible to define an observable that is similar to the thermodynamics temperature:

$$T = \left(\frac{\partial S}{\partial E^*}\right)^{-1} \qquad (1.7)$$

where S is the entropy of the system. For values of mass high enough and high values of excitation energy of the nucleus, as in the cases of interest, a good approximation to the entropy S of the nucleus could be the entropy of a Fermi gas in the grand-canonical ensemble. It is defined as $S = 2\sqrt{aE^*}$, in which a is a parameter related on the density level at the Fermi energy and

the E^* is the excitation energy. In the grand-canonical ensemble it is possible to obtain the temperature $T = \sqrt{E^*/a}$, in which $A/16 < a \leq A/8$.

The density of the levels $\rho(A, E^*)$ of a nucleus with A nucleons at an excitation energy E^*, using a Fermi gas model, can be written as

$$\rho(A, E^*) \approx \frac{e^{2\sqrt{aE^*}}}{\sqrt{48}\, E^*} \qquad (1.8)$$

The fact that the level density display an exponential dependence with the excitation energy implies that also the energy spectra of the γ-rays arising from the decay of a compound nucleus will have an exponential form.

The giant dipole resonance is characterized by a change in the slope of the γ-rays energy spectrum. The total γ spectrum obtained from a fusion-evaporation reaction has an decreasing exponential trend multiplied for a Lorentzian distribution.

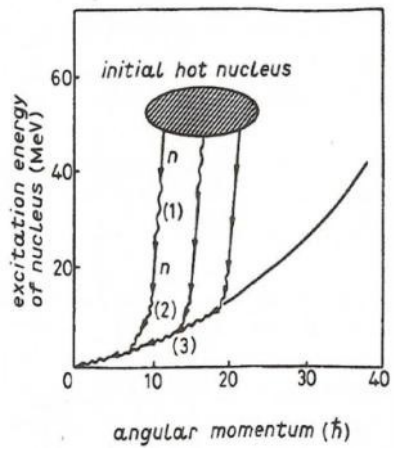

Fig. 1.3: A schematic view of the compound nucleus decay. Giant-dipole-oscillation photons are indicated by (1), lower γ transition by (2) and final decay along the yrast line by (3).

The giant-dipole-oscillation photons, indicated by (1) in Fig. 1.3, are emitted in the early stage in competition with neutrons. Following the neutron emission, slower γ-transitions have time to occur (these transitions are indicated by (2) in Fig. 1.3). Most of the angular momentum is carried off in the final decay by quadrupole radiation that is indicated by (3) in Fig. 1.3.

The probability of photons emission with an energy of E_γ is

$$\frac{d^2P_\gamma}{dE_\gamma dt} = \sigma_0 \frac{E_\gamma^2 \Gamma^2}{\left(E_\gamma^2 - E_{GDR}^2\right)^2 + E_\gamma^2 \Gamma^2} exp\left\{-\frac{E_\gamma}{T}\right\} \qquad (1.9)$$

but the CN nucleus could decay also by particle emission, in particular by neutron evaporation, because they are not affected by the coulomb barrier. In case of CN excitation energy greater than the neutron binding energy ($B_n \sim 8\, MeV$), the neutron emission is 1000 times more favorite respect the emission of a dipolar photons. For a compound nucleus at finite temperature T, the ratio between the photon emission rate and the neutrons emission rate ($dP_n/\, dt \;\approx\; T^2 exp\{-B_n/T\}$) is :

$$\frac{d^2P_\gamma}{dP_n dE_\gamma} = \sigma_0 \frac{\Gamma^2}{\left(E_\gamma^2 - E_{GDR}^2\right)^2 + E_\gamma^2 \Gamma^2} \frac{E_\gamma^2}{T} exp\left\{\frac{B_n - E_\gamma}{T}\right\}. \qquad (1.10)$$

Experimentally the measured emission spectrum could be divided in three regions, as shown in Fig. 1.4, the three region are labeled with a), b) and c).

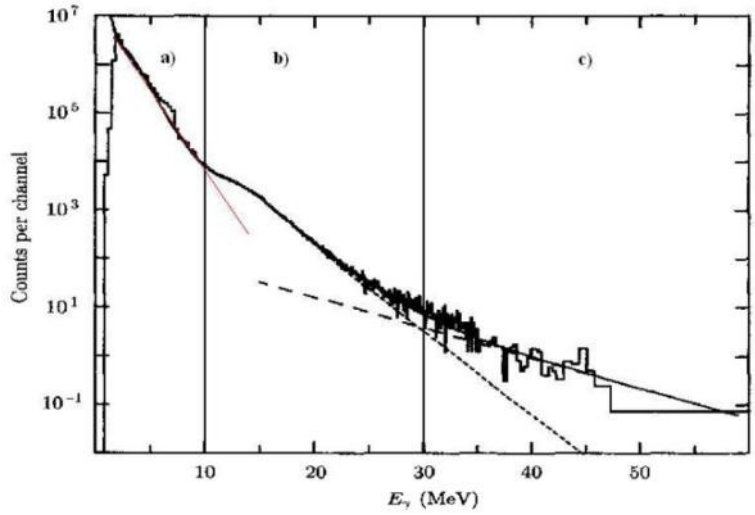

Fig. 1.4: The γ spectrum obtained from a fusion-evaporation reaction. The red line is the exponential fit of the a) region. The data are reproduced by the sum of the spectrum obtained from the statistical model (short dashed line) and the nucleon - nucleon bremsstrahlung (long dashed line) [2].

In region a) $E_\gamma < B_n$, in this case, the argument of the exponential in the equation 1.10 is positive; it become larger as the temperature decrease,

for this reason these low energy photos are emitted mainly when the CN become colder. The slope of the red line in Fig. 1.4 is proportional to the temperature of the emitting nucleus. In region b) $E_\gamma > B_n$, the argument of the exponential in the equation 1.10 is negative and its value increases as the temperature increases; for this reason the most of the photons are emitted in the first stage of the CN. In region c) in which $E_\gamma > 30MeV$, the GDR photons emission is present but the cross section becomes very small. The largest contribution in this region are the cosmic rays and the emission caused by the nucleon - nucleon bremsstrahlung.

In Fig. 1.5 it is shown the trend of GDR cross section for three different temperatures calculated using equation 1.10. It is important to note that the photons at low energy ($E_\gamma < 10\ MeV$) are principally emitted from a CN at low temperature, instead at high energy, photons, in particular the photons at 15 MeV that are typical of the GDR, are emitted from a CN at larger temperatures.

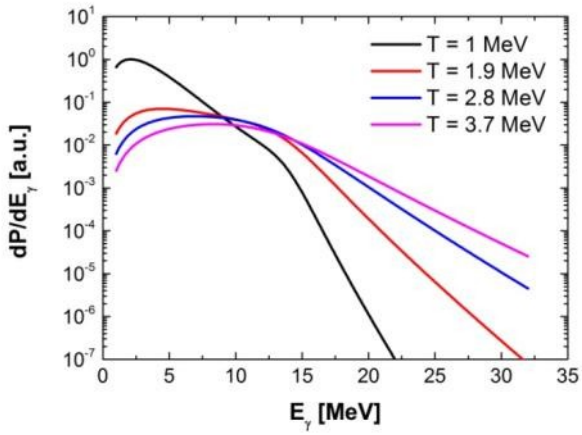

Fig. 1.5: The trend of the GDR cross section describe in equation 1.10 for different value of temperature (T= 1, 1.9, 2.8, 3.7 MeV). The used parameters are E_{GDR} = 14 MeV, Γ = 4.8, 8, 12.4, 14.1 MeV respectively at T=1, 1.9, 2.8 and 3.7 MeV) and B_n = 8 MeV.

The properties of the GDR are given by the parameters of the Lorentzian curve (centroid, FWHM and strength). Centroid and strength do not depend on the excitation energy of the states on which the resonance is built, but they depend only on the number of the nucleons and on the shape

of the nucleus (spherical or deformed). Also in the case of the GDR at finite temperature, the centroid depends on the mass A of the nucleus, in this way:

$$E_{GDR}\,(A) = \; 18\,A^{-1/3} + \; 25\,A^{-1/6}. \qquad (1.11)$$

This dependence is shown in Fig. 1.6; the parametrization of equation 1.11 is different from the one at zero temperature (equation 1.2).

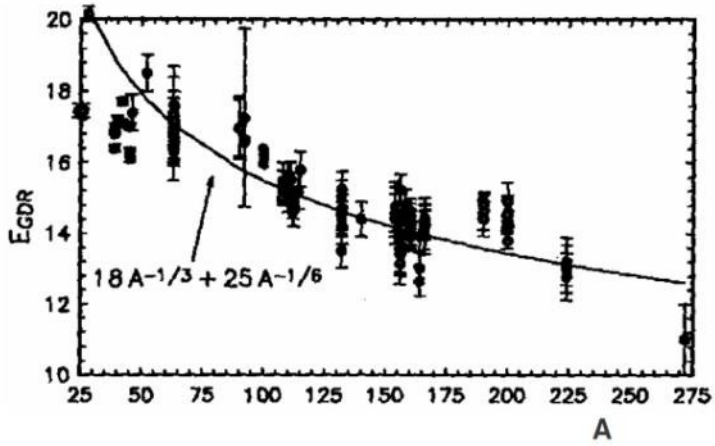

Fig. 1.6: The centroid position as a function of mass A in case of temperature different from zero. The points follows the parameterization of equation 1.11 [15].

The GDR built on a CN state has a width Γ greater than the one found in the ground state and generally increases with nuclear temperature and angular momentum [16]–[18]. The broadening of the GDR peak is only due to the fact that the nucleus experiences a continuous range of deformations and space orientations as described by the Thermal Fluctuation Model (TFM) [15]. Each deformation is parameterized in terms of the Bohr-Wheeler coordinates β, γ, and populated with a probability depending on the associated free energy at the temperature T:

$$P(\beta,\gamma) \sim exp(-F(T,\beta,\gamma)/T) \qquad (1.12)$$

The resulting GDR strength function is given by the weighted superposition of Lorentzian distributions corresponding to all the different deformations that are experienced by the nucleus:

$$\sigma(E) = \int \sum_{k=1}^{3} \sigma_k(E,\beta,\gamma)\, P(T,\beta,\gamma)\beta^4 |sin(3\gamma)| d\beta d\gamma. \qquad (1.13)$$

It is important to remember that each Lorentzian distribution has an intrinsic width that differs from the one at T=0 (Equation 1.6) only due to the fact that both initial and final CN states may have a decay width [19]. The total width is given by the decay width of the resonance $\Gamma^{\downarrow}$ and the spreading width of both initial and the final CN states and it could be written as:

$$\Gamma = \Gamma^{\downarrow} + 2\Gamma^{\uparrow} \qquad (1.14)$$

this description of the total width is however important only from temperature larger of 2 MeV of temperature. To conclude, the width at finite temperature is larger than the case at zero temperature due to the nucleus deformation and the CN decay.

2. Dynamical dipole mode in fusion-evaporation reactions

Fusion-evaporation reactions are one of the most useful tools to populate compound nuclear states, whose decay follows the rules of statistical equilibrium. It is however possible to have pre-equilibrium processes that take place before the thermalization of the compound nucleus, and could invalidate the experimental inference based on the statistical model. It is therefore important to know in detail the dynamics of the fusion process.

In particular, we focused in this work on the dynamical dipole emission, which is a process that takes place when there is a N/Z asymmetry between projectile and target in a fusion-evaporation reaction. This process is useful both to extract information on the dynamics of the fusion process and to obtain a measure of the symmetry term of the nuclear equation of state.

In section 2.1 the general properties of fusion-evaporation reactions will be given, while section 2.2 will described the dynamical dipole emission, in particular with respect to its relation to the nuclear equation of state (section 2.2.1), its dependence on the N/Z asymmetry (section 2.2.2) and on beam energy (section 2.2.3), and the angular distribution of the emitted γ-rays (section 2.2.4). Finally, in section 2.3 the theoretical model used in this work to evaluate the experimental results, the Boltzmann Nordheim Vlasov (BNV) model, will be discussed.

2.1. Fusion-evaporation reactions

The investigation of the photon emission from the dynamical dipole formed during the process leading to fusion in N/Z asymmetric heavy-ion reaction is important because it can provide information on isospin dynamics in the fusion process.

Heavy-ion fusion reactions are the reaction mechanism capable to produce highly-excited and rotating compound nuclei, whose features and decay mode do not depend on the entrance channel of the reaction except for energy, parity and angular momentum conservation. During a fusion-evaporation reaction a deep potential well is built from the overlap of the potentials of the two reaction partners. Inside this well the kinetic energy of the projectile is dissipated in collisions, until thermal equilibrium is achieved [20].

The fusion process can be schematically divided into three steps: an approach phase during which each nucleus feels only the Coulomb field of its partner and ends when the nuclear interaction starts to dominate, a second phase that is characterized by a rapid equilibration of the energy and the angular momentum transferred from the relative motion to the internal degrees of freedom, leading to the formation of a compound nucleus, and the last phase in which occurs the statistical decay of the CN.

The complete fusion cross section depends on: the incoming energy of the projectile, the mass, the charge asymmetry between projectile and target and the impact parameter of the collision.

There is a value of the angular momentum (or impact parameter) beyond which the fission barrier becomes smaller than the neutron binding energy and fission becomes the preferred decay mode. In first approximation, using a liquid drop model the critical value of angular momentum depends only on the compound nucleus mass (A) and as shown in Fig. 2.1 [21]. The dashed curve in Fig. 2.1 gives an indication of the maximum amount of angular momentum that a compound nucleus could support and still survive the risk of the fission in the deexcitation process.

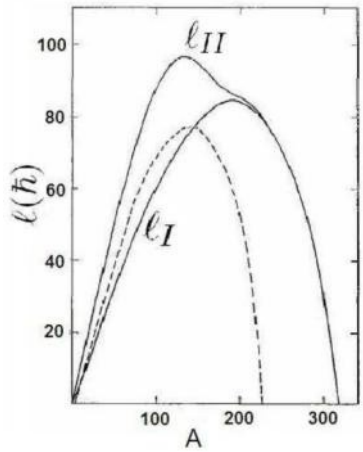

Fig. 2.1: The maximum angular momentum that a stable nucleus can support surviving fission is shown with a dashed line. It corresponds to the value of the angular momentum where the height of the fission barrier is equal to 8 MeV, corresponding to the average neutron binding energy. The barrier vanishes at the continuous line labeled l_{II} , while for angular momentum higher than the one labeled with l_I the nucleus undergoes a transition to a triaxial shape.

The timescale of a fusion-evaporation reaction is the following. From 10^{-24} s to 10^{-21} s there is the compound nucleus formation, where the energy and momentum equilibrates and if the colliding nuclei have a different N/Z ratio, a charge equilibration process takes place. The related neutron-proton motion has the features of a collective oscillation and it is associated to a γ emission, the so called Dynamical Dipole (DD) emission (that is called also prompt dipole emission). For time greater than 10^{-21} s there is the CN statistical decay a schematic view of the CN statistical decay is shown in Fig. 2.2. In the first stage of the statistical decay, when the excitation energy is larger of the neutrons separation energy there is the neutron evaporation; in this early state also the high-energy gamma rays of the GDR are emitted. The GDR gamma decay has a branching ratio of 0.1% with respect to the neutron emission. When the excitation energy become smaller than the neutron separation energy there is the low-energy γ decay.

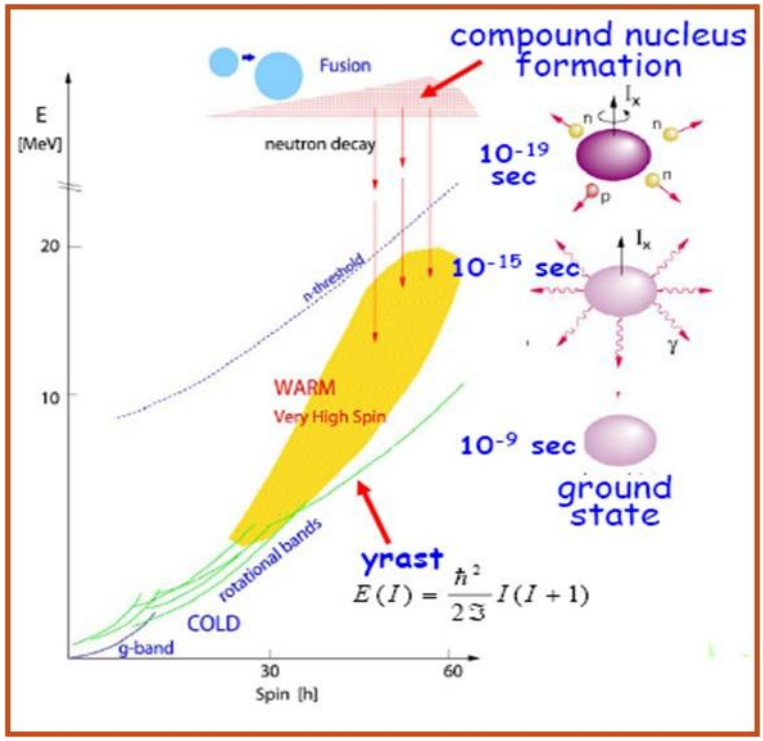

Fig. 2.2: A schematic view of the CN statistical decay.

2.2. The dynamical dipole emission

The Dynamical dipole emission provides information on isospin dynamics in a fusion process and on the symmetry term of the nuclear equation of state (EOS); the symmetry term of the nuclear EOS has implication in nuclear astrophysics problems such as neutrons stars and elements burning in supernovae.

When a heavy-ion reaction is performed, there could be a different N/Z ratio between projectile and target ($N/Z_{proj} \neq N/Z_{targ}$), in this case a charge equilibration process takes place before CN thermalization through a collective motion of nucleons generating an oscillating electric dipole which is damped after 3-5 vibrations [22]. If there is a charge asymmetry in the entrance channels, at the time of the compound nucleus formation, the pre-

equilibrium photon emission is expected from the dipole oscillations in the isospin transfer dynamics.

A way to quantify the N/Z asymmetry between projectile and target is to define the dipole moment D (t=0) of the system when the colliding nuclei (that could be approximated as rigid spheres with radius $r = r_0 A^{1/3}$) get in contact:

$$D(t=0) = \frac{NZ}{A}|X_z(t=0) - X_N(t=0)| = \frac{r_0\left(A_p^{1/3} + A_t^{1/3}\right)}{A} Z_p Z_t \left|\frac{N_t}{Z_t} - \frac{N_p}{Z_p}\right| \quad (2.1)$$

where X_n and X_p are the proton and the neutron coordinates in the center of masses reference frame and the subscripts p and t refer to projectile and target, respectively.

The DD emission could be identified by comparing the γ-rays spectra of a reaction in which projectile and target have the same N/Z and of a reaction in which projectile and target have a different N/Z ratio. By this comparison it is possible to see a difference in the γ yield in the energy range of 10-22MeV that could be attributed to the DD emission. The extra-gamma yield can be expressed in terms of the increase relative to the statistical decay. If we take a and b as the integrals of the yield for the N/Z asymmetric and symmetric reaction, the increase is defined as:

$$Increase = \frac{a-b}{b} \quad (2.2)$$

the increase has been measured up to now for the systems listed in Tab. 2.1.

The existing experimental data [3]–[6], [23], [24], shown in Tab. 2.1, are still rather scarce but some data exists especially in the region of $A = 132$. In all the tabulated experiments an γ extra-yield, that is associated with the pre-equilibrium dipole mode, were measured, that is attributed to the DD γ emission. The value of the dipole moment (D), in the systems where the DD emission has been studied, ranges from 8.4 fm [24] to 22.1 fm [23] as is shown in the third column of Tab. 2.1.

Ex.#	Reaction	CN	E_{beam} [MeV/u]	D [fm]	Increase	Ref.
1	$^{40}Ca + ^{100}Mo$	^{140}Sm	4.5	22.1	0.16	[23]
	$^{36}S + ^{104}Pd$	^{140}Sm	4.0	0.5	(8-18 MeV)	
2	$^{16}O + ^{98}Mo$	^{114}Sn	8.1	8.4	0.36	[24]
	$^{48}Ti + ^{64}Ni$	^{112}Sn	5.0	5.2	(8-20 MeV)	
3	$^{32}S + ^{100}Mo$	^{132}Ce	6.1	18.2	0.016	[4]
	$^{36}S + ^{96}Mo$	^{132}Ce	6.7	1.7	(8-21 MeV)	
3	$^{32}S + ^{100}Mo$	^{132}Ce	9.3	18.2	0.25	[4]
	$^{36}S + ^{96}Mo$	^{132}Ce	8.9	1.7	(8-21 MeV)	
3	$^{36}Ar + ^{96}Zr$	^{132}Ce	16.0	20.6	0.138	[5]
	$^{40}Ar + ^{92}Zr$	^{132}Ce	15.0	4.0	(8-21 MeV)	
4	$^{16}O + ^{116}Sn$	^{132}Ce	8.1	8.6	0.08	[6]
	$^{64}Ni + ^{68}Zn$	^{132}Ce	4.7	1.2	(10-22 MeV)	
4	$^{16}O + ^{116}Sn$	^{132}Ce	15.6	8.6	0.11	[6]
	$^{64}Ni + ^{68}Zn$	^{132}Ce	7.8	1.2	(10-22 MeV)	

Tab. 2.1: In the first column the system for which the DD emission has been measured up to now, in the second one the beam energy, in the third one the dipole moment calculated using equation 2.1the increase of the γ emission associated to the DD and in the last one the reference.

The experiment, labeled with 1 in Tab. 2.1, was performed at Chalk River Laboratories and the used set up was composed by a 8π spectrometer to detect the γ rays, which includes a spherical calorimeter of 71 bismuth germinate BGO scintillators surrounded by an array of 20 Compton suppressed HPGe detectors. It was found that in the asymmetric reaction (the first one in column two of Tab. 2.1) has a pre-equilibrium yield of 16% respect the symmetric reaction as described in [23] and as shown in Fig. 2.3. It was the first experiment in which the pre-equilibrium emission was studied.

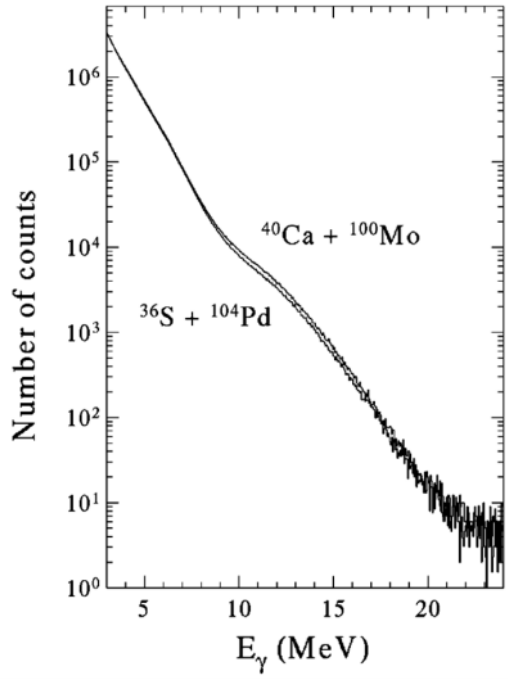

Fig. 2.3: The measured γ rays spectra of the reactions ($^{40}Ca + {}^{100}Mo$ the asymmetric one and $^{36}S + {}^{104}Pd$ the symmetric one). It is possible to see an excess of counts in the asymmetric reaction spectrum that could be attributed to the pre-equilibrium emission [23].

In the experiment, labeled with 2 in Tab. 2.1, the high-energy γ-ray spectra from the fusion reactions ^{16}O + ^{98}Mo at 130 MeV and ^{48}Ti + ^{64}Ni at 240 MeV, populating the ^{114}Sn and ^{112}Sn compound nuclei at the excitation energy of 110 MeV were measured. The experiment was performed at Laboratori Nazionali di Legnaro. The experimental set-up used was the 4π γ-ray spectrometer GASP, coupled to two large-volume, cylindrical (10 cm x 10 cm) bismuth germinate (BGO) crystals, temperature-stabilized and gain-monitored. The comparison of the spectra shows a ~36% enhancement of the γ-ray yield in the giant dipole resonance region ($E_\gamma \geq$ 8MeV) when the ^{16}O-induced reaction is considered as shown in Fig. 2.4. This enhancement is interpreted as due to effects related to the N/Z asymmetry between the target and the projectile in the entrance channel.

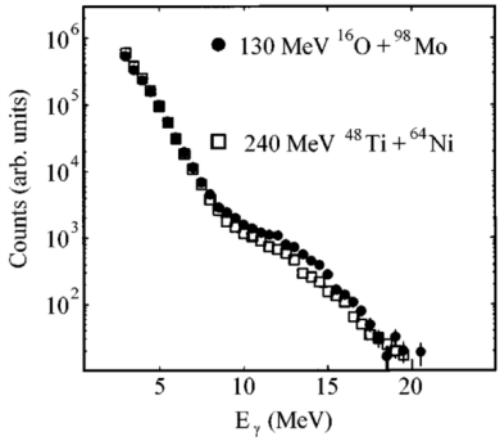

Fig. 2.4: The measured γ rays spectra of the reactions ($^{16}O + {}^{98}Mo$ the asymmetric one and $^{48}Ti + {}^{64}Ni$ the symmetric one). It is possible to see an excess of counts in the asymmetric reaction spectrum that could be attributed to the pre-equilibrium emission [24].

In the experiment labeled as 3 in Tab. 2.1, high-energy γ rays and light charged particles from the $^{32}S + {}^{100}Mo$, $^{36}S + {}^{96}Mo$, $^{36}Ar + {}^{96}Zr$, and $^{40}Ar + {}^{92}Zr$ reactions, were measured in coincidence with evaporation residues by MEDEA multidetector array coupled to four parallel plate avalanche counters. The aim of this experiment was to investigate the prompt γ radiation, emitted in the decay of the dynamical dipole mode, in $6 - 16$ MeV/u energy range and to map its beam energy dependence [3]–[5]. The results obtained in this experiment are shown in Fig. 2.8.

The results obtained from the experiment labeled as 4 in Tab. 2.1 are described in detail in this thesis, because as explained in section 2.2.3, the measurement of the DD pre-equilibrium γ emission for the system $^{16}O + {}^{116}Sn$ at an intermediate point (12 MeV/u) with respect to the data in reference [6] is the aim of this thesis.

2.2.1. Relation to the symmetry term of the nuclear equation of state

The energy per particle in a nuclear system characterized by a total density ρ (sum of the neutron and proton densities ρ_n and ρ_p), and by a local asymmetry $\delta = (\rho_n - \rho_p)/\rho$ is usually written as:

$$\frac{E}{A}(\rho, \delta) = \frac{E}{A}(\rho, \delta = 0) + S(\rho)\delta^2. \quad (2.3)$$

Odd power of δ are forbidden by the isospin symmetry and term proportional to δ^4 is not reported because it is negligible. The above equation defines the so-called symmetry energy that is $S(\delta)$ [25].

There are two different Skyrme parameterizations of the symmetry term of the Equation of State, namely an asy-stiff and an asy-soft one that are shown in Fig. 2.5 [26]. The symmetry term is usually written as:

$$S(\rho) = \frac{E_{symm}}{A} = \frac{\epsilon_F}{3} + \frac{C(\rho)}{2\rho_0}\rho \quad (2.4)$$

where ϵ_F is the Fermi energy and $C(\rho)/\rho_0 = a - b\rho$, in the soft case $a = 482\ MeV\ fm^{-3}$ and $b = -1638\ MeV\ fm^{-6}$. Whereas in the stiff case C does not depend to ρ and $C = 32MeV$. These values are obtained when the EOS is defined as Taylor sum formula. The derivative of the symmetry energy at saturation is related to the widely used "slope" parameter L_{symm} by:

$$L_{symm} = 3\rho_0 \frac{\partial(E_{symm}/A)}{\partial\rho}\bigg|_{\rho=\rho_0}. \quad (2.5)$$

Using equation 2.4 and 2.5, it is possible to calculate L_{symm} that is $L_{symm} = 72.6\ MeV$ for the stiff parameterization, instead $L_{symm} = 14.5\ MeV$ for the soft one.

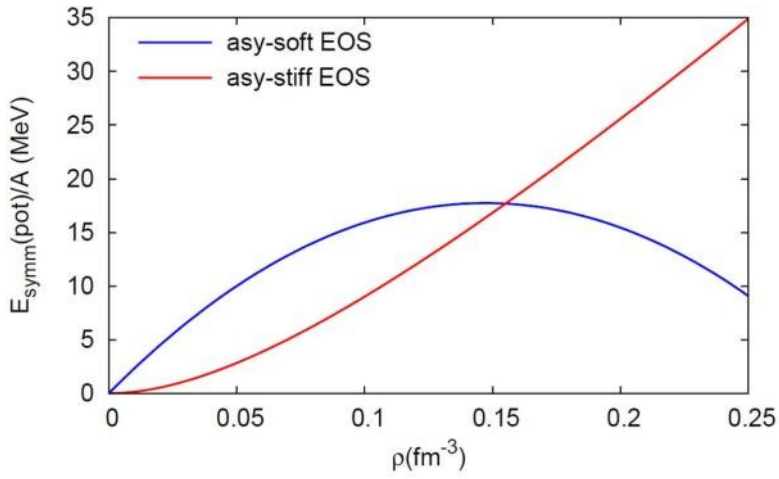

Fig. 2.5: Symmetry energy as a function of the density; the two parameterization stiff (red line) and soft (blue line) are shown.

The sensitivity of DD to the density dependence of the symmetry term of the EOS was investigated in [8], [27] with a system displaying a high N/Z asymmetry corresponding to $D(t = 0) = 45\ fm$ (calculated with equation 2.1). Such an asymmetry can be achieved only using a radioactive isotope as a projectile. In [8], [27] the used projectile was ^{132}Sn. The observables that display sensitivity to the different parameterizations of the density dependence of the EOS are: centroid, width, integral of the γ spectrum, the evolution of the emission probability. The difference in the Bremsstralung spectra between the two parameterization (stiff and soft) for the system ^{132}Sn + ^{58}Ni are shown in Fig. 2.6.

Asy-soft parameterization yields an higher restoring force for density lower than saturation (where DD oscillation develops) and therefore an higher frequency and a faster damping of the oscillation, corresponding respectively to an higher centroid (1 MeV) and larger width of the emission spectrum. Asy-stiff parameterization corresponds to a slower dynamics and therefore a weaker (respect to the asy-soft case) emission probability.

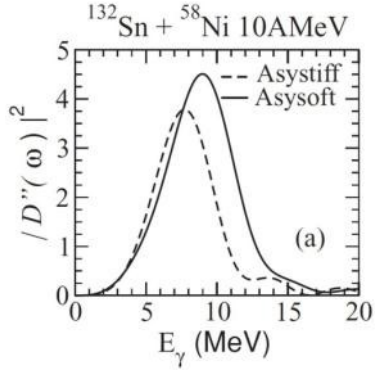

Fig. 2.6: Power spectra of the dipole acceleration at b=4 fm. Solid line correspond to asy-soft EOS and the dashed line to the asy-stiff EOS [8].

2.2.2. Dynamical dipole dependence on dipole moment

The dynamical dipole is expected to depend on the N/Z asymmetry that is related to the dipole moment (see equation 2.1). The experimental data to study this dependence are scarce and moreover do not seem to follow the expected theoretical trend. The data show a rather flat behavior in contrast with the theoretical predictions (see Fig. 2.7).

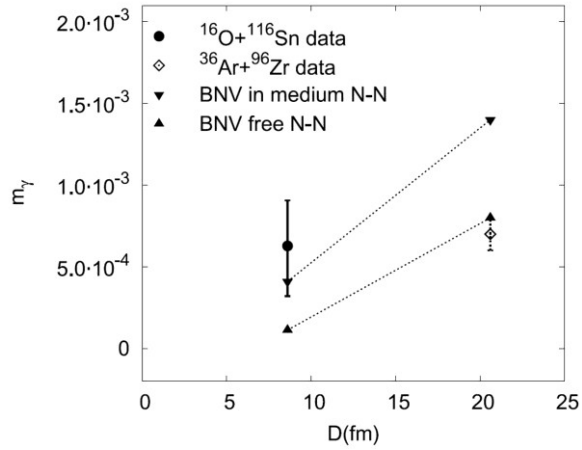

Fig. 2.7: The DD yield as function of the dipole moment. The datum at 15.6 MeV/u for the ^{16}O + ^{116}Sn reaction in comparison with the datum and calculations reported in [3] for the ^{36}Ar+^{96}Zr reaction at 16 MeV/u are shown.

To reach very asymmetric N/Z values one will need radioactive beam facilities and high beam intensities. However at the present time we need a better understanding of this effect.

2.2.3. Dynamical dipole dependence on beam energy

Although the data are still rather scarce, the existing experimental information shows that, in general, there is a dependence of the dynamical dipole strength on the beam energy. Three of the reactions listed in Tab. 2.1 produce the CN ^{132}Ce, with beam energies ranging from 6 to 16 MeV/u. This allows to make several observations on entrance-channel and beam-energy dependence of DD emission.

The beam-energy dependence observed with the systems ^{32}S+^{100}Mo [4] and ^{36}Ar+^{96}Zr [5] (with a very similar dipole moment D=18.2 and 20.6 fm, respectively) displays a rise and fall behavior (see Fig. 2.8) but the data do not seem in agreement with the theoretical prediction for the DD emission of these systems. The total γ yield, obtained from the experimental data, seems to increase almost a factor 10 going from 6 to 9 MeV/u; going from 9 to 16 MeV/u the yield seems to decrease of a factor 2.

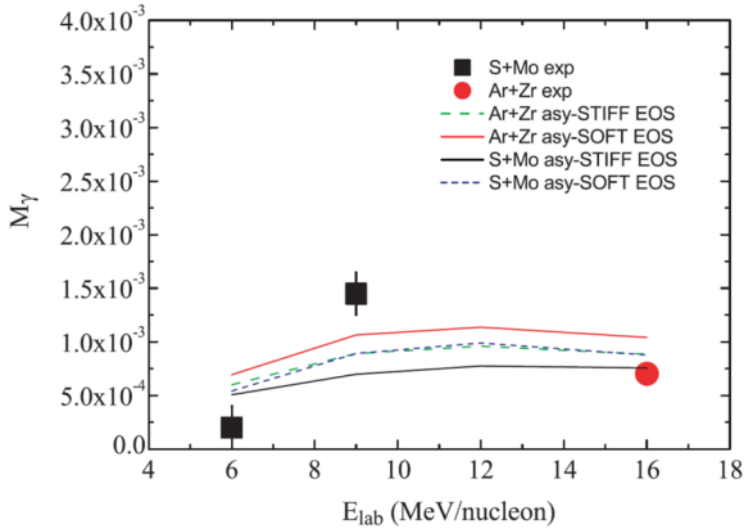

Fig. 2.8: The measured DD γ multiplicity is compared with theoretical calculations [3].

A low DD total γ yield for low beam energy is attributed to a slow dynamics in the neck region between projectile and target, where the DD oscillation develops, and therefore a reduced dipole acceleration results. A decrease of the total γ yield for high beam energies can be explained with the damping related to fast processes like pre-equilibrium neutron emission and nucleon-nucleon direct collisions that reduce the N/Z asymmetry (and $D(0)$) and damp the isovector oscillation. However, this simple arguments, are not able to characterize the calculated total yield which remains practically constant [3].

The aim of the experiment analyzed in this thesis is the study of the dependence of the DD γ emission on the beam energy for the system ^{16}O + ^{116}Sn. The pre-equilibrium γ yield was already measured for this system at 8.1 and 15.6 MeV/u, the result obtained for this system are represented in Fig. 2.9. In this thesis the DD γ emission has been studied at 12 MeV/u, that is an intermediate point. The point at 12 MeV/u is useful to verify if the rise and fall trend is confirmed in a similar system, to refine the theoretical calculation and to perform a more exclusive experiment.

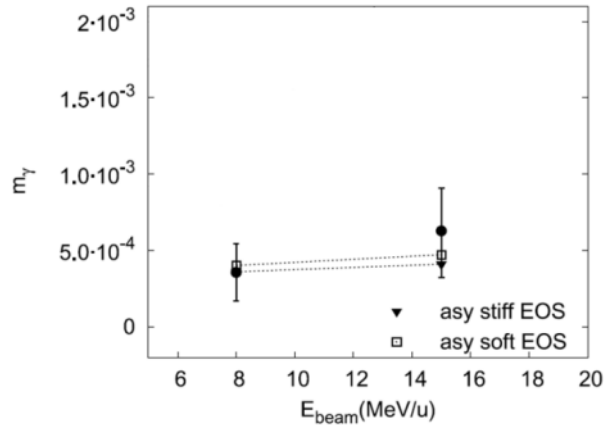

Fig. 2.9: The measured and calculated total γ multiplicity as a function of the beam energy for the system ^{16}O+^{116}Sn (blue point). The calculations performed with the BNV model correspond to the two different parameterizations (stiff in green and soft in red) of the symmetry term [6].

2.2.4. Angular distribution of the dynamical dipole emission

Angular distribution is expected to be dipolar ($W(\theta) = 1 - P_2(cos\theta)$) but due to the rotation of dipolar axis, such distribution is expected to be quenched, indeed the angular distribution could be described by this formula:

$$W(\theta) = 1 - a_2 P_2(cos\theta) \qquad (2.6)$$

where $P_2(cos\theta)$ is the Legendre polynomial and a_2 is a quenching factor.

Recently, also the angular distribution of the γ-ray emission produced by DD oscillation was measured [5], [6]. In both measurements the angular distribution displays a maximum at $\theta = 90°$ with respect to the beam axis. The result obtained, in the two references [5], [6] are different. Data reported in the left panel of Fig. 2.10 show a pure dipole angular distribution (not quenched) is the one of a pure dipole, instead data in the right panel of Fig. 2.10 show a quenched angular distribution with respect to a pure dipole.

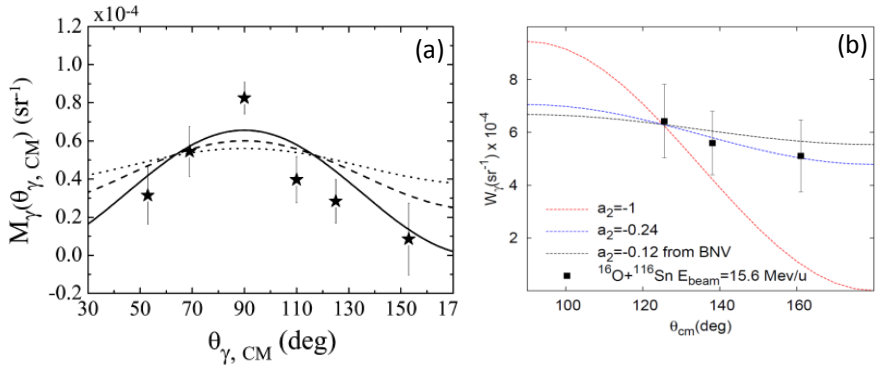

Fig. 2.10: In the panel (a) the angular distribution found in reference [5], in the panel (b) the angular distribution found in reference [6].

The data of [6] are in agreement with the theoretical model. The model predicts that the DD initially is preferentially oriented along the beam axis and then performs a rotation with an angular momentum depending on the relative velocity and impact parameters. As can be intuitively inferred from

Fig. 2.11, large angles with respect to the beam axis are probed mostly in a peripheral collision or in the latter stages of a DD oscillation.

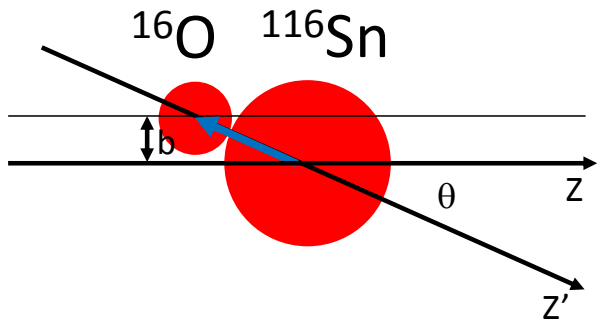

Fig. 2.11: Pictorial view of the fusion reaction: the projectile 16O impinges on the target ^{116}Sn with a given impact parameter b.

2.3. The Boltzmann Nordheim Vlasov (BNV) model

Several models have been developed to describe dynamical dipole emission, both statistical [23] and dynamical. In particular, semi-classical transport models were successfully developed in recent years to describe heavy-ion nuclear reactions at intermediate and high energies. These are, for example, Boltzmann-Nordheim-Vlasov (BNV) model [7], [8], [22], and Time-Dependent Hartree-Fock model [28], [29].

The study of a nuclear reaction is a typical many-body problem. Many features of nuclear dynamics at low energy beams (up to $\sim 15\ MeV/u$) can be studied using one-body models, such as the Time-Dependent Hartree-Fock theory, or it classical analog, the Vlasov equation [30]. The models aim to follow the evolution of the one-body density matrix, which is propagated in a self consistent mean field. This description is reliable as long as the energy is low enough that the residual two body correlations can be neglected because they are mostly suppressed by the Pauli blocking of the final state.

The BNV model is based on the Vlasov equation that permit to describe the time evolution of the one body distribution function, on the fact that the nucleon could do only binary collision (Boltzmann) and on the Pauli principle that was introduced in this formalism by Nordheim.

To obtain the Vlasov equation it is necessary to start from the fact that to describe the time evolution of one body distribution function, the two body distribution function has to be used. For this reason it was used the assumption of molecular chaos: the momenta of nucleons are not correlated. This approximation could be written as:

$$f_2(r_1, r_2, p_1, p_2, t) \sim f_1(r_1, p_1, t) f_1(r_2, p_2, t);$$

from this approximation it is possible to write the Vlasov equation:

$$\left[\frac{\partial}{\partial t} + \frac{p}{m}\frac{\partial}{\partial r} - \frac{\partial}{\partial r}\overline{U}(r,t)\frac{\partial}{\partial p}\right] f_1(r,p,t) = 0 \qquad (2.7)$$

where $f_1(r,p,t)$ is the one body distribution function and $\overline{U}(r,t)$ is a self consistent mean field term.

If the nucleons collide, it is possible to neglect the three body collisions and to consider only the binary collisions (that are the collisions between two nucleons). Moreover it is necessary to introduce the Pauli blocking principle, in this case not all the final states are available. In the case of the Pauli blocking principle, the Boltzmann transport equation can be written as:

$$\left[\frac{\partial}{\partial t} + \frac{p}{m}\frac{\partial}{\partial r} - \frac{\partial}{\partial r}\overline{U}(r,t)\frac{\partial}{\partial p}\right] f(r,p,t) = \int d^3p_2 \; d\Omega \, |v_1 - v_2| \frac{d\sigma}{d\Omega}(f_1' f_2' - f_1 f_2) \qquad (2.8)$$

that could be written in a shorter way that is the Boltzmann Nordheim Vlasov equation:

$$\frac{df}{dt} - \{h(f), f\} = I_{coll} \qquad (2.9)$$

where $h(f)$ is an effective Hamiltonian that include the mean field term and the $\{h(f), f\}$ are the Poisson brackets.

The collision integral is calculated using in-medium reduced nucleon-nucleon cross sections. It depends on nucleon isospin as well as energy and angle of the collision, the mean field is built from Skyrme forces.

The solution of Boltzmann-Nordheim-Vlasov equation is the one-body distribution function $f(r,p,t)$ for a system of A nucleons. This is defined with the technique of test particles, consisting in representing each nucleon with a set of N_{test} test particles in order to achieve more continuity in the nucleon distribution within the nuclear volume. The resulting nucleon distribution is obtained as the sum on N_{test} A distributions that are the product of a Dirac δ in momentum space and a Gaussian $G(r)$ in real space. The one-body distribution function could be written as:

$$f(r,p,t) = \frac{1}{N_{test}} \sum_{i=1}^{N_{test}A} G\big(r - r_i(t)\big)\, \delta\big(p - p_i(t)\big) \qquad (2.10)$$

Macroscopic quantities as the dipole moment of the system $D(t)$ are calculated for each simulated event at each time step averaging over all nucleons with the function $f(r,p,t)$ and then normalized to obtain a result that does not depend on N_{test}; an example of dipole moment evolution calculated with the BNV model is shown in left panel of Fig. 2.12. The γ emission associated with the DD mode is calculated with the Bremsstrahlung formula:

$$\frac{dp}{dE_\gamma} = \frac{2e^2}{3\pi\hbar c^3 E_\gamma}\left(\frac{NZ}{A}\right)^2 |D''(\omega)|^2 \qquad (2.11)$$

where $D''(\omega) = \int_{t_0}^{t_{max}} D''(t) e^{i\omega t}\, dt$ is the Fourier transform of the dipole acceleration $D''(t)$. The times $t_0$and t_{max} correspond to the onset of the DD and the damping of the collective oscillation and have to be evaluated event by event. Examples of the Bremsstrahlung spectra are shown in the right panel of Fig. 2.12. The spiral evolution of the dipole moment in phase space (see Fig. 2.13) is a signature of the collective character of the DD oscillation.

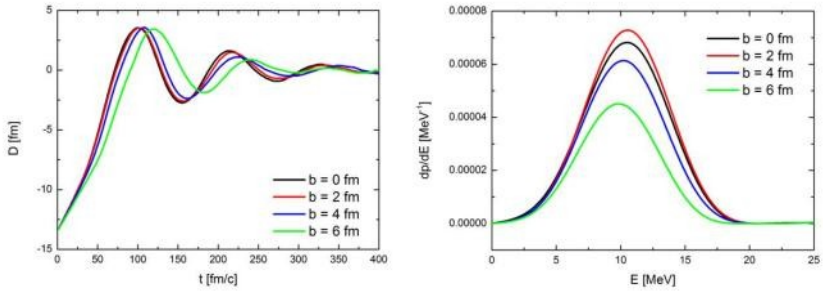

Fig. 2.12: In the left panel an example of the dipole moment evolution at with time from a BNV simulation for a ^{16}O + ^{116}Sn reaction at projectile energy of 12MeV/u for different impact parameters. In the right panel the γ emission probability, for the same system, calculated with bremsstrahlung formula (equation .2.11).

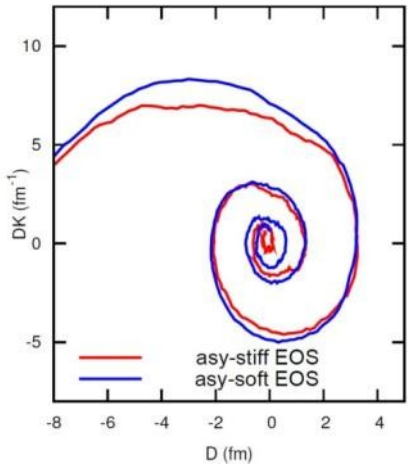

Fig. 2.13: The dipole moment evolution in the phase space.

In order to reproduce the measured observables, simulations are performed at several impact parameters relevant for fusion and the results are finally averaged on the experimental fusion cross section versus impact parameter curve. The average is performed with a weight proportional to the cross section corresponding to each impact parameter. For central collisions this is well approximated with annuli, but as soon as we move to more peripheral collisions (quasi-)fission and break-up reactions may compete with fusion and therefore the annuli might overestimate the fusion

cross section. The correct procedure to perform such weighted average is still an open problem and would require a theoretical link between the CN angular momentum (the experimental observable) and the impact parameter (the theoretical observable) through a complete simulation of the fusion-thermalization process. Indeed for high impact parameters the reaction cross section is high because the "annuli" has a large area. The contribution of non fusion reaction mechanism (quasi-fusion, deep inelastic, …) significantly reduce the fusion cross section. The pre-equilibrium particle evaporation reduce the CN angular momentum making the semi-classical relation (equation 5.1) overestimating the weights used to do the average.

3. Experimental set up of the dynamical dipole experiment

The experiment that will be discussed in this part of this thesis was performed in May 2009 in Laboratori Nazionali di Legnaro. The reaction studied is

$$^{16}O + ^{116}Sn = ^{132}Ce^{*} \qquad (3.1)$$

at 12 MeV/u. The beam of ^{16}O was produced using the TANDEM ALPI accelerators of Legnaro. The experimental set up used during this experiment is the GARFIELD - HECTOR apparatus.

The GARFIELD (General ARray for Fragment Identification and for Emitted Light particles in Dissipative collision) and HECTOR arrays have been used coupled in two experimental campaigns, one in 2002-2003 and one in 2008-2009. In this thesis the experimental set up, the data analysis and the results of the last experiment (May 2009) of these campaigns will be discussed.

The HECTOR array [31] consists of eight large volume (about 14x18 cm) BaF_2 crystals used for high energy γ-rays detection, and will be described in detail in section 3.1. Two clusters of the HELENA BaF_2 crystals were inserted in this experimental set up; the first one to be used as time reference and the second one to measure the pre-equilibrium neutrons; see section 3.2. The GARFIELD array [32] measures light charged particles, it consists of ΔE-E gaseous micro strip and CsI(Tl) scintillation detectors lodged in the same gas volume, and will be described in section 3.3. The evaporated residues are detected in a wall of 32 PHOSWICH detectors, from FIASCO array [33], placed at forward angle, appropriate to measure also fission fragments; the phoswich detectors are made of three different scintillation detectors: two inorganic scintillation detectors and a CsI(Tl); more information will be given in section 3.4. A schematic view of the detectors is shown in Fig. 3.1.

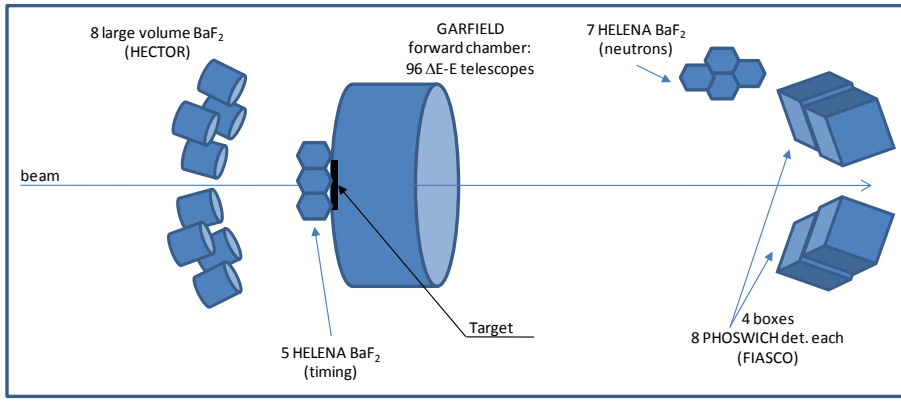

Fig. 3.1: Schematic layout of the GARFIELD-HECTOR experimental set up.

The all experimental set up is placed inside the GARFILED scattering chamber (a cylinder of ~3m of diameter and 5m of length). All detectors operated under vacuum (~10^{-5} mbar).

Both the GARFIELD array detectors and the PHOSWICH detectors use digital electronics, which will be described in section 3.5. Section 3.6 will detail the trigger conditions and the data acquisition system.

3.1. The HECTOR array

The HECTOR array was used to measure the high-energy gamma ray from the DD emission and from the GDR decay. They were also used to select the prompt gamma rays from the neutron background.

The HECTOR array is composed of 8 large volume (about 3dm^3) BaF_2 scintillators of 14.5 cm in diameter and 17.5 cm in length. Each crystal is coupled to a fast photomultiplier tube 9823QA connetcted to an active voltage divider. The BaF_2 scintillators have an high efficiency due to the high atomic number (Z=74). The density BaF_2 scintillators is quite high (4.88 g/cm^3). The time resolution of the HECTOR detector is very good (smaller than 1 ns), but they have a poor energy resolution of about 12% at 1 MeV. These characteristics made these detectors the best candidate for the measurement of high-energy γ rays from the GDR decay. Moreover, a very good time resolution allows to discriminate the neutrons from gammas

using the Time of Flight (ToF) technique. Instead, the poor energy resolution is not critical because we have to measure a continuum spectrum.

The HECTOR array was placed inside the GARFIELD scattering chamber in backward position with respect to the target as shown in Fig. 3.1, in Fig. 3.2 and in the left panel of Fig. 3.3. This configuration was chosen to minimize the detection of the light charge particles, due to the reaction kinematics. The detectors were placed at 30 cm from the target. The central angle of all detectors are listed in Tab. 3.1.

# BaF_2	**1**	**2**	**3**	**4**	**5**	**6**	**7**	**8**
θ	160°	137°	124°	150°	150°	124°	137°	160°

Tab. 3.1: The position of the hector detectors; θ is the angle of each detector with respect to the beam axis.

The absolute full energy peak efficiency of HECTOR array in the present configuration is about 3% at 10 MeV.

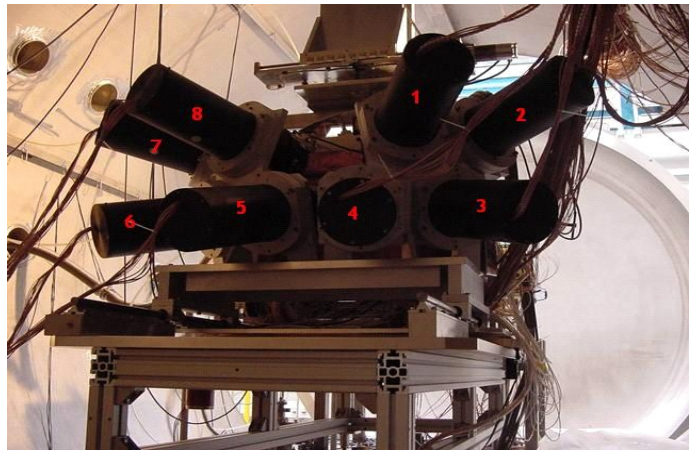

Fig. 3.2: Picture of the hector detectors inside the GARFIELD scattering chamber.

The detectors were used under vacuum (about 10^{-5} mbar) in the scattering chamber, for this reason, to avoid the overheating of the electronics, the voltage dividers are placed outside the GARFIELD chamber.

Two signals are provided by the voltage divider, a fast signal and a slow one, collected at the anode and at an intermediate dynode, respectively.

The fast signal is sent also to the temporal electronic chain, while the slow one is used to build the energy chain, both operating with analog electronics.

3.2. The HELENA detectors

Two clusters of HELENA detectors were inserted into the experimental set up; the first one as time reference and the second one was used to measure the pre-equilibrium neutrons.

The HELENA detectors are BaF_2 scintillators with a volume smaller than the HECTOR detectors, the volume is about 77cm^3. The time resolution of these scintillators is very good (about 500 ps), but they have an energy resolution about 9% at 1 MeV. The energy resolution in average and the time resolution are better than the HECTOR detectors ones, due to their smaller volume.

The HELENA scintillators has been placed inside the GARFIELD scattering chamber. The first cluster, called HELENA BACKWARD, was positioned in a backward position with respect to the target (see Fig. 3.3, left picture); instead the second cluster was placed in forward position with respect to the target, for this reason it is called HELENA FORWARD (see Fig. 3.3 right panel). The HELENA BACKWARD detectors were placed near the target to be used as time reference instead of the beam radiofrequency. The HELENA FORWARD detectors were used to detect the pre-equilibrium neutrons, using the ToF technique, for this reason they were placed in forward direction at 80 cm from the target, due to the reaction kinematic.

As for the HECTOR detectors, these detectors are used under vacuum (about 10^{-5} mbar) in the GARFIELD scattering chamber, but the HELENA detectors did not have the voltage divider outside the scattering chamber. Furthermore, they are not equipped to work under vacuum; for this reason some of the detectors had some discharges in some the photomultiplier tube, that prevent them to correctly work.

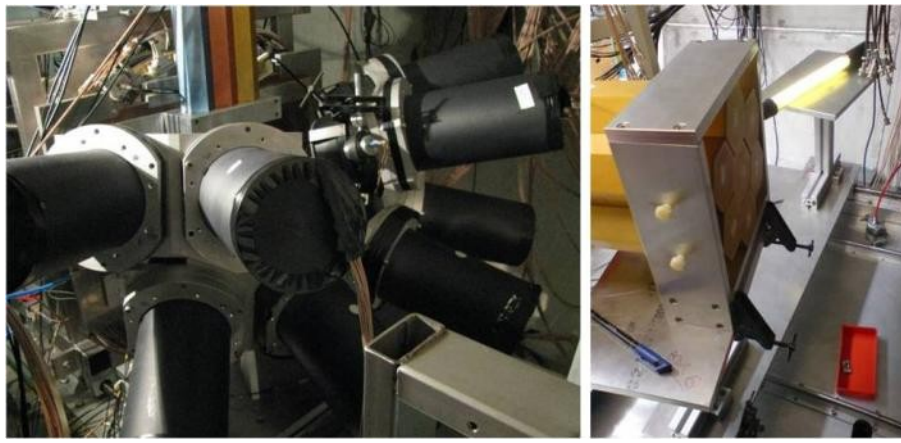

Fig. 3.3: In the left picture the HECTOR detectors and three of the HELENA detectors in vertical in the top of the picture. The HELENA BACKWARD surrounding the target to be used as time reference. In the right picture the HELENA FORWARD detectors.

The fact that some of these detectors did not work properly implies a low efficiency, which prevented us from using them as a time reference except for cross checks. We anyway verified that, even with low statistics, the HECTOR ToF obtained using HELENA time signal as a time reference has the same resolution as the one obtained with the radio frequency (RF) signal associated with the pulsed beam delivered by the Tandem-Alpi accelerator as shown in Fig. 3.4.

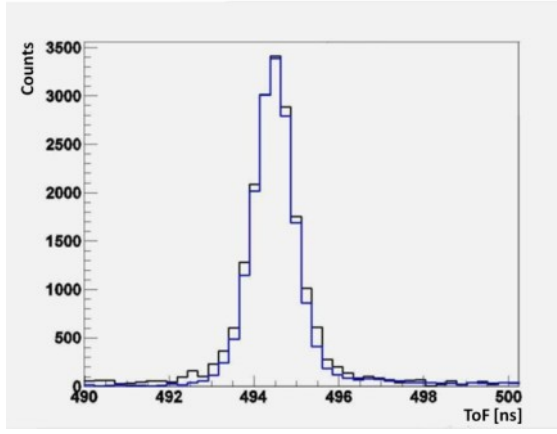

Fig. 3.4: The comparison between the Hector ToF spectrum obtained with the beam RF (blue line) and the Hector ToF spectrum obtained with the HELENA time (black line). The time resolution is the same in both cases.

A lot of HELENA forward detectors did not work owing to some discharges in a lot of the photomultiplier tube. For this reason these detectors were not used to measure the pre-equilibrium neutrons, due to their low statistic.

3.3. The GARFIELD array

The GARFIELD array is a high-granularity 4π array dedicated to charged-particle identification [32]. Isotopic identification can be achieved with ΔE-E technique or with pulse shape analysis of the signal coming from the stop detector (E). The setup is conceived in order to allow the simultaneous identification, with low energy threshold, of both light charged particles and heavy ions with an only two-stage telescope. The detector is characterized by a wide acceptance in Z, from 1 up to at least 28, with an identification and detection threshold of about 1-2 MeV/nucleon.

In this experiment only the forward chamber was used as shown in Fig. 3.5, because in the backward position there was the HECTOR array. The forward chamber of the GARFIELD apparatus is dedicated to the measurement of light charged particles (LCP) emitted during the different steps of the fusion-evaporation process.

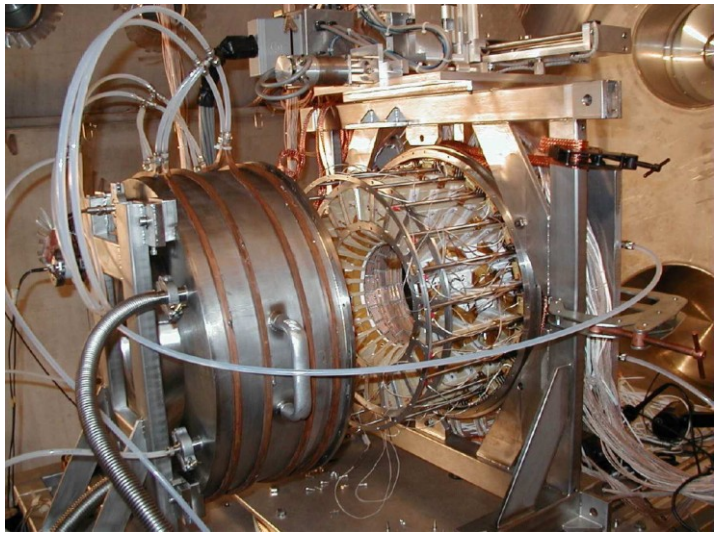

Fig. 3.5: Forward chamber of GARFIELD detector.

The GARFIELD array, in the used configuration, is an array composed of micro-strip gas chamber and CsI(Tl) scintillator telescopes for the identification and measurement of light charged particles and fragments. It covers an angular range from $\theta = 29°$ to $\theta = 82°$ and 2π in ϕ. It is divided in 24 sectors each one containing 8 ΔE-E telescopes. The ΔE signal is given by the gaseous micro-strip detectors which collect and amplify the primary electrons produced along the ionization track of the incident particle. The chamber is filled with CF4 gas, which is characterized by an high stopping power and drift velocity of the electrons produced in the ionization process (10 cm/μs at 1 V/cm/Torr). The pressure is set at 48 mbar and the electrical drift field is kept uniform by a field cage to a value of ≈1.2 V/cm/Torr The main advantage of using micro-strip gas chambers is the low threshold for Z identification from protons up to highly ionizing heavy ions. The residual energy signal is provided by CsI(Tl) scintillators which are also lodged in the gas volume.

The GARFIELD electronics has been upgraded from analog to digital signal elaboration [34]–[36]. More details on the digital electronis are reported in section 3.5.

CsI(Tl) scintillators, which act as E detectors, have a good energy resolution (3% for α particles at 5.5 MeV), high stopping power and they are not very sensitive to radiation damage. The scintillation light has two components, a fast (~ 700 ns) and a slow (~ 2 μs) one, allowing to perform pulse-shape analysis (psa) and particle identification.

The ΔE detector is a MicroStrip Gas Chamber (MSGC) as shown in Fig. 3.6. This gas detector that has a large dynamical range, a small signal-to-noise ratio for the low ionizing ions and a low detection threshold. Each MSGC is divided in four regions of charge collection that we labeled up-right, up-left, bottom-right and bottom-left. Left and right parts give a division in the ϕ angle, while bottom and up parts are the ones closer to the entrance window and to the CsI, respectively.

A telescope was built up combining one microstrip up-right (left), one microstrip down-right (left) and one CsI as shown in the top part of Fig. 3.6. The GARFIELD array is composed by 192 telescopes (24 sectors × 4 CsI × 2 microstrip) in the forward chamber. Before reaching one of the four CsI

detectors, the particle entering the telescope has to cross the gas chamber. The electrons produced by ionization are collected by the four anodes constituting the MSGC. The combined information of the CsI and the MSGC can be used to improve the position resolution beyond the angular span of each CsI detector. The resolution in ϕ can improve from 15° up to 7.5° using the left-right division of the MSGC, while a better resolution in θ can be achieved using the information of the electron drift time in MSGC, related to the position of the ionization track with respect to the microstrip. This information is reliable only for high-ionization particles.

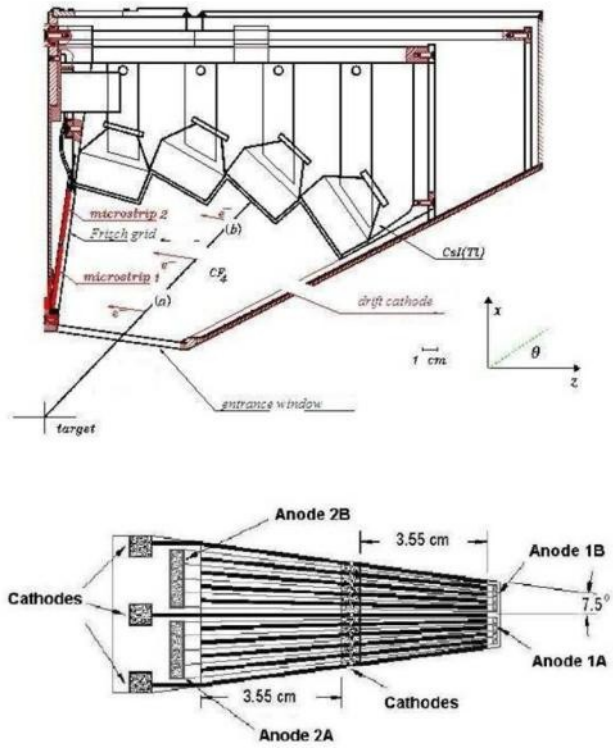

Fig. 3.6: Scheme of a sector of GARFIELD detector for a fix azimuthal angle ϕ (top part of the figure) and a MSGC (bottom part of the figure).

The data analysis of the GARFIELD array is explained in section 4.2 and some example of spectra are also shown in section 4.2.

3.4. The PHOSWICH detectors

The phoswich detectors of the FIASCO array [33] are placed in four boxes in the very forward direction (5° - 13°), as shown in Fig. 3.7. The position closest to the beam was left empty since the elastic scattering cross section is to high at these small angle (about 3°). The phoswich detectors were used as an evaporation residue trigger and selector, and as a proton/alpha multiplicity counter. Inside one of the PHOSWICH boxes, at an angle of ~ 2° with respect to the beam axis, was also placed a fast plastic scintillator of small dimensions, meant to detect the elastically scattered beam and to be used as beam monitor.

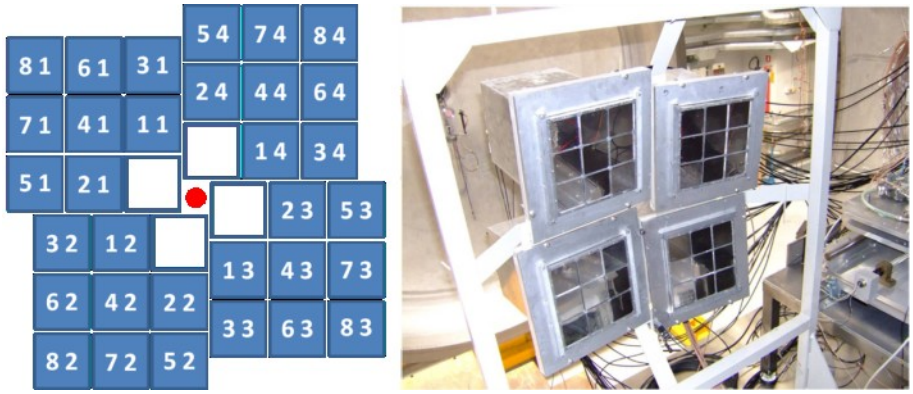

Fig. 3.7: A scheme of the phoswich position around the beam axis (the red point). In the left panel a picture of the phoswich detectors.

Each box contains eight phoswich detectors made of three layer scintillators. The first two stages are respectively a thin 200 μm and a 5 mm plastic material, while the last one is a 50 mm CsI(Tl). The light produced in the three ranges is collected by a common photomultiplier. This three stage were coupled to one photomultiplier, as shown in Fig. 3.8; the scintillation light of the different stages has different decay constants as detailed in the bottom part of Fig. 3.8.

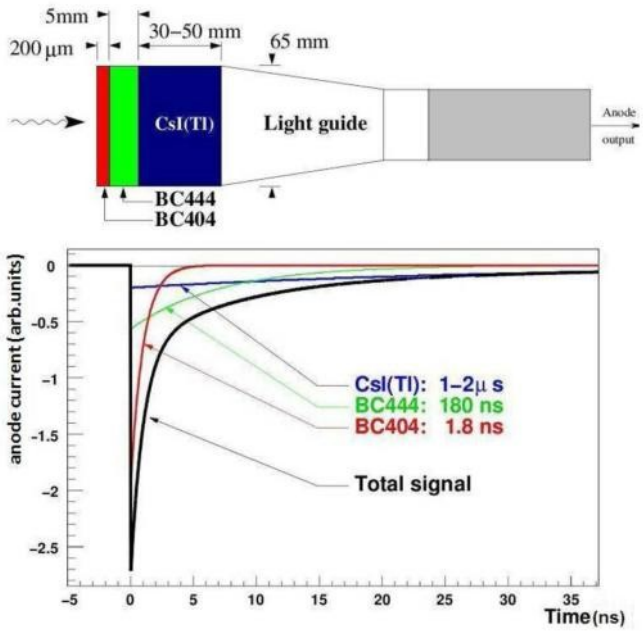

Fig. 3.8: A schematic view of a phoswich detector (in the top part of the figure) The three layer of scintillators are followed by a light guide and a phototube. The three detectors have a different decay constant; the signal of the three scintillator is shown in the bottom part of the figure.

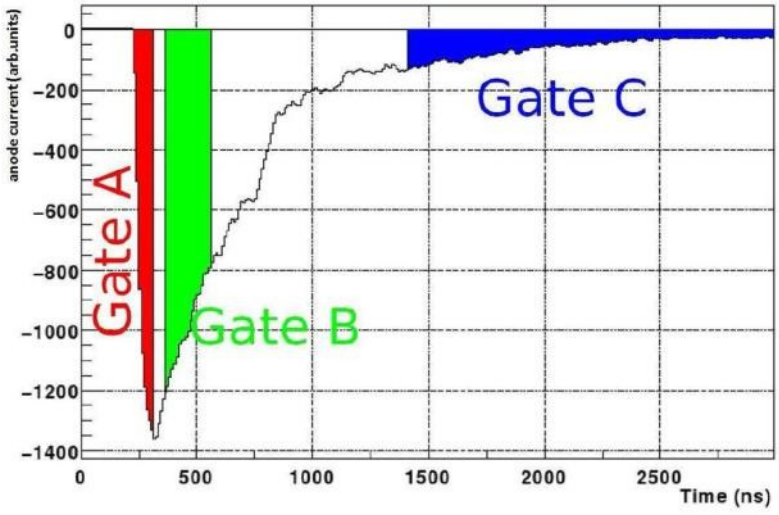

Fig. 3.9: The three interval of integration of phoswich signals (labeled GA, GB and GC) for a signal produced by a Z=1 particle.

The light output is integrated in three different gates labeled as A, B and C, each maximizing the light output from one stage and minimizing the ones from the others. An example of how the integration is performed is given in Fig. 3.9.

The phoswich detectors have a digital electronic, the details of digital electronics will be given in section 3.5 and in [34]–[36].

3.5. Signal Processing

The use of digital electronics reduces the complexity of the electronics of a high-granularity 4π array such as GARFIELD. Both the GARFIELD array and the phoswich detectors are equipped with digital electronic [34]–[36]. This electronic is developed by Sezione di Firenze of INFN and it is based on fast sampling ADC (Analog to Digital Converter) and on DSP (Digital Signal Processor). In this way it is possible to maintain the same precision of the analog electronic and to obtain more information that could be used in Pulse Shape Analysis (PSA) application.

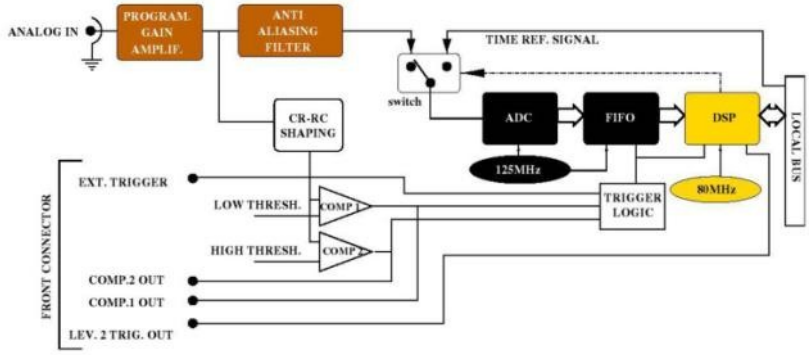

Fig. 3.10: A scheme of the digitalization process [36].

The digitizer scheme is shown in Fig. 3.10 and it is composed of the following main blocks:

- the ADC at 12 bit samples: the analog input coming from preamplifiers with a frequency of 125 MHz;

- the FIFO (First In First Out) is used for a temporary storage of data and is filled when a validation signal is send by a trigger box;
- the DSP reads the signal from the FIFO and process it online;
- after being processed the data are sent to the acquisition.

In a event-based system the DSP stay in a waiting stage till the arrival of a trigger signal. The trigger signal allows to store the digitized signals in the FIFO and to move these signals to the memory of the digitizer and it starts to process the data waiting the acquisition validation [35]. The DSP system is ”triggered”, i.e. the FIFO is filled and the signal is processed only when a validation signal is received. This validation can come from the main trigger.

3.6. Triggers and acquisition system

Fusion-evaporation events are characterized by the emission of an heavy residue, emitted in the forward direction, associated to a light charged particle (emitted in forward directions) and gammas (emitted isotropically). Therefore a fusion-evaporation event can be selected by requiring the coincidence between:

1. Phoswich and GARFIELD (an evaporation residue in coincidence with a light charged particle),
2. Phoswich and HECTOR (an evaporation residue in coincidence with a high-energy γ ray).

The triple coincidences are good events but they have a low probability, for this reason were not included in the trigger; but they appear as a “special case” of trigger 1 or 2. There were also the coincidence between phoswich and HELENA forward (an evaporation residue in coincidence with an evaporation neutron); instead the HELENA backward are acquired in a slave mode.

When the energy deposited in a detector produces an electronic signal higher than a given threshold (the threshold was set just above the level of the electronic noise for phoswich and GARFIELD; just above the internal

radioactivity in the case of the HECTOR detectors), a logical signal produced by the CFD (analog or digital) is sent to the trigger box. In the case of the phoswich detectors also a second high threshold is implemented and a logical signal is sent to the trigger box only when the electronic signal falls between the low and high thresholds. The low threshold allow to acquire events that are not electronic noise and the high one allows to reduce the elastic scattering (that has a higher cross section at forward angles) and for this reason might induce spurious coincidences.

The trigger used in the experiment were the following (the OR of the phoswich detectors was called OR PHOSWICH FUSED):

- PULSER HECTOR,
- OR PHOSWICH FUSED,
- OR HECTOR,
- OR GARFIELD,
- (OR HECTOR) AND (OR PHOSWHICH FUSED),
- (OR GARFIELD) AND (OR PHOSWHIC FUSED),
- (OR HELENA) AND (OR PHOSWHICH FUSED),
- PLASTIC SCINTILLATOR.

The selection of the events is preformed in a "trigger box" by requiring that the combination of the trigger signal coming from the different detectors satisfies given conditions. A schematic view of the trigger box is shown in Fig. 3.11.

The acquisition system, based on FAIR front-end (Fast Advanced Interface Read-out) developed by INFN Sezione di Napoli, is an ECL BUS dedicated to the fast read-out of electronic data-acquisition modules. The transmission velocity of data on the BUS is 1.25 GBits/s and the architecture of the system is organized on two levels. The low one in which the single electronic modules labeled by a Virtual Station Number (VSN) are grouped in segments. Every group of segments is controlled by its own Segment Controller. The high one, in which every Segment Controller can communicate with the System Controller. Segment controllers allow to associate with each event written on disk a trigger pattern accounting for the

combination of trigger signals received by the trigger box. The data were collected in a common start configuration.

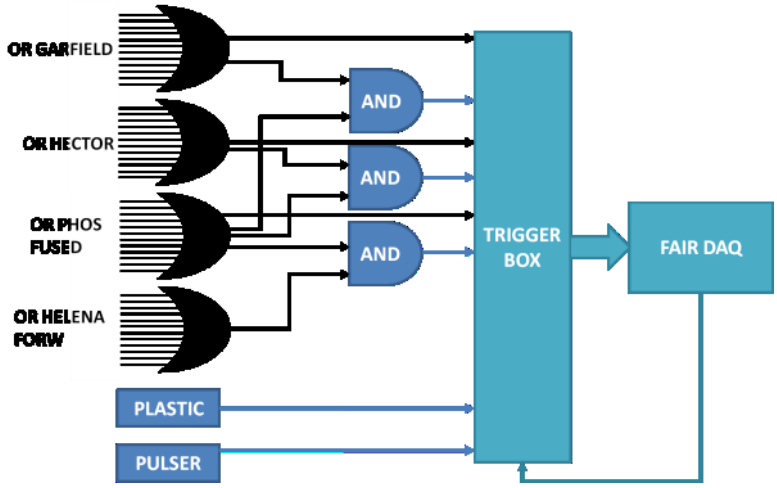

Fig. 3.11: Scheme of the trigger box. The logic signal, the single or the coincidences, coming from the detectors and are sent to the trigger box.

The trigger box sends a validation signal (common start) to the data-acquisition system, corresponding to the logical OR of the incoming signals. In order to have an efficient collection of coincidences, the singles were downscaled by a factor $D = 2^n$ $(3 < n < 10)$. Therefore the singles were acquired and a valid trigger is gave only for one event after D events. The acquired single events were written on disk.

4. Data Analysis of the dynamical dipole experiment

In this chapter details on calibration, event identification and data analysis for each detector will be given, pointing out the gating conditions used to select the events of interest for the subsequent analysis. The analysis code is based on ROOT Data Analysis Framework [37].

The selection of physical events was done keeping in mind that the GDR decay in fusion-evaporation reactions has the following signatures in our detection apparatus: 1) detection of one fusion-evaporation residue in PHOSWICH detectors, 2) detection of one high-energy γ-ray in HECTOR detectors and 3) detection of one (or more) light charged particle in GARFIELD or PHOSWICH detectors.

Once the clean γ-ray spectrum has been obtained, the DD yield can be extracted by comparing it with the statistical model predictions. Particular care has to be taken to account for the pre-equilibrium energy loss from particle emission. Both the absolute yield of the DD emission and its angular distribution can be extracted.

The calibration and data reduction of the PHOSWICH detectors will be described in section 4.1. Section 4.2 details both the calibration of the GARFIELD array and the extraction of the pre-equilibrium energy loss. In section 4.3 the final γ-ray spectrum of physical interest is obtained. Section 4.4 will show how the DD yield at 12 MeV/u is then extracted and compared to the values measured at 8.1 and 15.6 MeV/u, and section 4.5 will show the corresponding angular distribution.

4.1. Analysis of the phoswich detectors

The first step in the analysis of PHOSWICH detectors is the calibration and the alignment of the ToF spectra. The TDC (Time-to-Digital Converter) calibration was performed by using a pulse generator. Both the

phoswich TDC and the one used to process the radio frequency (RF) signal have to be calibrated, as the ToF is defined as $T_{phoswich}$ - T_{RF}. The procedure use to aligned the GA (GA is the energy deposited in the first layer of the phoswich, see section 3.4) versus ToF matrix is the following. In Fig. 4.1, an example of phoswich GA vs ToF spectra is shown; it is possible to observe that there is a long vertical structure around -600 ns, which correspond to the alpha particle structure. We used the projection of this structure, on the x axis, for value of GA larger than 2500 a.u., to align the ToF spectra. In these projections a peak at 600 ns is clearly visible. The peaks were fitted and the centroids are translated in order to have all the centroids in the same channel, in our case in -600 ns. It is important to align these spectra because in this way it is possible to compare different phoswich to produce a global sum spectra with all statistics.

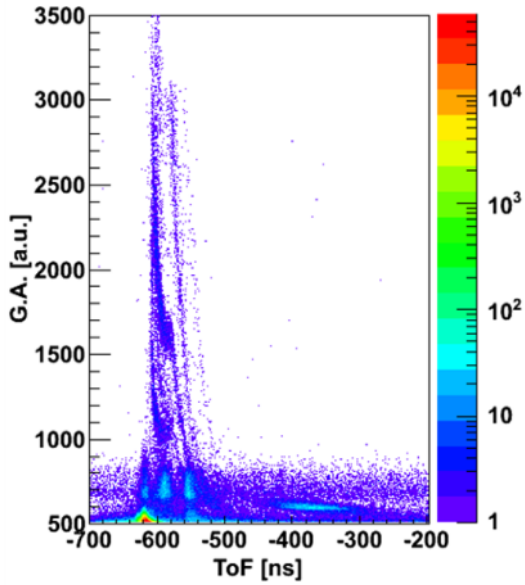

Fig. 4.1: An example of GA versus ToF spectrum of a phoswich detector is shown.

The GA, GB and GC variables (the light output from the three scintillator stages, see section 3.4) were used without calibration that is unnecessary because they measure only a part of the total light yield.

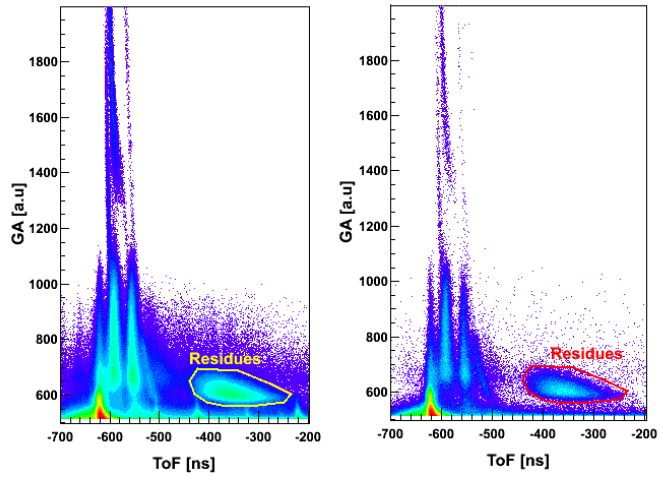

Fig. 4.2: The GA versus ToF spectra of one of the phoswich detectors. In the left panel there is the spectrum without gate conditions, the residues are identified by ToF and they are indicated with a white circle. Instead in the right panel there is the same spectrum gated on the prompt γ peak in HECTOR.

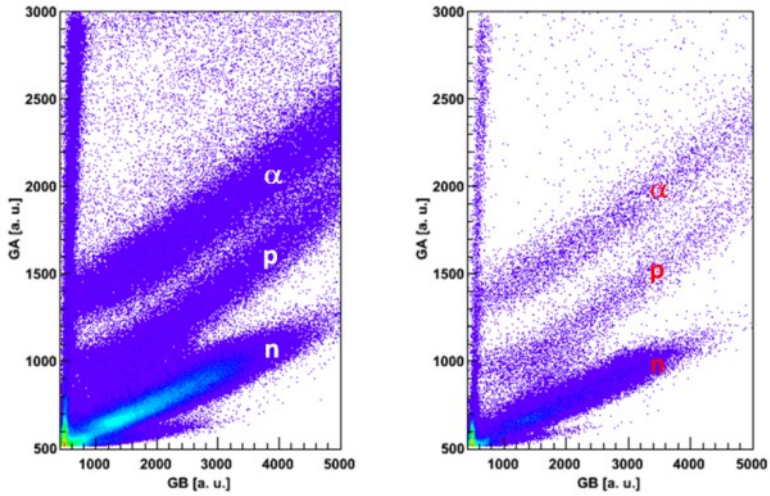

Fig. 4.3: The GA versus GB spectra of one of the phoswich detectors. In the left panel there is the spectrum without any gating conditions, it is possible to identify neutrons, protons and α particles (they are indicated with white letters). Instead in the right panel there is the same spectrum gated on the prompt γ peak in HECTOR. The vertical line at low GB correspond to the events stopped in the first layer, for example the evaporation residues.

Residues identification was done using the correlation between GA and ToF as shown in Fig. 4.2. A better separation of the evaporation residues from other reaction products is achieved in the these spectra after gating on the γ prompt peak in HECTOR ToF spectra (see Fig. 4.22) as displayed in the right panels of Fig. 4.2.

The detected particles might have different ranges, A, Z and kinetic energy. While elastically scattered beam particles and fusion-evaporation residues are stopped in the first stage, light charged particles punch through the first scintillator stage (and part of the protons also through the second stage). Therefore, light-particle identification can be also obtained studying the correlation between light outputs from first and second (or second and third) scintillator stages, as shown in Fig. 4.3.

To better understand the phoswich detector matrixes, the GA versus ToF matrixes were extracted gated on the cuts on GA versus GB matrixes. The cuts are shown in panel a) of Fig. 4.4. The results produced with this gates are shown in panels b), c) and d) of Fig. 4.4. In Fig. 4.5 the GA versus ToF matrix is shown without any gate in panel a) and with the gate of Fig. 4.4 in panel b) c) and d). In this way, in Fig. 4.5 it is possible to have a direct comparison between the total matrix and the gated ones. It is evident that phoswich are capable to clearly identify the different type of the evaporated particles together with the evaporation residues.

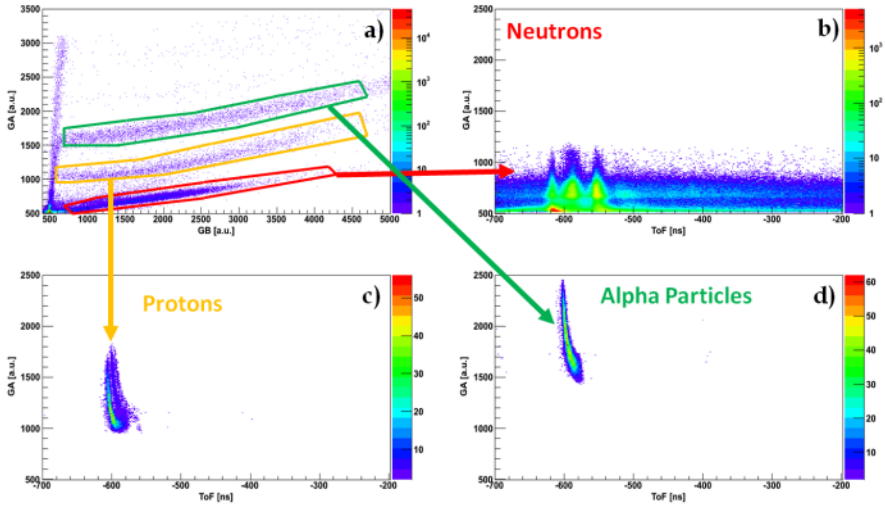

Fig. 4.4: The GA versus ToF spectra (panels b), c) and d)) obtained with the gate on GA versus GB spectrum. The gate used are shown in panel a).

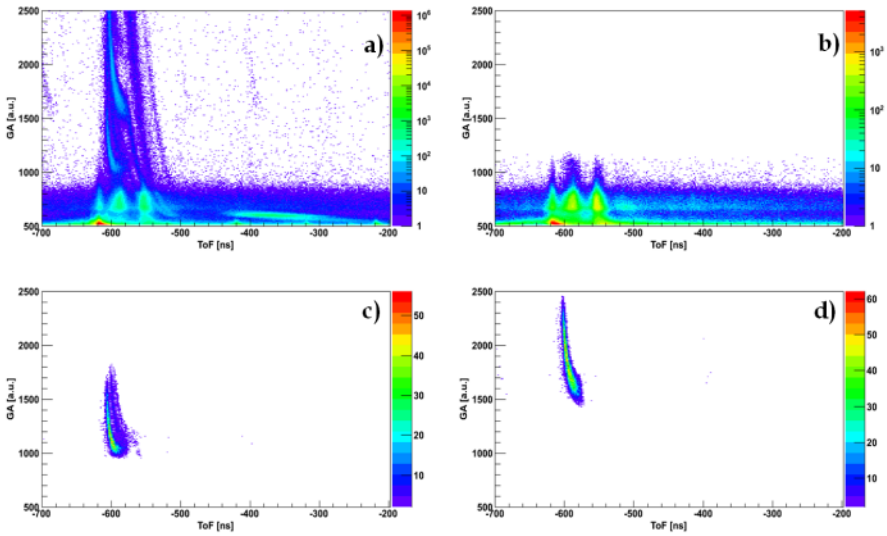

Fig. 4.5: In panel a) the spectrum of GA versus ToF of one of phoswich detectors. In panel b), c) and d) there are the same spectrum of panel a) gated with the gate show in panel a) of figure Fig. 4.4.

4.2. Analysis of the GARFIELD array

The energy spectra of the light charged particles measured in GARFIELD were analyzed in order to obtain the value of the energy loss during the pre-equilibrium phase. Light charged particles were detected both in the GARFIELD and PHOSWICH array but only the first one yields information on their energy. A detailed analysis of the GARFIELD array can be found in [38], a brief summary will be reported in this section.

The first step of the GARFIELD array analysis is the isotopic identification. To identify the lighter ions in charge and mass it is possible to use the CsI scintillators of GARFIELD array. The ΔE-E technique applied at GARFIELD chamber can identify the light charge particles only in charge especially for the particles with Z=1. Instead, using the fast versus slow technique with CsI scintillators, it is possible to distinguish in mass the particles (for example the protons from deuterium and from tritium nuclei). Moreover the α particles are clearly separated from the particles with $Z = 1$. In Fig. 4.6, an example of a fast versus slow matrix is reported: the protons, the deuterium and tritium nuclei and α particles are well separated.

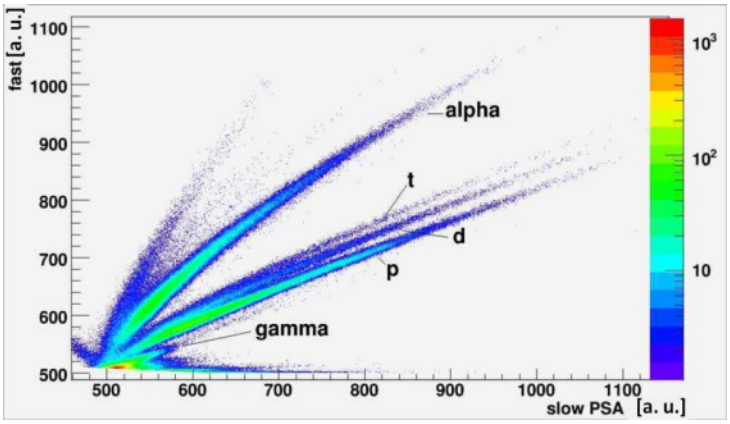

Fig. 4.6: An example of a fast versus slow matrix of one CsI scintillators of GARFIELD array. The lighter particles are discriminate in mass and charge [38].

The ΔE-E technique was not used in our case. To calculate the pre-equilibrium energy loss, it is necessary to obtain the value of the average kinetic energy of protons and alpha particles. For this reason, we used the

fast vs slow matrix to identify the LCPs, and we used the energy deposited in the CsI scintillators of GARFIELD array to obtain the average kinetic energy.

The high granularity of the GARFIELD array, implies a large number of detector and therefore a time consuming procedure of particles identifications. So an automatic procedure [39] was implemented by the group of the nuclear physics of Bologna using ROOT [37]. An example of the results of this procedure it is shown in Fig. 4.7.

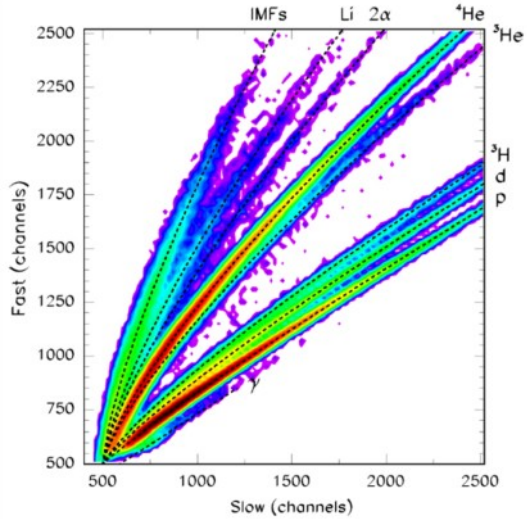

Fig. 4.7: A fast versus slow matrix, in this case the dashed lines correspond to the fit done with the automatic procedure [38].

After the identification it is necessary to calibrate the GARFIELD array spectra, to convert the slow signal from arbitrary unit to MeV. The results of the identification procedure were associated with each cell of the fast vs slow matrix. A value of A and Z is needed in order to apply the formula that converts light output (LO) in energy. The differential energy loss of each light charged particle in CsI is different as accounted for by Birks formula [40]:

$$LO = \gamma E + \beta(exp(-\alpha E) - 1) \qquad (4.1)$$

where α, β and γ are isotope-dependent parameter. More details are reported in [40]. The calibrated spectra for the energy distribution of the alpha particles and protons are shown in Fig. 4.8 and in Fig. 4.9, respectively.

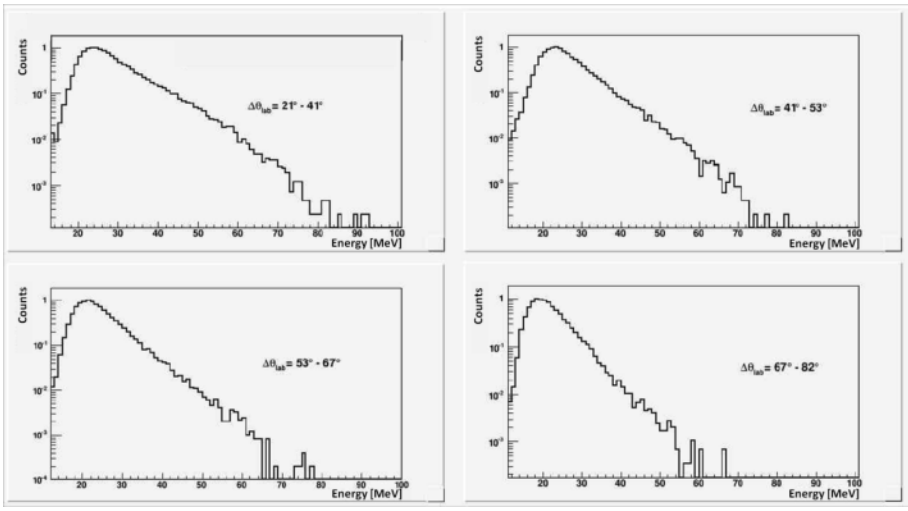

Fig. 4.8: The energy distribution of the α particles in the laboratory system. These spectra are for different angles. The spectra are obtained with an evaporation residues in coincidence in phoswich detectors [38].

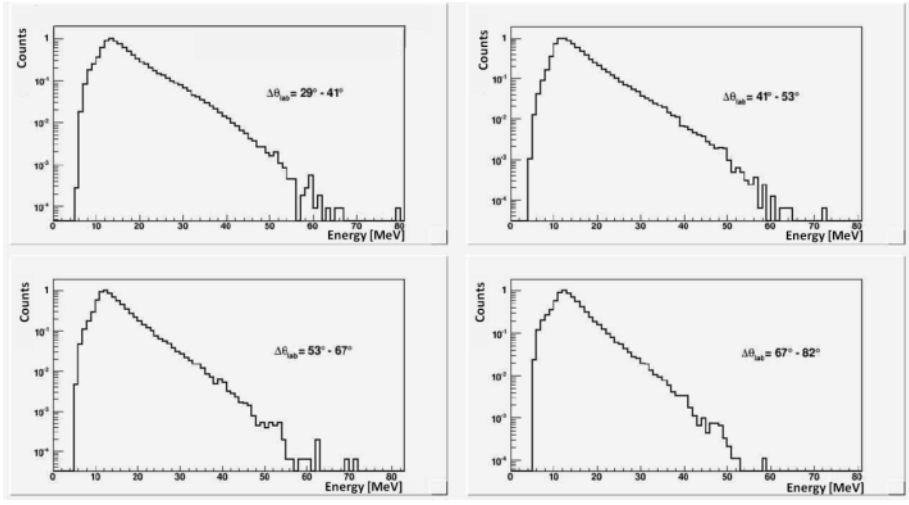

Fig. 4.9: The energy distribution of the protons in the laboratory system. These spectra are for different angles. The spectra are obtained with an evaporation residues in coincidence in phoswich detectors [38].

Once calibrated, the energy spectra have to be transformed from the laboratory to the center of mass (CM) frame. This transformation was done, event by event, with the following relation:

$$E_{cm} = E_{lab} + \frac{1}{2}mv_s^2 - 2cos(\theta_{lab})\sqrt{\frac{1}{2}mv_s^2 E_{lab}} \qquad (4.2)$$

where the velocity of the emitting sources v_s is taken as the velocity of the recoil CN. The spectra in the center of mass frame are represented in Fig. 4.10 and Fig. 4.11, in the first figure there is the α particles energy distribution, in the second one there is the protons energy distribution.

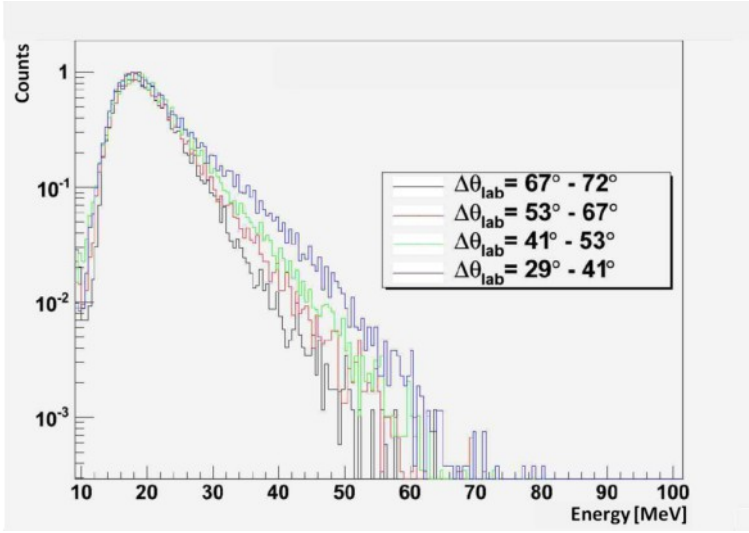

Fig. 4.10: Energy distribution of α particles in the center of mass system. The different angles are represented with different colors. Also in this case, the spectra are in coincidence with an evaporation residues in a phoswich detector [38].

The presence of pre-equilibrium contribution is clearly shown in Fig. 4.10. The energy spectra for evaporated LCP should be isotropic, instead the pre-equilibrium emission is forward peaked. In Fig. 4.10 it is possible to notice that in the spectra at the forward angles there is a larger contribute, with respect to the backward angles due to the pre-equilibrium emission.

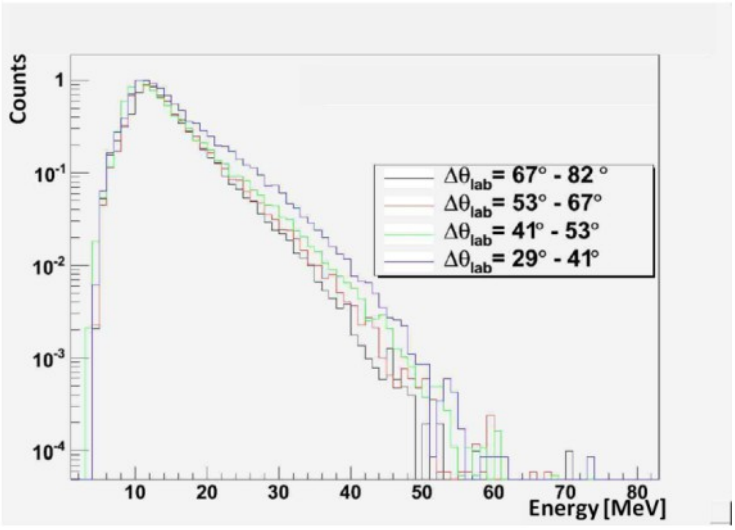

Fig. 4.11: Energy distribution of protons in the center of mass system. The different angles are represented with different colors. Also in this case, the spectra are in coincidence with an evaporation residues in a phoswich detector [38].

From the experimental spectra of the light charge particles (alpha and protons) in Fig. 4.10 and in Fig. 4.11, we have to extract the values of the parameters that are necessary to calculate the pre-equilibrium energy loss. The energy loss during the pre-equilibrium phase of the CN was determined using the following formula:

$$E_{loss} = (E_{kn} + E_{bn})M_n^{PE} + (E_{kp} + E_{bp})M_p^{PE} + (E_{k\alpha} + E_{b\alpha})M_\alpha^{PE} \qquad (4.3)$$

where E_{kp}, $E_{k\alpha}$ are the experimentally obtained average kinetic energies of the pre-equilibrium protons and α particles, respectively. Instead, E_{kn} is the average kinetic energy for the neutrons. E_{bn}, E_{bp} and $E_{b\alpha}$ are the binding energies for neutrons, protons and alpha particles, respectively. M_p^{PE}, M_n^{PE} and M_α^{PE} are the pre-equilibrium multiplicities for protons, neutrons and alpha particles, respectively. The values of the pre-equilibrium multiplicities for protons and alpha particles could be extracted from the experimental data. Instead the neutron pre-equilibrium multiplicity could not be extracted from data. The value of M_n^{PE} has to be calculated using a theoretical model that describes both the pre-equilibrium phase and both the CN particles evaporation. This model named MCFx is described in details in [41]. The

value of the pre-equilibrium neutron multiplicity will be compared with the values extracted from the systematic in [42].

The pre-equilibrium energy loss could be calculated in two different methods: in the first one the multiplicities all particles were extracted from the predictions of the MCFx model; in the second one the multiplicities of protons and alpha particles were extracted directly from the data using a fit program (the moving source fit). While, in both method the value of the M_n^{PE} will be extracted from the theoretical model predictions [41].

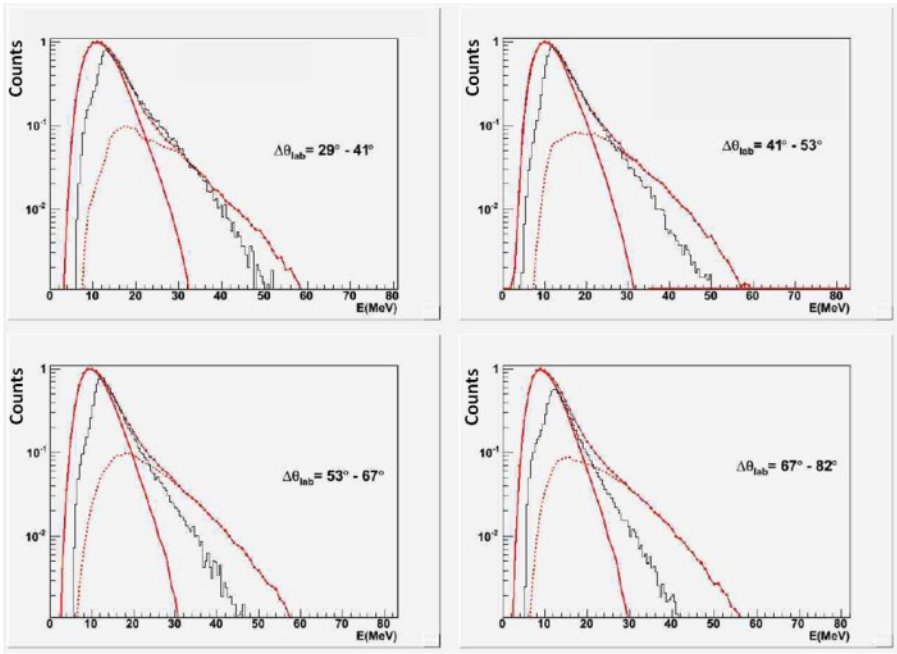

Fig. 4.12: Comparison between the theoretical predictions and the data of the energy distribution of protons. The red points connected with a black line is the model that include the evaporative and the pre-equilibrium contribution, the red-dashed line represents the theoretical model that include only the pre-equilibrium contribution, the red line represents the theoretical model in which is included only the evaporative contribution and the black line are the experimental data [38].

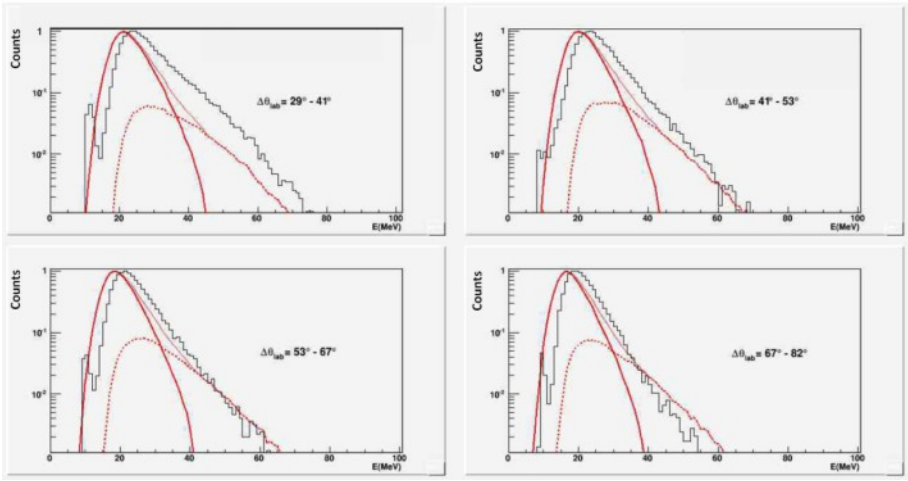

Fig. 4.13: Comparison between the theoretical predictions and the data of the energy distribution of alpha particles. The red points connected with a black line is the model that include the evaporative and the pre-equilibrium contribution, the red-dashed line represents the theoretical model that include only the pre-equilibrium contribution, the red line represents the theoretical model in which is included only the evaporative contribution and the black line are the experimental data [38].

Concerning the first method, the experimental data were compared with the theoretical model predictions. In Fig. 4.12 and in Fig. 4.13 are shown the spectra calculated with the theoretical model compared with the experimental data. From the comparison between the data and the model it is possible to extract the value of the protons and α particles multiplicity. The value found for the protons multiplicity is $M_p^{PE} = 0.33$, the value for the α-particles is $M_\alpha^{PE} = 0.22$. In Fig. 4.12 and in Fig. 4.13, however it is possible to observe that the pre-equilibrium part obtained from the model did not reproduce exactly the experimental data. The MCFx model does not reproduce the alpha particles spectra at high energy, especially for the backward angles, as shown in Fig. 4.12. Instead, in the case of protons, the model does not reproduces the high energy part, only for the forward angles, as shown in Fig. 4.13. Furthermore the model overestimates the high energy part for the alpha particles, while it underestimates the high-energy part at forward angles.

The M_n^{PE} could not be compared directly from data, because with the GARFIELD array it is possible to detect only the charged particles. The value of the neutrons multiplicity could be obtained only from the theoretical model [41]. The contribution of the energy loss due to the neutrons is very important because it is the larger contribution, the calculated spectra are shown in Fig. 4.14. The value of the neutrons multiplicity calculated from the theoretical model is $M_n^{PE} = 0.45$. This value calculated from the theoretical model has to be compared with the values extracted from the data of other experiments reported in [42]. This comparison is shown in Fig. 4.15, the black squares are the values of the M_n^{PE} for the $^{16}O + ^{116}Sn$ reaction, instead the red squares are the data reported in [42]. It is possible to see that the values found using the theoretical model follow the same trend of the experimental data reported in [42].

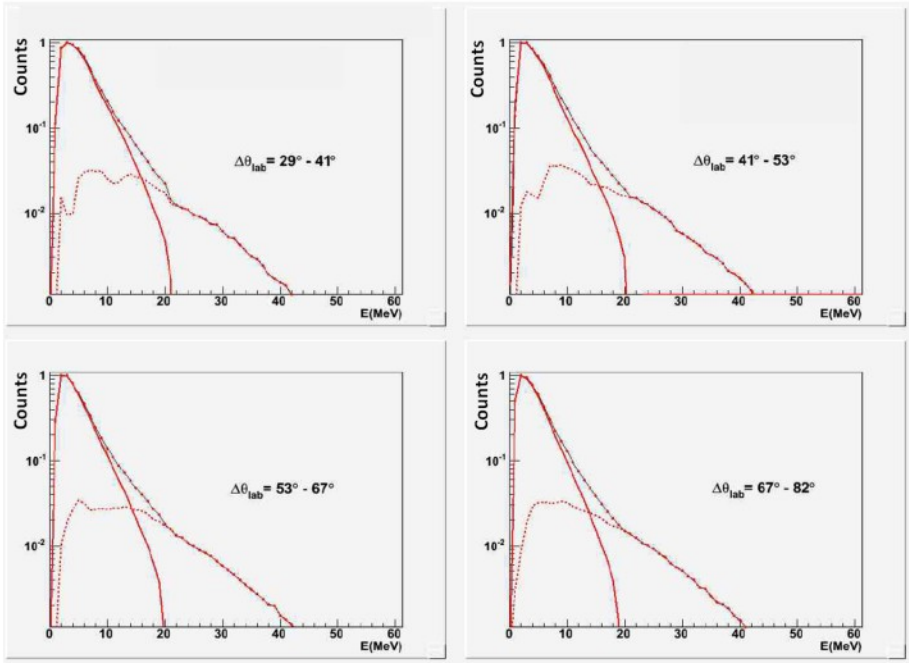

Fig. 4.14: The results obtained from the theoretical model, to calculated the neutron multiplicity. The red points connected with a black line is the model that include the evaporative and the pre-equilibrium contribution, the red-dashed line represents the theoretical model that include only the pre-equilibrium contribution, the red line represents the theoretical model in which is included only the evaporative contribution [38].

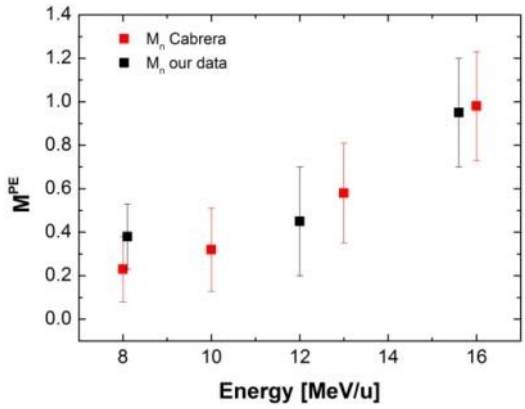

Fig. 4.15: The pre-equilibrium neutron multiplicity extracted from the theoretical model for our data is represented with black squares. By red squares are represented the M_n^{PE} reported in [42].

From the spectra in Fig. 4.12, Fig. 4.13 and Fig. 4.14 it is possible also to obtain the average kinetic energies for neutrons, protons and α particles (E_{kp}, $E_{k\alpha}$and E_{kn}). By equation 4.3 it is possible to calculate the value of the pre-equilibrium energy loss. The value of the energy loss obtained by this method is 18.4 MeV, all the values used to calculated this value are listed in Tab. 4.1.

Particle	**M_{PE}**	**E_k**
Protons	0.33	14.8
Alpha Particles	0.22	21.7
Neutrons	0.45	4.3
Pre-equilibrium E_{loss}		**18.4**

Tab. 4.1: The values of the pre-equilibrium multiplicities extracted from MCFx model and the values of the average kinetic energies extracted from data for protons and alpha particles and from model for neutrons are listed.

Concerning the second method, to describe the experimental LCP spectra, a commonly used moving source fit analysis technique was used. The moving source fit is generally used in the description of the LCP emission in fusion-fission reactions [42]. This fit procedure allows to

consider different sources of emitted particles. Two sources for the moving source fit analysis were considered: the first one that is pre-equilibrium source and the second one that is the evaporative source. Fig. 4.16 shows that the pre-equilibrium source is relevant, as expected, especially at forward angles. In Fig. 4.16 it is possible to note that at the forward angles there is a large contribution at high energy, that are related to the pre-equilibrium emission. The experimental spectra have to be fitted by two Maxwell distributions, the first one that include the pre-equilibrium source and the second one that include only the evaporative one. The total fit will be the sum of these two distributions.

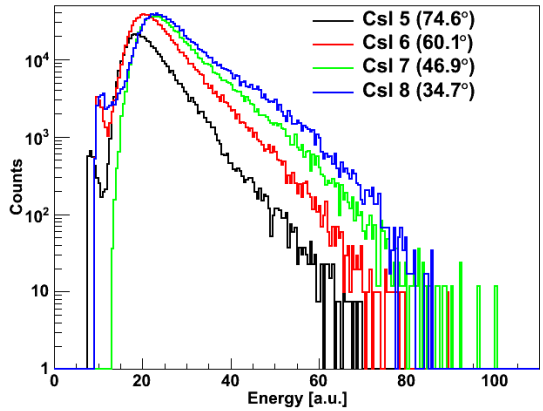

Fig. 4.16: The GARFIELD array spectra at four different angles. It is possible to see that at the forward angles there are larger tails at high energy, that are related to the pre-equilibrium emission.

The pre-equilibrium distribution is described in the following way:

$$\frac{N_1}{2(\pi T_1)^{\frac{3}{2}}}\sqrt{E_1}\sqrt{\frac{(E-E_{C1})}{E_1}}exp\left(\frac{-E_1}{T_1}\right) \qquad (4.4)$$

where E is the energy of the particle, E_{C1}, T_1 and N_1 are the Coulomb energy parameter, the apparent nuclear temperature and the total number of the particle emitted from the pre-equilibrium source, respectively. Instead, E_1 is given by the following transformation:

$$E_1 = E - E_{C1} - 2\sqrt{\frac{1}{2}m_{LCP}v_s^2(E - E_{C1})}cos\theta_{lab} + \frac{1}{2}m_{LCP}v_s^2 \qquad (4.5)$$

where m_{LCP} is the mass of the light charge particle and v_s is the source velocity, and θ_{lab} is the emission angle in the laboratory frame.

The evaporative source is based on the surface emission after the equilibration process in the compound nucleus and it is associated with the statistical particle distribution. The evaporative source could by described by a Maxwell distribution, as follow:

$$\frac{N_2[1 + \alpha_2 P_2(cos\theta_{CM})]}{4\pi T_2^2}(E_2 - E_{C2})\sqrt{\frac{E}{E_2}}exp\left(-\frac{E_2 - E_{C2}}{T_2}\right) \qquad (4.6)$$

where E is the energy of the particle, E_{C2}, T_2 and N_2 are the Coulomb energy parameter, the apparent nuclear temperature of the emitting evaporative source and the total number of the particle emitted from the evaporative source, respectively, while α_2 is an angular coefficient, P_2 is the Legendre polynomial and θ_{CM} is the emission angle in the center of mass frame. Instead, E_2 is given by the following transformation:

$$E_2 = E - 2\sqrt{\frac{1}{2}m_{LCP}v_{CM}^2 E}cos\theta_{lab} + \frac{1}{2}m_{LCP}v_{CM}^2 \qquad (4.7)$$

where m_{LCP} is the mass of the light charge particle and v_{CN} is the velocity of the compound nucleus, and θ_{lab} is the emission angle in the laboratory system.

Particle	**E_{c1} [MeV]**	**T_1 [MeV]**	**N_1**	**v_s [v/c]**	**E_{c2} [MeV]**	**T_2 [MeV]**	**N_2**	**α_2**
α	13.4	5.6	$6.6\ 10^5$	0.07	13.0	3.8	$2.63\ 10^6$	0.6
p	5.5	3.8	$9.0\ 10^5$	0.09	3.3	3.8	$1.1\ 10^7$	0.0

Tab. 4.2: The parameters obtained from the moving source fit for the alpha particles and protons.

The fitting free parameters are 8: E_{C1}, T_1, N_1, E_{C2}, T_2, N_2, α_2 and v_s. The velocity v_s could vary between v_{CN} and v_{beam}. The results obtained by the moving source fit are shown in Fig. 4.17 and Fig. 4.18 for alpha particles and

protons respectively. The parameters obtained from the fits are listed in Tab. 4.2. From N_1 it is possible to calculated the alpha particles and protons pre-equilibrium multiplicity.

As already discussed, we remembered that the neutrons cannot detected by GARFIELD array. The pre-equilibrium neutron multiplicity was obtained using the same consideration of the previous method. The value of the pre-equilibrium energy loss, found from data, is 13.3 MeV, the values used to calculated this number are listed in Tab. 4.3.

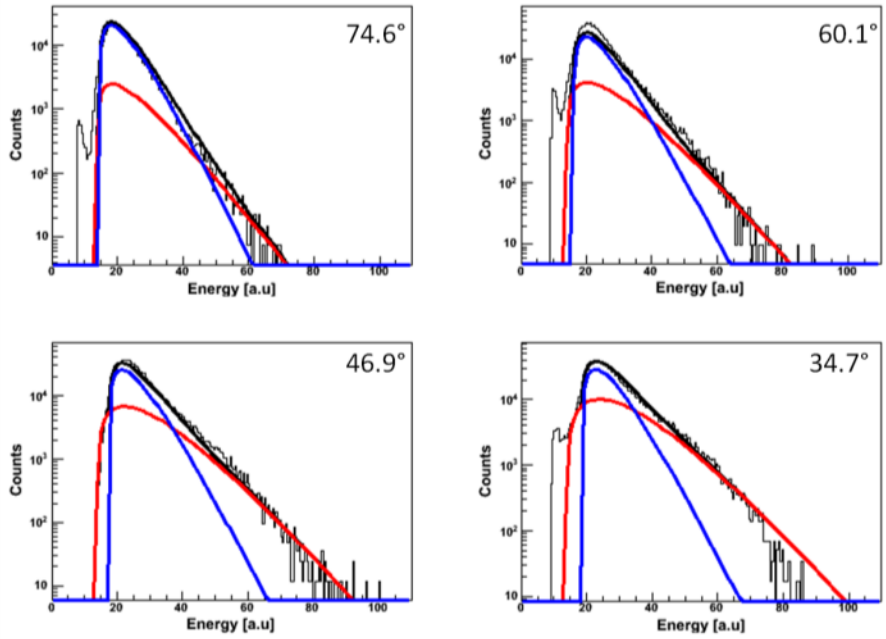

Fig. 4.17: The alpha particles spectra of GARFIELD array (for the different four angle of the CsI scintillators used during the measurement) fitted using the moving source fit. The red line represents the pre-equilibrium distribution, the blue one represents the evaporative source contribution and the black one is the total fit including the evaporative and the pre-equilibrium contribution.

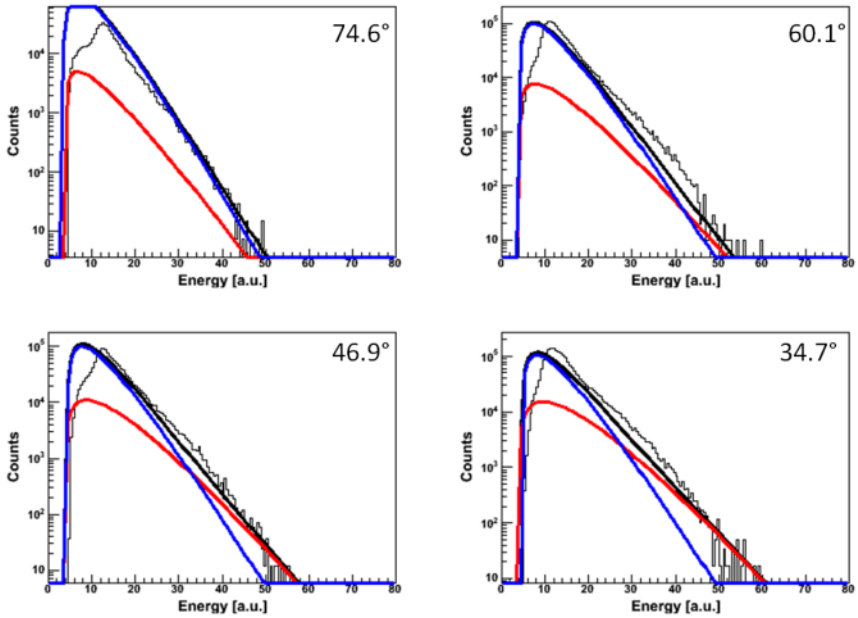

Fig. 4.18: The protons spectra of GARFIELD array (for the different four angle of the CsI scintillators used during the measurement) fitted using the moving source fit. The red line represents the pre-equilibrium distribution, the blue one represents the evaporative source contribution and the black one is the total fit including the evaporative and the pre-equilibrium contribution.

Particle	**M_{PE}**	**E_k**
Protons	0.18	14.8
Alpha Particles	0.13	21.7
Neutrons	0.45	4.3
Pre-equilibrium E_{loss}		**13.3**

Tab. 4.3: The values of the pre-equilibrium multiplicities extracted from data for protons and alpha particles and from model for neutrons and the values of the average kinetic energies extracted from data for protons and alpha particles and from model for neutrons are listed.

4.3. Analysis of the HECTOR detectors

The energy calibration of the HECTOR detectors was done with sources of different γ-rays energies in order to have a reliable calibration in a wide energy range (1-30 MeV). Before, during and after the experiment we have measured the emission from a source of ^{60}Co and the internal radioactivity of BaF_2. The emissions of the ^{60}Co source are used to calibrate the detector while the internal activity is used to monitor the detector gain stability. The internal activity is present due to small impurities of Ra (an alkaline earth as Ba) and its daughter nuclei which α, β decay yielding a measured peaks structure. The energy range of the internal activity peaks is about $1 - 4\ MeV$ (see Fig. 4.20). The shape, position and intensity of these peaks is a characteristic of each detector; therefore, the energy assignment was done just before the experiment using the calibration obtained with ^{60}Co source ($E_{\gamma 1} = 1173\ keV$ and $E_{\gamma 2} = 1332\ keV$). The calibration with the ^{60}Co source provides two barely resolved peaks and could be affected by some systematic errors. The detectors have an energy resolution of 12% at 1 MeV and so they are not able to distinguish the two peaks of the ^{60}Co source (as shown in Fig. 4.19). In order to obtain consistent results, some fit parameters were constrained: the FWHMs of the two peaks was imposed to be equal and the ratio between the height of one peak and the height of the other is fixed.

At the end of the experiment, a new calibration measurement was performed with a beam of ^{11}B at $E_{lab} = 45\ MeV$ delivered by the Tandem accelerator of Laboratori Nazionali di Legnaro. A gold absorber foil was placed before the D target in order to reduce the energy of the impinging ^{11}B down to the value of $E_{lab} = 19\ MeV$ allowing to populate a resonant state of ^{12}C with the $^{11}B(D,n)^{12}C$ reaction. This state decays with a γ emission of 15.1 MeV. In this range of energy, the dominant mechanism of γ-ray interaction is the pair production; therefore, two peaks corresponding to first and second escape peaks due to positron annihilation are present but not resolved in the spectrum (see Fig. 4.21).

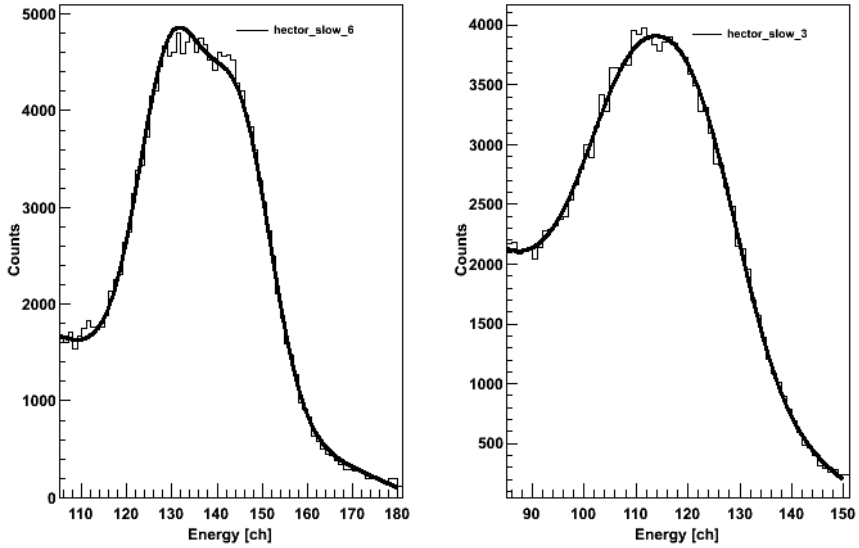

Fig. 4.19: The calibration spectra with ^{60}Co source for two of the HECTOR detectors. The two γ emission are not separated, especially in the detectors with a bad energy resolution. In the left panel the detector with the best energy resolution, in the right panel the detector with the worst energy resolution.

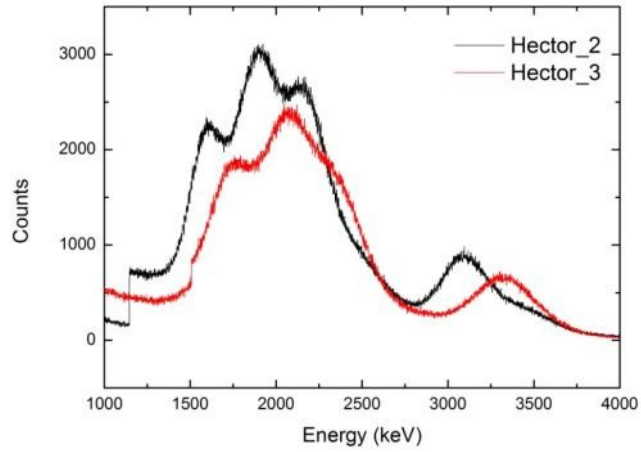

Fig. 4.20: The energy spectra of the internal radioactivity of two HECTOR detectors. It is possible to see that positions and intensity of these peaks are characteristic of each detector.

The peak at 15 MeV is fitted with the sum of 3 Gaussian peaks properly modeled (plus background). Also in this case, in order to obtain consistent results, some fit parameters were constrained. The differences between the three centroids are fixed at 511 keV and the widths are constrained to be equal. The centroid of the first escape peak is the fitting parameter. This peak, was used for the final calibration that was done with the linear regression technique. The fitting procedure is based on standard fitting methods implemented in ROOT framework [37] and is explained in detail in the manual [43].

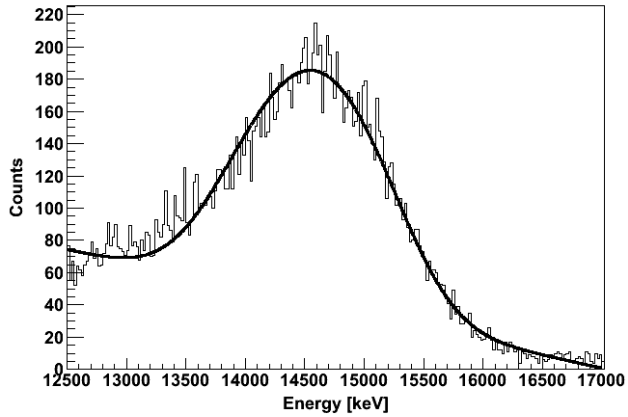

Fig. 4.21: The γ spectrum of the reaction $^{11}B(D,n)^{12}C$ detected by one of the HECTOR detectors. It is not possible to distinguish the full energy peak from the first and the second escape peaks. The line is the fit performed with the sum of three Gaussian and a background.

The calibrated energy spectrum has to be corrected for Doppler effect. The source velocity is non-relativistic, therefore we have applied the following formula:

$$E_{DC} = E_{\gamma} \frac{1 - \beta cos(\theta)}{\sqrt{1 - \beta^2}} \qquad (4.8)$$

where $\beta = v/c$.

Neutrons interact in BaF_2 mainly through (n,γ) reactions. Therefore, their signals are difficult to disentangle in the fast vs slow matrix; for them a clean discrimination can be achieved only via ToF, relying on the difference in ToF of γ rays and neutrons. In Fig. 4.22 the neutron were distinguished from the prompt γ peak; the time difference of between neutrons and

gammas is about 8 ns. It is possible to use the ToF technique due to the good time resolution of BaF_2 scintillators.

The time calibration of the HECTOR TDC was done using a pulse generator. ToF spectra were obtained using the difference between the time of the HECTOR detectors and the beam RF. All the ToF spectra were aligned so that the centroid of the prompt γ peak is in the same channel.

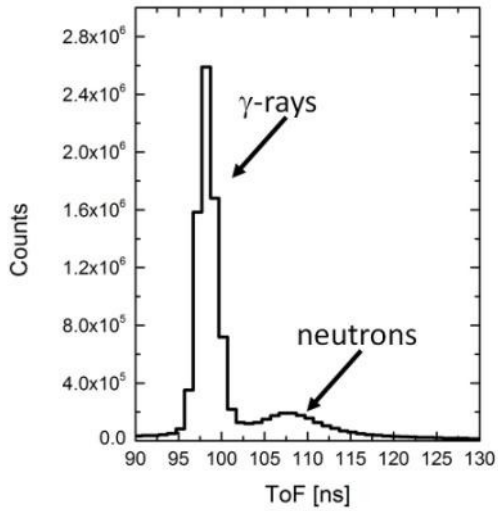

Fig. 4.22: The ToF spectrum of one of the HECTOR detector. It is possible to see the prompt γ-peak and the second small peak is the neutron peak.

In the sorting code, some conditions are applied in order to select the fusion-evaporation events. To obtain the high-energy spectra of HECTOR detectors, we applied the following conditions:

- the existence of a good signal from RF,
- the presence of a signal in HECTOR and in phoswich TDC,
- the energy of HECTOR detectors has to be between 5 and 32 MeV,
- the prompt γ peak in HECTOR was selected with a window of 4 ns,
- the γ multiplicity of the high-energy γ rays has to be equal to one,
- an evaporation residue (multiplicity of the residue as to be equal to one) was selected by a graphical cut as shown in Fig. 4.2,
- the presence of a stopped particle in GA of phoswich detector was also selected in the GA versus GB spectra (see Fig. 4.3).

In Fig. 4.23 the high-energy spectrum without gates (black squares) is compared with the spectra with different conditions.
The spectrum with the first 5 gates is shown in Fig. 4.23 by red points. The spectrum represented with blue triangles in the left panel of in Fig. 4.23 and alone in the right panel of Fig. 4.23 is obtained with all the gates described here.

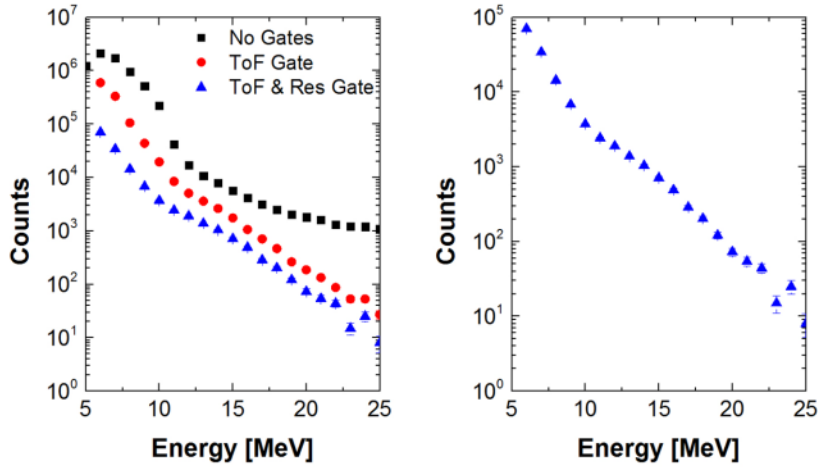

Fig. 4.23: In the left panel, an energy spectrum of one of HECTOR detectors with different gate conditions. The black squares represent the spectrum without gate, the red points the spectrum with a gate on the prompt γ peak of Fig. 4.22 and the blue triangles the spectrum with the gate on the prompt γ peak and the gate on the residues in phoswich GA versus ToF spectra (see Fig. 4.2). In the right panel, the high-energy spectrum with the same gate of the blue triangles spectrum in left panel; it is possible to see that the spectrum has the typical shape of a GDR spectrum, that is the superposition of an exponential and a Lorentzian curve.

Two of the HECTOR detectors were excluded from the data analysis. The first one, detector number 7 was excluded because it had a gain drift during the calibration with the ^{60}Co source and the threshold, used during the calibration, was too high and the first of ^{60}Co emission was cut. For this reason it was impossible to have a good calibration of this detector. The second one, detector number 4, drifted so much that, during the measurement, its threshold was at 7.5 MeV. In this way it was impossible to normalize the spectra of this detector at 7-8 MeV on the exponential part.

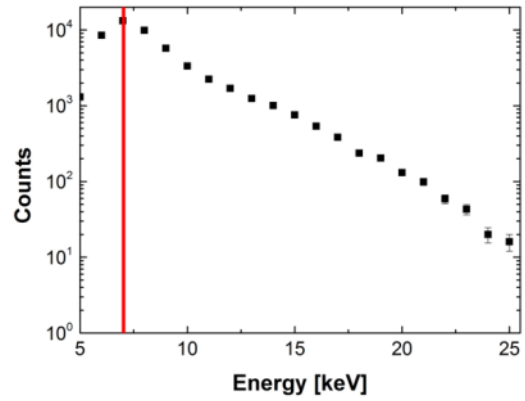

Fig. 4.24: The high-energy spectrum of the detector number 4. The threshold (the red line) was set at 7 MeV, that is too high for this kind of measure.

4.4. Extraction of the DD gamma multiplicity

The GDR and the DD pre-equilibrium emissions have the same dipolar nature and the same energy. To separate the two contribution it is necessary to subtract a spectrum in which the DD emission is present with one in which is present only the statistical decay. The experimental signature of the DD emission is an excess of counts in the energy region of 10-22 MeV with respect to the statistical decay as it is shown in Fig. 4.25. The experimental spectrum and the one in which is present only the statistical decay have to be normalized. The two spectra were normalized between 7-8 MeV, because the exponential part includes only the statistical dacay.

One important parameter of the statistical model is the beam energy, used to calculate the excitation energy of the compound nucleus. In the presence of a pre-equilibrium emission, however, part of the excitation energy is carried away by particles and the energy available for the statistical decay is smaller. It is therefore important to know the pre-equilibrium energy loss, in order to subtract it from the total.

The statistical model calculations were carried out with the CASCADE code [44], which only accepts the beam energy as an input. It was

therefore necessary to calculate an effective beam energy, which gives the same excitation energy to the compound as the energy left after the pre-equilibrium phase.

To have a validation of the statistical model a symmetric reaction was measured at 8.1 and 15.6 MeV/u, and was used to tune the other parameters of the statistical model.

Another method to measure the DD contribution is described in [3]–[5]. In these references, the statistical model was not used: the asymmetric reaction high-energy spectrum is compared with the one obtained from a symmetric reaction. In this case is not necessary to know the pre-equilibrium, because the beam energy in the two reactions was chosen so that they have the same pre-equilibrium contribution.

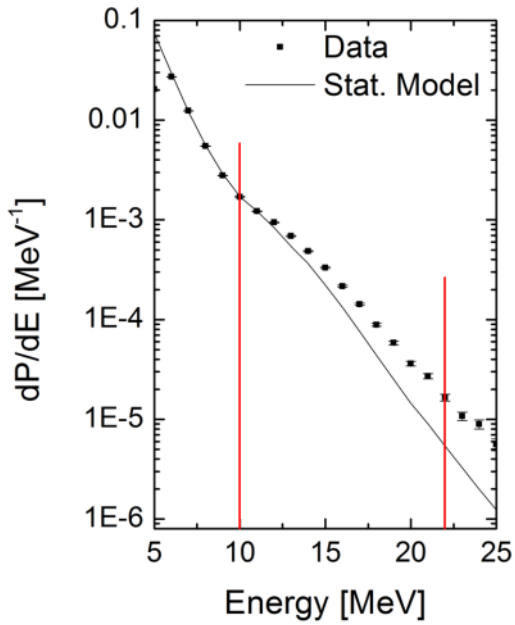

Fig. 4.25: The comparison between the experimental data and the results obtained from the statistical model. The statistical model does not include the DD contribution, in the experimental data the DD pre-equilibrium γ emission is characterized by an excess of count in the region between 10-22 MeV.

As it was explained in section 2.2.3, the aim of this experiment is the measure of the pre-equilibrium γ emission at an intermediate value of the

beam energy (12 MeV/u) with respect to a previous experiment [6] in which the aim was the measurement of this emission at 8.1 MeV/u and at 15.6 MeV/u. In the previous experiment two different reactions were populated to produce the same CN: the asymmetric one (^{16}O + ^{116}Sn) and a symmetric one in (^{64}Ni + ^{68}Zn) as is shown in Tab. 4.4. The high-energy spectrum of the symmetric reaction is fitted with a statistical model (CASCADE) to find the GDR parameters. In the previous cases, at 8.1 and 15.6 MeV/u, the GDR parameters were set to be use in the CASCADE statistical model, by using the symmetric reaction ^{64}Ni + ^{68}Zn. At 12 MeV/u, we used the CASCADE model with the parameter that were set in the previous experiment [6]. The maximum angular momentum is fixed in the CASCADE code at $70\hbar$, because it is the maximum value that the nucleus could stand before fissioning.

The high-energy spectra of asymmetric reaction were compared with statistical model calculation (with the same GDR parameter of the symmetric reaction) and the difference was expected to be originated by the presence of the pre-equilibrium emission. At 12 MeV/u, the symmetric reaction was not measured but can be easily extracted from the previous data/calculation.

Reaction	E_{beam} [MeV/u]	E^* [MeV]	D[fm]	Reference
^{64}Ni + ^{68}Zn	4.7	100	1.2	[6]
^{64}Ni + ^{68}Zn	6.2	150	1.2	[6]
^{64}Ni + ^{68}Zn	7.8	200	1.2	[6]
^{16}O + ^{116}Sn	8.1	100	8.6	[6]
^{16}O + ^{116}Sn	12	155	8.6	This work
^{16}O + ^{116}Sn	15.6	206	8.6	[6]

Tab. 4.4: The reactions used to populate ^{132}Ce are listed here. E^* is the excitation energy and D is the dipole moment.

In the comparison with the BNV theoretical calculation, as will be explained in section 5.3, the maximum angular momentum was fixed also at $63\hbar$, at 12 MeV/u, because it is the maximum possible value calculated using the CF code [45].

4.4.1. Evaluation of the pre-equilibrium γ emission at 12 MeV/u

In order to study the statistical decay of CN one has to calculate first the pre-equilibrium contribution. Both light particles and γ rays can be emitted before CN thermalization adding a non-evaporative contribution to the measured spectra, that can be evaluated once the shape of the evaporative contribution is known. Pre-equilibrium light-particle emission has the effect of cooling down the compound nucleus, while the γ-emission in the cases under analysis is too low to have a significant effect on the excitation energy of the CN. From this statement we can deduce that the information needed in order to extract the DD emission in $^{16}O + {}^{116}Sn$ is: i) the energy loss associated with pre-equilibrium light-particles emission and ii) the statistical γ emission from ^{132}Ce at the proper excitation energy.

The experimental data have to be compared with the statistical model spectrum in which the excitation energy is the kinematic excitation energy corrected by the energy loss during the pre-equilibrium phase. It is possible to extract the pre-equilibrium energy loss from LCPs in three different ways. The first one is using a linear interpolation between the values found at 8.1 and 15.6 MeV/u. The value of the pre-equilibrium energy loss obtained by this interpolation is 26 MeV, that is the same of the value that could be calculated by using the parameterization of [17]. In Fig. 4.26 ([17]), the trends of the excitation energy minus the pre-equilibrium contribution as a function of the excitation energy is reported. The dotted line represents the complete fusion energy, which ranges from 108 to 186 MeV in the measurements of reference [17]. The dashed line that correspond to E_{init} represents the initial compound nucleus excitation energy following pre-equilibrium emission. From the dashed line, it is possible to extract the pre-equilibrium energy loss for different values of the excitation energy. In our case, if we used this curve, we obtained a pre-equilibrium energy loss of 26 MeV.

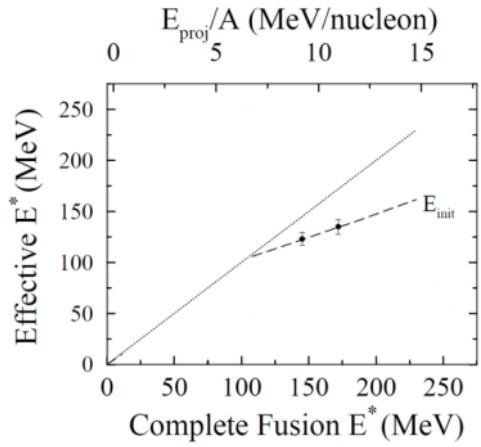

Fig. 4.26: The energetics of ^{18}O + ^{100}Mo reaction are shown. The dotted line represents the complete fusion energy, which ranges from 108 to 186 MeV in measurements of reference [17]. The dashed line that correspond to E_{init} represents the initial compound nucleus excitation energy following pre-equilibrium emission [17].

The second and the third ways are the two method described in section 4.2. The comparison between the experimental data and the statistical model (in which the pre-equilibrium energy loss of 26 MeV is included) is shown in Fig. 4.25. The value of the DD γ multiplicity is the integral, between 10-22 MeV, of the experimental spectra, subtracted from the spectrum obtained from the statistical model. The spectra are normalized on the total fusion cross section. The value of the DD γ multiplicity found in this way is obviously different for the three different values of the pre-equilibrium energy loss. The values of the DD contribution for the different values of the pre-equilibrium energy loss are reported in Tab. 4.5.

Method for E_{loss}	**E_{loss} [MeV]**	**M_γ**	**Error**
Data	13.3	$2.37\ 10^{-4}$	$1.3\ 10^{-4}$
Theoretical model	18.4	$4.63\ 10^{-4}$	$1.2\ 10^{-4}$
Interpolation and Ref. [17]	26	$7.88\ 10^{-4}$	$2.0\ 10^{-4}$

Tab. 4.5: The values of the DD γ multiplicity for the three different values of E_{loss}.

The pre-equilibrium energy loss is a critical value, since the DD γ multiplicity strongly depend on this value, as it is shown in Tab. 4.5.

The error bars are the sum of the statistical error, in this case practically negligible, and the error due to the uncertainty on the value of the pre-equilibrium energy loss. To estimate the latter contribution, the experimental data were compared with the results of the statistical model calculations where:

$$E^*_{st\_model} = E^* - E_{loss} \pm \sigma_{E_{loss}}. \qquad (4.9)$$

In literature [6], [42], [46], it is possible to find the values of the pre-equilibrium energy loss for different systems. These value are listed in Tab. 4.6.

E_{beam} [MeV/u]	Reaction	E^* [MeV]	E_{loss} [%]	Error E_{loss} [%]	E_{loss} [MeV]	Error E_{loss} [MeV]	Ref.
7.8	^{64}Ni + ^{68}Zn	203	3.6	2.0	7.3	4.1	[6]
8.1	^{16}O + ^{116}Sn	100	5.6	2.9	5.6	2.9	[6]
11.1	^{18}O + ^{100}Mo	174	21.4	2.6	37.2	4.5	[46]
13.0	^{20}Ne + ^{169}Tm	197	12.7	1.5	25.0	3.0	[42]
13.0	^{20}Ne + ^{159}Tb	201	13.9	1.5	27.9	3.0	[42]
15.6	^{16}O + ^{116}Sn	206	19.9	3.4	41.0	7.0	[6]
16.0	^{20}Ne + ^{169}Tm	251	15.9	2.4	39.9	6.0	[42]
16.0	^{20}Ne + ^{159}Tb	254	18.5	2.4	47.0	6.1	[42]
12.0	^{16}O + ^{116}Sn	155	8.6	1.6	13.3	2.5	This work

Tab. 4.6: the systematic present in literature about the pre-equilibrium energy loss.

In Fig. 4.27 the pre-equilibrium energy loss is show as a function of the beam energy. We reported also the point at 12 MeV/u for the ^{16}O + ^{116}Sn

reaction, calculated from the experimental data. It is possible to see that this value is consistent with the systematic reported in literature.

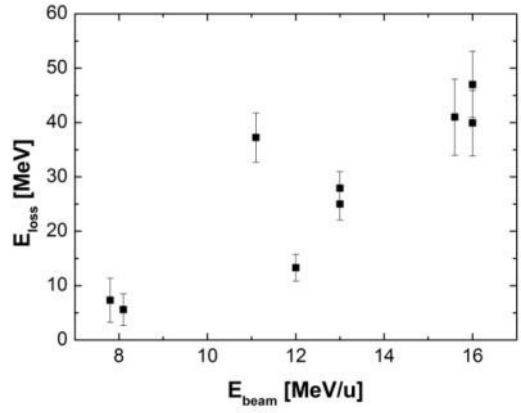

Fig. 4.27: The energy loss during the pre-equilibrium phase as a function of the beam energy is shown. This picture shows the systematic present in literature ([6], [42], [46]). The point at 12 MeV is the value extracted from the data in this work.

4.4.2. Comparison with the values at 8.1 and at 15.6 MeV/u

The values of the DD yield obtained at 12 MeV/u has to be compared with the values at 8.1 and 15.6 MeV/u [6]. In Fig. 4.28, in Fig. 4.29, and in Fig. 4.30, the DD γ multiplicity is reported as a function of the beam energy. The values show at 12 MeV/u were obtained using as pre-equilibrium energy loss equal to 13.3 MeV in Fig. 4.28, equal to 18.4 MeV in Fig. 4.29, and equal to 26 MeV in Fig. 4.30.

By using the pre-equilibrium energy loss calculated from [17], a strong increase of the DD contribution is found between 8.1 MeV/u and 12 MeV/u, as shown in Fig. 4.30. This strong increase is not predicted by the BNV theoretical model (see section 5.3).

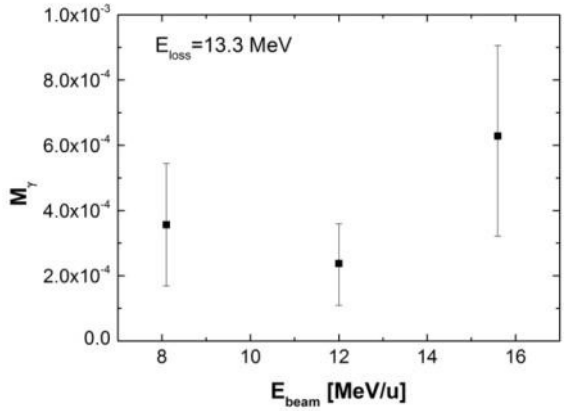

Fig. 4.28: The trend of the DD contribution as a function of the beam energy for the system ^{16}O + ^{116}Sn. In this case, the pre-equilibrium energy loss is the one obtained from the data (13.3 MeV).

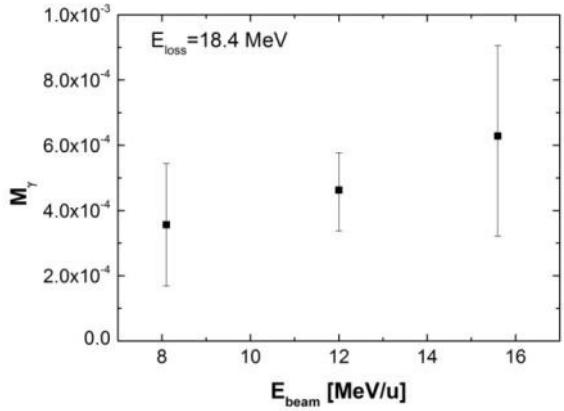

Fig. 4.29: The trend of the DD contribution as a function of the beam energy for the system ^{16}O + ^{116}Sn. In this case, the pre-equilibrium energy loss is the one obtained from the theoretical model calculations [41] (18.4 MeV).

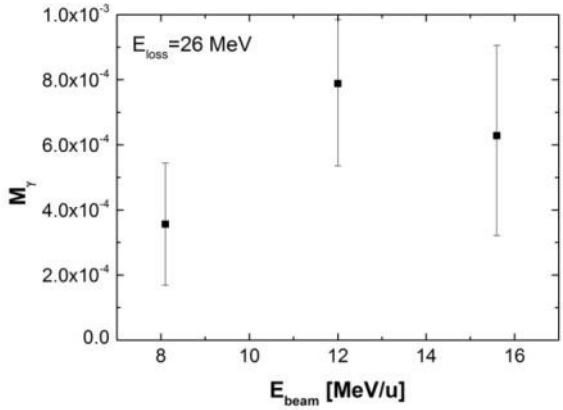

Fig. 4.30: The trend of the DD contribution as a function of the beam energy for the system ^{16}O + ^{116}Sn. In this case, the pre-equilibrium energy loss is the one obtained from the a liner interpolation of the values at 8.1 and at 15.6 MeV/u. This value is the same of the one that could be calculated by using [17](26 MeV).

As discussed previously, the most accepted systematic (see Fig. 4.27 and Tab. 4.6) in pre-equilibrium energy loss is consistent with the GARFIELD measure value. The value of the pre-equilibrium energy loss obtained from the data and the one from the theoretical model [41] are compatible within the error bars. In this case the DD contribution has a rise trend as a function of the beam energy, as shown in section 5.3 this values for DD contribution at 12 MeV/u are in agreement with the prediction of the BNV theoretical model as will be shown in section 5.3.

4.5. Extraction of the angular distribution

From the data it is possible to also extract the DD angular distribution. The DD angular distribution is expected to be dipolar but due to the rotation of the dipolar axis is expected to be quenched. The angular distribution could be calculated using the following formula:

$$W(\theta) \approx 1 + a_2 P_2(cos\theta) \qquad (4.10)$$

where P_2 is the Legendre polynomial $P_2(cos\theta) = \frac{1}{2}(3cos^2(\theta) - 1)$ and a_2 is a quenching factor.

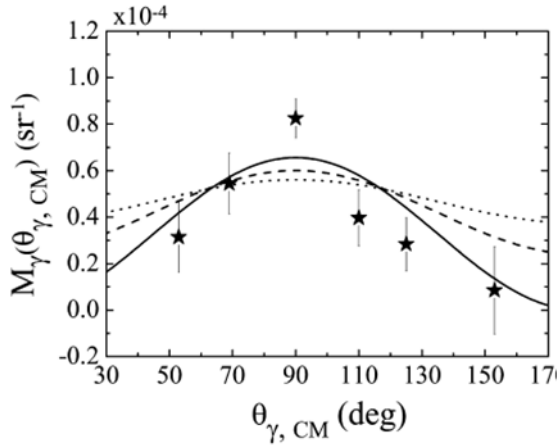

Fig. 4.31: The angular distribution reported in [5]. When a_2 = - 1 the angular distribution is the one from a dipole oscillation along the beam axis (solid line), while a_2 = - 0.5 (dashed line) and a_2 = - 0.25 (dotted line) correspond to more diffuse angular distributions. The experimental angular distribution is strongly anisotropic with a maximum around 90°, consistent with emission from a dipole oscillating along the beam axis (solid line).

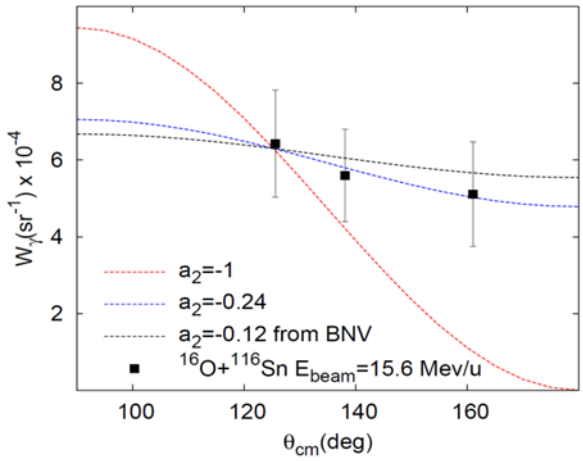

Fig. 4.32: The angular distribution reported in [6]. When a_2 = - 1 the angular distribution is the one from a dipole oscillation along the beam axis (red-dashed line), while a_2 = - 0.24 (blue-dashed line) and a_2 = - 0.12 (black-dashed line) correspond to more diffuse angular distributions; the first one that reproduce the experimental data and the second one obtained from the BNV theoretical model.

In literature, it is possible to find two different trend for the DD dipole angular distribution. The angular distribution, reported in [5] and shown in Fig. 4.31, is consistent with emission from a dipole oscillating along the beam axis (pure dipole). On the other hand, the angular distribution, reported in [6] and shown in Fig. 4.32, is quenched due to the rotation of the dipolar axis.

To extract the angular distribution from the data it is necessary to compared the high-energy γ-rays spectra of the HECTOR detectors at different angles. The angles that were used during the experiment were four and were reported in Tab. 3.1. The spectra were normalized using the 15.1 MeV γ-ray data from ^{11}B + D calibration reaction: the 15.1 MeV γ-rays emitted by this reaction are emitted isotropically, meaning that the different number of counts in the 15.1 MeV peak in different detectors is only due to geometrical effects or due to the dead time. The area of the 15.1 MeV peak was measured for each detector and a normalization factor was found. These normalized factors, shown in Tab. 4.7, were applied to the HECTOR γ-ray spectra for the DD emission.

HECTOR #	**Normalization Factor**
0	0.82
1	1.00
2	0.85
3	1.18
4	0.88
5	1.08
6	0.97
7	0.79

Tab. 4.7: The normalization factors find using the 15.1 MeV γ-ray data from the ^{11}B + D calibration.

The normalized high-energy spectra of the HECTOR detectors were compared with the CASCADE model prediction. The difference in the energy range of 10 to 22 MeV between the different detectors is caused by

the angular distribution of the DD emission. To have a better result, we summed the spectra of the two HECTOR detectors at the same angle (detectors 0 and 7 are at 160°, detectors 1 and 6 are at 137°, detectors 2 and 5 are at 124° and detectors 3 and 4 are at 150°). The obtained contributions at the same angle are shown in Fig. 4.33.

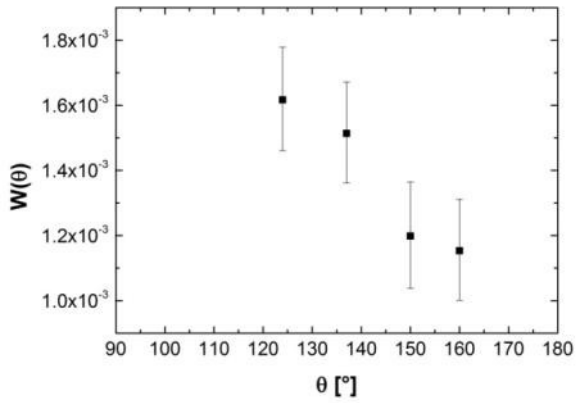

Fig. 4.33: The DD angular distribution extracted from the data.

The angular distribution found from our data is quenched respect a pure dipole. To find the quenching factor of the angular distribution obtained from our data, the points in Fig. 4.33 were fitted with the analytic expression of equation 4.10. The value of the quenching factor a_2 is - 0.36. The data with the fit are shown in Fig. 4.34.

The GDR decay has an angular distribution as a function of the energy [47]. As consequence, the measured quenching factor includes the DD angular distribution and the quenching factor of the GDR angular distribution, it is possible to write the a_2 coefficient as follow:

$$a_{2\_Measured} = a_{2\_GDR} + a_{2\_DD}. \qquad (4.11)$$

To have the value of the quenching factor of the DD angular distribution it is necessary to calculate the GDR angular distribution factor and to subtract it from the measured one.

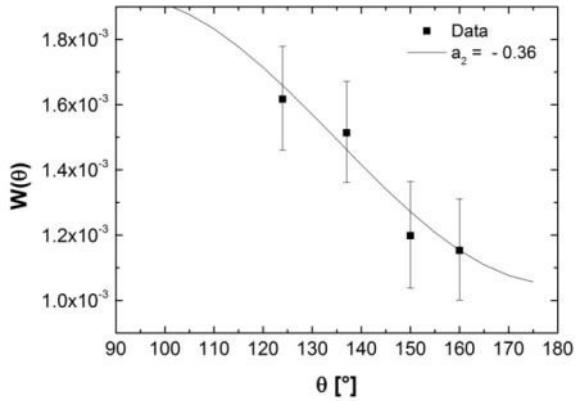

Fig. 4.34: The angular distribution obtained from data is compared by the expected angular distribution of equation 4.10. The angular distribution from data is quenched and the quenching factor of the equation 4.10 is $a_2 = -0.36$.

The GDR angular distribution was calculated using a theoretical model, the Lublin Strasbourg Drop model [48], [49]. The coefficient a_2 trend as a function of the γ energy, for ^{132}Ce compound nucleus, is shown in Fig. 4.35. To obtain the value a_{2_GDR} it is necessary to do a weighted average of a_2 on energy, in which the weights are the counts at that energy, as follow:

$$a_{2\_GDR} = \frac{\sum_{10}^{22} a_2(E) N_{counts}(E)}{\sum N_{counts}(E)}. \qquad (4.12)$$

The value of a_{2_GDR} found in this way is - 0.04.

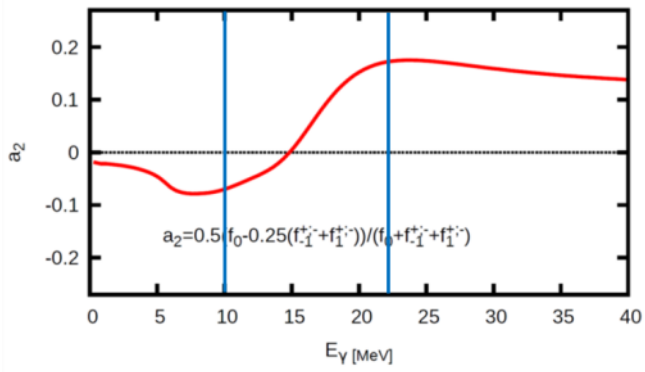

Fig. 4.35: The calculated GDR angular distribution.

From equation 4.11, it is possible to calculated the quenching factor of the DD angular distribution. The value that is found is:

$$a_{2\_DD} = a_{2\_Measured} - a_{2\_GDR} = 0.36 - 0.04 = 0.32. \quad (4.13)$$

For the ^{16}O + ^{116}Sn reaction at 12 MeV/u, a quenched angular distribution respect a pure dipole was found, as for the same reaction at 15.6 MeV/u as reported in [6]. Moreover our data are compatible with the $a_2 = -0.24$, that was the value of the quenching factor found at 15.6 MeV/u, as shown in Fig. 4.36. The angular distribution found from our data is not compatible with a pure dipole one, in fact the blue line in Fig. 4.36 (pure dipole) does not reproduce the experimental data.

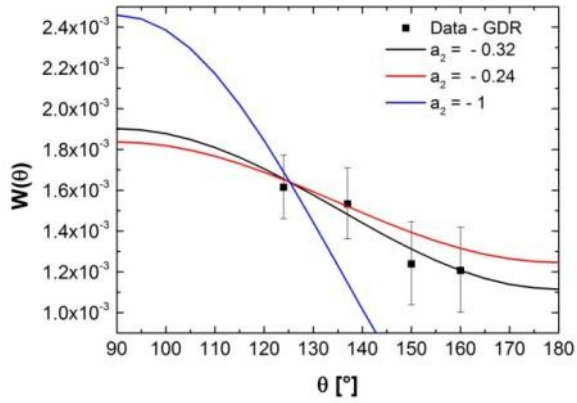

Fig. 4.36: The angular distribution calculated for ^{16}O + ^{116}Sn at 12MeV/u. When a_2 = - 1 the angular distribution is the one from a dipole oscillation along the beam axis (blue line), while a_2 = - 0.32 (black line) and a_2 = - 0.24 (red line) correspond to more diffuse angular distributions; the first one reproduces the experimental data and the second one is the value obtained for the same system at 15.6 MeV/u.

5. Theoretical predictions for the dynamical dipole yield

In this chapter the results of the theoretical predictions will be presented. In particular, after a small introduction on the model (section 5.1), the analysis of the BNV simulations for the $^{16}O+^{116}Sn$ reaction will be described in section 5.2. These simulations were analyzed as a function of the number of test particles (section 5.2.1), and their statistical fluctuations were studied in section 5.2.2. The relation between the dynamical dipole total yield and the impact parameter will be presented in section 5.2.3. The sensitivity on the symmetry term of the nuclear equation of state will be discussed in section 5.2.4.

The results of the simulations will be then compared to the experimental results in section 5.3 concerning the total yield, and in section 5.4 concerning the angular distribution.

To better understand the results of the theoretical model, simulations were performed also for two other reactions: one, $^{64}Ni + ^{68}Zn$, in which projectile and target have the same N/Z ratio (section 5.5); and one, $^{132}Sn + ^{58}Ni$, in which there is a large asymmetry in N/Z between projectile and target (section 5.6). The predictions for these two reactions will be compared to those for the $^{16}O + ^{116}Sn$ reaction in section 5.7.

5.1. The BNV model simulations

To theoretically estimate the amount of pre-equilibrium γ emission we have used the BNV model described in 2.3. It is important to notice that pre-equilibrium collective dipole radiation can be emitted in a fusion-evaporation reaction only if the colliding nuclei have a different N/Z ratio between projectile and target. An asymmetry in mass reduce a γ pre-equilibrium emission but with such emission that is very weak [29].

One possible approach to face the problem of the quantification of the pre-equilibrium dipole emission is to directly simulate the fusion process

and to apply a bremsstrahlung approach for the γ emission. This is achieved by considering the evolution of the collective dipole acceleration from the time when it suddenly rises, until it is completely damped to a pure "thermal" component. In this way it is possible to consistently calculate the whole contribution of the pre-equilibrium dipole radiation to the photon yield.

The total photon emission probability from the dipole mode oscillations, is, therefore, given by the bremsstrahlung formula (equation 2.11). In summary, the BNV approach follows the time evolution of the dipole mode along the fusion dynamics and it evaluates, the corresponding pre-equilibrium photon emission [7].

Using this model, we simulated the fusion dynamic for the system $^{16}O + {}^{116}Sn$ at 8.1, 12 and 15.6MeV/u (the energies of the experimental data analyzed in this thesis and reported in [6]). The calculations were also performed for a system with a larger dipole moment, $^{132}Sn + {}^{58}Ni$ at the same beam energies of the experimental data.

In the code, to calculate the collision integral of the equation 2.9, the parameterizations of the neutron-neutron and the proton-proton cross section discussed in [50] was used and for the neutron-proton cross section the parameterization discussed in [51] was used. These cross section parameterizations include the medium effects, the isospin, the energy and the scattering angle dependence.

5.2. BNV simulations for the asymmetric reaction: $^{16}O + {}^{116}Sn$

For the system $^{16}O + {}^{116}Sn$ we did the simulations at each beam energy (8.1, 12 and 15.6 MeV/u) at different impact parameters (b = 0, 2, 4, 4.5, 5, 5.5, 6, 6.5, 7, 7.5, 8 fm). We chose this impact parameters because the fusion cross section is expected to be practically zero for impact parameter larger than 6.5 fm. The same simulations were repeated for two different parameterizations of the nuclear EOS (asy-stiff and asy-soft). As explained in section 2.2.1, the asy-stiff parameterization is characterized by L_{symm} =

72.6 MeV, instead Asy soft is characterized by $L_{symm} = 14.5\ MeV$, these values are calculated by equation 2.5.

A simulation starts when the two colliding nuclei have a distance of 14 fm/c and it stops after 400 fm/c. This time interval could be divided in three phases: the first one that is the approaching phase, the second one that is called dinuclear phase and the third one that is the compound nucleus phase. The dinuclear phase is where the kinetic energy of the relative motion is converted in thermal energy due to the collisions between nucleons and where, if there is a finite dipole moment, the dynamical dipole emission appears.

To have a good estimation of DD yield from the BNV model it is necessary to do an average on different BNV calculations with fixed parameters. One BNV calculation simulates one fusion-evaporation event. One event mimics one fusion reaction with: a fixed impact factor, a given beam energy and a chosen projectile and target. A BNV calculation calculates for one event: the dipole moment evolution with time, the density evolution with time (in Fig. 5.2 there is a graphical view of the density distribution during the simulation) and the conjugated of dipole moment evolution with time. As an example Fig. 5.1 shows the evolution with time of the dipole moment and of its conjugated moment for the system $^{16}O + {}^{116}Sn$ at 12 MeV/u with an impact parameter $b = 0$ fm and Fig. 5.2 shows the density plot for the system $^{16}O + {}^{116}Sn$ at 12 MeV/u with an impact parameter $b = 4$ fm. From the time evolution of the dipole moment it is possible to calculate the DD γ emission using equation 2.11; an example of Bremsstrahlung spectra, relative to the case of Fig. 5.1, is shown in Fig. 5.3. The value of the total DD γ multiplicity yield is obtained from the integral of the Bremsstrahlung spectrum between 0-22 MeV.

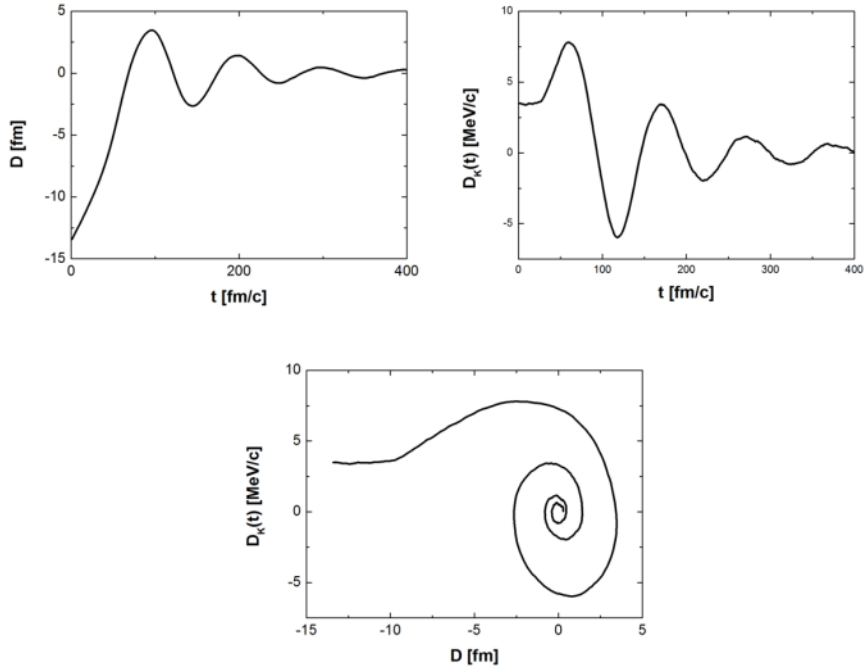

Fig. 5.1: In the top left panel there is an example of the dipole moment evolution in time. In the top right panel there is an example of the conjugate dipole moment evolution in time. In the bottom panel there is the evolution of the correlated variables. The BNV simulation was done at 12 MeV/u, at impact parameter $b = 0\ fm$ *and for the asy-soft parameterizations of EOS.*

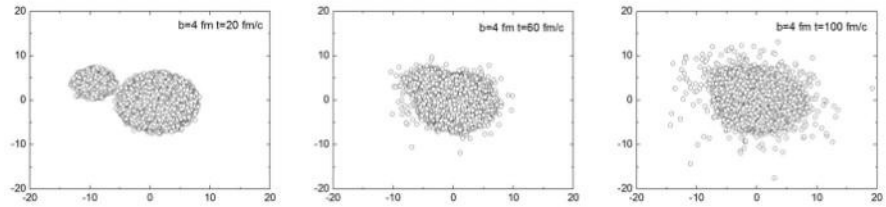

Fig. 5.2: A prepresentation of the nucleon density at different times from the start of the simulation, at t=20 fm/c the two nuclei are approaching, at t=60 fm/c there is the contact between the two nuclei and at t=100 fm/c it is not anymore possible to identify the projectile and the target, but compound nucleus.

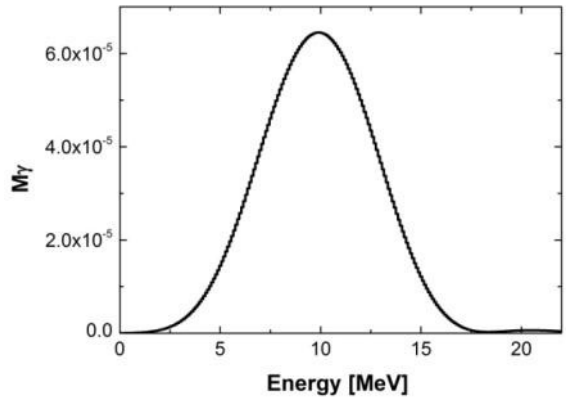

Fig. 5.3: The Bremsstrahlung spectrum obtained from a BNV simulation.

From the BNV simulations one can obtain the integral of the Bremsstrahlung spectrum, that is the yield of the DD emission, for a fixed impact parameter. The value of the total yield was extracted through a weighted average on the impact parameters. One of the critical points is the calculation of the weights of each impact parameter. In a fusion-evaporation reaction with the semi-classical approximation, each impact parameters can be associated with the corresponding angular momentum transferred to the CN:

$$l\hbar = \mu v_p b \qquad (5.1)$$

where μ is the reduced mass and v_p is the projectile velocity. It is possible to estimate the fusion cross section as a function of the angular momentum using some model, such as DCASCADE model. The fusion cross section as a function of the impact parameter can be obtained by using equation 5.1. With the semi classical approximation it is possible to associate a range of impact parameters (centered at b=0, 2, 4, 5, 5.5, 6 and 6.5 fm) with a correspondent range of angular momenta. In this way it is possible to perform a weighted average on the multiplicity corresponding to each impact parameters and we can obtain the total DD multiplicity that can be directly compared to the measured one. It must be remembered, however, that thus technique is not exact but only an approximation. It does not

consider the angular momentum removed by the emitted pre-equilibrium particles or the quasi fission reaction channel.

The BNV approach is a deterministic one, however, because of the discretization of particles and computational techniques statistical fluctuations in the results are unavoidable. To have a more precise estimation of the reliability of the calculations to estimate the DD γ emission, it is therefore necessary to simulate several events to reduce the uncertainness of the model.

Moreover, the BNV approach is for a continuous medium which, unfortunately, cannot be solved in a numerical way. The solution which was chosen is to discretize this continuum with a large number of test particles. A better continuum approximation can be achieved with a larger number of test particles, but with an increasing cost in terms of CPU time. Consequently, as well discussed in section 5.2.1 some compromises in term of the number of test particle were necessary.

Furthermore, to have a better comprehension of the BNV model we performed simulations for systems ($^{64}Ni + {}^{68}Zn$, $^{16}O + {}^{116}Sn$ and $^{132}Sn + {}^{58}Ni$) with a different dipole moment ($D(0) = 1.2fm$, $D(0) = 8.6fm$ and $D(0) = 45.4fm$) and simulations in which the EOS parameters are changed. We analyzed the results of the BNV as a function of the number of the simulated fusion events, as a function of the beam energy, as a function of the impact parameter and as a function of the number of test particles.

5.2.1. Influence of the number of test particles

We did simulations of 10 events with different values of the number of test particles (100, 200, 400, 600 and 700) with impact parameter $b = 4fm$ at the three different energies (8.1, 12, 15.6 MeV/u). The number of test particles is limited by the available computer memory. The results obtained from these simulations are shown in Fig. 5.4. It is possible to see that the DD increases with the number of test particles (N) up to $N = 400$, then saturates. Simulations with $N = 100, 200$ underestimate the DD yield; but results with larger N are within the error bars were consistent with the asymptotic value and there are no significant changes for $N \geq 400$. This general trend is not

followed by the asy-soft parameterization at 15.6 MeV/u, in which the DD γ multiplicity seems to increase with the test particle number.

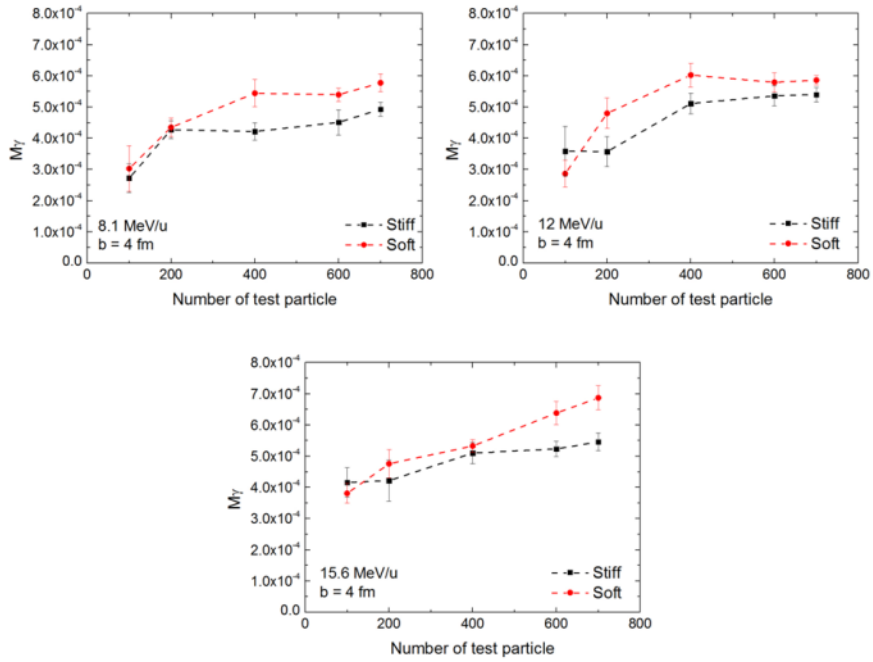

Fig. 5.4: The DDγ multiplicity as a function of the number of the test particles used in these BNV simulations. In the top panel left there are the results at 8.1 MeV/u, in the top right one the results at 12 MeV/u and in the bottom panel the results at 15.6 MeV/u, in all cases the simulations has been done with the impact parameter $b = 4fm$. In both panel the black squares are the results for the asy-stiff parameterization and the red points are the results for the asy-soft one.

5.2.2. Statistical fluctuations of the yield

Fluctuations are present due to the numerical approach in the resolution of the BNV equation. A way to reduce these fluctuations is to increase the number of the test particles, in fact the BNV equation describes a continuum (namely a fluid). Our system, however consist of a discrete number of nucleons. In the model each nucleon is therefore represented by a discrete number of test particles. The increase in the number of the test

particles allows a better approximation of a continuum, but requires more CPU power.

As each fusion reaction can be different from the other, it is necessary to quantify the fluctuations which are intrinsic in the model. Namely, it is important to check on an event by event basis how the DD γ-rays yield changes for fixed parameters. To understand the amount of these fluctuations we produce 50 fusion events for fixed parameters.

For each beam energy and impact factor we calculated 50 events using 200 test particles. It is possible to see in Fig. 5.5 the histogram of the DD γ yields for each event which has the shape of a Gaussian distribution.

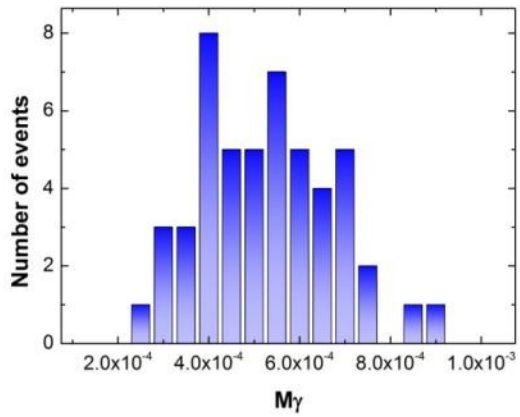

Fig. 5.5: The distribution of the values of the yield (50 events), obtained from the BNV, for each event. We obtain a Gaussian distribution for all values of the impact parameter and for the three different values of the energy. From this Gaussian distribution it is possible to extract the a mean value and a standard error.

From the distributions of the total yields as the one of Fig. 5.5, we have extracted an average yield and a standard deviation (which is approximately 30%). The expected uncertainty in the gamma yield is given by the standard error, which corresponds approximately to 4% (see Fig. 5.5).

It is important to notice that we expected that the importance of such fluctuations will decrease as the number of the test particles increases and viceversa.

In Fig. 5.6 we plot the standard deviation of the DD yield extracted from the 10 calculated events relative to the number of test particles. It is possible to notice that the error bars decrease with the number of test particle.

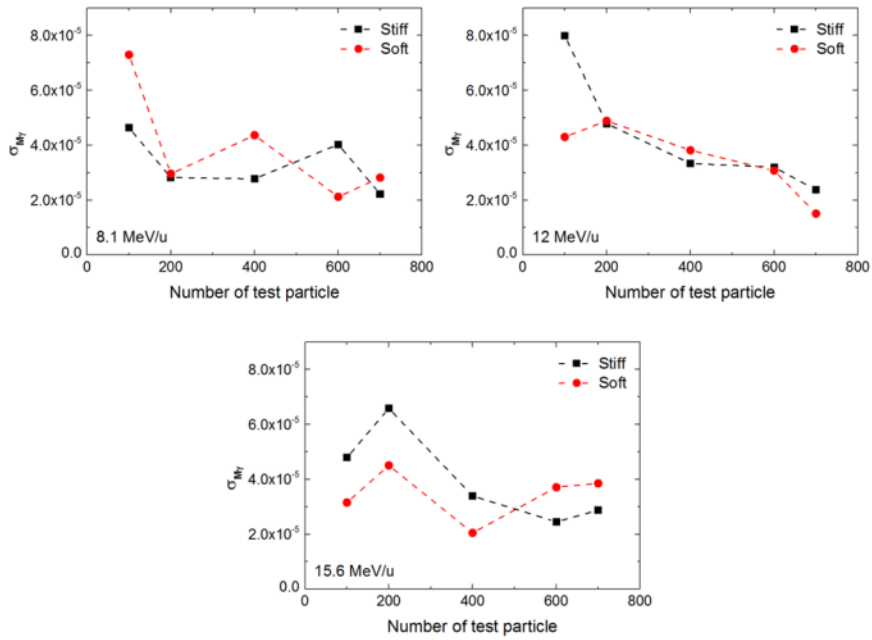

Fig. 5.6: The trend of the errors as a function of the number of the test particles at the three different beam energies.

In the previous work in 2008 [6], the BNV simulations were done using 200 and 250 test particles, which was the maximum approachable for 2008 CPUs. Indeed an event with 200 test particle in 2008 required 1 or 2 days while now it requires some hours.

The first part of the simulations, reported in this work, were done with 200 test particles. In a second moment when more powerful CPU were available we decided to performed the simulation with 700 test particles.

5.2.3. Dependence on the impact parameter

Simulations with different impact parameters were performed, the chosen impact parameters were 0, 2, 4, 5, 5.5, 6, 6.5 fm. These parameters were chosen because the maximum of the cross section as a function of the impact parameter is in the range of 4-5 fm for the three different beam energies. The value of b larger than 7 fm are meaningless because the two nuclei do not interact as fusion is expected for impact factor between 0-7 fm.

For each beam energy, we have calculated the value of the integral of the Bremsstrahlung spectra in the interval of 0-22 MeV and its trend as a function of the impact parameters as shown in Fig. 5.7.

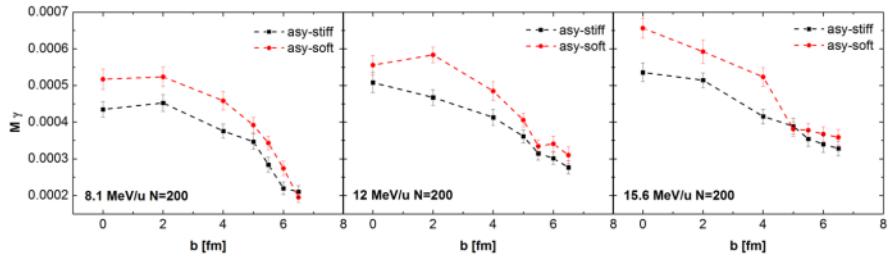

Fig. 5.7: The DD γ multiplicity obtained from the BNV simulations as a function of the impact parameter for ^{16}O + ^{116}Sn reaction.

The plots of Fig. 5.7 show that there is a clear dependence of DD γ multiplicity with the impact factor. The DD yield is almost constant for small values of b while there is a smooth decrease of its value for larger value of b. The asy-stiff parameterization of the EOS always has a smaller yield relative to the asy-soft one. An experimental measurement at low impact parameters could discriminate between the two different parameterizations of the EOS.

At high angular momentum and beam energies the total DD yield become almost independent of impact parameter and EOS parameterization.

A very similar behavior of the dynamic dipole total DD yield as a function of the impact parameter was found also for a very N/Z asymmetric ^{132}Sn + ^{58}Ni reaction, as shown in Fig. 5.8. More information on the calculations for ^{132}Sn + ^{58}Ni reactions are in section 5.6.

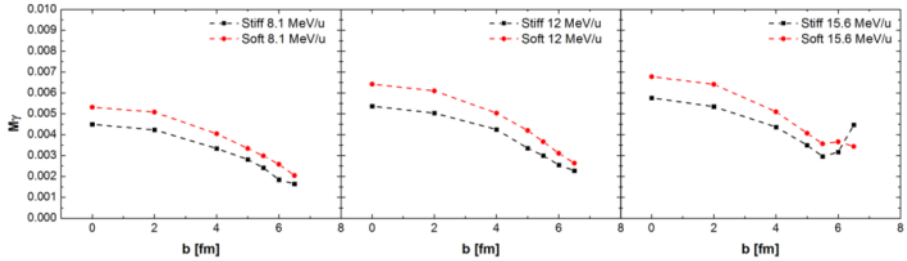

Fig. 5.8: The DD γ multiplicity obtained from the BNV simulations as a function of the impact parameter for $^{132}Sn + ^{58}Ni$ reaction.

The common behavior observed in the studied reactions ($^{16}O + ^{116}Sn$ and $^{132}Sn + ^{58}Ni$) suggests the possibility to parameterize with such curves in terms of physics observables. This could provide a fast estimation of the DD yield avoiding BNV calculations (which require a rather heavy CPU load) for different reactions. Furthermore, the parameterization could help to gain a deeper understanding of the physics inside such kind of mechanism. The simplest shape that the points of Fig. 5.7 and Fig. 5.8 suggests is a Fermi function:

$$y(D(0), E_{lab}) = \frac{p_0(D(0), E_{lab})}{1 + exp\left\{\frac{x - p_1(D(0), E_{lab})}{p_2(D(0), E_{lab})}\right\}} \qquad (5.2)$$

where p_0 is the normalization factor, p_1 is the radius and p_2 is the diffuseness and these parameter are related to physical observables such as the beam energy E_{lab} and the dipole moment $D(0)$. These parameter could depend also on the properties of the formed CN.

As a first step we plotted the total yield calculated at b = 0 fm as a function of the beam energies for the $^{16}O + ^{116}Sn$ and $^{132}Sn + ^{58}Ni$ reactions. The values of the total yield at b = 0 fm are reported in Tab. 5.1. The plots with the total yield at b=0 fm as a function of the beam energy are shown in Fig. 5.9, as the points seems to follow a rise trend followed by a saturation. Therefore we tried to fit the point in Fig. 5.9 with the following function:

$$y = a\big(1 + \exp\left(-\mathrm{bx}\right)\big) \qquad (5.3)$$

where x is the beam energy and a and b are the fit parameters. The extracted parameters are listed in Tab. 5.2.

This rise trend followed by a saturation could be explained by the fact that the DD yield has to increase with the beam energy, but, if the energy become too high, the pre-equilibrium emission particles could reduce the dipole moment and consequently the total yield.

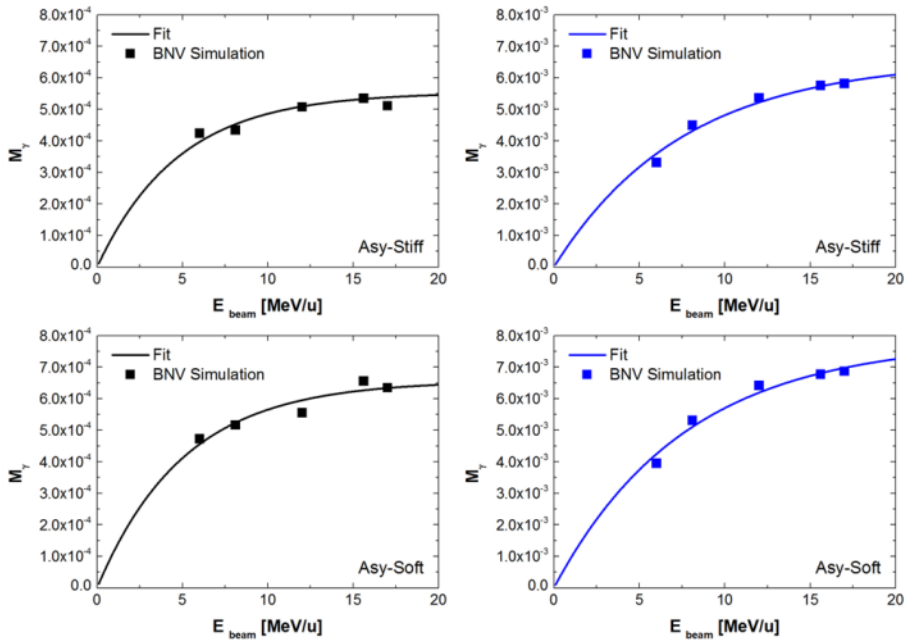

Fig. 5.9: The results obtained from BNV simulations at impact parameter equal to 0 fm as a function of the beam energy. The black squares are the results of the simulations for the ^{16}O + ^{116}Sn reaction, while the blue squares for the ^{132}Sn + ^{58}Ni reaction, the lines are the fit for both reactions and for both asy-stiff parameterization asy-soft one. In the top panels there are the results for asy-stiff parameterization, instead in the right ones the results for asy-soft one.

It is possible to notice that the ratio between the values of the a fit parameter for one reaction with respect to the other, as reported in Tab. 5.2, is approximately 10. That ratio is about two times the ratio of the N/Z asymmetry dipole between the reactions ($D(0)$ = 45 fm for ^{132}Sn + ^{58}Ni and $D(0)$ = 8.6 fm for ^{16}O + ^{116}Sn). Therefore we can parameterize the a parameter in the followed way:

$$a_{reaction} = \frac{1}{2}\frac{D(0)_{reaction}}{D(0)_{^{132}Sn+^{58}Ni}} a_{^{132}Sn+^{58}Ni} \qquad (5.4)$$

where the ^{132}Sn + ^{58}Ni reaction is used as reference.

	asy-stiff		asy-soft	
E_{beam} [MeV/u]	$^{16}O + ^{116}Sn$	$^{132}Sn + ^{58}Ni$	$^{16}O + ^{116}Sn$	$^{132}Sn + ^{58}Ni$
6	4.25 10^{-4}	3.32 10^{-3}	4.73 10^{-4}	3.95 10^{-3}
8.1	4.35 10^{-4}	4.50 10^{-3}	5.17 10^{-4}	5.32 10^{-3}
12	5.08 10^{-4}	5.37 10^{-3}	5.56 10^{-4}	6.42 10^{-3}
15.6	5.36 10^{-4}	5.76 10^{-3}	6.56 10^{-4}	6.78 10^{-3}
17	5.12 10^{-4}	5.82 10^{-3}	6.35 10^{-4}	6.87 10^{-3}

Tab. 5.1: The values of the DD yield obtained from the simulations at b = 0 fm, for both the parameterizations (asy-stiff and asy-soft) and both reactions (^{16}O + ^{116}Sn and ^{132}Sn + ^{58}Ni).These values are the same represent in Fig. 5.9.

	asy-stiff		asy-soft	
Fit parameters	$^{16}O + ^{116}Sn$	$^{132}Sn + ^{58}Ni$	$^{16}O + ^{116}Sn$	$^{132}Sn + ^{58}Ni$
a	5.5 10^{-4}	6.6 10^{-3}	6.6 10^{-4}	7.8 10^{-3}
b	0.21	0.13	0.20	0.13

Tab. 5.2: The parameters obtained from the fits of the data in Fig. 5.9 with this function $y = a(1 - exp(-bx))$. *These parameters are for both the nuclear EOS parameterizations and for both reactions (^{16}O + ^{116}Sn and ^{132}Sn + ^{58}Ni).*

Moreover the a parameter is different for the two parameterization of the nuclear EOS, because the asy-stiff parameterization gives a total yield that is about 20% smaller of the value of the asy-soft parameterization.

The b parameter probably depend on the reaction, for example it could depend on the mass of the compound nucleus, as shown in Tab. 5.2, it is about 0.2 for ^{16}O +^{116}Sn and 0.13 for the ^{132}Sn + ^{58}Ni. The dependence of b parameter could be investigated in a better way by doing BNV simulations for other reactions.

From the fits of the results obtained from BNV simulations at impact parameter equal to 0 fm as a function of the beam energy, it is possible to extract the value of the p_0 parameter of the Fermi function, using equation 5.3, for both reactions and both parameterizations of nuclear equation of state.

The radius of the Fermi function (p_1) is expected to depend on the touching radius (the distance between the two mass center when the two nuclei are in contact) or from the radius of the compound nucleus. The touching radius is 8.9 fm for ^{16}O + ^{116}Sn reaction and 10.7 fm for the ^{132}Sn + ^{58}Ni reaction instead the radius of the compound nucleus is 6.1 fm for ^{16}O + ^{116}Sn reaction and 6.9 fm for the ^{132}Sn + ^{58}Ni. This dependence is expected because the DD γ emission is expected only if there is a fusion reaction. The radius of the Fermi function is expected to depend also on the beam energy, but this dependence is not expected to be so strong because it is related to two opposite effects. In the first one the p_1 parameter is expected to decrease with the increase of the beam energy and it is related to the fact that at high beam energy the nucleus could be fissioning. For this reason, it is not possible to reach high impact parameter. Whereas in the second one p_1 parameter is expected to increase with the beam energy and because if the beam energy is not enough, the a pre-equilibrium emission could not occur. For this reason in Fig. 5.10 and in Fig. 5.11 in which the Fermi function interpolation of the results of the BNV simulation the p_1 parameter is fix at 6 fm for the asy-stiff parameterization and is fix at 6.1 for the asy-soft one. This value is about the radius of the compound nucleus ^{132}Ce that is the product of the ^{16}O + ^{116}Sn reaction.

The diffuseness of the Fermi function is expected to vary as a function of the beam energy, as shown in Fig. 5.7and in Fig. 5.8. The diffuseness at 8.1 MeV/u has to be smaller than the one at 15.6 MeV/u for both reactions.

The interpolations of the trend of the total yield as a function of the impact parameter were done with the previous considerations. The results obtained from this interpolations are shown in Fig. 5.10 and in Fig. 5.11 and the used parameters are listed in Tab. 5.3 and in Tab. 5.4.

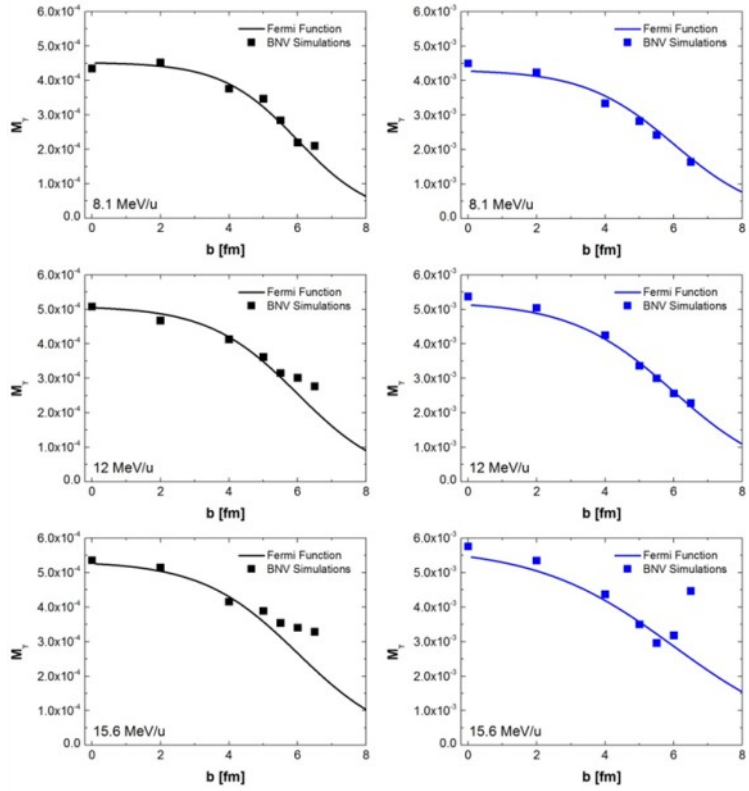

Fig. 5.10: The interpolation with a Fermi function of the DD yield as a function of the impact parameter for both reaction (in black ^{16}O + ^{116}Sn, in blue ^{132}Sn + ^{58}Ni). The plots shown here are for the asy-stiff parameterization of the nuclear equation of state.

	^{16}O + ^{116}Sn			^{132}Sn + ^{58}Ni		
Fermi Parameters	**8.1 MeV/u**	**12 MeV/u**	**15.6 MeV/u**	**8.1 MeV/u**	**12 MeV/u**	**15.6 MeV/u**
p_0	$4.5\ 10^{-4}$	$5.1\ 10^{-4}$	$5.3\ 10^{-4}$	$4.3\ 10^{-3}$	$5.2\ 10^{-3}$	$5.7\ 10^{-3}$
p_1	6	6	6	6	6	6
p_2	1.1	1.3	1.6	1.3	1.5	2

Tab. 5.3: The parameter obtained from the interpolation with a Fermi function of the DD yield for both reactions and for the asy-stiff parameterization. The parameters were chosen as explained in the test.

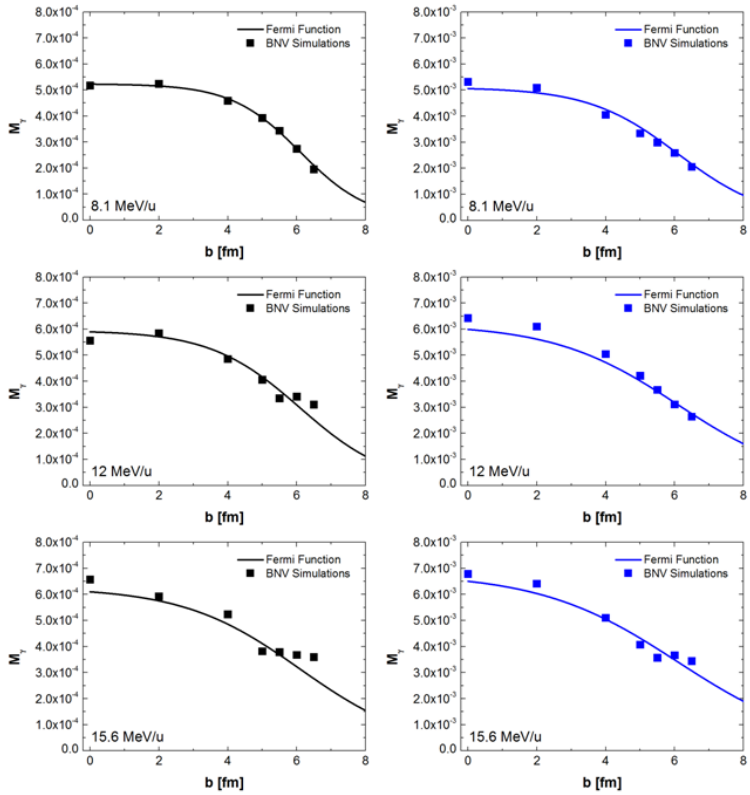

Fig. 5.11: The interpolation with a Fermi function of the DD yield as a function of the impact parameter for both reaction (in black ^{16}O + ^{116}Sn, in blue ^{132}Sn + ^{58}Ni). The plots shown here are for the asy-soft parameterization of the nuclear equation of state.

	^{16}O + ^{116}Sn			^{132}Sn + ^{58}Ni		
Fermi Parameters	**8.1 MeV/u**	**12 MeV/u**	**15.6 MeV/u**	**8.1 MeV/u**	**12 MeV/u**	**15.6 MeV/u**
p_0	$5.2\ 10^{-4}$	$6.0\ 10^{-4}$	$6.3\ 10^{-4}$	$5.1\ 10^{-3}$	$6.1\ 10^{-3}$	$6.8\ 10^{-3}$
p_1	6.1	6.1	6.1	6.1	6.1	6.1
p_2	1	1.3	1.7	1.3	1.6	2

Tab. 5.4: The parameter obtained from the interpolation with a Fermi function of the DD yield for both reactions and for the asy-soft parameterization. The parameters were chosen as explained in the test.

In Tab. 5.3 and in Tab. 5.4, it is possible to note that the p_2 parameter increase with the beam energy. For this reason, we parameterized the diffuseness parameter as a function of the beam energy with a linear curve, as:

$$p_2 = mE_{beam} + q \qquad (5.5)$$

where m and q are the slope and the intercept. The linear fits of the p_2 parameter as a function of the beam energy are shown in Fig. 5.12 and the parameters are listed in Tab. 5.5. It is possible to note that the slope is constant for both reactions (^{16}O + ^{116}Sn and ^{132}Sn + ^{58}Ni), whereas the intercept is the same for the asy-stiff and the asy-soft nuclear EOS parameterizations, but is different for the two reactions.

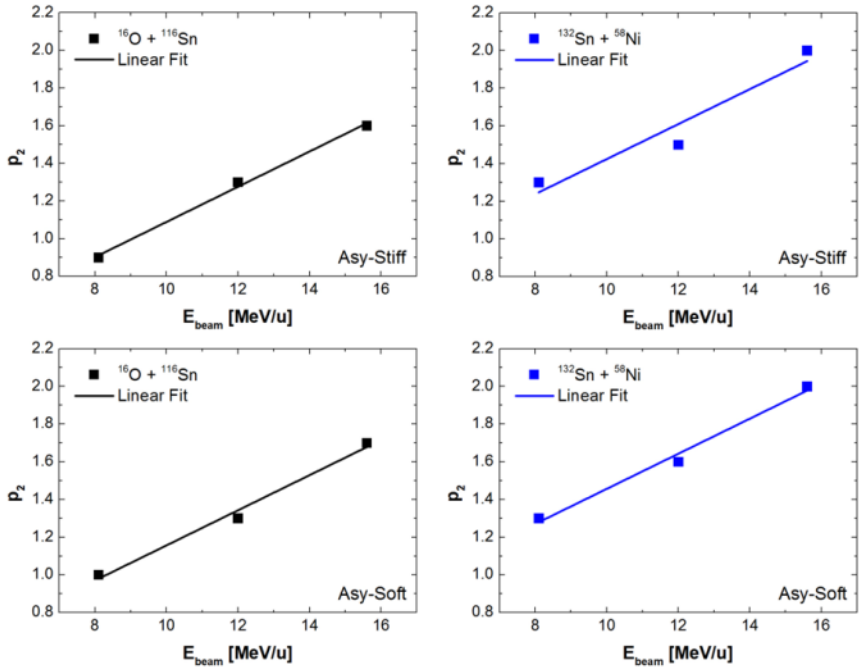

Fig. 5.12: The liner fit of the p_2 parameters as a function of the beam energy.

	^{16}O + ^{116}Sn		^{132}Sn + ^{58}Ni	
Fit Parameter	**Stiff**	**Soft**	**Stiff**	**Soft**
m	0.09	0.09	0.09	0.09
q	0.15	0.23	0.50	0.53

Tab. 5.5: The fit parameters (slope and intercept) for the diffuseness of the Fermi function as a function of the beam energy.

The Fermi function parameterization could be used to do a rough estimation for of the total dynamical dipole yield for other reactions. To verify the accuracy of this interpolation, the DD yield for the reaction (^{32}S + ^{100}Mo) was calculated at 8 MeV/u and compared with the value reported in [3]. The parameter p_0 is calculate by using equation 5.3, in particular the parameter a was obtained from the relation in equation 5.4, using the dipole moment of the ^{132}Sn + ^{58}Ni reaction as reference and the value of the a parameter obtained for the asy-soft parameterization for this reference reaction. Whereas, the parameter b of the equation 5.3 is chosen at 0.2, because it is the value of that parameter for ^{16}O +^{116}Sn reaction. It is, indeed, expected that the parameter b depends on the compound nucleus properties and the ^{32}S + ^{100}Mo reaction forms the same compound nucleus of the ^{16}O + ^{116}Sn one. The radius of the Fermi function p_1 is expected to depend on the compound nucleus radius and for this reason was chosen at 6 as for the two reactions studied in this work. The diffuseness of the Fermi function (p_2) was calculated by using the parameterization in equation 5.5, the slope was chosen at 0.09, because it is the same for both simulates reactions, instead the intercept was chosen at 0.2 because the ^{32}S + ^{100}Mo reaction forms the same compound nucleus of the ^{16}O + ^{116}Sn reaction. In Fig. 5.13 a prediction of the DD yield as a function of the impact parameter for the ^{32}S + ^{100}Mo reaction is shown. To have a rough estimation the values of the DD γ multiplicity, the value at b = 4.5 fm was chosen because it is the values of the impact parameter that corresponds to the maximum of the fusion cross section. As shown in Fig. 5.13 the value of the DD total yield is 1.06 10^{-3}; this value has to be compared with the value reported in [3] that is 1.25 10^{-3}. The difference between the two values is about 20%. For this reason the interpolation with

the Fermi function could be a good method to have a rough estimation of the DD total yield without performing the BNV simulations. The BNV simulation have to be however performed to obtained the precise value of the DD pre-equilibrium emission.

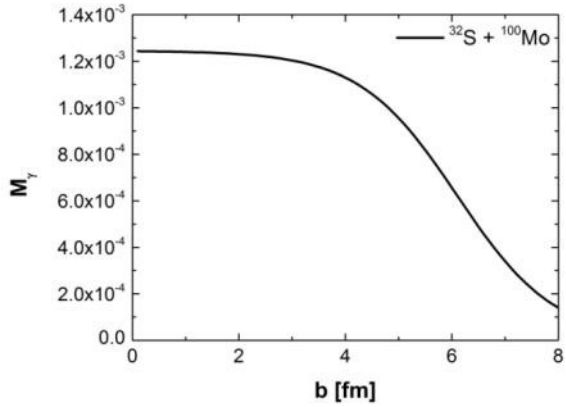

Fig. 5.13: The predicted DD γ multiplicity as a function of the impact parameter for the ^{32}S + ^{100}Mo reaction by using the Fermi function interpolation.

5.2.4. The asy-stiff and asy-soft parameterizations

The study of DD pre-equilibrium emission is very important because it is related to nuclear equation of state and its symmetry term (asy-stiff and asy-soft), but this sensitivity becomes more meaningful in the case of exotic system (for example $^{132}Sn + {}^{58}Ni$, the BNV simulations for this reaction will be described in section 5.6). For this reason to give information about the two parameterizations of the EOS exotic beams are necessary, but, as already noticed, some sensitivity is present also in case of stable beams.

In the case of stable beams (for example for the system $^{16}O + {}^{116}Sn$) there is a sensitivity at the asy-stiff and at the asy-soft parameterizations at small value of the impact parameters, as shown in Fig. 5.7. For this reason, to have information about the two parameterizations of the nuclear EOS, it is necessary to select, from the experimental data, fusion-evaporation reactions at small impact parameter, namely at small value of the angular momentum l.

In a future experiment, also with stable beams, by selecting small value of the angular momentum for example using a multiplicity filter, it would be possible to reach the sensitivity to discriminate between the asy-stiff and the asy-soft parameterizations of the nuclear EOS.

5.3. Comparison between experimental results and theory

As previously discussed, the BNV simulations of the $^{16}O + ^{116}Sn$ reaction were performed with 200 test particles. Fifty events were simulated for each impact parameter (0, 2, 4, 5, 5.5, 6 and 6.5 fm) at three different beam energies (8.1, 12 and 15.6 MeV/u) to be compared with the experimental data analyzed in this thesis (12 MeV/u) and with the data of the reference [6] (8.1 and 15.6 MeV/u).

The nucleon-nucleon cross section inside a medium is defined as:

$$\sigma_{nn-medium} = \sigma_{nn-free}\left(1 - \alpha\frac{\rho}{\rho_0}\right) \qquad (5.6)$$

where $\sigma_{nn-free}$ is the free nucleon-nucleon cross section, ρ_0 is the density of the nuclear matter at the saturation point, ρ is the density that in our case is fixed at 0.14 fm^{-3} and α is a proportionality factor. In the BNV code the nucleon-nucleon cross section is set to zero for collisions with energy lower than 50 MeV in order to reduce spurious low energy collisions.

As explained in section 5.2, BNV simulations were performed with a fixed impact parameter while measured DD yields is relative to a spin distribution. Therefore the correct weight at each impact parameter, must be extracted. The selection of the weights was done using equation 5.1. We calculated the spin distributions using CASCADE code, fixing the maximum of the angular momentum at $58\hbar$ in the case of beam energy of 8.1 MeV/u, at $63\hbar$ in the case of 12 MeV/u and at $64\hbar$ in the case of 15.6MeV/u. These values of the angular momentum were chosen because they are the maximum values of the angular momentum that the compound nucleus could support before fission obtained from the CF code that is a model useful to calculated the fusion-evaporation reaction parameters [45]. The

spin distributions calculated for the three beam energies and the cross sections as a function of the impact parameter (obtained by using equation 5.1) are shown in Fig. 5.14.

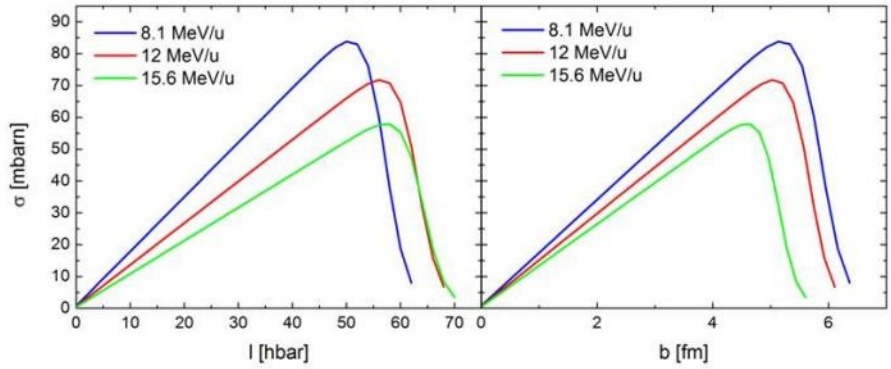

Fig. 5.14: In this picture the maximum angular momentum was calculated with CF code for each beam energy. It was $58\hbar$ *at 8.1 MeV/u,* $63\hbar$ *at 12 MeV/u and* $64\hbar$ *at 15.6 MeV/u. In the left panel the cross section (from CASCADE code) as a function of the angular momentum, in the right one the cross section as a function of the impact parameter calculated by using equation 5.1.*

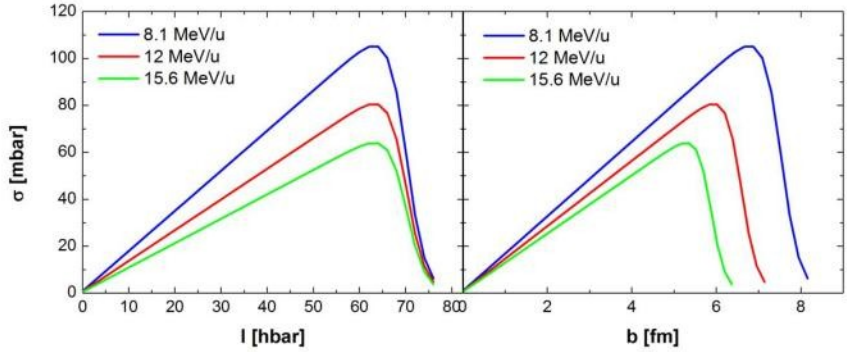

Fig. 5.15: In this picture the maximum angular momentum was fixed at $70\hbar$ *for each beam energy. In the left panel the cross section (from CASCADE code) as a function of the angular momentum, in the right one the cross section as a function of the impact parameter calculated by using equation 5.1.*

A second possibility is, as in reference [6], to fix the angular momentum at $70\hbar$ for the three beams energies. The value of $70\hbar$ was chosen using the curve in Fig. 2.1; which fix that maximum angular

momentum for a system with a mass $A = 132$ is $70\hbar$. The fusion cross section calculated fixing the maximum angular momentum at $70\hbar$, as a function of the angular momentum and as a function of the impact parameter is show in Fig. 5.15. This technique is the one used in [6] for the same system $^{16}O + ^{116}Sn$ at 8.1 and 15.6 MeV/u.

The weights are calculated assigning at each impact parameter the value of the fusion cross section that correspond at annulus centered in a specific impact parameter; for example for b=2 fm we integrated the values of the fusion cross section between b=1 fm and b=3 fm. The weights, obtained for the case where the maximum angular momentum is fixed at $70\hbar$ (see Tab. 5.7), are slighter different from the weights obtained using the maximum angular momentum calculated with CF code (see Tab. 5.6). The weighted average of the DD γ yield in both cases is shown in Fig. 5.16, the differences between the two methods are however within 5%-20% as shown in Fig. 5.17.

	b [fm]						
E_{beam} [MeV/u]	**0**	**2**	**4**	**5**	**5.5**	**6**	**6.5**
8.1	0.018	0.134	0.195	0.147	0.083	0.137	0.286
12	0.027	0.173	0.254	0.166	0.141	0.146	0.094
15.6	0.027	0.227	0.322	0.234	0.137	0.051	0.003

Tab. 5.6: The weights for each impact parameter obtained using the cross sections calculated with l_{max} from CF code are shown.

	b [fm]						
E_{beam} [MeV/u]	**0**	**2**	**4**	**5**	**5.5**	**6**	**6.5**
8.1	0.028	0.209	0.320	0.235	0.161	0.041	0.006
12	0.024	0.158	0.282	0.282	0.158	0.083	0.013
15.6	0.044	0.294	0.455	0.180	0.028	0	0

Tab. 5.7: The weights for each impact parameter obtained using the cross sections calculated with $l_{max} = 70\hbar$ are shown.

The error bars of each point are calculated propagating the error bar obtained for each impact parameter as explained in section 5.2.2. The value of the DD γ yield is weighted average on impact parameters, the weights are considered without error. This is the reason why the weighted average reduces the errors of BNV calculations. This is in fact equivalent to have much more events (50 events per 7 impact parameters is equal to have 350 events). The values of the DD pre-equilibrium emission calculated by BNV simulation are shown in Fig. 5.16 and Fig. 5.17. The DD γ multiplicity for asy-stiff is 16% smaller than asy-soft. Furthermore, from 8.1 MeV/u to 15.6 MeV/u (b= 4fm) there is an increase of DD yield 12%.

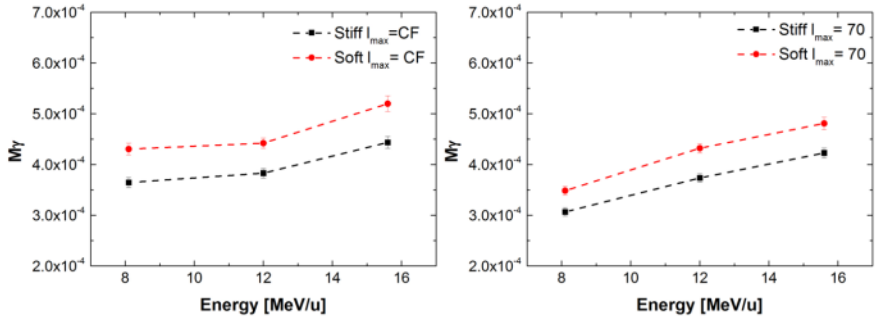

Fig. 5.16: The values of the DD yield for the two parameterizations asy-stiff and asy-soft, calculated for the three beam energies. To obtain these points we have simulated 50 events using 200 test particles. In the left panel there are the values given by l_{max} the calculated by CF code; in the right fixing $l_{max} = 70\ \hbar$.

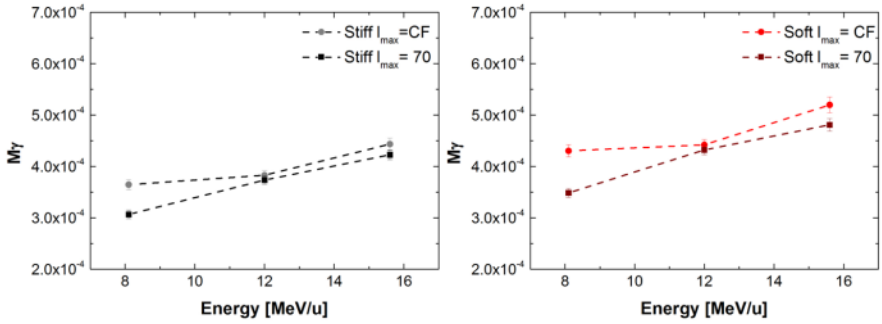

Fig. 5.17: The total DD yield obtained using the two spin distributions described in the test. In the right the calculations for the asy-soft parameterization of the EOS, and in the left one the calculations for the asy-stiff one are shown.

The calculated values of the DD yield must compared with the experimental data. The plots in Fig. 5.18 show the results of a BNV calculations compared with the data as in [6]. The left panels are relative to $E_{loss} = 13.3\ MeV$, while the right ones to $E_{loss} = 18.4\ MeV$. In the top panels the weights obtained by fixing $l_{max} = 70\hbar$ were used, while in the bottom the weights obtained by fixing l_{max} with CF code were used. It is interesting to point out that the data and the calculation remains in the error bars.

The Fourier transform of dipole moment is calculated for Δt of about $200\ fm/c$ from the contact of the two nuclei to obtain the Bremsstrahlung spectrum. To extract the DD multiplicity the integral of the Bremsstrahlung spectrum was calculated between 0 and 22 MeV. It should be noted that this is a larger energy range compared to the one used to extract the experimental data (10 - 22 MeV). This is because the theoretical spectrum has the maximum at about 9 MeV, and therefore it is necessary to integrate it over the full range. The experimental DD yield, instead, has the maximum at 14 MeV, and is known from previous measurements [6] to be negligible below 10 MeV. Therefore the difference in integration ranges does not introduce systematic errors.

The results obtained from the BNV simulations are in within the error bars with the experimental data, independently of the hypothesis on l_{max} and E_{loss} as shown in Fig. 5.18, the different panels show the results obtained from the two different values of the pre-equilibrium energy loss and the results obtained with the two different methods to calculated the weights. A different trend (a rise and fall trend) for the experimental data was found in [3] and it is shown in Fig. 5.19, in which the same compound is populated with a different entrance channel. In this case the theoretical model (BNV) does not manage to reproduce the experimental data, indeed it shows a trend which not reproduced the data in [3].

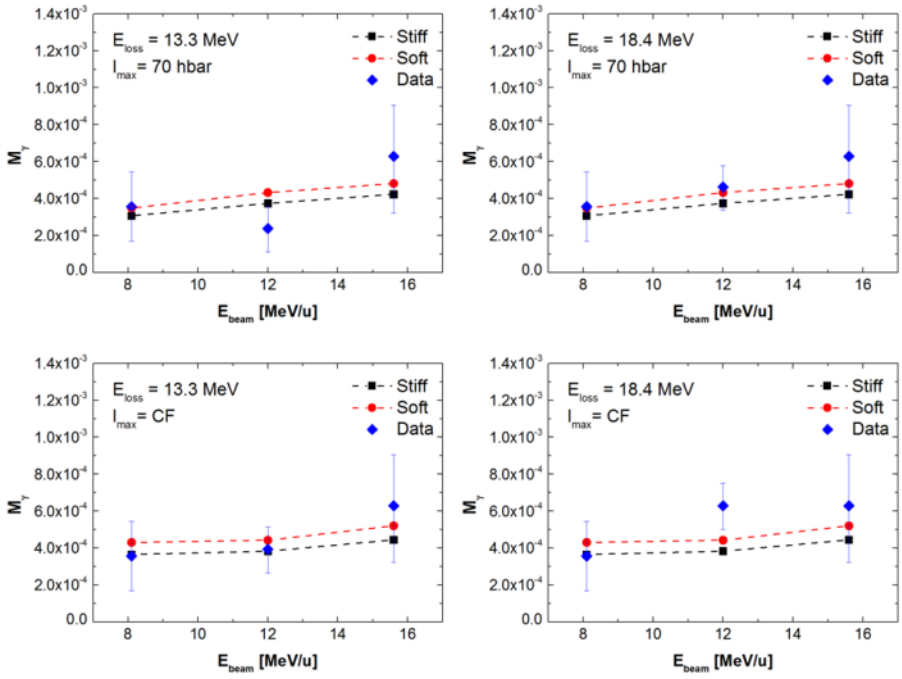

Fig. 5.18: The comparison between the DD yield calculated by the BNV simulations (black squares asy-stiff parameterization and red points the asy-soft one) and the DD yield obtained from the experimental data (blue diamonds). For the theoretical simulations, in the two top panels, the weights obtained fixing $l_{max} = 70\ \hbar$ are used; in the two bottom panels the weights obtained fixing as l_{max} the value of CF code are used. In the two left panels the DD γ multiplicity was calculated using the pre-equilibrium energy loss obtained from data (13.3 MeV), instead in the two right panels the DD γ multiplicity was calculated using pre-equilibrium energy loss equal to 18.4 MeV.

It is important to remember that the parameterization of [17] for the energy loss by LCP in the pre-equilibrium phase, gives a value of $E_{loss} = 26\ MeV$. The correspondent DD total yield value is 7.5 10^{-4}, which is extremely high and far from the theoretical curve. Therefore, the value of the DD γ multiplicity extracted from our data could not be reproduced by the theoretical model, if the pre-equilibrium energy loss is calculated by the parameterization of [17], (see Fig. 5.22). In section 4.4.2, we saw that there is a rise and fall trend with this value of the pre-equilibrium energy loss. This behavior is similar, even though much smaller to the one of reference [3].

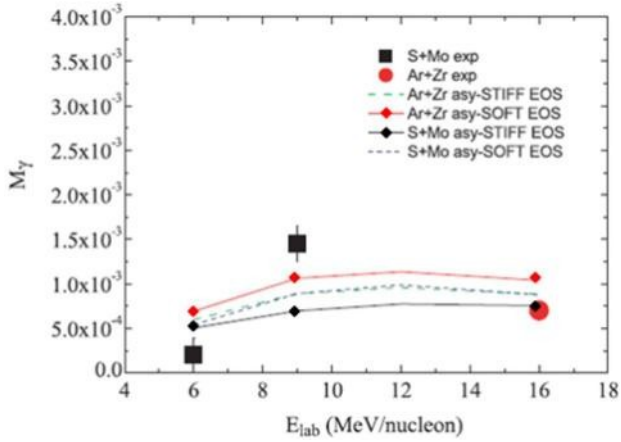

Fig. 5.19: The comparison between the BNV simulations and the experimental data reported in [3].

5.3.1. Simulations with 700 test particles

To achieve a better understanding of the theoretical model, in the previous sections we have shown the the different parameterization or parameters affect the BNV calculation. One of the most interesting tests is the increase of test particles from 200 to 700, to reproduce in a more precise way a fluid as explained in section 5.2.1.

The simulations with 700 test particles were performed for the three beam energies and for the same impact parameters used with 200 test particles. For each energy and impact parameter 10 events were simulated. The results of these simulations as a function of the impact parameter are shown in Fig. 5.20. As for the case of 200 test particles there is a dependence of the DD γ multiplicity as a function of the impact parameter. The DD contribution is constant for small value of b and decrease for larger value of b. Also in this case there is a sensitivity at the EOS at small value of the impact parameter.

The results found with 700 test particles are not very different from the results obtained at 200 test particles. The largest difference is the fact that the DD γ multiplicity obtained with 700 test particle is larger than the one obtained with 200 test particles.

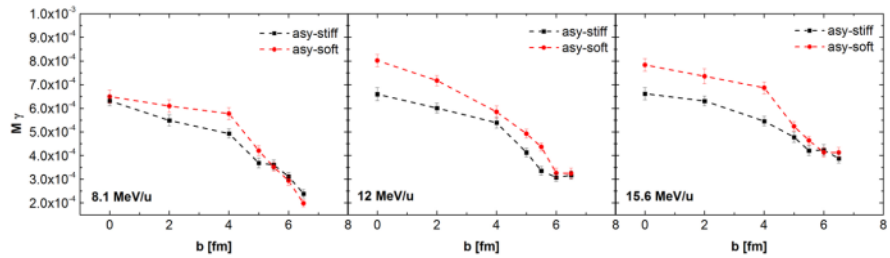

Fig. 5.20: The DD γ multiplicity obtained from the BNV simulations as a function of the impact parameter. For these simulations 700 test particles were used.

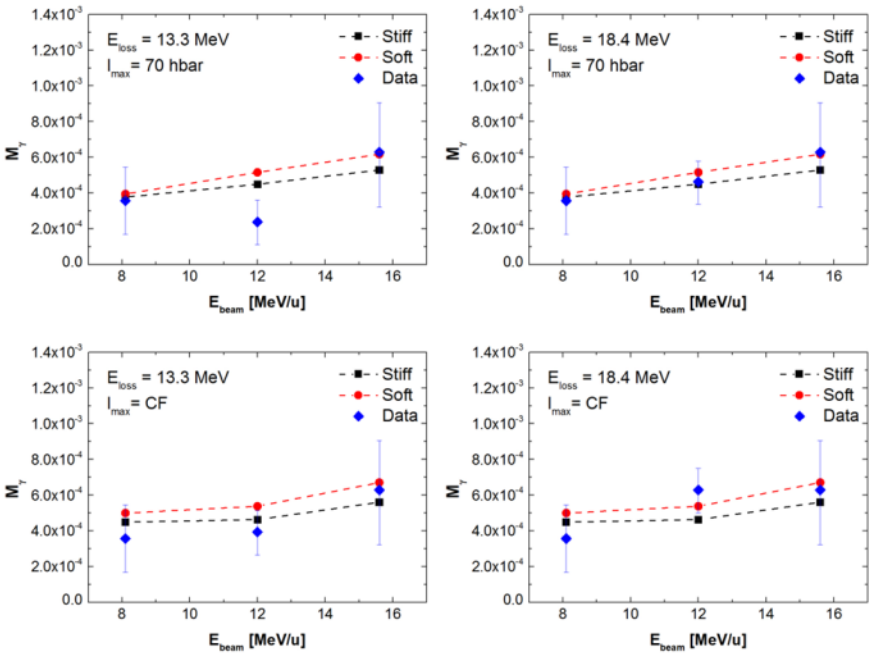

Fig. 5.21: The comparison between the DD yield calculated by the BNV simulation (black squares asy-stiff parameterization and red points the asy-soft one) and the DD yield obtained from the experimental data (blue diamonds). For the theoretical simulations, in the two top panels are used the weights obtained fixing $l_{max} = 70\ \hbar$; in the two bottom panels one are used the weights obtained fixing as l_{max} the value of CF code. In the two left panels the DD γ multiplicity was calculated using the pre-equilibrium energy loss obtained from data (13.3 MeV), instead in the two right panels the DD γ multiplicity at 12 MeV/u was calculated using pre-equilibrium energy loss equal to 18.4 MeV.

In summary, the results obtained from the BNV simulations with 700 test particles are in agreement with the experimental data, indeed the theory reproduced the rise behavior of the experimental points.

The results obtained from the BNV simulations are in within the error bars with the experimental data, indeed the theory reproduced the rise behavior of the data. The results obtained from BNV model are shown with the experimental data in Fig. 5.21, the different panels show the results obtained from the two different values of the pre-equilibrium energy loss and the results obtained with the two different methods to calculated the weights.

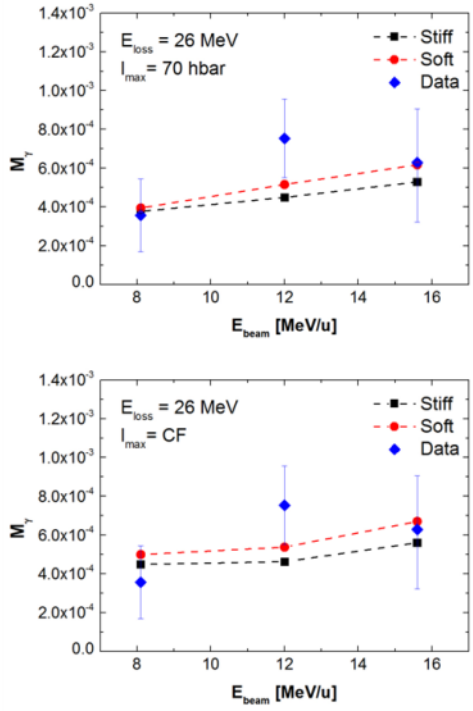

Fig. 5.22: The comparison between the DD yield calculated by the BNV simulations (black squares asy-stiff parameterization and red points the asy-soft one) and the DD yield obtained from the experimental data (blue diamonds). For the theoretical simulations, in the top panel the weights obtained fixing $l_{max} = 70\ \hbar$ are used; in the bottom panel the weights obtained fixing as l_{max} the value of CF code are used. The DD γ multiplicity was calculated from data by using the pre-equilibrium energy loss equal to 26 MeV (linear interpolation or calculated as in [17]).

Nevertheless, whatever the input parameters, there is a difference between the two parameterizations asy-stiff and asy-soft in the weight average values, of the DD γ multiplicity. This difference is however too small due to the large error bars of the experimental data. To obtain information about the nuclear equation of state it is necessary to reduce the error bars of the experimental data, mainly on the systematic errors. The largest contribution to the systematic error is the uncertainty on the energy loss during the pre-equilibrium phase, as it is explained in section 4.4.2 and shown in Fig. 5.18 and Fig. 5.22. For this reason to gain a sensitivity to the two parameterizations of the nuclear EOS it is necessary to have an experimental set up in which is possible a clean determination of the pre-equilibrium energy loss and, as explained in section 5.2.4, a selection of a small value of the angular momentum.

5.4. Angular distribution for the ^{16}O + ^{116}Sn reaction

A quantity that could be measured from the data and calculated using the BNV theoretical model is the angular distribution (see section 4.5).

The BNV model calculates the angular distribution using the integral γ-emission probability and the time evolution of the cosine of the angle θ, defined as the angle between the dipole with respect the beam axis (for the evolution of the cosine see Fig. 5.24). The integral emission probability, calculated for the three different beam energies (8.1, 12 and 15.6 MeV/u) is found to saturate around 200 fm/c implying that the emission probability is concentrated at the beginning of the fusion process in an interval of $\sim 150\ fm/c$ after the collision as shown in Fig. 5.23.

BNV predicts an angular dependence, called $W(\theta)$, as $W(\theta) \approx 1 + a_2 P_2(cos\theta)$, smeared out by the rotation of the dipole axis (the quenching factor is the a_2 parameter. If b=0 fm the angular distribution is expected to be like a pure dipole, if b≠0 fm there is a rotation of the dipolar axis and the angular distribution changes (as shown in Fig. 5.25). In case of the highest for impact parameters (that imply very peripheral collisions) the angular

distribution have an opposite sign relatively to the one at b = 0 fm, in fact the oscillating dipole is rotated of 90°.

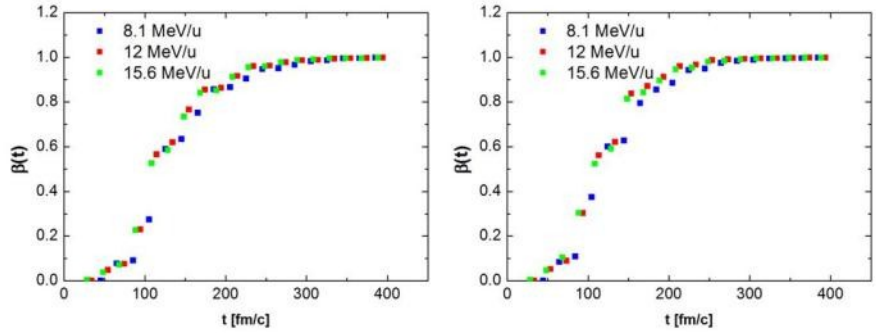

Fig. 5.23: The integral emission probability at b=2fm for the three different beam energies, in the left panel there asy-stiff parameterization in the right one the asy-soft one.

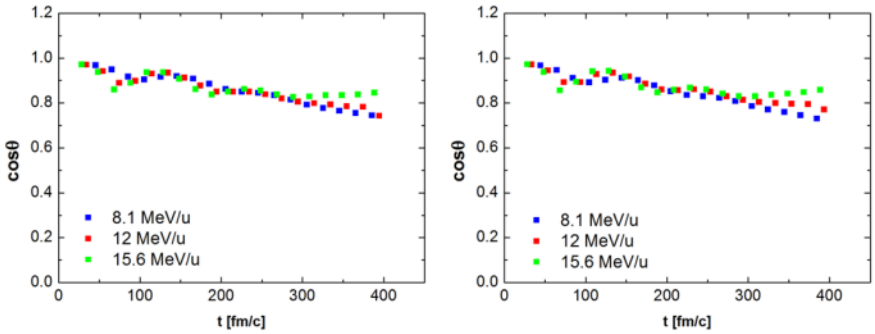

Fig. 5.24: The time evolution of $cos\theta$, with θ defined as the angle between the beam and the dipole axis. It is represented for the three different beam energies at b=2 fm. In the left panel there is asy-stiff parameterization in the right one the asy-soft one

Angular distribution is extracted from BNV model as a weighted average on impact parameters. The weights are obtained as explained in section 5.3. Due to the axis rotation for impact parameters $b \neq 0\ fm$, the angular distribution predicted from the BNV model will be quenched in respect to a pure dipole. By comparing the angular distribution calculated from the BNV simulations with equation 4.10, it is possible to determinate the value of the quenching factor a_2. The value of the quenching factor obtained from the simulations is extremely small and positive at 12 MeV/u

(see Tab. 5.8), whereas at 15 MeV/u it was found negative both in [6] and in our calculations (see Tab. 5.8). The average angular distributions at 12 MeV/u and at 15.6MeV/u obtained from the simulation for the two parameterizations are shown in Fig. 5.26 and in Fig. 5.27.

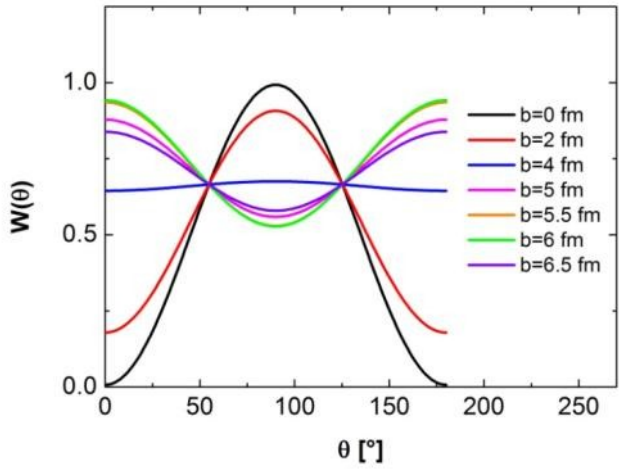

Fig. 5.25: The angular distribution obtained from BNV simulations for all tested impact parameters at 12 MeV/u. The angular distribution of b = 0 fm is a pure dipole angular distribution. For the other value of the impact parameter the angular distribution is quenched.

	l_{max} **from CF code**		$l_{max} = 70\hbar$	
Energy [MeV/u]	**Stiff**	**Soft**	**Stiff**	**Soft**
12	0.045	0.032	0.036	0.026
15.6	-0.19	-0.20	-0.039	-0.053

Tab. 5.8: The values of the quenching factor obtained from the BNV simulations.

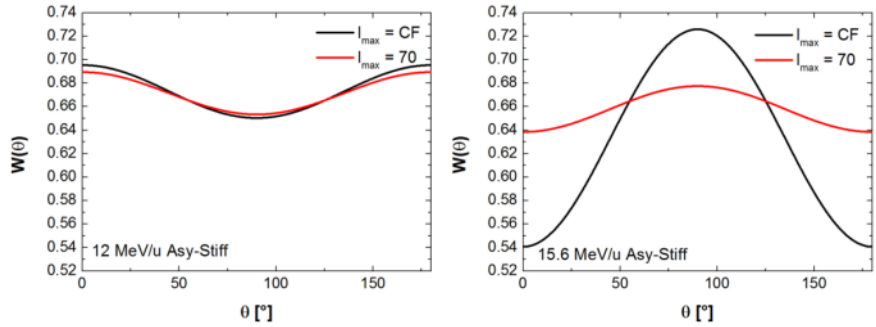

Fig. 5.26: The angular distribution obtained from BNV simulations after the weighted average. The red line represents the case in which the angular momentum was fixed at 70ħ, instead the black line represents the case in which the maximum angular momentum was chosen by using CF code. In the left panel there is the average angular distribution at 12 MeV/u, in the right one the average angular distribution at 15.6 MeV/u. The values of quenching factors for this curves are shown in Tab. 5.8.

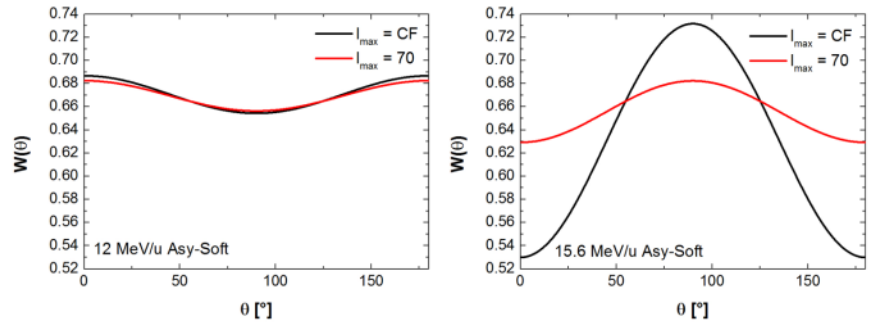

Fig. 5.27: The same of Fig. 5.26, but in this case for the asy-soft parameterization. Also in this case the value of the quenching parameters are shown in Tab. 5.8.

5.4.1. Comparison between experimental data and theory

In section 4.5 we showed the angular distribution found from the experimental data. The angles of the used detectors were only four (as shown in Tab. 3.1), for this reason we could compare the angular distribution obtained from the simulations only for these four value of the experimental data. The comparison between the angular distribution

calculated from BNV simulations and the one obtained from the data is shown in Fig. 5.28.

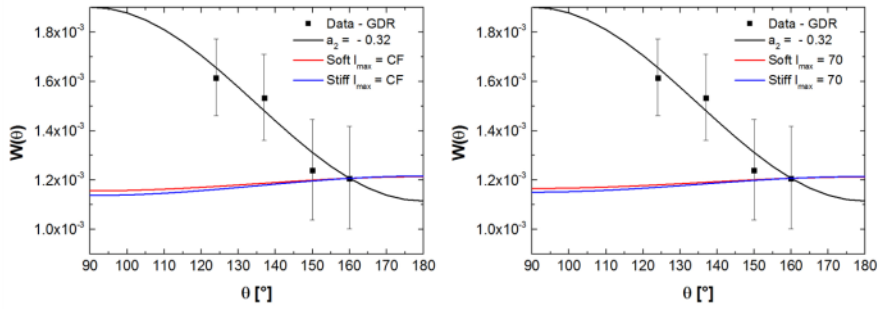

Fig. 5.28: The comparison between the angular distribution obtained from the data (black squares) and the angular distribution obtained from the BNV simulations for asy-soft parameterization (red line) and for asy-stiff one (blue line). The BNV angular distribution is normalized at the experimental datum at 160°. In the left panel there are the results from BNV in the case in which the weights were obtained by using l_{max} calculated by CF code. In the right panel there are the results from BNV in the case in which the weights were obtained by using $l_{max} = 70\hbar$.

The angular distribution obtained from BNV simulations is flat and does not reproduce the experimental data. Moreover, the angular distribution extracted from data is quenched in respect a pure dipole but with a maximum at 90°, instead the one obtained from BNV model has a minimum at 90°, as shown in Fig. 5.28.

From the data it seems that peripheral collision has a smaller contribution to the total yield. One possible way to explain such different behavior is the emission of neutrons and LCPs in the pre-equilibrium phase. Such kind of emission reduce dramatically the total value of the N/Z asymmetry and therefore the total yield. In the extreme case that this pre-equilibrium particle emission is manly present, in peripheral collision and in the very first steps of the reaction, a pure dipole angular distribution (as the one observed in [5]) might appear.

5.5. BNV simulations for an N/Z symmetric reaction

The DD yield was calculated by BNV model for three reactions: the first one ^{16}O + ^{116}Sn, called the N/Z asymmetric reaction, the second one ^{64}Ni + ^{68}Zn, called N/Z symmetric reaction and the last one ^{132}Sn + ^{58}Ni, called very N/Z asymmetric reaction. In the N/Z asymmetric reaction and very asymmetric reaction the N/Z of projectile is different from the N/Z of target, instead in the N/Z symmetric reaction the N/Z ratio is the same for projectile and target. The list of the N/Z for the projectiles and targets used in BNV simulation is shown in Tab. 5.9.

Projectile	**Target**	**N/Z$_{proj}$**	**N/Z$_{targ}$**
^{16}O	^{116}Sn	1	1.32
^{64}Ni	^{68}Zn	1.28	1.27
^{132}Sn	^{58}Ni	1.64	1.07

Tab. 5.9: N/Z ratios for the three reaction for which the DD yield was calculated by BNV model.

We, moreover, performed calculations for an N/Z symmetric system reaction to have a better understanding of the DD γ-emission mechanism. The studied reaction has a dipole moment very small: $D(0) = 1.2\ fm$, (the simulated reaction is $^{64}Ni + {}^{68}Zn$ that is a symmetric reaction studied in [6]). Instead the very asymmetric reaction has a dipole moment very high $D(0) = 45.5\ fm$, (the reaction is $^{132}Sn + {}^{58}Ni$ see section 5.6).

For the symmetric reaction, the DD pre-equilibrium emission is expected to be equal to zero. From the calculation we have found a DD yield that is two order of magnitude smaller than the one studied in this thesis, the $^{16}O + {}^{116}Sn$ reaction. In addition, as it possible to see in Fig. 5.29, there is not a well defined trend between the DD γ multiplicity as a function of the impact parameter.

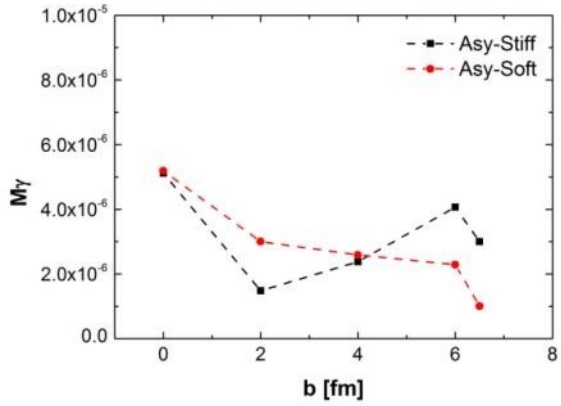

Fig. 5.29: The DD γ multiplicity calculated by the BNV simulations for the system $^{64}Ni + {}^{68}Zn$ *at 12 MeV/u.*

5.6. BNV simulations for a very N/Z asymmetric system

In very asymmetric reaction $^{132}Sn + {}^{58}Ni$ a large DD pre-equilibrium contribution is expected. The calculations results show that the total DD γ multiplicity for the very asymmetric reaction was found to be of one order of magnitude larger than the $^{16}O + {}^{116}Sn$ reaction as shown in Fig. 5.30.

The DD pre-equilibrium γ emission become really significant in the case of exotic beams as explained in section 2.2.1 (see in particular in Fig. 2.6). The calculations for the $^{132}Sn + {}^{58}Ni$ reaction at beam energy of 8.1, 12 and 15.6 MeV/u were performed for the same value of the impact parameter used for the ^{16}O + ^{116}Sn reaction studied in this thesis (b = 0, 2, 4, 5, 5.5, 6 and 6.5 fm).

From the simulations, it was found that the DD pre-equilibrium contribution for $^{132}Sn + {}^{58}Ni$ reaction is one order of magnitude larger than the one for the $^{16}O + {}^{116}Sn$ one, as shown in Fig. 5.30. Also in the case of $^{132}Sn + {}^{58}Ni$ there is a clear dependence of γ multiplicity with the impact factor, indeed the DD pre-equilibrium γ emission decreases with impact

factor and the differences between asy-stiff and asy-soft parameterizations are larger at small value of impact parameter, but in this case the difference between the two parameterizations remains also at larger values of impact parameters.

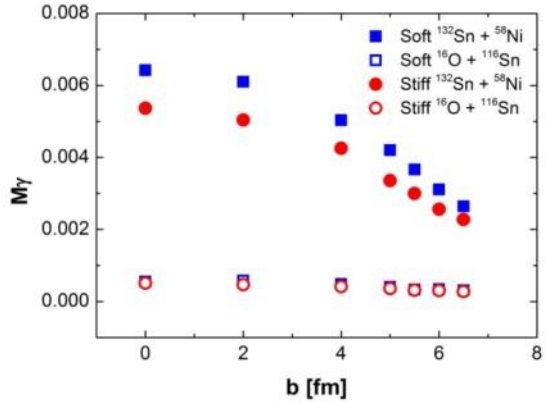

Fig. 5.30: The comparison between the DD γ multiplicity for the systems $^{132}Sn + ^{58}Ni$ (red points and blue squares) and $^{16}O + ^{116}Sn$ (light-blue squares and orange points). The two different series of points for each reaction represent the stiff and the soft parameterizations.

Using the results of these simulations, it could be possible to find the scale factor between the DD pre-equilibrium γ emission for the ^{132}Sn + ^{58}Ni reaction and the one for the ^{16}O + ^{116}Sn reaction. This scale factor is about 10, as shown in Fig. 5.30. We used this scale factor to multiply the experimental data in order to extract, in a pictorial way, a prediction of the measured spectrum of ^{132}Sn + ^{58}Ni (see Fig. 5.31). In the figure the spectrum expected without the DD emission (as in N/Z symmetric reaction), is represented with a red line, the experimental points found in this thesis are represented by light blue squares, and the prediction for the system ^{132}Sn + ^{58}Ni is represented by blue squares. It is important to note that with exotic beam the DD pre-equilibrium emission could be 10 time larger. In this case will be more easy to separate the DD signal from the background (that in this case is the GDR emission).

In section 5.2.4 we obtained that there is a sensitivity to EOS at small b using stable beams (system $^{16}O + ^{116}Sn$). The simulation for the system

$^{132}Sn + {}^{58}Ni$ show a much larger DD signal (ten times bigger that the case of the system studied in this work see Fig. 5.30 and Fig. 5.31) and consequently a larger EOS sensitivity.

It is however important to evidence that these simulations do not take in account the pre-equilibrium particle evaporation which could dramatically reduce the value of the dipole moment and therefore the yield of the DD.

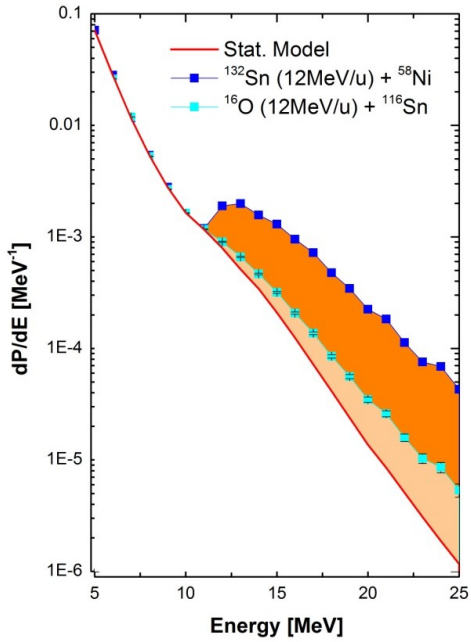

Fig. 5.31: From the theoretical simulations we could extract a prediction for the yield that could be obtained from the experimental data for the system $^{132}Sn + {}^{58}Ni$ (blue squares and dark orange area). This prediction has been compared with the experimental data of the system $^{16}O + {}^{116}Sn$ (light blue squares and light orange area).

5.6.1. Dependence on the impact parameter

Calculations with different impact parameters were performed also in the case of $^{132}Sn + {}^{58}Ni$; the chosen impact parameters are 0, 2, 4, 5, 5.5, 6, 6.5 fm, that are the same used for the system $^{16}O + {}^{116}Sn$ reaction.

These calculations, for the system $^{132}Sn + {}^{58}Ni$, could be interpolated with a Fermi function as the data of the reaction studied in this thesis ($^{16}O + {}^{116}Sn$). For this reason these data were used to have some benchmarks to do the interpolation with a Fermi function of the reaction studied in this thesis (see section 5.2.3).More details on the Fermi function interpolation are explained in section 5.2.3.

5.7. Comparison between the three systems

A comparison of the results obtained from the simulations for three reactions is shown in Fig. 5.32. It is possible to see that the signal of the symmetric reaction is practically equal to zero, the signal of the $^{16}O + {}^{116}Sn$ reaction is smaller than the signal of the very asymmetric reaction that could be obtained only by exploiting exotic beams with high intensity.

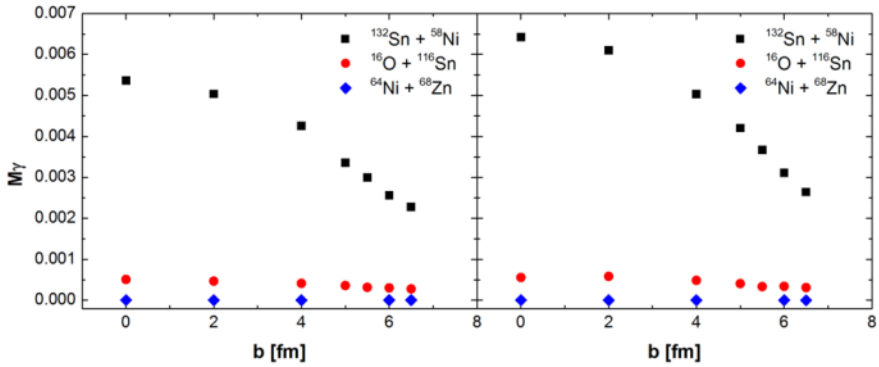

Fig. 5.32: The comparison of the results of the BNV simulations for the three systems at 12 MeV/u: the symmetric one (blue diamonds), the one studied in this thesis (red points) and a very asymmetric one (black squares). In the left panel the results for the asy-stiff parameterization and in the right one the results for the asy-soft parameterization.

6. Properties of very large volume $LaBr_3$:Ce detectors

The excellent properties of very large volume $LaBr_3$:Ce scintillator detectors generated a large interest in the scientific community which works with γ-rays. Its properties make it the best scintillation detector for gamma detection and spectroscopy. In some cases, the $LaBr_3$:Ce detectors could be a possible alternative to HPGe ones. An experimental setup based on $LaBr_3$:Ce scintillator (eventually coupled with HPGe detectors) will constitute an extremely performing, efficient, cost-effective and easy to use gamma detector array. $LaBr_3$:Ce detectors are the best scintillators to measure high-energy γ ray, for example to measure the GDR γ decay. $Labr_3$:Ce scintillators coupled to the AGATA Demonstrator (HPGe segmented detectors) were used to measure the isospin mixing in ^{80}Zr, as discussed in chapters 8 and 9.

In literature, it is possible to find detailed studies of the properties of small or medium size crystals, but no information about large volume ones is available at the moment. The performances of 3.5" x 8" $LaBr_3$:Ce crystals could not easily deduced from those of smaller ones [12], due to, for example, the self absorption or incomplete reflections of the scintillation light, count rate effects, large PMTs, crystal non-homogeneities and a much higher sensitivity to high energy γ rays.

We have investigated the properties of 3.5" x 8"crystal of the HECTOR$^+$ array coupled to a HAMAMATSU R10233-1000SEL photomultiplier tube and an active voltage divider, specifically designed for our large volume LaBr3:Ce scintillation detectors, developed by the electronic group of INFN of Milano. The performances measured with the active VD will be compared with those obtained with HAMAMATSU E1198-26 voltage divider, that is a passive one.

The characterization of these detectors was focused on the pulse lineshape (section 6.1), the energy resolution and linearity studied with γ rays from 5.7 keV (section 6.3) up to 22.6 MeV (section 6.4), and the stability with the count rate (section 6.2).

6.1.Properties of the signal

The signal of a 3.5″ x 8″ crystal was measured and compared with the signal properties (for example pulse rise and fall time) of small or medium crystals (1″ x 1″ and 3″ x 3″). To study the effects induced by a large surface PMT and to quantify the scintillation light collection time.

The pulses were measured for different volume $LaBr_3$:Ce crystals coupled to different PMTs and different voltage dividers. The detectors were supplied with a voltage between 500 up to 1000 V.

Size	PMT	VD	#
1″ x 1″	XP2000B	184K/T	1
1″ x 1″	XP2020	AS20	2
3″ x 3″	R6233	active	3
3.5″ x 8″	R10233-10sel	active	4
3.5″ x 8″	R10233-10sel	E1198-26	5

Tab. 6.1: List of different volume $LaBr_3$:Ce crystals coupled with different PMTs and VDs used to digitize the signal. In the first column there is the detector size, in the second one the PMT model, in the third one the VD and in the fourth there is the identification number used in Fig. 6.1.

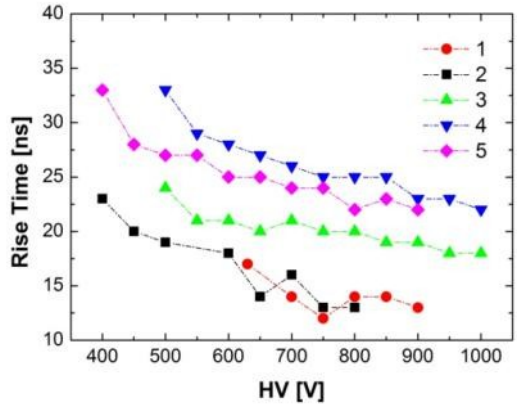

Fig. 6.1: The rise time of different crystals coupled with different PMTs and VDs. The Dimensions of the crystal, the PMT model and the VD model are listed in the legend of the picture. The estimate error in each measurement is about 1-2 ns.

The pulses of five $LaBr_3$:Ce detector configurations listed in Tab. 6.1 were measured in case of 661.6 keV energy pulses, acquired using a 500 MHz bandwidth, 2 GHz sampling frequency digital oscilloscope (Lecroy Wavejet 354). The rise times (defined as the time required to the pulse to rise from 10% to the 90% of its maximal amplitude) of the signals were measured and estimated with 1 ns of uncertainty and they are shown in Fig. 6.1.

The minimum rise time for a large volume crystal (3.5″ x 8″) is about 24 ns, instead for a small one (1″ x 1″), the minimum rise-time is about 13 ns. The 3.5″x8″ crystal shows a longer rise-time with respect to a smaller one due to the scintillation collecting time and to the different PMT intrinsic rise time. Furthermore, the applied voltage is relevant but, for a given PMT, the pulse rise time reaches an asymptotic value as the applied voltage increases.

In situations where a $LaBr_3$:Ce detector is expected to work in a limited energy range, from 100 keV up to 3 MeV, it is not necessary to have an anode pulse of 30 mV amplitude for a deposited energy of 661.6 keV. In this energy range there is no difference between the custom-made active VD and the E1198-26 by HAMAMATSU VD. However, in the case large dynamic ranges from 300 keV up to 30 MeV, a non linear response of the detector is a critical issue. Gamma rays calibration up to 3 MeV has to be used to extrapolate the calibration at higher energy up to to 30 MeV. The non linear response is a very important in case, for example, of measurement of GDR γ decay in which the expected energy range is from few MeV up to 30 MeV. In this energy range it is necessary to have an anode pulse of 30 mV amplitude for a deposited energy of 661.6 keV. The measurement of the non linear response in the energy response was performed using high-energy γ rays as discussed in section 6.4.

A large volume $LaBr_3$:Ce detector (3,5″ x 8″) coupled to the active VD has to be supplied at 900 V to produce an anode pulse of 30 mV of amplitude for a deposited energy of 661.6 keV, whereas the same detector coupled to E1198-26 by HAMAMATSU has to be supplied at 600 V to produce an anode pulse of 30 mV amplitude. The rise time is about 25 ns for the large volume crystal coupled to active VD supplied at 900 V, and it is again 25 ns for the same crystal coupled to E1198-26 supplied at 600 V, as shown in Fig. 6.1. The use of the PMT at low voltage, namely in a non

optimal condition, affects both energy and time resolution. Low voltage implies small gain and a worst signal to noise ratio. The variance σ^2 in the PMT gain for one photoelectron (in case of a constant partition) is $\sigma^2 = 1/(\delta-1)$ [52], where δ is the dynode gain. As δ is proportional to the applied voltage. The higher is the voltage the smaller is σ^2 and therefore the gain fluctuations. Moreover, the signal rise time depends on the applied voltage and consequently the best time resolution is achieved with an high value of the applied voltage. In this case the E1198-26 by HAMAMATSU VD has to be supplied at low voltage (about 500 V), as explained before a low applied voltage provides a worst time and energy resolution.

The detector size effects in the rise time were measured by using H6533 HAMAMATSU PMT. For each of the three detector configurations (1″ x 1″, 3″ x 3″ and 3.5″ x 8″ coupled to H6533 tube) we acquired a few tens of 661.6 keV energy pulses with a 400 MHz bandwidth, 5 GHz sampling frequency digital oscilloscope (LeCroy Waverunner 44X1) and subsequently estimated the three reference signals (represented in Fig. 6.2), by averaging the corresponding data sets of pulses, in order to improve the signal to noise ratio especially in the case of the last two crystals, for which only a small fraction of the emitted photons were actually collected by the PMT. The measured rise time is 4 ns, 7 ns and 14 ns respectively for 1″ x 1″, 3″ x 3″ and 3.5″ x 8″ crystals, as shown in Fig. 6.2.

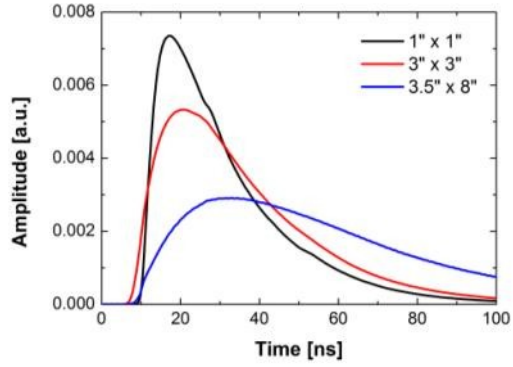

Fig. 6.2: The pulse line-shape measured using a H6533 PMT coupled to three different volume $LaBr_3$:Ce crystals (1″ x 1″, 3″x3″ and 3.5″ x 8″). The difference in pulse line-shape comes from the different scintillation photons arrival time.

The fall time (defined as the time required to the pulse to fall from 10% to the 90% of its maximal amplitude) were also measured for different detectors coupled to different PMTs and voltage. It was found that the fall time for a large volume crystal is about 70 ns.

6.2.Response to high counting rate

We investigated the response of the $LaBr_3$:Ce to different counting rates. A high counting rate, indeed, increases the average current inside the PMT; in a passive voltage divider this could reduce the potential between the last dynodes and the anode, thus producing an increase in the PMT gain. This gain drift could deteriorate the energy resolution. In the active voltage divider, the effect, on the PMT gain, are not expected at high counting rate.

The centroid drift and the energy resolution deterioration were measured (extracted from digitized pulses) for different counting rates (from a few kHz up to 250 kHz) for a standard voltage and the active one. The centroid and FWHM for the 898 keV full energy peak have been extracted from the signals digitized using a LeCroy waverunner 44X1 5Gs 400MHz oscilloscope. The deposited energy was obtained using a simple integration algorithm in a time window of 250 ns with baseline subtraction (250 ns integration window for the baseline subtraction). No significant deterioration of the energy resolution was measured for both detectors (see Fig. 6.3 and Fig. 6.4). The centroid drift, for different counting rates is shown in Fig. 6.3 for the crystal coupled to the active voltage divider, while in Fig. 6.4 for the crystal coupled to HAMAMATSU E1198-26. The centroid drift is smaller than 1% for the active VD, at 250 kHz, instead it was about 5% at 250 kHz for the standard VD.

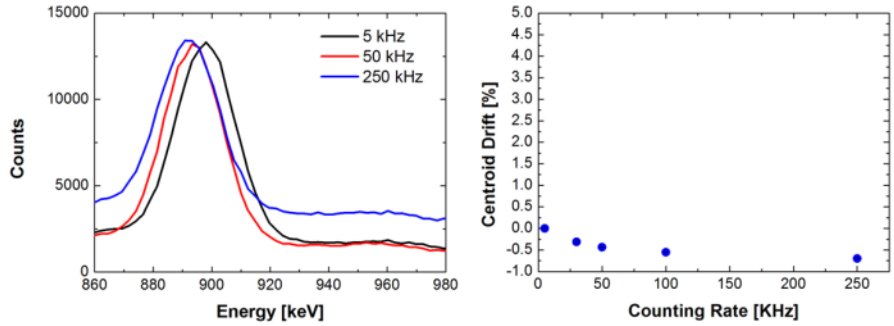

Fig. 6.3: The 898 keV peak from a ^{88}Y source measured for different count rates with an active voltage divider. The drift is less than -0.7% at 250 kHz.

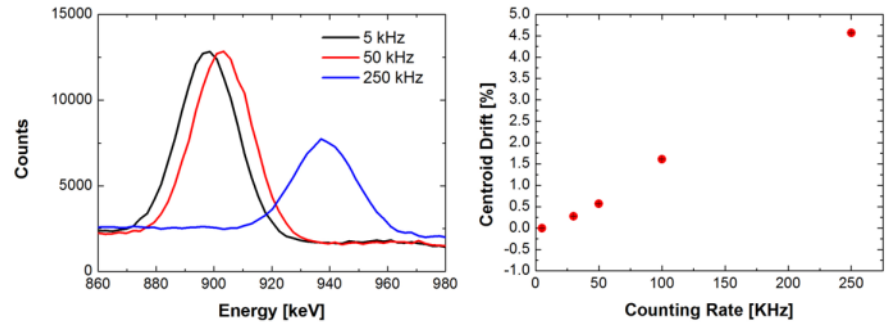

Fig. 6.4: The 898 keV peak from a ^{88}Y source measured for different count rates with E1198-26 by HAMAMATSU voltage divider. The drift is about 5% at 250 kHz

6.3.Response to low-energy γ rays

The response of $LaBr_3$:Ce crystal in term of number of photons versus the gamma deposited energy is extremely linear; unfortunately the linearity of the PMT and the VD is not guaranteed, especially for high-energy γ rays. The first indication of a non linearity is usually the presence of a distortion in the pulse shape. In order to measure monochromatic γ rays in a energy range of 1 MeV up to 22.6 MeV, (p, γ) reactions were used [53]. The pulse shape distortions and non linearity was discussed in details in section 6.4.

The energy resolution was measured from 5.7 keV up to 22.6 MeV. In Fig. 6.5 there is the γ spectrum measured at the low sides of the energy range. The peak at 5.7 keV and the peak at 32 keV are present due to the internal radioactivity of $LaBr_3$:Ce scintillators. In these scintillators, the unstable isotope ^{138}La is present as explained in section 8.2. The two peaks, in Fig. 6.5, are originated from the energy released by the cascade products following the refill of the hole, left behind by the captured electron, in the K or L atomic shell of the daughter nucleus ^{138}Ba. The peak at 80 keV is the gamma emission of ^{133}Ba source, that was present during the measurement.

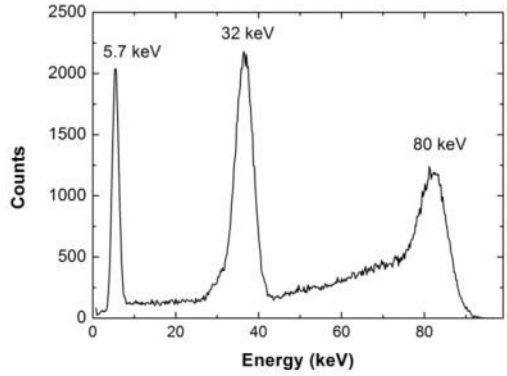

Fig. 6.5: In this plot it is shown the γ spectra in a low-energy range measured with a 3.5" x 8" detector coupled with a custom-design active VD. The first two peaks are originated by the electron capture in K or L shell of ^{138}Ba that is the daughter nucleus of ^{138}La.

6.4. Measurement of high energy γ rays

Test measurements, concerning detector linearity and energy resolution, were performed in the Institute of Nuclear Research of the Hungarian Academy of Sciences (ATOMKI). Low-energy γ-rays were studied using ^{60}Co (1173.2 keV and 1332.5 keV) and ^{66}Ga (γ rays with energy range from 1500 keV to 4800 keV) isotope sources, while the high-energy region was covered by γ-rays emitted in (p,γ) reactions (see Tab. 6.2). Protons were accelerated to the resonance energies (from 441 keV up to 1416.1 keV) by a 5MV Van de Graff accelerator, and impinged on different

thin evaporated targets: Al, Na_2WO_4, K_2SO_4 and $LiBO_2$. The produced γ-rays energies are from 1.4 MeV up to 17.6 MeV. Protons were also accelerated at 7250 keV by the cyclotron accelerator of the ATOMKI laboratories and impinged on a $LiBO_2$ target to produce γ rays of 22.6 MeV. Two large volume $LaBr_3$:Ce crystals, coupled by a standard HAMAMATSU R10233-1000SEL photomultiplier and to the active voltage divider were used. They were placed in the distance of 15.5 cm from the target and at the angle of 55° in respect to the proton beam line. The same (p, γ) reactions of [53] were populated to produce γ rays up to 17.6 MeV. The details of reactions and target are listed in Tab. 6.2.

Reaction	**Q value [keV]**	**E_p [keV]**	**E_γ [keV]**	**Target and its thickness [μg/cm³]**
$^{23}Na(p,\gamma)^{24}Mg$	11693	1323	1368.6 11584.6	Na_2WO_4 20
$^{23}Na(p,\gamma)^{24}Mg$	11693	1422	2754.0 8925.2	Na_2WO_4 20
$^{27}Al(p,\gamma)^{28}Si$	11585	770	2838.7 7706.5	Al 15
$^{39}K(p,\gamma)^{40}Ca$	8328	1351	3904.4 5736.5	K_2SO_4 20
$^{11}B(p,\gamma)^{12}C$	15957	676	4438.0 12137	$LiBO_2$ 75
$^{11}B(p,\gamma)^{12}C$	15957	7250	22600.0	$LiBO_2$ 75
$^{7}Li(p,\gamma)^{8}Be$	17225	450	17619.0	$LiBO_2$ 75

Tab. 6.2: Parameters of the (p,γ) reactions populated at the ATOMKI laboratories. E_p is the energy of the protons and E_γ is the energy of the emitted γ rays.

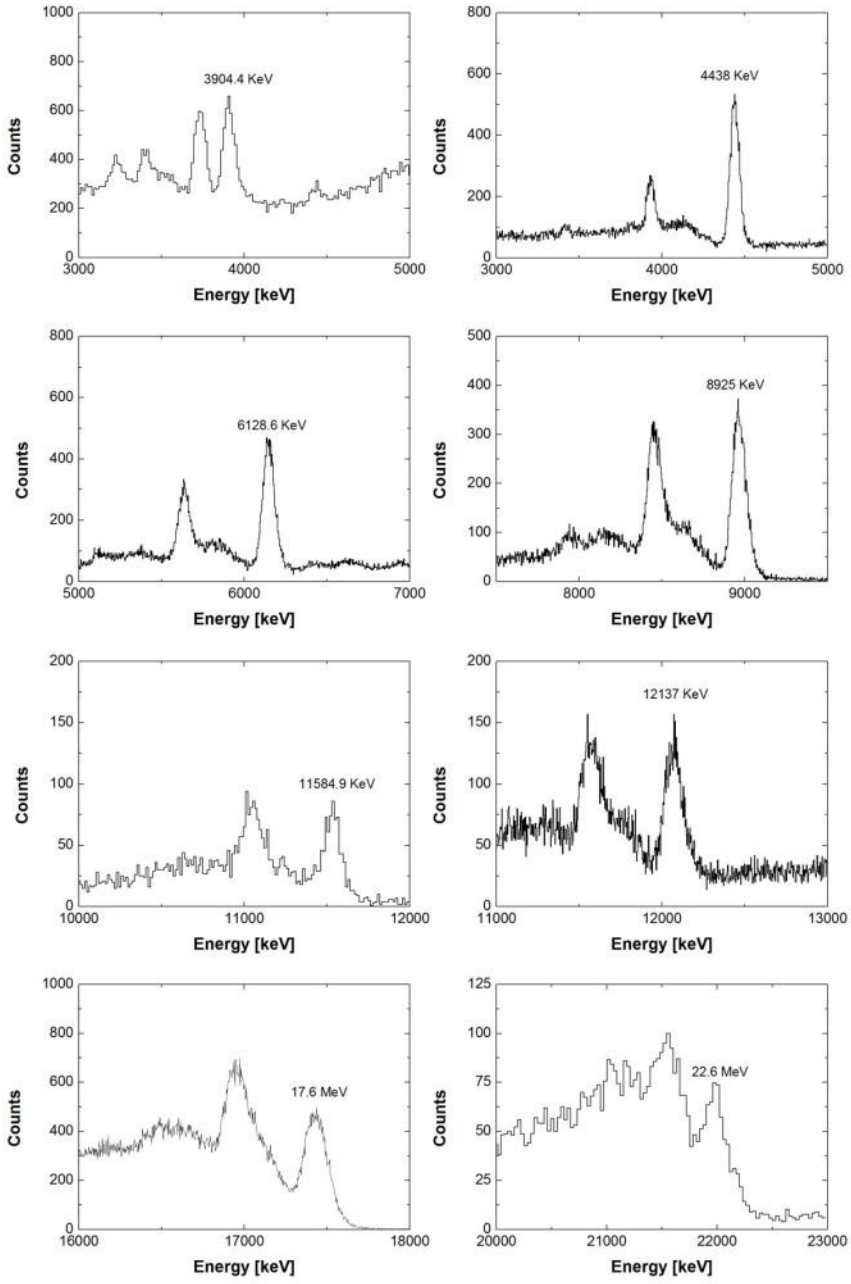

Fig. 6.6: Gamma-ray spectra obtained from (p,γ) *reactions. It is shown the* γ *peaks at the different energy up to 22MeV.*

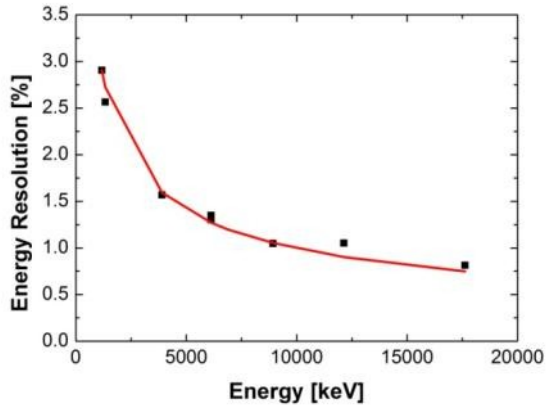

Fig. 6.7: The energy resolution of one $LaBr_3$:Ce detector till 17.6 MeV measured in ATOMKI laboratories (black points). The red line represent the $\frac{FWHM}{E} \propto \frac{1}{\sqrt{E}}$ trend.

Due to good energy resolution of the $LaBr_3$:Ce detectors, the full energy and the first escape peaks are clearly separated up to 22.6 MeV as shown in Fig. 6.6. The energy resolution trend, as expected, follows $FWHM/E \propto 1/\sqrt{E}$ (see Fig. 6.7). The spectra obtained at the various energies up to at 22.6 MeV are shown in Fig. 6.6.

The non linearity, defined as $(E_{true} - E_{measured})/E_{true}$, is smaller than 1% at 17.6 MeV (see Fig. 6.8), instead is 2.6% at 22.6 MeV.

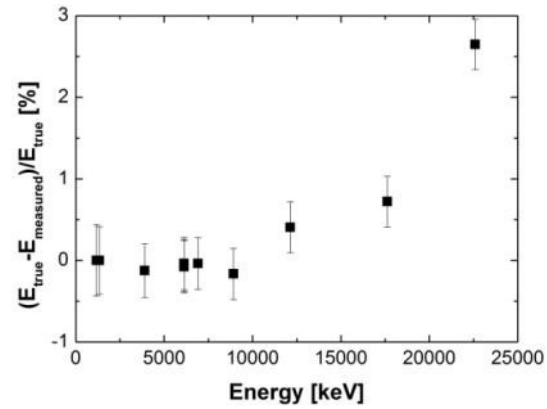

Fig. 6.8: The non linearity extracted using a linear calibration in the case of the 3.5" x 8" with the active voltage divider measured using the reactions of Tab. 6.2.

7. Isospin mixing

In this part of this work, the physics case and the preliminary steps of the data analysis of an experiment that aimed to measure the isospin mixing in the $N = Z$ nucleus ^{80}Zr at temperature $T = 2.4$ MeV will be discussed. This is a follow up of a 2008 GARFIELD-HECTOR experiment, in which isospin mixing was measured in a much higher temperature window, namely at ~ 3 MeV [54]. This new experiment will integrate and complete the previous dataset and, in addition, it will validate the technique which allows to extract the value of isospin mixing at zero temperature from the one measured at T > 0. This topic is particularly important, especially for nuclei near A=100 in connection with the properties of the Isobaric Analog States (IAS) and with the Fermi β decay of the N=Z nuclei around the proton drip line. The evaluation of the isospin impurity provides an important correction to the Fermi-transition rates allowing the extraction, in a nucleus-independent way, of the up-down quark-mixing matrix element of the Cabibbo-Kobayashi-Maskawa matrix.

The main objectives of this experiment are: the measurement of the temperature dependence of isospin mixing in ^{80}Zr, the extraction of the value of isospin mixing at zero temperature, the validation the theoretical calculations to extract the T=0 mixing value from the one at T≠0 and the measurement of the Coulomb spreading width.

The two symmetric fusion-evaporation reactions ^{40}Ca + ^{40}Ca and ^{37}Cl + ^{44}Ca to form the nuclei ^{80}Zr and ^{81}Rb were populated in order to extract the isospin mixing probability from the comparison of the high-energy γ-ray yield from the giant dipole resonance decay. The experimental setup is the AGATA Demonstrator coupled to an array of 7 large volume $LaBr_3$:Ce, named HECTOR$^+$.

In this chapter the physics case of the isospin mixing experiment will be described. In particular, the concept of the isospin quantum number (section 7.1), the isospin mixing at zero temperature and at finite temperature (sections 7.2 and 7.3), the GDR decay as a tool to measure the

mixing probability (section 7.4) and the existing data (section 7.5) will be described.

7.1. Isospin formalism

In the isospin formalism neutrons and protons are assumed to be different states of the same particle, the nucleon. The isospin symmetry is preserved by nuclear interaction; while the isospin symmetry is broken by Coulomb interaction, because it depends on the charge of the nucleon. For this reason the isospin is not a good quantum number due to the fact that it is not a conserved quantity.

The isospin quantum number (I) was introduced by Heinsemberg in 1932 [55] to describe the wave function symmetry respect neutrons and protons exchange. Neutrons and protons have values of $1/2$ and $-1/2$ of the projection I_z of the isospin operator. According to this definition the projection I_z of the isospin operator for a nucleus with N neutrons and Z protons can be written as:

$$I_z = \frac{N - Z}{2}. \tag{7.1}$$

The value of I_z is the minimum value of the isospin, this means that the possible values of I are included in the following range:

$$\frac{1}{2}|Z - N| \leq I \leq \frac{1}{2}(Z + N). \tag{7.2}$$

The nuclear force drives the nuclei towards a configuration with the lowest possible imbalance between protons and neutrons, that means the lowest possible I_z. The tendency of the nuclear force towards nuclei with $N = Z$ is opposed by the Coulomb force, which favors an excess of neutrons over protons. Since the Coulomb force does not saturate, its effect becomes eventually dominant for large A (approximately $A > 40$), leading to a deviation of the β-stability valley from the $N = Z$ line. The "lowest possible isospin" rule holds well for all even-even and odd-mass nuclei and it breaks down only in some odd-odd self-conjugate nuclei like ^{34}Cl, ^{42}Si, ^{42}Sc and ^{46}V, where $I = 0$ and $I = 1$ states are almost degenerate [56].

7.2. Isospin mixing at zero temperature

The isospin is not a good quantum number because the operator I does not commute with the Hamiltonian due to the presence of the Coulomb term. The Coulomb interaction mixes states with isospin I and states with isospin $I+1$. In the first order perturbation theory the admixture of $I = I_0 + 1$ states into $I = I_0$ states (isospin mixing) can be written as:

$$(\alpha^{I_0+1})^2 = \sum_{I=I_0+1} \frac{|\langle I = I_0 + 1|H_c|I = I_0\rangle|^2}{\left(E_{I=I_0+1} - E_{I=I_0}\right)^2} \qquad (7.3)$$

where H_c represents Coulomb interaction. Since the Coulomb potential preserves angular momentum J and parity π, it can couple only states with the same J^π and, more efficiently, with similar spatial wave function. Such states at low excitation energy usually lie at rather different energies, so the mixing probability is kept small by the large denominator in equation 7.3. In light nuclei, at low value of excitation energy, states with a large mixing were found, such as the 2^+ state of ^8Be [57].

At higher excitation energy, the levels come closer and the width Γ becomes larger than the level spacing. This fact can be still accounted for in first-order perturbation theory introducing a complex energy which produce the finite lifetimes in equation 7.3:

$$(\alpha^{I_0+1})^2 = \sum_{I=I_0+1} \left| \frac{\langle I = I_0 + 1|H_c|I = I_0\rangle}{\left(E_{I=I_0+1} + i\Gamma_{I=I_0+1}/2\right)^2 - \left(E_{I=I_o} + i\Gamma_{I=I_0}/2\right)^2} \right|^2 . \qquad (7.4)$$

Theoretical calculations of isospin mixing in the ground state, therefore at zero temperature, were performed and the results of these calculations of isospin mixing in ^{80}Zr are summarized in Tab. 7.1 and the mixing probability $(\alpha^{I_0+1})^2$ ranges from 1% to 4.5%.

Fig. 7.1 displays the A dependence of the isospin mixing probability, found in [9], for several self-conjugated nuclei with Z up to 50.

$(\alpha^{I_0+1})^2$	Method	Interaction
1%	analytic	
3.6%	HF + TDA	SG2
3.1%	HF + TDA	SIII
3%	HF spherical	SIII
2.5%	HF deformed	SIII
3.9%	HK	SIII
2.21%	analytic	
4.5%	EDF	SLy4

Tab. 7.1: Available theoretical calculations of $(\alpha^{I_0+1})^2$ are quoted from the references [9], [58]–[61]. The abbreviation HF stands for Hartree-Fock, EDF for Energy Density Functionals, TDA for Tamm-Dancoff approximation. In the third column the parameterization of Skyrme interaction used is given only for non-analytic approaches.

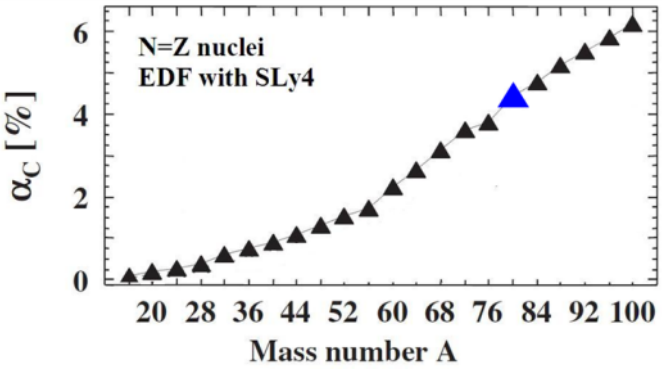

Fig. 7.1: The A dependence of the isospin mixing probability, found in [9], for several self-conjugated nuclei, the blue triangle represent the value for the ^{80}Zr nucleus [9].

7.3. Isospin mixing at finite temperature

As the excitation energy increases the level width become larger than the level spacing. In this case a definition of isospin mixing in term of levels is not valid anymore and consequently, it is necessary a description in term of level density. To describe the isospin mixing it is useful to introduce the concept of the Coulomb spreading width $\Gamma^{\downarrow}$, that is the energy range in

which the state is distributed because of Coulomb interaction. The value of the spreading width is not expected to depend on the populated nucleus and on the excitation energy [62].

A compound nucleus can directly decay via γ or particle emission. The decay process can be described associating to the states a finite decay width $\Gamma^{\uparrow}$ corresponding to a lifetime τ through the Heisenberg rule:

$$\Gamma^{\uparrow} \sim \frac{2\hbar}{\tau} \tag{7.5}$$

Due to the limited CN lifetime, a time-dependent approach to the isospin mixing problem is demanded as suggested by Wilkinson [56] and later formalized by Harney, Richter and Weidenmuller [63]. In this approach, the mixing probability is determined by the competition between CN lifetime and the timescale of isospin mixing process. A simplified model used in reference [57], it is useful to understand isospin mixing in this new scenarios. In this model it is supposed to have $I = 0$ states with the same level spacing energy D, stretching to plus and minus infinity. A state of isospin $I = 1$ in the unperturbed Hamiltonian lies in their midst at energy $E_{I=1}$. Consider a perturbation with a constant matrix element v between the state and each underlying states. One can solve the resulting Hamiltonian matrix analytically. In the limit of $v \gg D$, the result for the probability $P_{I=1}(E)$ to find the system in the $I = 1$ configuration per unit energy interval of the spectrum is given by:

$$P_{I=1}(E) = \frac{1}{2\pi} \frac{\Gamma_c^{\downarrow}}{(E_{I=1} - E_{I=0})^2 + (\Gamma_c^{\uparrow}/2)^2} \tag{7.6}$$

where $\Gamma_c^{\downarrow}$ is the spreading width of $I = 1$ state due to the Coulomb interaction, the so called Coulomb Spreading Width. The probability at the time t of finding the system initially populated in the I=1 state still in the I=1 state is given by the Fourier transform of the equation 7.6:

$$P_{I=1}(t) = exp\left(-\frac{\Gamma_c^{\downarrow}}{2\hbar}t - \frac{i}{\hbar}E_{I=1}t\right) \tag{7.7}$$

from where one can deduce that a relation similar to equation 7.5 also links the Coulomb spreading width $\Gamma_c^{\downarrow}$ and the timescale τ_{mixing} of isospin mixing:

$$\Gamma_c^{\downarrow} = \frac{2\hbar}{\tau_{mixing}}. \qquad (7.8)$$

With increasing temperature, CN lifetime becomes too short to allow a complete mixing, therefore a decrease of isospin mixing parameter α is expected, corresponding to a partial restoration of isospin symmetry at high temperature. The values of CN decay width, Coulomb spreading width and the corresponding timescales are listed in Tab. 7.2 for three different temperatures along the decay path of the CN ^{80}Zr.

T[MeV]	$\Gamma_{CN}^{\uparrow}$ [MeV]	τ [s]	$\Gamma_c^{\downarrow}$ [MeV]	τ_{mixing} [s]
2.1	0.23	2.8 10-21	0.01	6.4 10-21
1.9	0.15	4.4 10-21	0.01	6.4 10-21
1.8	0.13	4.9 10-21	0.01	6.4 10-21

Tab. 7.2: The CN decay width $\Gamma_{CN}^{\uparrow}$ [MeV] and Coulomb mixing width $\Gamma_c^{\downarrow}$ followed by the corresponding lifetime τ and τ_{mixing} for the CN ^{80}Zr calculated within the Statistical Model.

Harney, Richter and Weidenmuller [63] take into account two classes of CN states with pure isospin, $|I_<\rangle = |I, I_Z\rangle$ and $|I_>\rangle = |I+1, I_z\rangle$. By analogy with other symmetry breaking mechanisms, they describe the isospin mixing of states $|I_<\rangle$ into states $|I_>\rangle$ in terms of the spreading width $\Gamma_c^{\downarrow} \equiv \Gamma_>^{\downarrow}$ defining the timescale of symmetry breaking induced by the Coulomb interaction H_c:

$$\Gamma_>^{\downarrow} = 2\pi\overline{|\langle I_>|H_c|I_<\rangle|^2}\rho(I_<)\,. \qquad (7.9)$$

$\Gamma_<^{\downarrow}$ can be defined exchanging > and < and it is linked to $\Gamma_>^{\downarrow}$ by the following relation:

$$\Gamma_<^{\downarrow} = \frac{\rho(I_>)}{\rho(I_<)}\Gamma_>^{\downarrow} \qquad (7.10)$$

The fraction $\alpha_<^2$ of states $|I_<\rangle$ that mix to states $|I_>\rangle$ can be written in term of the Coulomb spreading width $\Gamma_c^{\downarrow}$ and CN decay width $\Gamma^{\downarrow}$ as:

$$\alpha_<^2 = \frac{\Gamma_{c,<}^{\downarrow}/\Gamma_<^{\uparrow}}{1 + \frac{\Gamma_{c,<}^{\downarrow}}{\Gamma_<^{\uparrow}} + \frac{\Gamma_{c,>}^{\downarrow}}{\Gamma_>^{\uparrow}}}, \qquad (7.11)$$

Similarly, the fraction $\alpha_>^2$ of states $|I_>\rangle$ that mix to states $|I_<\rangle$ can be written as:

$$\alpha_>^2 = \frac{\Gamma_{c,>}^{\downarrow}/\Gamma_>^{\uparrow}}{1 + \frac{\Gamma_{c,>}^{\downarrow}}{\Gamma_>^{\uparrow}} + \frac{\Gamma_{c,<}^{\downarrow}}{\Gamma_<^{\uparrow}}}. \tag{7.12}$$

7.3.1. Theoretical description

A theoretical model to study the isospin mixing probability as a function of the temperature was developed [62], [64]. It is based on microscopic calculations. This model was applied at ^{208}Pb but it could be adapted at ^{80}Zr.

The Hamiltonian is divided in two part, the first one H_0 isospin conserving and the second one H_1 that does not conserve the isospin, as follows:

$$H = H_0 + H_1. \tag{7.13}$$

The whole model space of nuclear configurations is built up with states which are eigenstates of the isospin-conserving nuclear Hamiltonian H_0 and is divided in two subspaces P and Q. The P space contains only two states, the parent ground state and the Isobaric Analog State (IAS), that is the state obtained by changing a neutron with a proton, which have isospin $|I, I-1\rangle$. The other nuclear states in the daughter nucleus form the space Q. This state can be written as:

$$\begin{aligned} |P\rangle &= |\pi\rangle, |IAS\rangle \\ |Q\rangle &= 1 - |P\rangle \end{aligned} \tag{7.14}$$

where $|\pi\rangle$ is the ground state and $|IAS\rangle$ is the isobaric analog state. The IAS has a spreading width due to the presence of H_1 that connects the subspaces P and Q. The spreading width of the IAS can be formally written as:

$$\begin{aligned} \Gamma_{IAS}^{\downarrow}(E) &= 2Im \sum_q \frac{|\langle IAS|H_1|q\rangle|^2}{E - E_q + i\Gamma_q(E)/2} \\ &= \sum_q \Gamma_q(E) \frac{|\langle IAS|H_1|q\rangle|^2}{\left(E - E_q\right)^2 + \left(\Gamma_q(E)/2\right)^2} \end{aligned} \tag{7.15}$$

where Γ_q and E_q are the total width and the energy of the states belonging to the Q space.

For many nuclei near the shell closure, the dominant contribution to the sum in equation 7.15 comes from the isovector monopole state (IVM) with isospin $I_0 - 1$, I_0, $I_0 + 1$ and therefore equation 7.15 can be rewritten as:

$$\Gamma_{IAS}^{\downarrow}(E) = \sum_{M} \Gamma_M\,(E_{IAS})\,\frac{|\langle IAS|H_1|M\rangle|^2}{(E_{IAS} - E_M)^2 + (\Gamma_M(E_{IAS})/2)^2} \qquad (7.16)$$

where $\Gamma_M(E_{IAS})$ is the width of the IVM state at the energy of the IAS. From equations 7.4 and 7.16 it is possible to obtain the isospin mixing probability at finite temperature as:

$$(\alpha^{I_0+1})^2 = \frac{1}{(I_0+1)F(I_0)}\,\frac{\Gamma_{IAS}^{\downarrow}(E^*)}{\Gamma_{CN}^{\uparrow}(E^*) + \Gamma_M(E^*)} \qquad (7.17)$$

where $F(I_0)$ is a geometrical factor that include the isospin dependence of the width of the IVM state, E^* is the excitation energy of the nucleus, $\Gamma_{IAS}^{\downarrow}(E^*)$ is the spreading width of the isobaric analog state and $\Gamma_M(E^*)$ is the width of the IVM state.

Equation 7.17 shows the relation between the IAS spreading width and the isospin mixing probability of the parent nucleus as a function of the nuclear temperature. $\Gamma_{CN}^{\uparrow}(E^*)$ is expected to vary in a significant way with excitation energy, instead $\Gamma_M(E^*)$ and $\Gamma_{IAS}^{\downarrow}(E^*)$ are expected to be rather constant with the excitation energy. In Fig. 7.2 it is represented the temperature dependence of isospin-mixing probability $(\alpha^{I_0+1})^2$ in ^{208}Pb. The two curves correspond to two different parameterization of the temperature dependence of $\Gamma_{IAS}^{\downarrow}(E^*)$ (the temperature dependence is defined in [62]: $\Gamma_{IAS}^{\downarrow}(E^*) = \Gamma_{IAS}^{\downarrow}(T=0)(1+cT)$, the $\Gamma_{IAS}^{\downarrow}(E^*)$ slightly vary with the temperature); the two curves are very similar, this conform the fact that the $\Gamma_{IAS}^{\downarrow}(E^*)$ is weakly dependent on the nuclear temperature.

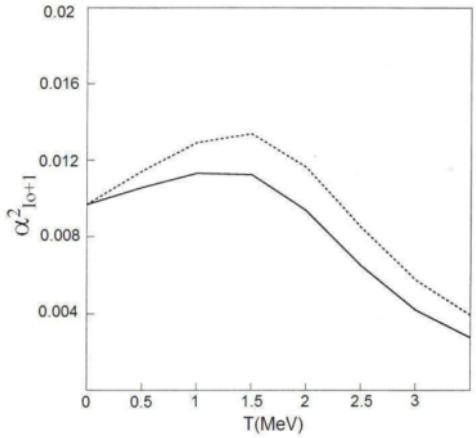

Fig. 7.2: Temperature dependence of isospin-mixing probability in ^{208}Pb [62]. Solid and dashed curves correspond to two different parameterizations of the (mild) temperature dependence of $\Gamma^{\downarrow}_{IAS}$ and Γ_{IVM} adopted in [62].

7.4. GDR as a tool to measure the isospin mixing

The GDR decay is used as a tool to measure the isospin mixing probability, this means that the isospin mixing value will be deduced from the decay of the GDR built on the excited state of the compound nucleus. In the case of the γ decay of the GDR the selection rule for the isospin quantum number is $\Delta I = \pm 1, 0$ (with the transition $0 \rightarrow 0$ forbidden) due to the isovector nature of the GDR (see section 1.1.1). In the ground state, the value of isospin is the lowest possible as consequence in case of the $N \neq Z$ nuclei are allowed the $\Delta I = 1, 0$ transitions, while for the $N = Z$ nuclei are allowed only $\Delta I = 1$ transitions. A schematic view of the GDR transition rules in ^{80}Zr is show in Fig. 7.3. For this reason, there will be a strong inhibition of the first step of GDR decay in the case of $N = Z$ nuclei.

The Coulomb interaction mixes the states with isospin $I = 0$ with states with isospin $I = 1$, as a consequence, if the mixing is present, $I = 1$ states are present in the wave function and the GDR decay to $I = 0$ states becomes possible. In such situation one can imagine two extreme scenarios: in the first mixing by Coulomb interaction is not present and in this case there will be a strong inhibition of the first step of the gamma decay of the

GDR (represented by a red line in Fig. 7.4); in the second one a full mixing is present and there is no inhibition of the gamma decay of the GDR (represented by a black line in Fig. 7.4).

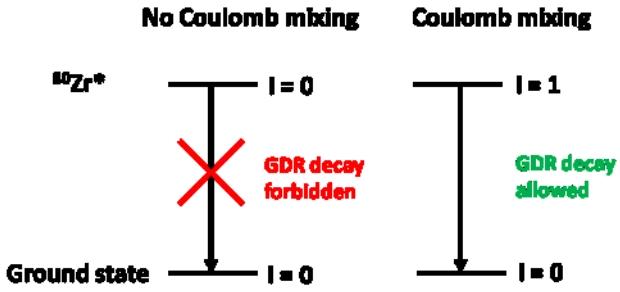

Fig. 7.3: The GDR decay selection rules in ^{80}Zr. The CN is populated in a state with I = 0, but the GDR decay from states with I = 0 to states with I = 0 is forbidden. Strong inhibition of GDR decay if there is no Coulbum mixing. Instead if there is mixing due to the Coulomb interaction some states with I = 1 are available. The GDR decay between states with ΔI = 1 is allowed.

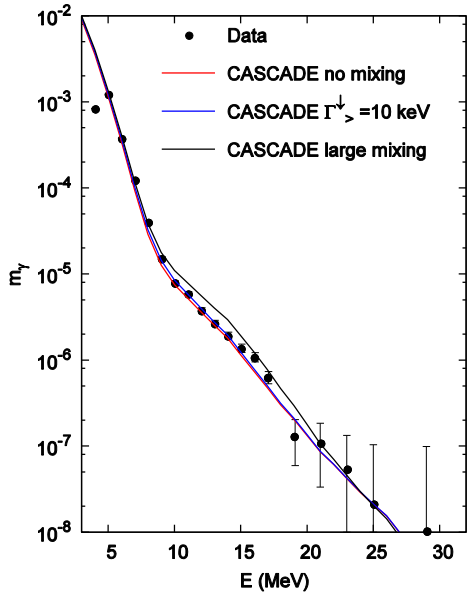

Fig. 7.4: Measured γ-ray spectrum of ^{80}Zr compared with Statistical Model calculations without isospin mixing (red), with isospin mixing that reproduce the experimental data (blue) and with a large degree of isospin mixing (black) [65].

It is expected a value of the mixing probability that is between these two extreme case (in Fig. 7.4 is represented by a blue line). Fig. 7.4 shows the result obtained from the previous experiment in which the isospin mixing was measured at $T = 3\ MeV$ [54], [65]. The isospin mixing in $^{80}Zr^{*}$ at T=2.4 MeV is expected to be in a intermediate case between these two extreme scenarios, as found in the case of $^{80}Zr^{*}$ at T=3 MeV.

7.5. Existing data

In literature some experimental data are present which provide the isospin mixing probability. If we restrict the comparison to the results obtained using the same experimental technique, the data available for systems with Z=16-40 at T=2-3 MeV were studied. Even though these data are not homogeneous in CN temperature, Coulomb spreading width, angular momentum spread, there is a clear increase of the degree of isospin mixing with increasing Z and a decrease with increasing temperature (if the triangles in Fig. 7.6 were not considered) [10], [11], [66], [67]. A list of the parameters involved in this measurement are shown in Tab. 7.3.

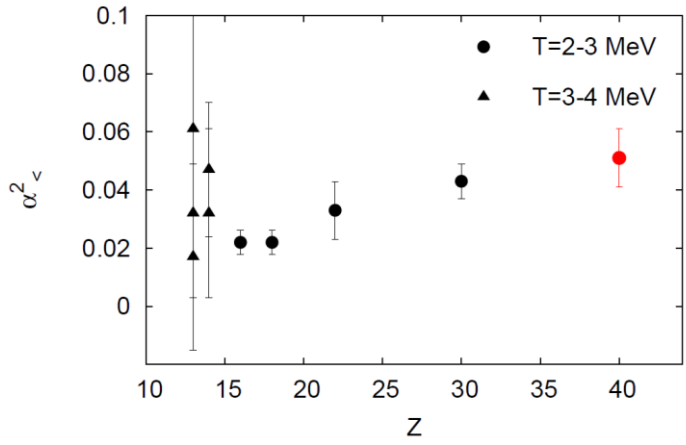

Fig. 7.5: The dependence of isospin mixing probability on atomic number Z. Systematic of isospin mixing probability measured via GDR decay of the hot CN with Z=13-14 and T=3-4 MeV (triangles) and with Z=16-40 and T=2-3 MeV (dots). The result obtained for ^{80}Zr at T=3 MeV belongs to the second group and is plotted with a red dot.

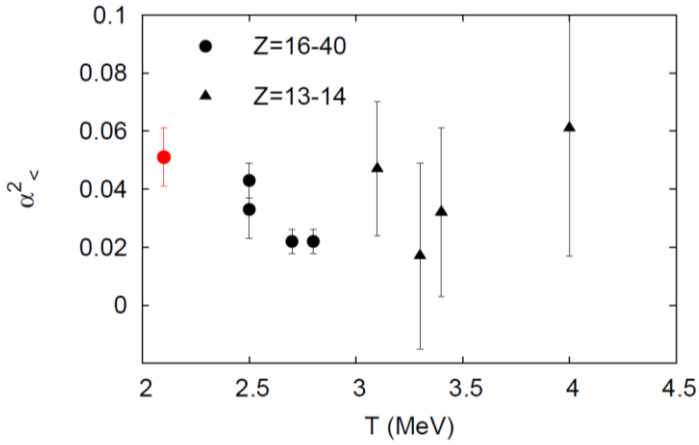

Fig. 7.6: The dependence of isospin mixing probability on temperature. Systematic of isospin mixing probability measured via GDR decay of the hot CN with Z=13-14 and T=3-4 MeV (triangles) and with Z=16-40 and T=2-3 MeV (dots). The result obtained for ^{80}Zr at T=3 MeV belongs to the second group and is plotted with a red dot.

As previously described, the fact that both T and Z are different for each measurement does not allow to completely separate the two effects.

Z	T [MeV]	α^2	Ref.
16	2.7	0.022	[66]–[69]
18	2.8	0.022	[66]–[69]
22	2.5	0.033	[66]–[69]
30	2.5	0.043	[66]–[69]
13	3.3	0.017	[10]
13	3.4	0.032	[10]
13	4	0.061	[10]
14	3.4	0.032	[10]
14	3.1	0.047	[10]
40	2.1	0.050	[54]

Tab. 7.3: A list of the existing data about isospin mixing. Z is the number of the protons, T is the nuclear temperature and α^2 is the isospin mixing probability. The data are from [10], [54], [66]–[69].

There are not measurements of the isospin mixing probability for the same system changing one parameter at time. For this reason, the present experiment intends to measure the temperature dependence of isospin mixing in ^{80}Zr in the same condition as those measured in [54]. The possibility to explore $Z > 40$ is currently limited by the technical difficulties involved in the production of nuclei close to the proton drip line.

7.5.1. Isospin mixing in ^{80}Zr

The experiment, that is described in this part of the thesis, aims to measure the isospin mixing probability in ^{80}Zr at T=2.4 MeV. The data for the same system at different temperature ($T = 3\ MeV$) have been already analyzed and the results are reported in [54] and in Tab. 7.4.

T [MeV]	$\Gamma_c^{\downarrow}$ [keV]	α^2	$\langle J \rangle$
2.1	10	0.05 ± 0.01	38

Tab. 7.4: The results found for the isospin mixing probability of 80Zr [54]. Z is the number of the protons, T is the nuclear temperature, $\Gamma_c^{\downarrow}$ is the Coulomb spreading width, α^2 is the isospin mixing probability and $\langle J \rangle$ is the average angular momentum.

The ^{80}Zr was populated in a state of $I = 0$ using the ^{40}Ca +^{40}Ca fusion-evaporation reaction (isospin in entrance channel equal to zero), this compound nucleus could decays only in state with $I = 1$ due to the selection rules in section 7.4. The number of states with $I = 1$ are smaller than those with $I = 0$ as consequence there will be an inhibition of the GDR decay. It is important to point out that this description is true only for the first step of the GDR decay, because when the nucleus emits protons or neutrons the isospin of the daughter nucleus is not anymore equal to zero.

From the value of the isospin mixing probability at $T = 2.4$ MeV and from the value at $T = 3$ MeV [54], [65] it will be possible to obtain the value at zero temperature following the theoretical approach of [64]. In Fig. 7.7 the trend of the isospin mixing probability as a function of T for ^{80}Zr is represented.

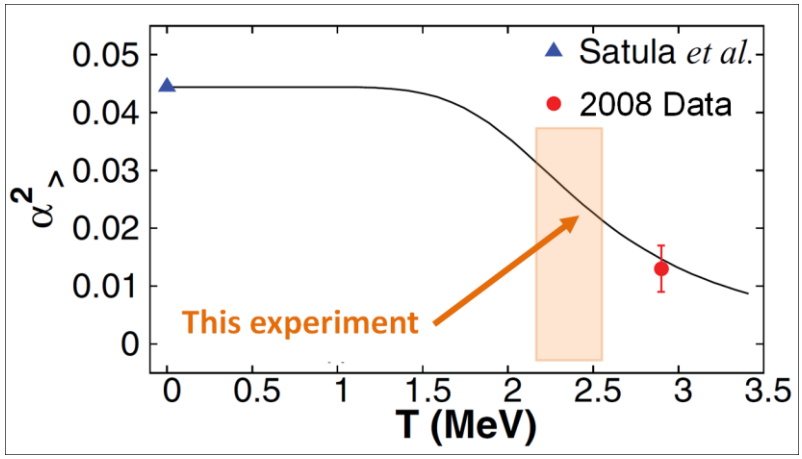

Fig. 7.7: The trend of the isospin mixing probability as a function of T. The blue triangle is the value of the isospin mixing at $T = 0\ MeV$ obtained in [9]. The red point is the value obtained from the experimental data at $T = 3\ MeV$ reported in [54]. The orange region to be studied in this thesis.

8. Experimental set up for the isospin mixing experiment

The experiment was performed in May 2011 in Laboratiori Nazionali di Legnaro. During this experiment, two reactions were studied, the principal characteristics of these reactions are shown in Tab. 8.1.

Projectile	Target	CN	E_{beam} [MeV]	σ [mb]	E^* [MeV]	I_z
^{37}Cl	^{44}Ca	^{81}Rb	95	338.1	54	7/2
^{40}Ca	^{40}Ca	^{80}Zr	136	548.2	54	0

Tab. 8.1: Principal characteristics of the reactions. σ is the reaction cross section, E^* is the CN excitation energy, while I_z is the projection of isospin operator.

The beams of ^{37}Cl and of ^{40}Ca were produced by TANDEM accelerator of Legnaro. The beam current was 3.5 pnA for the ^{40}Ca and 3 pnA for the ^{37}Cl. The data taking was of ~110 h for the ^{40}Ca + ^{40}Ca reaction and ~70 h for the ^{37}Cl + ^{44}Ca reaction.

Moreover, eight hours of calibration beam of ^{11}B to produce high energy γ rays of 15.1 MeV were performed. The reaction was ^{11}B +D, the beam energy was 45 MeV, but was reduce to 19 MeV with a gold degrader to populate a (n,γ) reaction.

The experimental set up used during this experiment is the AGATA (Advanced GAmma Tracking Array) Demonstrator coupled to the HECTOR+ array, shown Fig. 8.1. The AGATA Demonstrator [70], consists of 5 triple cluster of segmented HPGe detectors (during the experiment only 4 triple clusters were available). The HECTOR+ array consists of seven large volume LaBr3:Ce scintillation detectors (6 of them are 3.5″ x 8″ and one is 3″ x 3″).

Fig. 8.1: A picture of the experimental set-up, in the middle there are 4 AGATA triple clusters surrounding by 6 large volume $LaBr_3$:Ce detectors.

To extract physical information, it is necessary to have an experimental set up that is able to identify the evaporation residues, to measure high-energy gamma rays and the CN temperature. In the previous experiment, which measured isospin mixing in ^{80}Zr at higher temperature, the experimental set up was composed by an array of large volume BaF_2 scintillators, called HECTOR, to measure the high-energy gamma rays of the GDR decay; the GARFIELD array (see section 3.3) to measure the light charged particles; an array of phoswich detectors to select a fusion-evaporation reaction, by measuring the evaporation residues. From the measurement of the emitted LCPs it is possible to check if the temperature of the two compound nuclei is the same. For more details, on the GARFIELD-HECTOR apparatus, see chapter 3.

In the experiment discussed in this thesis, the evaporation residues were identified by the low-energy gamma rays, thank to the good energy resolution of the AGATA Demonstrator. The high-energy gamma rays from the GDR decay were measured by HECTOR$^+$ array. The use of $LaBr_3$:Ce scintillators, instead of BaF_2 scintillators, provides a better energy resolution and the possibility to identify the evaporation residues also with HECTOR$^+$ array. With this set up, however, it is not possible to measure the temperature of the compound nuclei, but that is not necessary because it was already verified that the ^{80}Zr and ^{81}Rb nuclei are produced at the same temperature in the previous experiment.

In this chapter, the main features of the AGATA Demonstrator (section 8.1) and HECTOR$^+$ (section 8.2) arrays will be described, as well as the data acquisition (section 8.3) and the trigger for the experiment (section 8.4).

8.1. The AGATA Demonstrator

AGATA is a project, within an European collaboration, aimed at developing, building and employing a 4π gamma-ray tracking array for nuclear spectroscopy. The principle of gamma-ray tracking is to reconstruct the sequence of interactions of each gamma-ray inside the array, in order to achieve a good suppression of the Compton background and a high efficiency, overcoming the limits of Compton-suppressed HPGe arrays.

The present phase of the AGATA project is the so called AGATA Demonstrator, an array composed by 15 HPGe detectors, divided in 36 segments, organized in 5 triple-clusters. The Demonstrator has been employed from the beginning of 2009 to the end of 2011 in an experimental campaign at Legnaro National Laboratories.

At the time of our experiment, however, one of the triple-clusters was not yet available, therefore we had to perform the measurement with only 4 triple-clusters, for a total of 12 HPGe detectors.

More details on AGATA project can be found for example in [70], [71].

8.2. The HECTOR+ array

$LaBr_3$:Ce detectors are the best scintillators for γ rays detection and spectroscopy, providing energy resolution of 2.7-3.3% at 662keV, a time resolution better than 1 ns, they have a good efficiency due to the density of 5.1 g/cm^3. Moreover, pulse shape analysis techniques allow to discriminate between alpha and gamma-rays [14]. In Tab. 8.2, the properties of this scintillator are compared with the properties of the most common scintillators used in nuclear physics. The energy spectra obtained using a ^{60}Co source from different scintillators are compared and shown in Fig. 8.2.

Detector	Light Yield [10^3 photon/MeV]	Decay Time [ns]	Density [g/cm^3]
NaI:Tl	38	250	3.67
$LaCl_3$:Ce	49	28	3.85
$LaBr_3$:Ce	63	16	5.08
BaF_2	1.8	0.7	4.88
BGO	9	300	7.13

Tab. 8.2: Properties of the scintillator detectors used in nuclear physics. The light yield is correlated with the energy resolution, the decay time with the time resolution and the density with the efficiency.

The $LaBr_3$:Ce crystal is characterized by an internal activity. The internal activity of the $LaBr_3$:Ce crystal is due to the presence of an unstable isotope, ^{138}La, and the contamination with the ^{227}Ac element, chemical homologue of lanthanum.

Fig. 8.3 displays a self-activity spectrum of a $LaBr_3$:Ce detector [12]. The peak at 1460 keV was found to have a structure. This peak, in fact, consists of a superposition of the two components, the centroids of the two structure are at ~1440 and ~1470 keV, respectively. The difference is approximately equal to the energy of the X-ray of ^{138}Ba (32 keV) which is not always detected with the 1436 keV γ-ray of ^{138}Ba. The structure superimposed over the β continuum, observed in the 800–1000 keV energy range is produced by the sum of the 789 γ-ray and a the associated

continuum β^- decay of ^{138}La. At higher energy, between 1600 and 2800 keV, one can observe a more complex structure which is due to the α emission from ^{227}Th, ^{223}Ra, ^{219}Rn, ^{215}Po, and ^{211}Bi populated by the ^{227}Ac α decay chain.

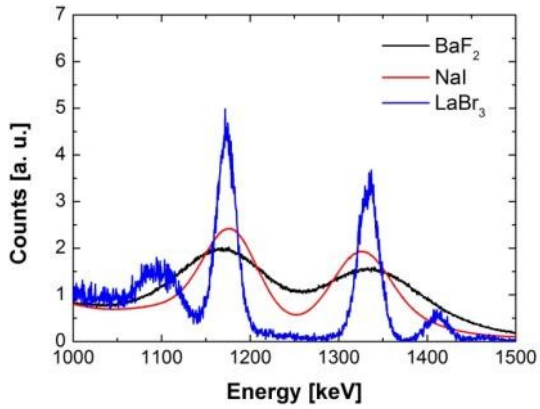

Fig. 8.2:The comparison between the energy spectra obtained with three different scintillator detectors. It is possible to see that the two peaks of the ^{60}Co source are completely solved only by the LaBr$_3$:Ce detector.

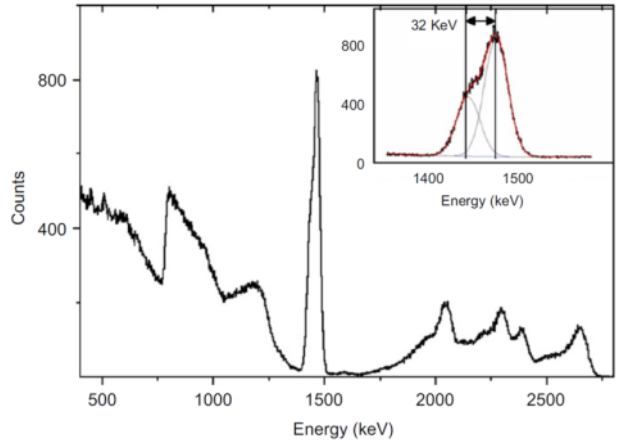

Fig. 8.3: The internal activity of a LaBr$_3$:Ce detector. The events with energy smaller than 1.5MeV are mainly due to the decay of ^{138}La while the structure between 1.5 and 3 MeV is produced by the decay chain of ^{227}Ac. In the inset, the peak structure centered around 1460 keV is shown together with the result of a fit procedure. There are two peaks centered at ~1440 *and* ~1470 *keV [12].*

The energy resolution and the efficiency are a crucial factors in case of high-energy γ-rays measurement. The possibility to have crystal volume larger than 1000 cm^3 offers a valid alternative to the HPGe detectors; $LaBr_3$:Ce detectors are a good compromise between efficiency, energy resolution and time resolution. Lanthanum bromide detectors allow clear separation of the full energy from the first escape peak up to 25-30 MeV (which was previously possible only with HPGe detectors). For this reason, they are particular suited for measurements of the Giant resonances that are characterized by the emission of high-energy γ rays.

Large volume crystals are also available only from few years. An array of 10 $LaBr_3$:Ce scintillators with a size of 3.5″ x 8″ was built in Milano, called HECTOR+. These crystals are the largest produced till now. The measure of the isospin mixing in ^{80}Zr is the first experiment performed with the HECTOR+ array. This means that this experiment could be used as a commission to study the performances of these detectors in beam experiment. A measured high-energy monochromatic γ-ray spectra acquired with one of the crystal of the array HECTOR+ is shown in Fig. 8.4, it is possible to see the full energy peak and the first escape peak clearly resolved.

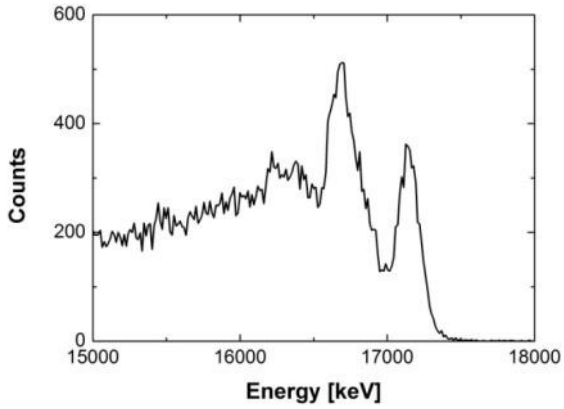

Fig. 8.4: The gamma spectrum of the reaction $^{11}B(p,\gamma)^{12}C$ at 17.6 MeV. It is possible to see the clear separation between the full energy peak and the first escape peak.

8.3. Data acquisition system

The HECTOR+ data were acquired by an independent data acquisition system run on a KMAX environment [72]. The AGATA data were acquired by NARVAL data acquisition system. The two system communicate via TCP/IP.

A data acquisition system for the HECTOR+ array based on VME standard modules was designed for test setup and for small and medium size nuclear physics experiments. The system is composed of a VME crate housing different kind of front-end modules (in our case TDC and ADC) and of a personal computer physically connected to the hardware by means of a gigabit PCI to VME interface optical fiber. VME transactions are handled by a DSP server sequencer that collects data from front-end modules and organizes them in formatted buffers that are read by a complete application based on a KMAX environment. Diagnostic functions and error report messages are also available to detect hardware failures or incorrect setting for the used modules. Integration in a more complex data acquisition system, for example in our case with NARVAL acquisition, was already performed in several experiments performed in different laboratories. The data from the HECTOR+ array were insert in the NARVAL acquisition of AGATA and there are synchronized by AGAVA (AGATA Ancillary VME Adapter) module.

As discussed above, the AGATA data are acquired by NARVAL acquisition. The pulses of each of the 36 segments of each crystal of the AGATA Demonstrator is digitised with a frequency 100 MHz. For every accepted event, a pulse trace of 60 samples (600 ns) is extracted and acquired. With a counting rate of 50 kHz/crystal the dataflow for each detector is therefore of the order of 100 MB/s (with zero suppression). Furthermore, in order to have an online analysis, the PSA has to be performed in real time for each of the acquired traces, and tracking algorithms must reconstruct the detected gamma-rays from the PSA information.

This means that the DAQ software for AGATA has to be able to handle large quantities of data, control a computing farm for the PSA and

tracking algorithms, and coordinate the flow of information between the digitizers, the computing farm, and the disk server where all the data are written. All of this is performed by a NARVAL-based DAQ software [73].

In NARVAL, each task is performed by an actor, associated to a process running on a Linux machine. There are 3 types of actors:

- producer: they interface with the hardware and read out the data
- intermediary: they perform operations on the data, receiving input and sending output from/to one or more other actors
- consumer: they can only receive input from the other actors, and store the data to disk or act as histogrammers

From the point of view of NARVAL, each AGATA crystal is considered as a separate entity and the whole detector may be considered as the aggregation of synchronized data supplied by the individual crystals. The synchronization is guaranteed by the AGATA Global Trigger and Synchronization (GTS) hardware with a common 100 MHz digital clock.

For each AGATA detector there is a producer actor reading the pulse traces from the front-end electronics; the traces are sent (together with the timestamp information) to an intermediary that performs the PSA and to a consumer that writes them to disk; the PSA data from all detectors are sent to an intermediary that acts as event builder, matching the data from different detectors through the timestamp information.

For the HECTOR$^+$ array, there is a producer actor that receives the data from the KMAX acquisition, kept synchronized to the GTS via the AGAVA module. The producer sends the VME data to a consumer that writes them to disk and to an intermediary that decodes the VME words and sends only the actual data words to the event builder, discarding VME header and trailer words. The builder then matches the ancillary data to the AGATA data and sends the event to another intermediary that performs the online tracking.

8.4. Triggers and acquired events

In this experiment, a standard NIM electronic was used to built, the energy and the time chain of the HECTOR+ detectors and the Master Gate signal. A scheme of the Master Gate is shown in Fig. 8.5, it is the OR logic signal of 4 conditions:

- Coincidence between AGATA & HECTOR+
- HECTOR+ gamma multiplicity equal or larger than 2 ($M_\gamma \geq 2$)
- AGATA singles scaled down
- HECTOR+ singles scaled down

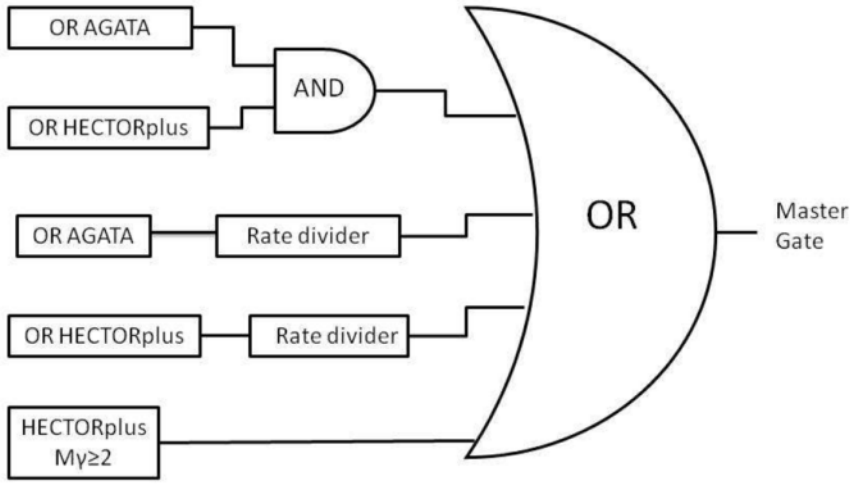

Fig. 8.5: Scheme of the triggers. The logic signal, the single or the coincidences, coming from the detectors and were sent to the trigger system.

The logic signal "OR AGATA" was obtained by using the signal of NIM Constant Fraction Discriminator (CFD) of the AGATA Demonstrator. The logic signal "OR HECTOR+" is given directly by the CFD of the BaFpro module [74]. The logic multiplicity signal was produced by a multiplicity module that sum the CDF outputs of the $LaBr_3$:Ce detectors. To identify the 4 event classes 4 TDC channels were used as marker of the acquired event.

These markers allow to know what it is the activated trigger during that event and to select different type of events in the sorting code.

In Tab. 8.3 there are the events acquired for the different triggers for the two reaction studied in this experiment. The total of the event is larger than the 100% because one event could be triggered by two different triggers.

^{40}Ca + ^{40}Ca **N. of events: 8.9 10^8**		**^{37}Cl + ^{44}Ca** **N. of events: 9.5 10^8**	
Trigger	Events [%]	Trigger	Events [%]
AGATA & $LaBr_3$:Ce	85%	AGATA & $LaBr_3$:Ce	83%
$LaBr_3$:Ce $M_\gamma \geq 2$	20%	$LaBr_3$:Ce $M_\gamma \geq 2$	22%
AGATA single	4%	AGATA single	5%
$LaBr_3$:Ce single	2%	$LaBr_3$:Ce single	2%

Tab. 8.3: Number of the events in percent for the different triggers. The single were scaled down.

To better understand the different type of events, some conditions in the sorting code were inserted to complete the information obtained from the electronic trigger conditions. In the sorting code the triggers were redefined as:

- *Software trigger AGATA & $LaBr_3$:Ce*: the marker AGATA and $LaBr_3$:Ce has to be > 0, there has to be at least a γ ray in AGATA with an energy signal in the range of 50-24000 keV and time signal in the range of 500-3000 ns, there has to be at least a γ ray in HECTOR$^+$ with an energy signal in the range of 200-24000 keV and time signal in the range of 2-490 ns;
- *Software trigger $LaBr_3$:Ce $M_\gamma \geq 2$*: the marker $LaBr_3$:Ce $M_\gamma \geq 2$ has to be > 0, there has to be at least 2 γ rays in HECTOR$^+$ with an energy signal in the range of 200-24000 keV and time signal in the range of 2-490 ns, there has not to be events in AGATA;
- *Software trigger $LaBr_3$:Ce single*: the marker $LaBr_3$:Ce single has to be > 0;

- *Software Trigger AGATA single*: the marker AGATA single has to be > 0.

In the sorting code, four types of "event" was defined. Two of these type have a physical meaning and these types are used for the data analysis, while the other two are the single of the detectors.

- *AGATA event*: in this type of event the trigger *AGATA & $LaBr_3$:Ce* was on, the ToF was selected and the singles were rejected. To do this in the sorting code the following condition were used: there were the trigger *AGATA & $LaBr_3$:Ce*, there has to be at least a γ ray in AGATA with an energy signal in the range of 50-24000 keV and time signal in the range of 1600-1900 ns and at least a γ ray in HECTOR+ with an energy signal in the range of 50-24000 keV and time signal in the range of 2-490 ns, the marker AGATA single has to be $= 0$.
- *$LaBr_3$:Ce event*: in this type of event the trigger *$LaBr_3$:Ce* $M_\gamma \geq 2$ was on and the singles were rejected. To do this, in the sorting code the following condition were used: the trigger *$LaBr_3$:Ce* $M_\gamma \geq 2$ was on, the marker $LaBr_3$:Ce single has to be $= 0$. There has to be at least two γ ray in HECTOR+ with an energy signal in the range of 50-24000 keV and time signal in the range of 2-490 ns
- *$LaBr_3$:Ce single event*: in this type of event the trigger *$LaBr_3$:Ce single* was on.
- *AGATA single event*: in this type of event the trigger *AGATA single* was on.

In Tab. 8.4 there are the events acquired for the different events defined in the sorting code for the two reaction studied in this experiment, it is important to point out that the single were scaled.

^{40}Ca + ^{40}Ca **N. of events: 7.3 10^8**		**^{37}Cl + ^{44}Ca** **N. of events: 7.5 10^8**	
Event	Events [%]	Event	Events [%]
AGATA	81%	AGATA	76%
$LaBr_3$:Ce	11%	$LaBr_3$:Ce	12%
AGATA single	1.8%	AGATA single	1.8%
$LaBr_3$:Ce single	4.3%	$LaBr_3$:Ce single	5%

Tab. 8.4: Number of the events in percent for the different events defined in the sorting code.

9. Preliminary data analysis of the isospin mixing experiment

In this chapter the first steps of the analysis of the isospin mixing experiment will be described. The aim of this process is to select high-energy γ-rays emitted by a hot ^{80}Zr CN formed in a complete fusion reaction, which come mostly from the γ decay of the GDR.

The GDR decay is going to be used in later analysis to extract a measure of the isospin mixing probability in ^{80}Zr, but in the scope of this thesis its study is useful to compare the performances of the HECTOR$^+$ and AGATA demonstrator arrays.

In order to measure the isospin mixing probability we need to compare the GDR γ decay in ^{40}Ca + ^{40}Ca and ^{37}Cl + ^{44}Ca reactions. Unfortunately the γ decay from the GDR has a branching ratio of approximately 0.1% if compared to neutron proton decay. Neutrons interacting with γ detectors create a spurious increase of counts in the 8-10 MeV energy region which can compromise the physical interpretation of the spectra. For this reason, neutron emission has to be identified and rejected.

Typically, neutrons are identified by the ToF information, therefore it is necessary to have a good time resolution to separate them from the prompt γ peak. This means that if neutron emitting channels are populated it is not possible to use the AGATA demonstrator data at high energy, due to its bad time resolution (~ 25 ns). However, the good energy resolution of the AGATA Demonstrator make it possible to identify all reaction channels where only protons are emitted, removing the need of ToF identification.

As will be shown in sections 9.4 and 9.5, the ^{40}Ca + ^{40}Ca reaction only populated proton and alpha particle emitting channels, therefore the full efficiency of the AGATA Demonstrator plus HECTOR$^+$ set up can be exploited. In case of the ^{37}Cl + ^{44}Ca reaction, however, all dominant channels are neutron emitting, and only $LaBr_3$:Ce data can be used for the GDR analysis.

The data analysis was focused up to now on 1) the detector calibrations (section 9.1), 2) Doppler correction (section 9.1), 3) evaporation residues identification (section 9.2) and 4) the extraction of low-energy ($E_\gamma \leq 2$ MeV) and high energy ($E_\gamma \geq 4$ MeV) γ-rays spectra (sections 9.3, 9.4, 9.5 and 9.6) with different conditions for the two arrays (AGATA Demonstrator and HECTOR+).

9.1. Detector Calibration and Doppler correction

The energy calibration of the detectors (AGATA and HECTOR+) was done in low energy range (100-2000 keV) before and after the experiment with standard γ sources (^{60}Co, ^{137}Cs, ^{133}Ba, ^{88}Y and ^{152}Eu). The calibration in high-energy range was performed by a composite AmBe(Fe) source and with ^{11}B + D reaction that produce 15.1 MeV γ rays.

Time calibration was performed using the different arrival time of the detectors signal. The TDCs were calibrated using a pulse generator and some known delay cables.

The evaporation residues produced in our experiment, have a $\beta = v/c$ that is about 4%, for this reason, as the detectors were positioned at angles different than 90°, a Doppler correction is necessary to have the true value of the energy of the low energy transition of the evaporation residues.

9.1.1. AGATA Demonstrator calibration

The spectroscopic performance of the AGATA array is based on the principles of pulse-shape analysis (PSA) and γ-ray tracking. During the experiment, these operations are performed in real time on a subset of the data by the NARVAL Acquisition system (see also section 8.3), but they also can be performed again after the experiment with a C++ emulator of NARVAL.

The acquisition writes to disk a list-mode file for each detector, containing for each event the digitized pulse signals from the segments and the timestamp information. The emulator mimics the data taking processing

all the files, performing the PSA and the time matching of the data from different crystals, as well as the time matching between AGATA and ancillary data. This procedure is called "replay", because from the point of view of the data processing it is essentially a repetition of the experiment.

The replay was performed in two steps: in the first one, the Pulse Shape Analysis (PSA) was performed for all AGATA detectors, and data with energy, position, and time information for all the segments were saved to disk. In the second step, the data from all the segments were merged and the tracking was performed. The advantage to perform two different steps lays in the fact that the PSA is a very slow process, taking up a large amount of computing power and memory: it took about 1 week to perform the first step with 6 computers working in parallel. The tracking, instead, is a much faster task and could be repeated several times to optimize the parameters, without having to perform the PSA again.

After PSA and tracking processes are completed, the process provides a list-mode file in ROOT tree format (see [37] for more information on ROOT). For each event, the file contains the list of reconstructed gammas, together with their energy, timestamp information and the position of the first interaction, as well as the data of the ancillary detectors received from the VME crate spectra. A sorting code was developed by R. Nicolini and modified to be adapted to our experiment.

9.1.1.1. Time Calibration

Each γ-ray reconstructed by the tracking algorithm is associated to a timestamp, which measures the absolute time from the start of the GTS clock in steps of 10 ns. A more precise information is given by the PSA, that uses a linear interpolation algorithm to determine the start time of the signal. The sum of these two values gives the detection time of the gamma relative to the start time of the GTS.

To have a measurement of the time between an event in AGATA and an event in HECTOR$^+$ it is necessary to compare the AGATA time information (from the timestamp) with the time information provided by AGAVA and processed by the GTS. To achieve the precision required for fast scintillators it is necessary to add to AGATA timestamp the so-called

"phase shift", which is acquired by one channel of the TDCs and measures when the VME master gate was opened relatively to the GTS clock. In simple words the phase shift is the time difference between the clock of the trigger timestamp (10 ns) an the real arrival time of the trigger measured with a precision of 0.1 ns. A schematic view of the trigger signal and the GTS clock is shown in Fig. 9.1, the AGATA phase shift is enlighten in red.

The AGATA time relative to the trigger time was therefore built as:

$$t_{gamma} = T_{AGATA} + T_{PSA} - T_{AGAVA} - T_{phaseshift} \qquad (9.1)$$

where T_{AGATA} and T_{AGAVA} are the timestamps for the gamma and for the ancillary branch of the acquisition system.

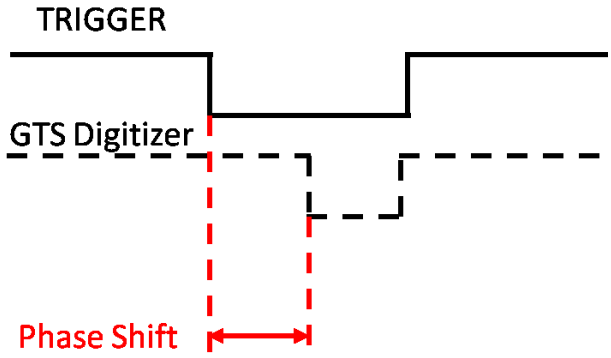

Fig. 9.1: A schematic view of the AGATA phase-shift.

In Fig. 9.2 the time spectra of AGATA and $LaBr_3$:Ce detectors for the two reaction are shown without conditions. Different peaks are associated to different triggers (as shown in Fig. 9.3). The most intense peak is associated to the trigger *AGATA & LaBr3:Ce* and has a FWHM of $\sim 25\ ns$. The second most intense peak is associated to the trigger *AGATA single* and it has a FWHM of $\sim 21\ ns$. This difference become more clear in Fig. 9.3, in which the time spectra of AGATA with different trigger conditions are shown. It is evident that the time resolution is characterized by the HPGe AGATA detectors. AGATA detectors were not aligned but this is a minor correction that does not change the overall resolution.

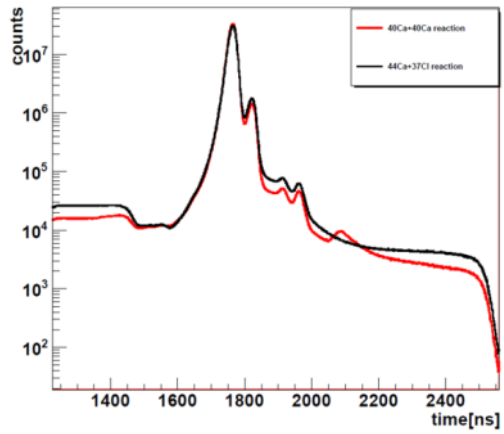

Fig. 9.2: The time spectra of AGATA without conditions in the sorting code. The red line is for the ^{40}Ca + ^{40}Ca reaction, while the black line is for the ^{37}Cl + ^{44}Ca reaction.

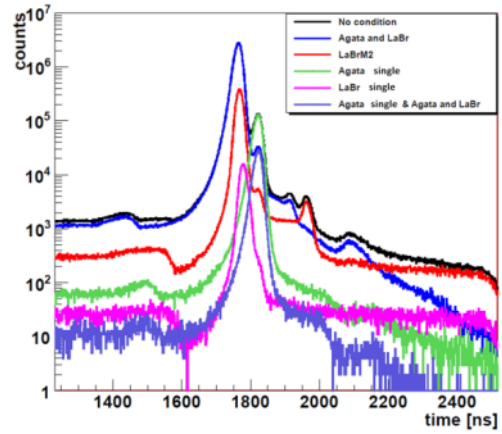

Fig. 9.3: The time spectra of the AGATA detectors for the ^{40}Ca +^{40}Ca reaction with different trigger conditions.

It is important to point out that the time resolution of AGATA, that is about 25 ns, is not enough to discriminate a γ from a neutron using the ToF technique. The neutrons emitted in this kind of reaction (fusion-evaporation reactions) has an energy of about 2-3 MeV, and for this reason, the time difference between γ rays and neutrons is expected to be about 10 ns.

9.1.1.2. Energy Calibration and Doppler correction

The energy calibration of the AGATA detectors was performed together with the PSA. The calibration coefficients for each segment of the 12 detectors, as well as for the core signals, were calculated using data from ^{60}Co (1173 keV and 1332 keV) calibration run, performed at the beginning of the experiment and verified with the γ transitions measured during the experiment.

The γ radiation, measured in the experiment, was emitted in flight by the residues nuclei, moving with respect to the laboratory system. The γ-ray energy is not the same in the laboratory system and in the center of mass system, from the special relativity it is possible to connect the measured energy at the energy in the center of mass system, as follows:

$$E_{\gamma 0} = E_{\gamma} \frac{(1 - \beta cos\theta)}{\sqrt{1 - \beta^2}} \qquad (9.2)$$

where $E_{\gamma 0}$ is the γ-ray energy in the center of mass system, E_{γ} is the detected γ-ray energy in the laboratory system, $\beta = v/c$ and θ is the angle between the direction of motion and the emitted γ ray. Using equation 9.2 a recalibration of the experimental data was perform to obtain the measured γ-ray energy in the center of mass system.

It is important to take into account that the uncertainty on the angle ($\Delta\theta$) introduce an uncertainty on the value of the γ-ray energy in the center of mass system, called Doppler broadening [75]:

$$\Delta E = 2E_{\gamma 0}\beta sen\theta sen\Delta\theta. \qquad (9.3)$$

However PSA allows to achieve a ~5 mm precision on the position of the interaction, therefore reducing the Doppler broadening.

As a first step, it is necessary to identify the correct value of the β parameter. Since a great precision is required for β parameter, a value of β with an uncertain smaller than 1% cannot calculated from the reaction kinematics only but must directly extracted from data. A code that spans a range of different values of β was used to find the one that maximizes the peak intensity and better reproduces the tabulated value of the γ-ray energy. This procedure was done only for the most populated residues nuclei for the

two reactions (see section 9.2 for the population of the evaporation residues), that are ^{76}Kr (for ^{40}Ca + ^{40}Ca) and ^{78}Kr (for ^{37}Cl + ^{44}Ca).

In Tab. 9.1, the values of β obtained from the code are shown. These values are slightly smaller than the expected value, due to the fact that in theoretical calculation, performed to find the $\beta_{expcted}$ value, the energy loss in the target was not included.

Reactions	$\boldsymbol{\beta_{expcted}}$	$\boldsymbol{\beta_{simulation}}$
^{40}Ca + ^{40}Ca	0.042	0.038
^{37}Cl + ^{44}Ca	0.035	0.028
^{11}B + D	0.050	0.046

Tab. 9.1: Comparison between theoretical values of β ($\beta_{expected}$) and the same values obtained from the code $\beta_{simulation}$. This values maximize the peak intensity and they are the values of β that better reproduced the expected value of the γ-rays energy.

Fig. 9.4 shows the energy spectra of the ^{11}B +D reaction before and after the Doppler correction.

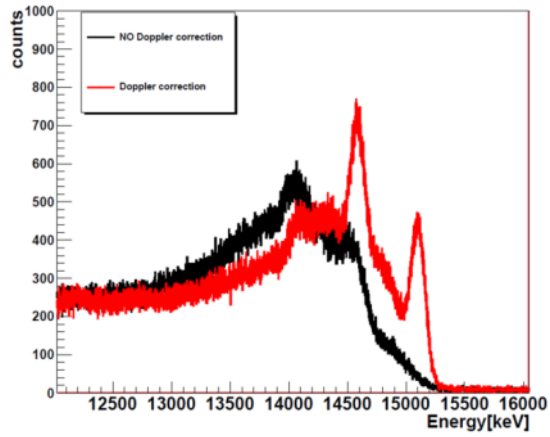

Fig. 9.4: The energy spectra at 15.1 MeV before (black line) and after the Doppler correction (red line).

After the Doppler correction, it is possible to extract the energy resolution (for the two reaction) and the linearity of the AGATA Demonstrator up to 15 MeV, that the detectors providing during the data

taking. The AGATA energy resolution trend for the two reactions is shown in Fig. 9.5. The linearity of AGATA Demonstrator (defined as $|E_{meas} - E_{true}|/E_{true}$ where E_{true} is the tabulated value for the γ line and E_{meas} is the measured value after the Doppler correction) is shown in Fig. 9.6. As can be observed in the plots the resolution is the order of 6 keV at 1 MeV and the linearity is below the 0.2% up to 15.1 MeV.

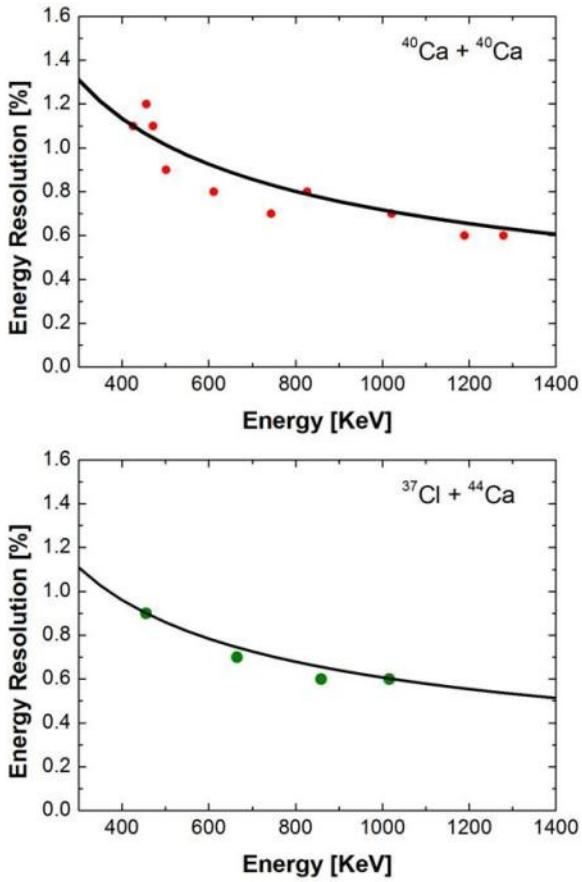

Fig. 9.5: The energy resolution of the AGATA Demonstrator for the two reaction (top panel ^{40}Ca + ^{40}Ca, bottom panel ^{37}Cl + ^{44}Ca) is shown. The black line represents the energy resolution trend ($FWHM/E \propto 1/\sqrt{E}$). In the top panel the points that are not exactly on the curve are the γ lines from the residues ^{74}Kr and ^{77}Rb; the optimization of β parameter was done only for the residue ^{76}Kr.

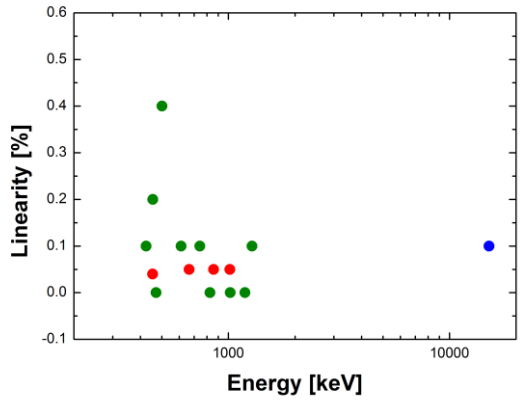

Fig. 9.6: The linearity of AGATA Demonstrator is shown. It is important to note the value at 15.1 MeV (the blue point).

9.1.2. HECTOR+ calibration

The aim of this section is to describe the calibration of the HECTOR+ array. In particular, in section 9.1.1.1 the time calibration will be presented, while in section 9.1.1.2 the energy calibration and the Doppler correction will be discussed.

9.1.2.1. Time Calibration

The same data analysis procedure described in the previous section was applied for *$LaBr_3$:Ce event*. The timing information was obtained from the CFD output of the BaFpro module, sent through a delay unit and then to the TDCs. During the experiment, a time signal was acquired for each $LaBr_3$:Ce crystal using a TDC. The TDCs worked in "common start" configuration, indeed all the TDCs have as start the master gate signal (described in section 8.4) and the stop is given by the CFD delayed signal of each detector. The time spectra are defined as the time difference between two events in HECTOR+ or one event in HECTOR+ and one event in AGATA (due to the definition of the event classes in section 8.4).

In Fig. 9.7 the $LaBr_3$:Ce time spectra are shown for the two reaction are shown without conditions. The different peaks were associated to different

triggers. The large structured peak was associated to the trigger *AGATA & LaBr3:Ce* and it has a FWHM of ~25 ns. The different peaks, between 75 and 80 ns, were associated to the trigger *LaBr3:Ce* $M_\gamma \geq 2$ and they have a FWHM of ~2 ns. The spike at 70 ns is the auto coincidence peak. The other structures were associated to the trigger *$LaBr_3$:Ce single* and *AGATA single*. The peaks associated to the different triggers are displayed in a clearer way in Fig. 9.8, in which the time spectra of $LaBr_3$:Ce detectors are shown with different trigger conditions.

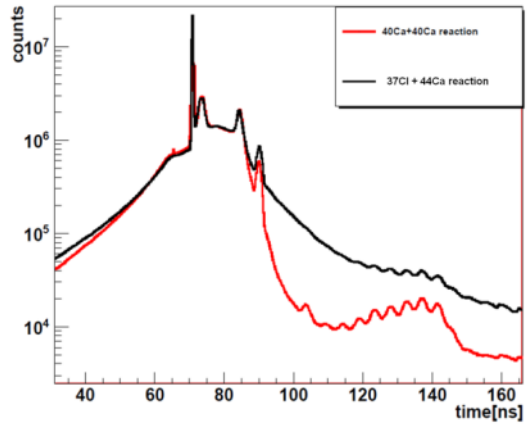

Fig. 9.7: The time spectra of one of $LaBr_3$:Ce detector without conditions in the sorting code. The red line is for the ^{40}Ca + ^{40}Ca reaction, while the black line is for the ^{37}Cl + ^{44}Ca reaction.

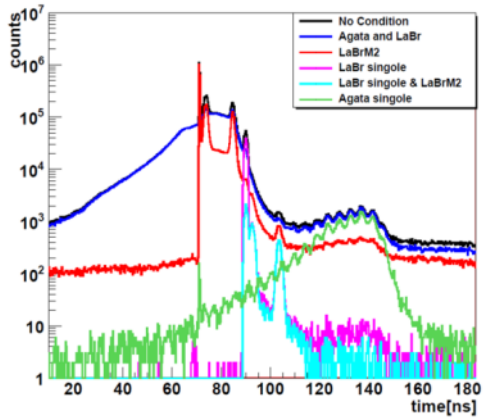

Fig. 9.8: The time spectra of one of the $LaBr_3$:Ce detectors for the ^{40}Ca +^{40}Ca reaction with different trigger conditions.

The spectra, in Fig. 9.9, are produced by selecting in the sorting code the *LaBr₃:Ce event* conditions, defined as in section 8.4 (in this type of event the trigger *LaBr₃:Ce* $M_\gamma \geq 2$ was on, the singles were rejected. In the sorting code the following condition were used: the trigger *LaBr₃:Ce* $M_\gamma \geq 2$ was on, the marker LaBr₃:Ce single has to be = 0). These time spectra were obtained by selecting one of the HECTOR⁺ detector in coincidence with another one. The peak, centered at 90 ns, has a time resolution of ~1.8 ns as shown in the right panel of Fig. 9.9 (that is a typical in beam $LaBr_3$:Ce time resolution produced using BaFpro module). There is also an evident background due to random coincidences. The background of the two reactions is different, in the $^{37}Cl + ^{44}Ca$ reaction is larger than in the $^{40}Ca + ^{40}Ca$ reaction. In the spectrum of $^{37}Cl + ^{44}Ca$ there is a second "bump" about 10 ns after the coincidence peak, that correspond to the neutrons peak.

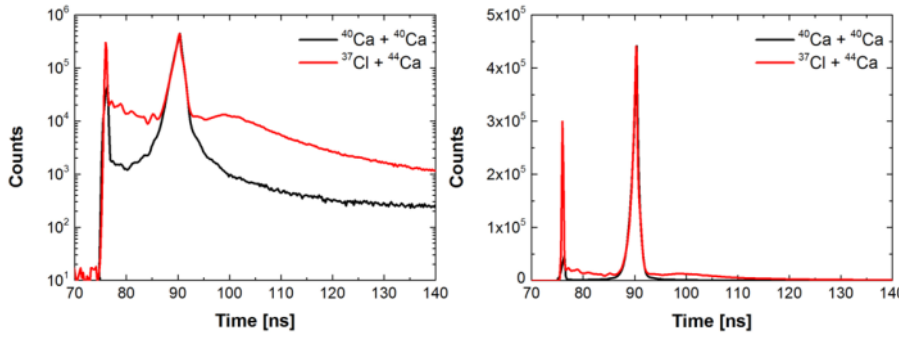

Fig. 9.9: The time spectra of one HECTOR⁺ detectors with respect to another one is shown. The black line is for the $^{40}Ca + ^{40}Ca$ reaction, while the red line is for the $^{37}Cl + ^{44}Ca$ reaction. In left panel in log scale to enhance the neutron peak in $^{37}Cl + ^{44}Ca$ and the background, in the right one in linear scale to enhance the good time resolution of $LaBr_3$:Ce detectors (FWHM ~ 1.8 ns).

In Fig. 9.10 the time spectra of one HECTOR⁺ detectors, in coincidence to AGATA Demonstrator are shown for the two reactions. The time peak is not symmetric due to the bad alignment of the AGATA crystals. In the preliminary part of the data analysis the crystals were not aligned, because of time resolution of the AGATA Demonstrator that is about 20 ns and alignment does not produce a significant improvement in time resolution, for the neutron rejection. As for Fig. 9.9, the background of the two reactions

is different: in the ^{37}Cl + ^{44}Ca reaction it is about 9 times larger than in the ^{40}Ca +^{40}Ca reaction.

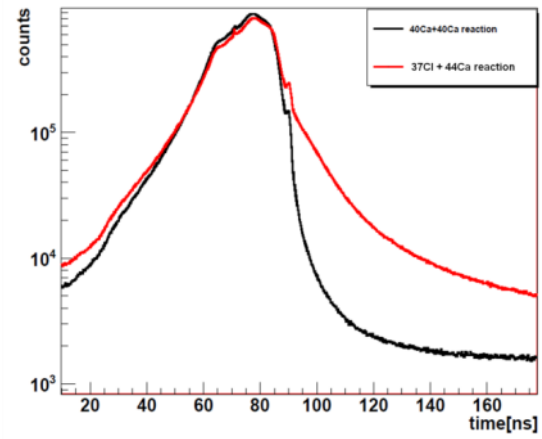

Fig. 9.10: The time spectra of one HECTOR+ detectors in coincidence to AGATA Demonstrator is shown. The black line is for the ^{40}Ca + ^{40}Ca reaction, while the red line is for the ^{37}Cl + ^{44}Ca reaction.

9.1.2.2. Energy Calibration and Doppler correction

$LaBr_3$:Ce were calibrated in energy with standard radioactive sources such as ^{60}Co, ^{137}Cs, ^{133}Ba and ^{88}Y before and after the experiment. Energy drifts were checked during all the experiment by using the internal activity peak (about 1460 keV) (see section 8.2). There were no energy drifts during the measurement. For this reason, from the different calibration runs, we have chosen those which were performed exactly after and before the data taking.

The Doppler correction of $LaBr_3$:Ce detectors was much more complicated than for the AGATA Demonstrator. There were a great uncertainty on the detector positions due to the size of the crystal and to the mechanical supports used in the experiment. Furthermore, it was not possible to exactly evaluate the distance of the detector from the target and their orientation with respect to the target. As consequence, the most intense gamma line, of the two reactions, was chosen; the angle (the detector position) was calculated in such a way that the Doppler-corrected energy corresponds to the tabulated value for that γ line. The used β was the same

that was calculated for the AGATA Demonstrator (see last column of the table Tab. 9.1).

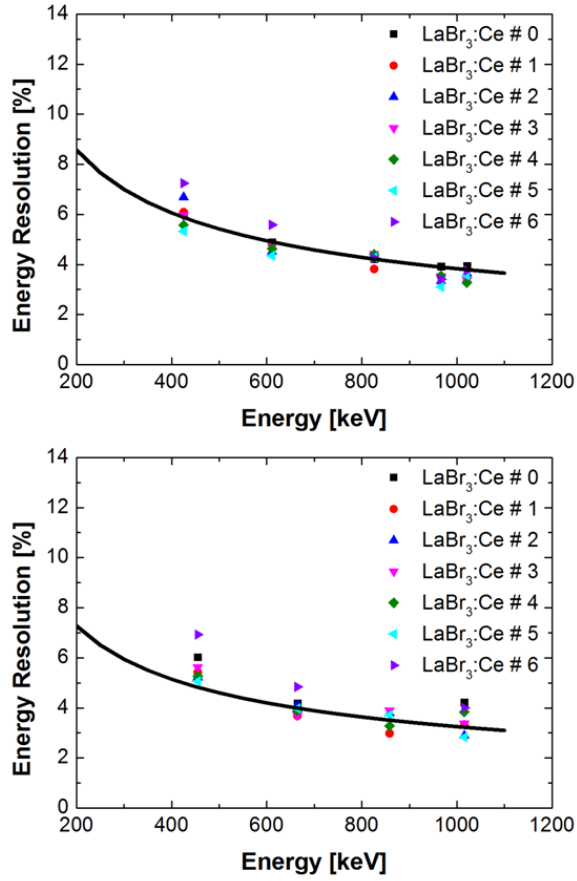

Fig. 9.11: The energy resolution of the $LaBr_3$:Ce detectors is shown (top panel ^{40}Ca + ^{40}Ca, bottom panel ^{37}Cl + ^{44}Ca). The black line represents the energy resolution trend ($FWHM/E \propto 1/\sqrt{E}$). The detector six has a worst energy resolution respect the others detectors.

After the Doppler correction, the energy resolution (for the two reaction) and the linearity of the $LaBr_3$:Ce detectors were evaluated and the results are shown in Fig. 9.11 and in Fig. 9.12. The FWHM was of a order of 40 keV at 1 MeV. The peaks in the ^{40}Ca+^{40}Ca reaction appear larger than in the ^{37}Cl + ^{44}Ca because a larger number of residues were populated and some γ transitions cannot be properly resolved with $LaBr_3$:Ce detectors. The

linearity is defined as $|E_{meas} - E_{true}|/E_{true}$ where E_{true} is the tabulated value for the γ line and E_{meas} is the measured value after the Doppler correction as shown in Fig. 9.12.

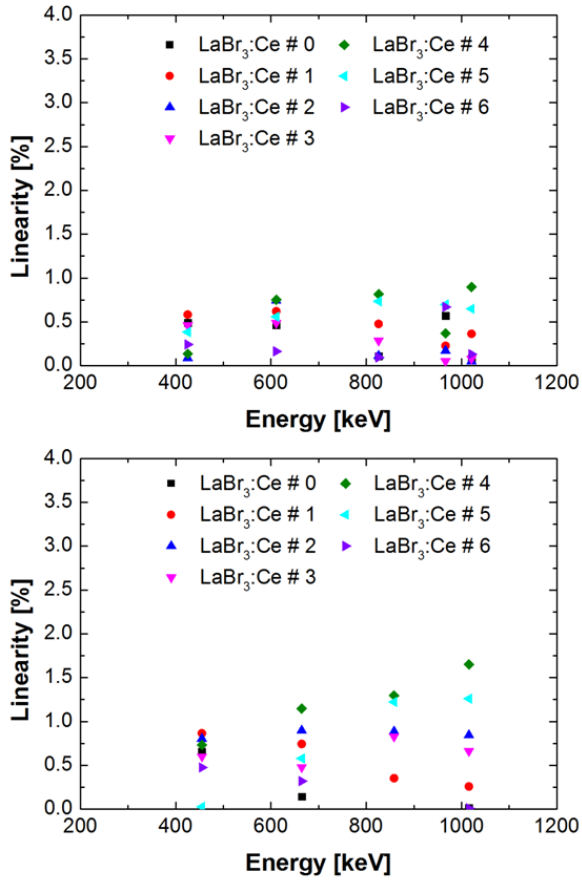

Fig. 9.12: The linearity of HECTOR+ array is shown (top panel $^{40}Ca + ^{40}Ca$, bottom panel $^{37}Cl + ^{44}Ca$).

After the Doppler correction procedure, the energy spectra of $LaBr_3$:Ce detectors were aligned. The aligned spectra were summed to have a spectrum, that will called *$LaBr_3$:Ce sum*. The energy resolution of the *$LaBr_3$:Ce sum* for the two reaction is shown in Fig. 9.13; as expected there is a little variation with respect to the energy resolution of the single detectors. The points also in this case generally follow the $FWHM/E \propto 1/\sqrt{E}$ trend. The differences in the energy resolution of the different evaporation residues γ

lines is due to the different β value (the different number of emitted particles could modify the velocity of the residual nucleus). The linearity of the *$LaBr_3$:Ce sum* is shown in Fig. 9.14. It is generally better than the one of the single detectors.

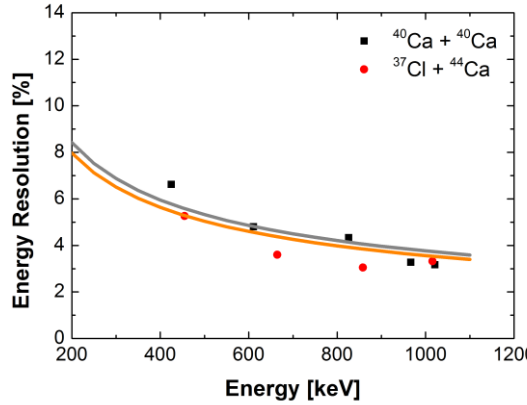

Fig. 9.13: The energy resolution of the $LaBr_3$:Ce is shown (^{40}Ca + ^{40}Ca black squares, ^{37}Cl + ^{44}Ca red points). The grey line (^{40}Ca + ^{40}Ca) and the orange (^{37}Ca + ^{44}Ca) represent the energy resolution trend ($FWHM/E \propto 1/\sqrt{E}$). The point are not exactly on the curves because they are obtained by the sum, and the curves are normalized on a specific γ line.

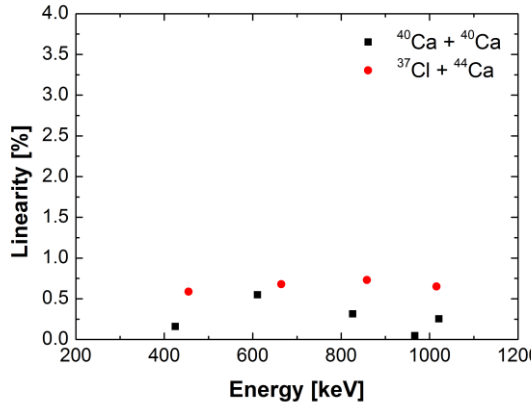

Fig. 9.14: The linearity of the $LaBr_3$:Ce sum is shown (^{40}Ca + ^{40}Ca black squares, ^{37}Cl + ^{44}Ca red points).

9.2. Identification of the evaporation residues

In the first stage of the statistical decay of the CN, when the excitation energy is larger than the nucleon separation energy, there is the particles evaporation process; as the excitation energy become smaller than the neutron separation energy γ emission is the only possible process to dissipate energy (see section 2.1). The evaporation residues are the nuclei that remains after the particles emissions. The particles emission probability and as consequence the evaporation residues population could be theoretical calculated by using DCASCADE code [44]. The theoretical calculation results are shown in Tab. 9.2 (^{37}Cl + ^{44}Ca reaction) and in Tab. 9.3 (^{40}Ca + ^{40}Ca reaction).

The evaporation residues population confirm the fact that, in the ^{40}Ca + ^{40}Ca reaction, neutron emitting channels are not populated. Theoretical calculations are consistent to the experimental data as shown in Fig. 9.9 in which the neutrons peak is present only for the ^{37}Cl + ^{44}Ca reaction.

Residue		**Z**	**N**	**Emitted particles**	**Population [%]**	**Strongest γ-line [keV]**
Even-even	^{78}Kr	36	42	1p, 2n	38.6	454.9
	^{74}Se	34	40	1α, 1p, 2n	4.5	634.6
Even-odd	^{77}Kr	36	41	1p, 3n	17.2	724.3
	^{75}Br	35	40	1α, 2n	8.6	518.0
	^{77}Br	35	42	1α	7.3	575.9
	^{75}Se	34	41	1α, 1p, 1n	6.1	76.8
Odd-odd	^{78}Rb	37	41	3n	8.3	773
	^{78}Br	35	43	2p, 1n	4.3	180.9

Tab. 9.2: The list of the evaporation residues populated in the ^{37}Cl +^{44}Ca reaction. Z is the number of protons and N the number of neutrons. In the column "Emitted particle", n stay for neutrons and p for protons and α for alpha particles. The decay of the ^{81}Rb nucleus was calculated by using DCASCADE code [44].

Residue		Z	N	Emitted particles	Population [%]	Strongest γ-line [keV]
Even-even	^{76}Kr	36	40	4p	33.2	423.9
	^{74}Kr	36	38	1α, 2p	17.2	455.6
	^{70}Se	34	36	2α, 2p	3.3	944.5
Even-odd	^{77}Rb	37	40	3p	19.1	146.9
	^{73}Br	35	38	1α, 3p	11.4	177.9
	^{77}Sr	38	39	2p,1n	2.9	186
Odd-odd	^{76}Rb	37	39	3p,1n	13.1	101.3

Tab. 9.3: The list of the evaporation residues populated in the ^{40}Ca +^{40}Ca reaction. Z is the number of protons and N the number of neutrons. In the column "Emitted particle", n stay for neutrons and p for protons and α for alpha particles. The decay of the ^{80}Zr nucleus was calculated by using DCASCADE code [44]

The evaporation residues decay is characterized by the emission of a low-energy γ rays. These low-energy γ lines were detected by the AGATA Demonstrator and by the HECTOR$^+$ array.

In Fig. 9.15, in Fig. 9.16, in Fig. 9.17 and in Fig. 9.18 the low-energy spectra for AGATA Demonstrator and the HECTOR$^+$ array are shown. In the AGATA γ spectra it is possible to have a clear separation from the lines of one of an evaporation residue to the lines of another one; instead in $LaBr_3$:Ce detectors the separation is less clear, and it is not possible to have a complete separation of the gamma rays from different residues, especially in the ^{40}Ca + ^{40}Ca reaction. For the ^{37}Cl + ^{44}Ca reaction, also in $LaBr_3$:Ce detectors there is a good separation between the low-energy γ lines (see Fig. 9.18), because only a residue, ^{78}Kr, was populated with a great intensity.

To check that the measured γ-rays emitted from the evaporation residues are populated as predicted from the theoretical model, the spectra of the AGATA Demonstrator are weighted with the efficiency curve, for both reactions. The efficiency curve was calculated by using a calibration run in which a ^{152}Eu source was used. The comparison of the evaporation residues population between the theoretical model and the experimental data was done for both reaction, but it is more interesting for ^{40}Ca +^{40}Ca

reaction, because in case of ^{37}Cl + ^{44}Ca reaction only a residues (^{78}Kr) was populated in most of cases.

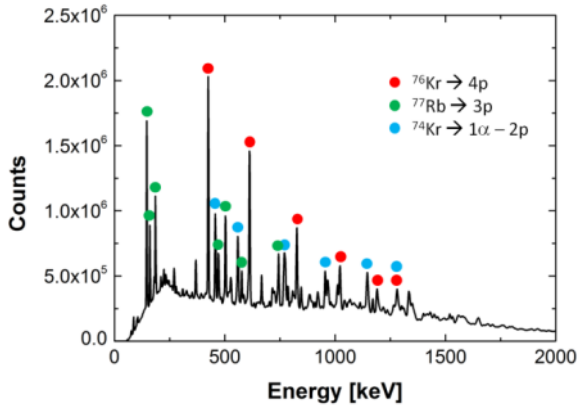

Fig. 9.15: Low-energy spectrum of AGATA Demonstrator for ^{40}Ca + ^{40}Ca reaction. The γ lines indicated by points are the identified emissions for different evaporation residues (red points ^{76}Kr, green points ^{77}Rb and blue points ^{74}Kr). There are some peaks, that are not marked by point. These peak are the γ lines of other residues (see Tab. 9.3).

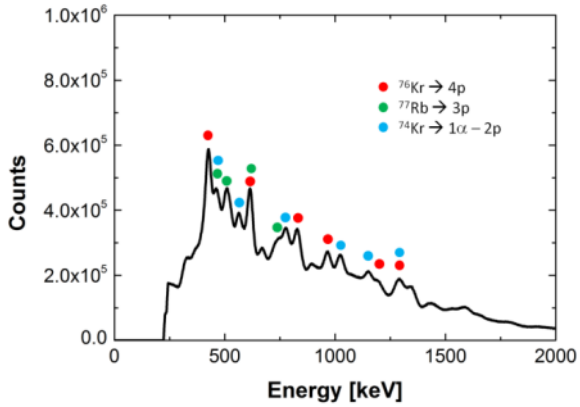

Fig. 9.16: Low-energy spectrum of $LaBr_3$:Ce detectors for ^{40}Ca + ^{40}Ca reaction. The γ lines indicated by points are the identified emissions for different evaporation residues (red points ^{76}Kr, green points ^{77}Rb and blue points ^{74}Kr).

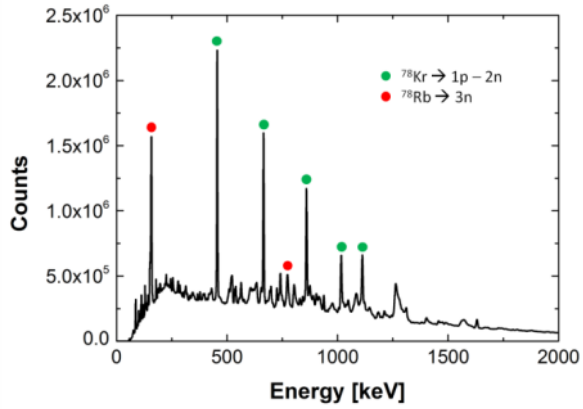

Fig. 9.17: Low-energy spectrum of AGATA Demonstrator for ^{37}Cl + ^{44}Ca reaction. The γ lines indicated by points are the identified emissions for different evaporation residues (green points ^{78}Kr and red points ^{78}Rb). There are some peaks, that are not marked by points. These peak are the γ lines of other residues (see Tab. 9.2).

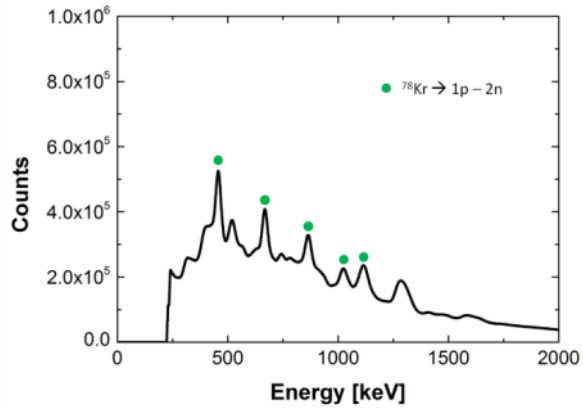

Fig. 9.18: Low-energy spectrum of $LaBr_3$:Ce detectors for ^{37}Cl + ^{44}Ca reaction. The γ lines indicated by points are the identified emissions for different evaporation residues (green points ^{78}Kr).

The residues that are mostly populated in ^{40}Ca + ^{40}Ca reaction are three: ^{76}Kr, ^{74}Kr and ^{77}Rb. The theoretical prediction of the DCASCADE code is compared to the experimental results in Tab. 9.4. The experimental data confirm the prediction of the model. The values of the DCASCADE model

reported in Tab. 9.4 are slight different from the ones of Tab. 9.3, because in this case only these three main residues are considered.

Residue	Population DCASCADE	Population Data
^{76}Kr	48%	47%
^{74}Kr	27%	22%
^{77}Rb	25%	31%

Tab. 9.4: Population of residues of the ^{40}Ca + ^{40}Ca reaction. The theoretical prediction of the DCASCADE code is compared to the experimental results.

9.3. Analysis of types of events

The CN could decay by emitting γ rays of different nature, as explained in section 2.1. The γ rays of different nature were detected in the different arrays of the experimental set up.

To select the events that satisfy trigger conditions, it is necessary to detect at least two γ rays in coincidence (see section 8.4) and to select γ rays coming from the target (their time signal has to be in the prompt-γ peak). The selection of the γ-line coming from the target was used to reduce the random coincidences.

In the following data analysis, the two classes of event (the *AGATA event* and the *$LaBr_3$:Ce event*), explained in section 8.4, will be consider separately. In these two classes of event was already included the conditions of detecting at least two γ rays in coincidence. The two classes of event were analyzed separately in sections 9.4.1 and 9.4.2 for the ^{40}Ca + ^{40}Ca reaction and in sections 9.5.1 and 9.5.2 for the ^{37}Cl + ^{44}Ca reaction.

In case of the *AGATA event*, the γ multiplicity in AGATA was selected equal to 1 or 2 ($M_{\gamma\_AGATA} = 1$ or $M_{\gamma\_AGATA} = 2$) and the γ multiplicity of $LaBr_3$:Ce detectors was selected equal to 1 ($M_{\gamma\_LaBr_3} = 1$). These conditions imply a loss of statistic of 3% with respect to the case in which there is not selection on the gamma multiplicity in AGATA and in HECTOR$^+$. Otherwise in case of *$LaBr_3$:Ce event,* the γ multiplicity in HECTOR$^+$ was selected equal to

2 ($M_{\gamma\_LaBr_3} = 2$) and the value of multiplicity larger than two were rejected. This condition imply a loss of statistic of 6%.

In the *AGATA event* the time resolution is dominated by the resolution of the AGATA Demonstrator (FWHM ~25 ns), instead in the *$LaBr_3$:Ce event* the time resolution is about 1.8 ns that is the typical resolution of the $LaBr_3$:Ce detectors during an experiment (see Fig. 9.19). The selection on the prompt γ peak was done only in the case of *$LaBr_3$:Ce event*, because only in this case it is possible to distinguish the prompt peak from the neutron peak. In $LaBr_3$:Ce time spectrum, for the *$LaBr_3$:Ce event*, in the ^{37}Cl + ^{44}Ca reaction (black line in Fig. 9.19) it is possible to see the neutrons peak.

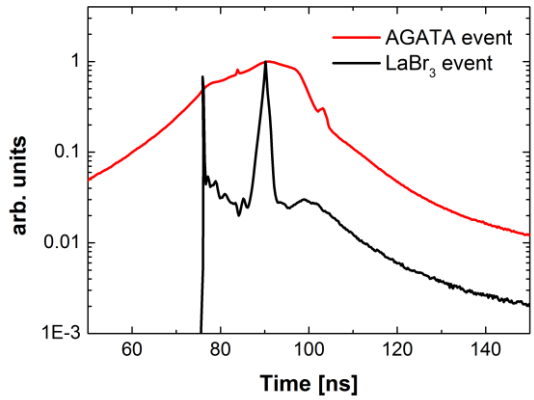

Fig. 9.19: Time spectra for the ^{37}Cl + ^{44}Ca reaction of one of $LaBr_3$:Ce for an AGATA event (red line) and for a $LaBr_3$:Ce event (black line). The time resolution of the $LaBr_3$:Ce event is better that the time resolution of AGATA event, because the black spectrum has the time resolution of the $LaBr_3$:Ce detectors (about 2 ns), instead the red one has the time resolution of the AGATA Demonstrator.

9.4. Data analysis of the ^{40}Ca + ^{40}Ca reaction

The ^{40}Ca + ^{40}Ca reaction produces the compound nucleus ^{80}Zr, a proton rich nucleus (it is near the proton drip line) and as consequence it decays by emitting protons and gammas. The neutron emitting channels were not expected as shown in section 9.2.

9.4.1. $LaBr_3$:Ce events

To produce the high-energy spectra, it is necessary to select the prompt γ peak to reduce the background.

The time spectrum of one of the HECTOR+ detectors is shown in Fig. 9.20. A gate on the prompt gamma emission was done. The region of the gate is identified by red lines in Fig. 9.20. The low-energy spectrum obtained with this gate is shown in Fig. 9.21 with a blue line. While, the off gate spectrum (red line in Fig. 9.21) was obtained by selecting the area outside the red lines in Fig. 9.20. The off gate spectrum (red line in Fig. 9.21) is composed only by the background (internal radioactivity and 511 keV) instead the time gated spectrum (blue line in Fig. 9.21) shows only the peaks that are from the evaporation residues without the background.

Fig. 9.22 shows the energy versus time matrix that was used to better understand the time spectra and to do more precise gate. The five regions in Fig. 9.22 correspond: 1) the prompt γ peak, 2) the auto coincidence peak, 3) the region between the auto coincidence and the prompt peak, 4) the region in which is expected the neutron peak and 5) the random coincidences background.

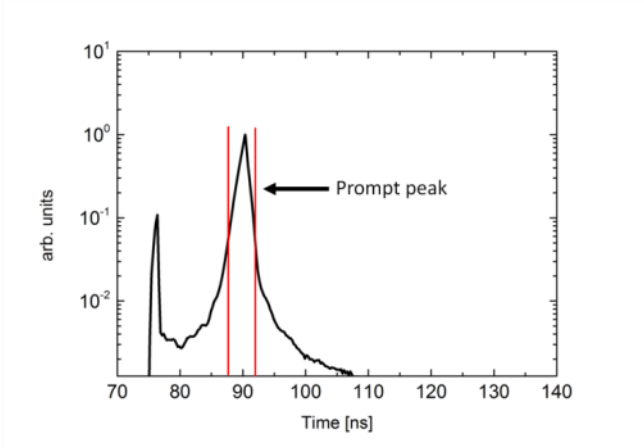

Fig. 9.20: The time spectrum of one of the HECTOR+ detectors. The two vertical-red lines indicated the gate on the prompt γ peak. The spike at the beginning of the spectrum is the auto coincidence peak.

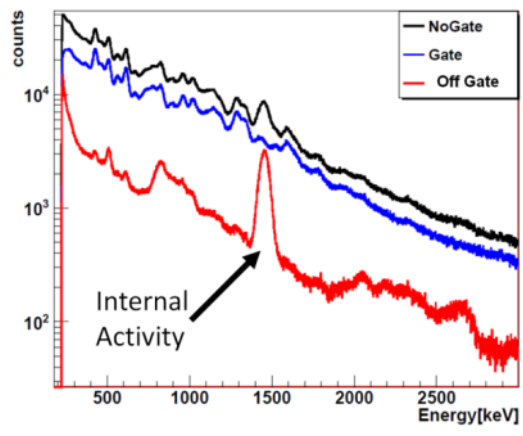

Fig. 9.21: The low-energy spectra of one of $LaBr_3$:Ce detector with different gate conditions are shown. The black line represents the spectrum without gate, the blue line represents the spectrum with gate on the prompt peak and the red line represents the spectrum with the gate in the regions outside the prompt peak.

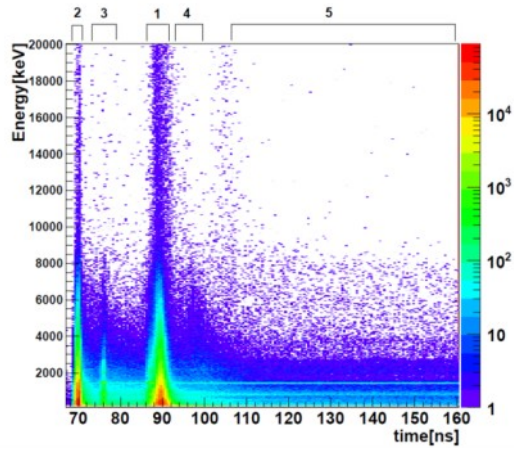

Fig. 9.22: Energy versus time matrix of one $LaBr_3$:Ce detector in the case of $LaBr_3$:Ce event.

The high-energy spectrum of *LaBr3:Ce sum*, obtained in coincidence with the prompt γ peak, is shown in Fig. 9.23 by black squares. This spectrum it is characterized by a constant background in the energy range of 20-22 MeV. In Fig. 9.23 it is possible to see also the same spectrum with a background subtraction, represented by red points. The background was obtained by fitting with a constant between 20-22 MeV. Using more

restrictive time gate it is possible to reduce (or to eliminate) the background without the constant subtraction. The spectrum obtained in this way is practically identical to the one shown in Fig. 9.23 by red points.

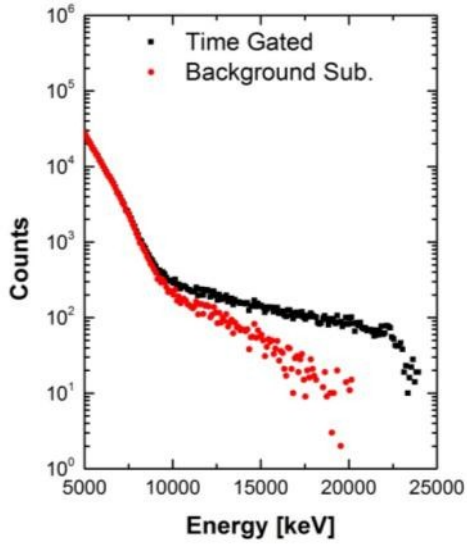

Fig. 9.23: The energy spectrum of $LaBr_3$:Ce sum with the time gate shown in Fig. 9.20 (black squares) and the same spectrum with background subtraction (red points).

9.4.2. AGATA events

To have a good high energy spectrum it is important to reject the neutrons, because they modify the shape of high energy spectrum in the energy range of 8 to 10 MeV. The time resolution in case of *AGATA event* is about 25 ns, and with this time resolution it is not possible to distinguish the neutrons from γ rays. In the case of the ^{40}Ca + ^{40}Ca reaction neutron evaporation is not expected (see section 9.2), for this reason the high energy spectrum produced in case of *$LaBr_3$:Ce event* is expected to be identical of the one produced in case of *AGATA event*.

The time spectrum of one of the HECTOR$^+$ detectors in coincidence with the AGATA Demonstrator is shown in Fig. 9.24. A gate on the prompt gamma peak was done. The region of the gate is identified by the two red lines in Fig. 9.24 as of in the case of *$LaBr_3$:Ce event*. The low-energy spectrum

obtained with this gate is shown in Fig. 9.25 with a blue line. The energy off gate (the area outside the red lines in Fig. 9.24) spectrum is shown by a red line in Fig. 9.25. This spectrum is composed by the internal radioactivity but in this case there are also some evaporation residues γ lines, due to the bad time resolution of the AGATA Demonstrator; indeed it is not possible to do a selective gate as in the case of *$LaBr_3$:Ce event*. Time gated spectrum (blue line) shows only the peaks that are from the evaporation residues of the reaction with a smaller background with respect to the black spectrum (the total one).

Also in case of *AGATA event*, the energy versus time matrix is reported in Fig. 9.26. In this case it is not possible to do different cuts so as to select the different time structures due to the bad time resolution of AGATA Demonstrator.

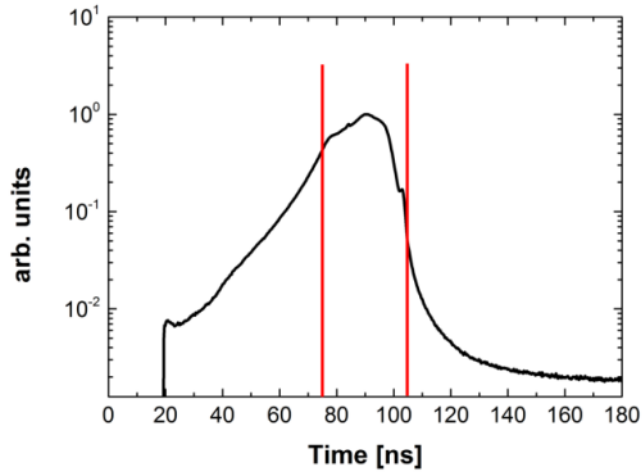

Fig. 9.24: The time spectrum of one of the HECTOR+ detectors in coincidence with AGATA Demonstrator. The two vertical-red lines indicated the gate on the prompt γ peak.

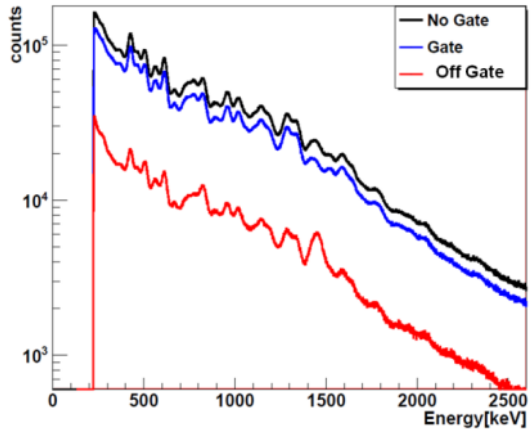

Fig. 9.25: The low-energy spectra of one of $LaBr_3$:Ce detector with different gate conditions. The black line represents the spectrum without gate, the blue line represents the spectrum with gate on the prompt peak for AGATA event (see Fig. 9.24) and the red represents line the spectrum with the gate in the regions outside the prompt peak.

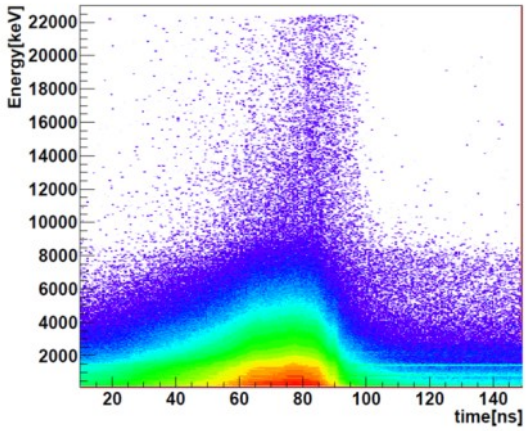

Fig. 9.26: Energy versus time matrix of one $LaBr_3$:Ce detector in the case of AGATA event.

The high-energy spectrum of *$LaBr_3$:Ce sum*, obtained in coincidence with the γ peak (using the gate of Fig. 9.24), is shown in Fig. 9.27 by black squares. This spectrum it is characterized by a constant background in the energy range of 20-22 MeV. In Fig. 9.27 it is possible to see also the same spectrum with a background subtraction, represented by red points (the background was obtained by fitting with a constant between 20 and 22

MeV). Using more restrictive time gate it is possible to reduce (or to eliminate) the background without the constant subtraction. The spectrum obtained in this way is practically identical to the one shown in Fig. 9.27 by red points.

In Fig. 9.28 there is the AGATA Demonstrator high-energy spectrum with time gate.

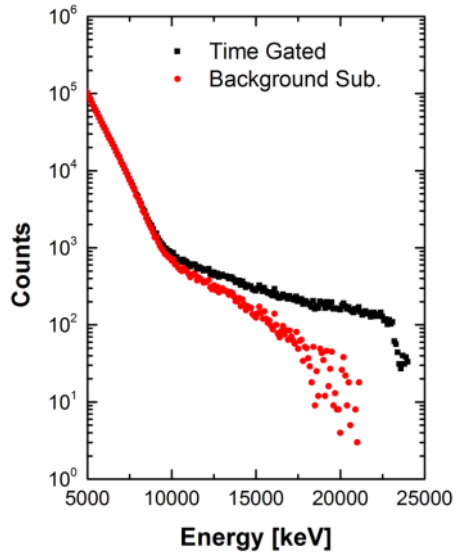

Fig. 9.27: The energy spectrum of $LaBr_3$:Ce sum with the time gate shown in Fig. 9.24 (black squares) and the same spectrum with background subtraction (red points).

In Fig. 9.29 there is the comparison between the *LaBr3:Ce sum* high-energy spectrum, in case of *AGATA event* (black squares) with a time gate of 30 ns (as shown in Fig. 9.24) and in the case of $LaBr_3$:Ce event (red points) and with a time gate of 2 ns (as shown in Fig. 9.20). There is not significant differences between the two spectra in the energy range of 8-10 MeV, and as consequence we can conclude that, as expected (see section 9.2) there is no neutron contribution, as is clearly shown in Fig. 9.30. This Fig. shows the ratio between the two spectra ($LaBr_3$:Ce event and AGATA event) represented by red points.

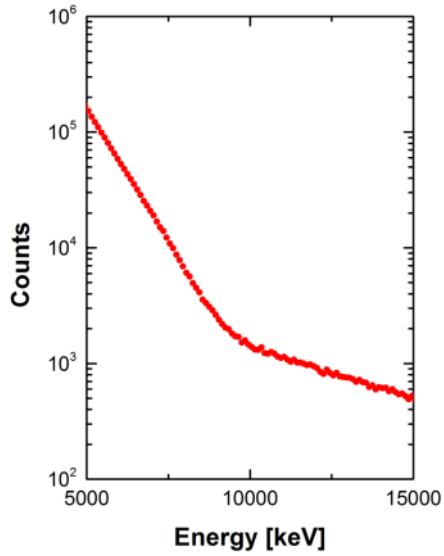

Fig. 9.28: The energy spectrum of AGATA Demonstrator with the time gate in Fig. 9.24 is shown.

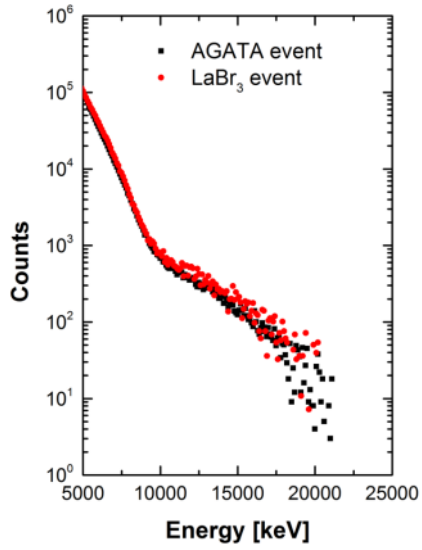

Fig. 9.29: Comparison between the $LaBr_3$:Ce sum spectrum in case of $LaBr_3$:Ce event (red points) and the one in case of AGATA event (black squares). The two spectra are normalized at 4 MeV.

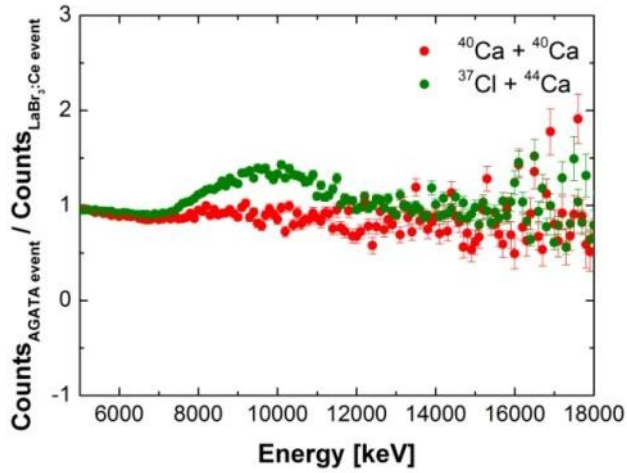

Fig. 9.30: The ratio between the $LaBr_3$:Ce sum spectrum for AGATA event and the same spectrum for $LaBr_3$:Ce event (^{40}Ca + ^{40}Ca red points, ^{37}Cl + ^{44}Ca green points).

9.5. Data analysis of the ^{37}Cl + ^{44}Ca reaction

The ^{37}Cl + ^{44}Ca reaction produces the compound nucleus ^{81}Rb, that is a nucleus near the stability valley, and as a consequence it decays by emitting neutrons, protons, alpha particles and gammas. The expected evaporation residues are shown in section 9.2. In this reaction is expected a contribution from neutron evaporation. The neutrons contribution modifies the high-energy spectrum in the energy region of 8-10 MeV, and for this reason, it will be very important to separate neutrons from γ-rays.

9.5.1. $LaBr_3$:Ce events

To produce the high-energy spectra, it is necessary to have a coincidence with the prompt γ peak. To have a good high energy spectrum it is important to reject the neutrons (that are present in ^{37}Cl + ^{44}Ca reaction). The time resolution of the HECTOR$^+$ array in case of *$LaBr_3$:Ce event* is about 1.8 ns, that allows to distinguish neutrons from γ rays.

The time spectrum of one of the HECTOR+ detectors is shown in Fig. 9.31. A gate on the prompt gamma peak was done (the region of the gate is identified by the red lines in Fig. 9.31). The low-energy spectrum obtained with this gate is shown in Fig. 9.32 with a blue line. The energy off gate (that is the area outside the red lines in Fig. 9.31) spectrum is shown by red line in Fig. 9.32. This spectrum (red line) is composed manly by the background (internal radioactivity and 511keV) whereas the time gated spectrum (blue line) shows only the peaks from the evaporation residues of the reaction whit a reduced background with respect to the total spectrum (black line).

Fig. 9.33 shows the energy versus time matrix that was used to better understand the time spectra and to do more precise gates. Five regions were selected: 1) the prompt γ peak region between 88 ns and 92 ns, 2) the auto coincidence peak region between 69 ns and 71 ns, 3) the region between the auto coincidence and the prompt peak (between 72 ns and 82 ns), 4) the neutron peak region between 94 ns and 104 ns and 5) the random coincidences background region (between 110 ns and 160 ns).

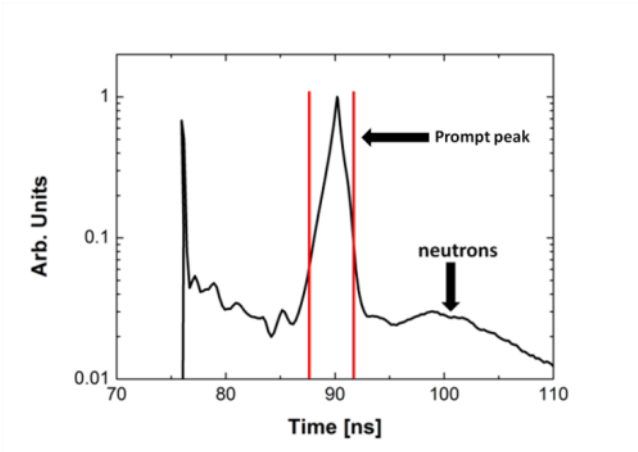

Fig. 9.31: The time spectrum of one of the HECTOR+ detectors. The two vertical-red lines indicated the gate on the prompt γ peak. The spike at the beginning of the spectrum is the auto coincidence peak. The peak centered in 100 ns is due the presence of neutron evaporation.

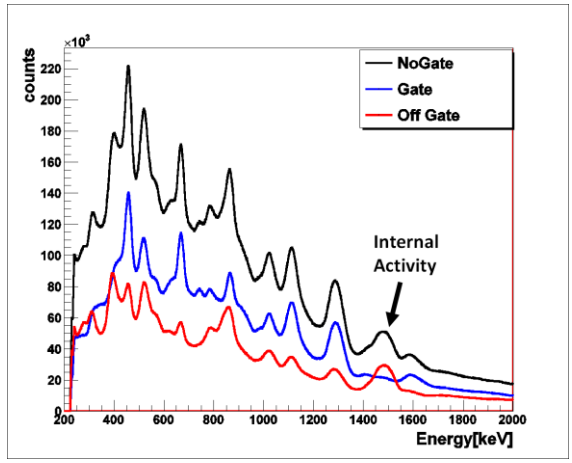

Fig. 9.32: The low-energy spectra of one of $LaBr_3$:Ce detector with different gate conditions. The black line represent the spectrum without gate, the blue line represent the spectrum with gate on the prompt peak of Fig. 9.31 and the red line the spectrum with the gate in the regions outside the prompt peak.

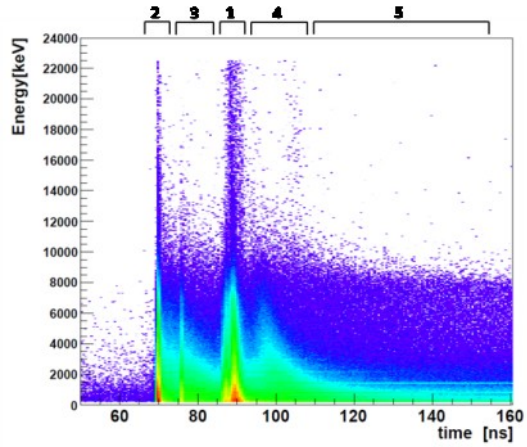

Fig. 9.33: Energy versus time matrix of one $LaBr_3$:Ce detector in the case of $LaBr_3$:Ce event.

The high-energy spectrum of *$LaBr_3$:Ce sum*, obtained in coincidence with the prompt γ peak (the used gate was the same of Fig. 9.31), is shown in Fig. 9.34 by black squares. This spectrum it is characterized by a constant background in the energy range of 20-22 MeV. In Fig. 9.34 it is possible to see also the spectrum with a background subtraction, represented by green points (the background was obtained by fitting with a constant between 20-

22 MeV). Using more restrictive time gate it is possible to reduce (or to eliminate) the background without the constant subtraction. The spectrum obtained in this way is practically identical to the one shown in Fig. 9.34 by green points.

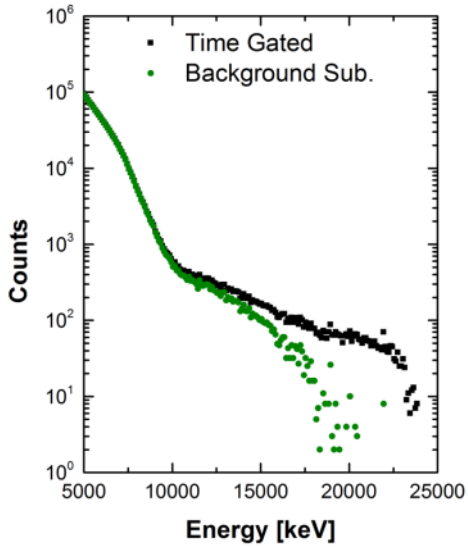

Fig. 9.34: The energy spectrum of $LaBr_3$:Ce sum with the time gate shown in Fig. 9.31 (black squares) and the same spectrum with background subtraction (green points).

9.5.2. AGATA events

As it was discussed before, the rejection of the neutrons is very important because neutron events modify the shape of high-energy spectrum in the energy range of 8 to 10 MeV. The time resolution, in case of *AGATA event,* is about 25 ns; with this time resolution it is not possible to distinguish the neutrons from γ rays. The $^{37}Cl + ^{44}Ca$ reaction produces the compound nucleus ^{81}Rb, and as a consequence neutron emitting channels were expected as discussed in section 9.2. Therefore the high-energy spectrum produced in case of *$LaBr_3$:Ce event* is expected to be different with respect to the one produced in case of *AGATA event*, in the region between 8 and 10 MeV.

The time spectrum of one of the HECTOR+ detectors in coincidence with the AGATA Demonstrator is shown in Fig. 9.35. A gate on the prompt-gamma peak was done (the region of the gate is identified by the red lines in Fig. 9.35 as of in the case of *$LaBr_3$:Ce event*). The energy spectrum obtained with this gate is shown in Fig. 9.36 with a blue line. The energy off gate (that is the area outside the two vertical-red lines in Fig. 9.35) spectrum is represented by a red line in Fig. 9.36. This spectrum (red line) is composed by the background but in this case there is also a contribution of the γ lines associated to fusion-evaporation residues, due to the bad time resolution. In case of *AGATA event* it is not possible to do a selective gate as in the case of *$LaBr_3$:Ce event*. Time gated spectrum (blue line) shows only the peaks from the evaporation residues of the reaction with a smaller background with respect to total spectrum (black line).

Also in case of *AGATA event*, the energy versus time matrix is reported in Fig. 9.37. In this case it is not possible to distinguish different regions due to the bad time resolution of AGATA Demonstrator. It is therefore not possible to separate the neutron contribution from the prompt gamma peak.

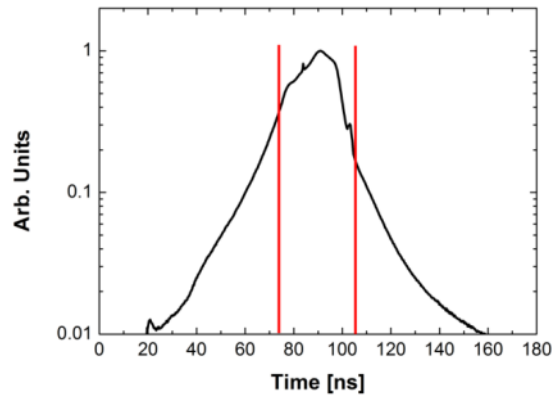

Fig. 9.35: The time spectrum of one of the HECTOR+ detectors in coincidence with AGATA Demonstrator. The two vertical-red lines indicated the gate on the prompt γ peak.

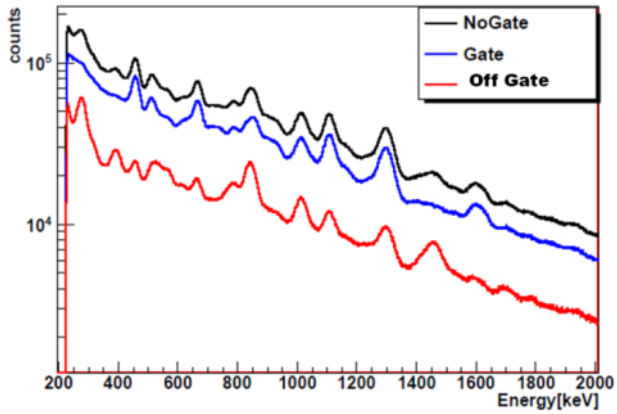

Fig. 9.36: The low-energy spectra of one of $LaBr_3$:Ce detector with different gate conditions. The black line represents the spectrum without gate, the blue line represents the spectrum with gate on the prompt peak for AGATA event (see Fig. 9.35) and the red line represents the spectrum with the gate in the regions outside the prompt peak.

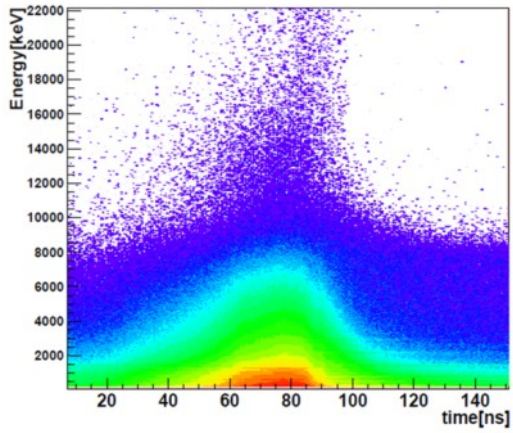

Fig. 9.37: Energy versus time matrix of one $LaBr_3$:Ce detector in the case of AGATA event.

The high-energy spectrum of *$LaBr_3$:Ce sum*, obtained in coincidence with the prompt γ peak (using the gate of Fig. 9.35), is shown in Fig. 9.38 by black squares. This spectrum it is characterized by a constant background in the energy range of 20-22 MeV. In Fig. 9.38 it is possible to see also the same spectrum with a background subtraction, represented by green points (the background was obtained by fitting with a constant between 20-22 MeV).

Using more restrictive time gate it is possible to reduce (or to eliminate) the background without the constant subtraction. The spectrum obtained in this way is practically identical to the one shown in Fig. 9.23 by red points.

In Fig. 9.39 there is the AGATA Demonstrator high-energy spectrum with time gate.

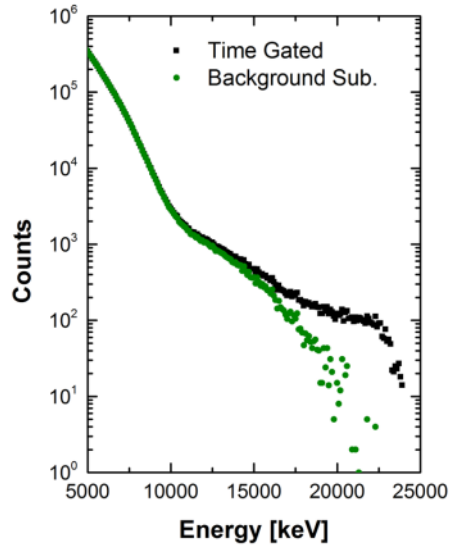

Fig. 9.38: The energy spectrum of $LaBr_3$:Ce sum with the time gate shown in Fig. 9.35 (black squares) and the same spectrum with background subtraction (green points).

In Fig. 9.40 there is the comparison between the *LaBr3:Ce sum* high-energy spectrum, in case of *AGATA event* (black squares) with a time gate of 30 ns (as shown in Fig. 9.35 and in Fig. 9.24) and the same spectrum in the case of *$LaBr_3$:Ce event* (green points) and with a time gate of 2 ns (as shown in Fig. 9.31). There is a significant differences between the two spectra in an energy range of 8-10 MeV, due to the presence of the neutrons. Indeed, in the *$LaBr_3$:Ce event* it is possible to reject the neutrons due to the good time resolution of the $LaBr_3$:Ce detectors instead in case of *AGATA event* it is not possible to separate the neutron due to the bad time resolution of AGATA Demonstrator.

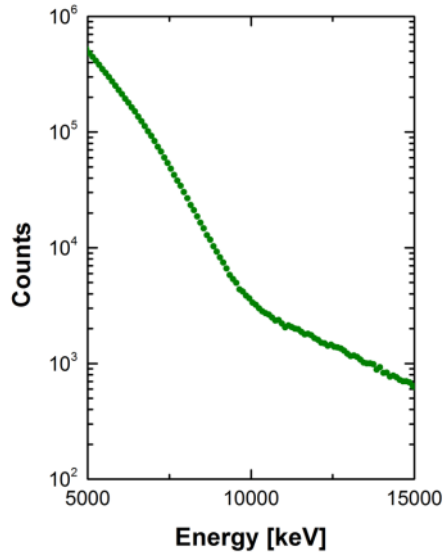

Fig. 9.39: The energy spectrum of AGATA Demonstrator with the time gate in Fig. 9.35 is shown.

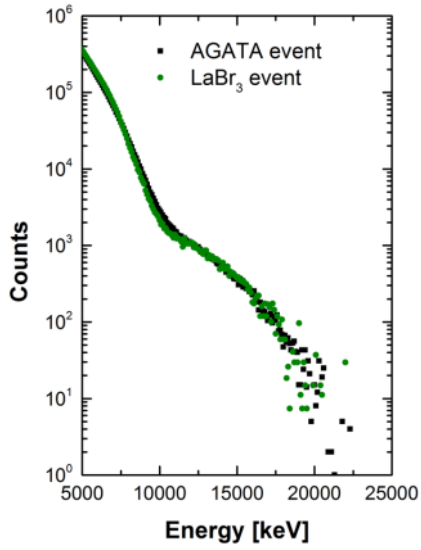

Fig. 9.40: Comparison between the $LaBr_3$:Ce sum spectrum in case of $LaBr_3$:Ce event (green points) and the one in case of AGATA event (black squares). The two spectra are normalized at 4 MeV.

To be sure that there is a significant differences between the two spectra in an energy range of 8-10 MeV in ^{37}Cl + ^{44}Ca reaction, due to the presence of the neutrons, the ratio between the $LaBr_3$:Ce sum spectrum for AGATA event and the same spectrum for $LaBr_3$:Ce event was done and it is shown in Fig. 9.41. This ratio is compared with the same quantity for the ^{40}Ca + ^{40}Ca reaction; it is possible to see that for the ^{40}Ca + ^{40}Ca reaction the ratio is always equal to 1, while for the ^{37}Cl + ^{44}Ca reaction the ratio is larger than 1 in the energy range of 8 to 10 MeV, due to neutron evaporation.

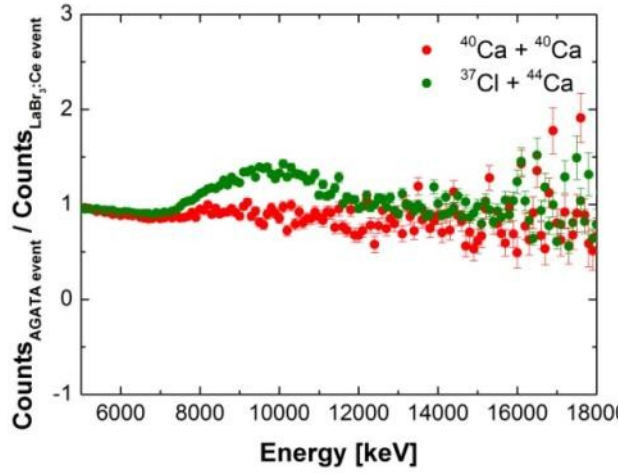

Fig. 9.41: The ratio between the $LaBr_3$:Ce sum spectrum for AGATA event and the same spectrum for $LaBr_3$:Ce event (^{40}Ca + ^{40}Ca red points, ^{37}Cl + ^{44}Ca green points). The difference from 1 in the case of ^{37}Cl + ^{44}Ca reaction is related to the neutron contribution.

9.6. Selection of evaporation residues

In case of *AGATA event*, the selection of events by a time gate (described in sections 9.4 and 9.5) is not able to reject the neutrons, due to the poor time resolution of the AGATA Demonstrator. To select the events by alternatively it is possible to use the AGATA energy versus *$LaBr_3$:Ce sum* energy matrix (shown in Fig. 9.42). On the x axis there is the deposited energy in AGATA Demonstrator and on the y axis there is the deposited energy in the HECTOR$^+$ apparatus. It is possible to do a gate on a γ line

detected in one of the two arrays and to study the gated spectrum on the other array. This technique results more accurate in the case of excellent energy resolution. The low energy gate is done on HPGe detectors because their excellent energy resolution. Energy resolution of HPGe allows gates that includes only one γ line and a reduced background, moreover it is possible to separate γ lines that have a very similar energy.

The energy resolution of $LaBr_3$:Ce detectors is good enough to separate most of the γ lines produced in the two reactions analyzed in this thesis (see Fig. 9.16 and Fig. 9.18). For this reason it is interesting to use this technique also on $LaBr_3$:Ce spectra, the results of this technique for the two reaction will be shown in sections 9.6.1 and 9.6.2.

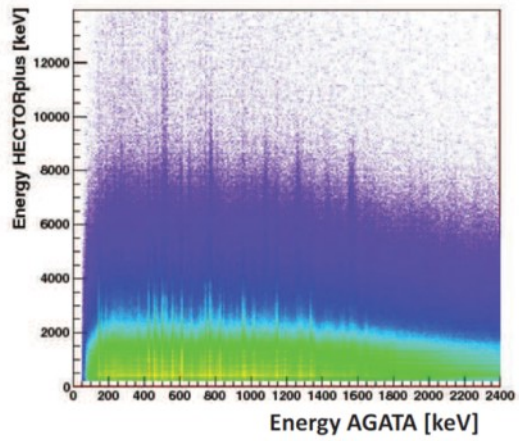

Fig. 9.42: The AGATA energy versus $LaBr_3$:Ce sum energy matrix for the ^{40}Ca + ^{40}Ca reaction.

9.6.1. ^{40}Ca + ^{40}Ca reaction

In the ^{40}Ca + ^{40}Ca reaction, the γ line at 1021 keV was chosen to do the gate. This is associate to a transition from an 8^+ state to a 6^+ state of the rotational band of ^{76}Kr. The γ lines associated to other bands or to other residues are expected to be suppressed. The results are shown in Fig. 9.43 and Fig. 9.44. In these two figures it is possible to see the effect of the gate on the line at 1020 keV both in the case in which the gate was done on AGATA and the result is shown on *$LaBr_3$:Ce sum* spectrum (Fig. 9.43) and in the case

in which the gate was done on *$LaBr_3$:Ce sum* spectrum and the result is shown on AGATA spectrum (Fig. 9.44). With the selection on AGATA the energy resolution of the LaBr3:Ce detectors is enough to separate the different γ lines of one residue as shown in Fig. 9.43.

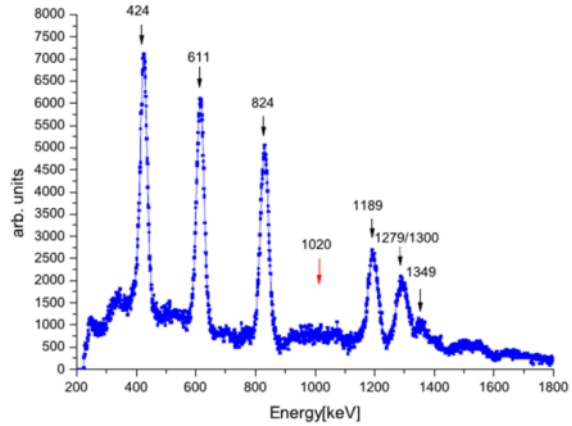

Fig. 9.43: The $LaBr_3$:Ce sum low-energy spectrum with a gate on AGATA on the line at 1020 keV.

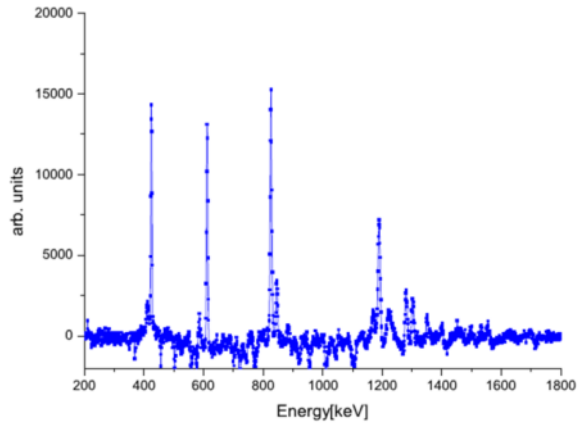

Fig. 9.44: The AGATA low-energy spectrum with a gate on $LaBr_3$:Ce sum on the line at 1020 keV.

9.6.2. $^{37}Cl + ^{44}Ca$ reaction

In the $^{37}Cl + ^{44}Ca$ reaction, the γ line at 1016 keV was chosen to do the gate. This is associate to a transition from an 8^+ state to a 6^+ state of the rotational band of ^{78}Kr. The γ lines associated to other bands or to other residues are expected to be suppressed. The results are shown in Fig. 9.45 and Fig. 9.46. In these two figures it is possible to see the effect of the gate on the line at 1016 keV both in the case in which the gate was done on AGATA and the result is shown on *$LaBr_3$:Ce sum* spectrum (Fig. 9.45) and in the case in which the gate was done on *$LaBr_3$:Ce sum* spectrum and the result is shown on AGATA spectrum (Fig. 9.46). With the selection on AGATA the energy resolution of the LaBr3:Ce detectors is enough to separate the different γ lines of one residue as shown in Fig. 9.45.

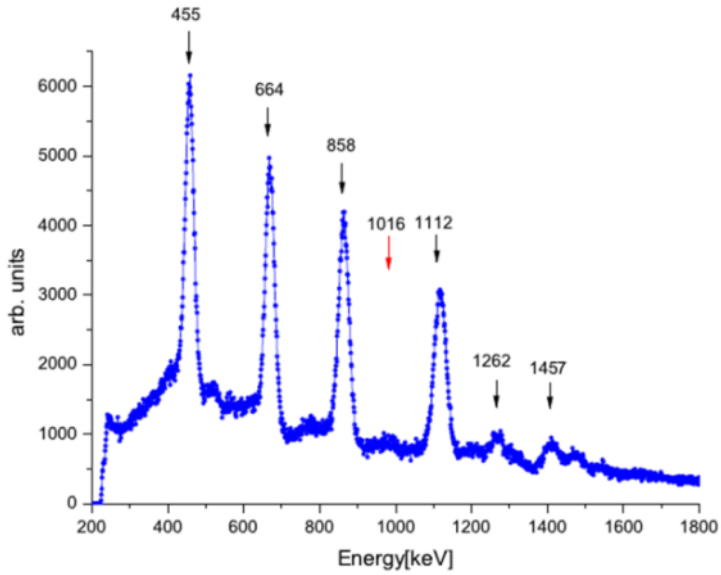

Fig. 9.45: The $LaBr_3$:Ce sum low-energy spectrum with a gate on AGATA on the line at 1016 keV

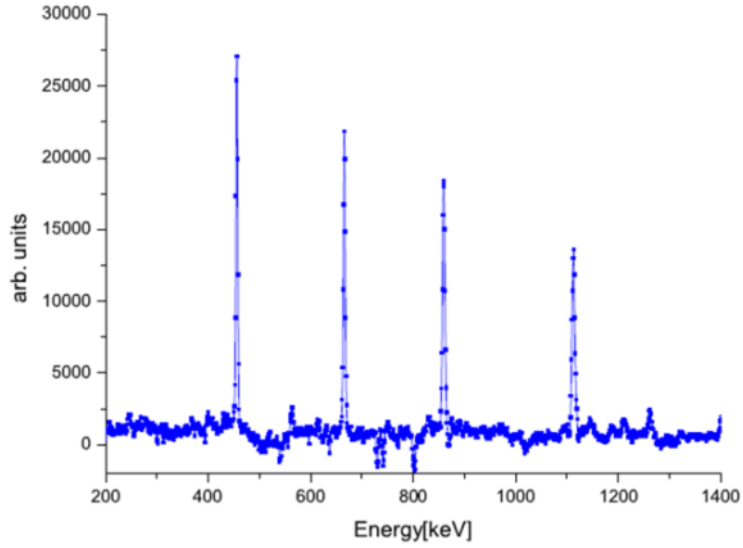

Fig. 9.46: The AGATA low-energy spectrum with a gate on $LaBr_3$:Ce sum on the line at 1016 keV

Conclusions

The collective properties of a nuclear system were used to understand the dynamics of the fusion process and to study the restoration of the isospin symmetry at high excitation energy. In the first case the data analysis was completed, while for the second it is still in progress and the results reported in this thesis were mainly finalized to show the performance of a large volume $LaBr_3$:Ce scintillator array in an in-beam experiment.

The main observable used to study the dynamical aspect of fusion-evaporation reactions is the yield of the high-energy γ-ray emission of the dynamical dipole (DD), which is a process that takes place during the compound nucleus formation in the case of an N/Z asymmetry between projectile and target. The experiment was performed at the Laboratori Nazionali di Legnaro (LNL) and studied the ^{16}O + ^{116}Sn reaction at 12 MeV/u. This measurement was a follow up of a previous experiment where the same reaction was studied at 8.1 and 15.6 MeV/u.

The technique used to extract the DD total yield requires the comparison between the high-energy γ-ray spectrum from an N/Z asymmetric reaction with one that includes only the contribution of the GDR γ decay. For both the experiments at 8.1 and 15.6 MeV/u [6] a N/Z symmetric reaction was measured as a reference, forming the same compound nucleus at the same excitation energy and angular momentum as the N/Z asymmetric one. In order to save beam time, the N/Z symmetric reaction was not measured in the case of the present analysis. The statistical model, tuned on the previous reference reactions, was used to obtain a reference spectrum.

The most critical parameter for the analysis is the excitation energy of the compound nucleus, for which the energy removed from the particles emitted in the pre-equilibrium phase has to be taken into account. This energy loss was measured with the GARFIELD array: light charged particles were measured at different angles, and the statistical contribution was separated from the pre-equilibrium one; from the multiplicity of the particles it is possible to estimate the pre-equilibrium energy loss. For the

neutron emission a theoretical estimation was used. In this way a pre-equilibrium energy loss of 13.4 MeV was measured. The same quantity can be estimated with theoretical models: a value of 18 MeV was obtained using [41]. Both values are very different from the one extracted from the parameterization reported in [17], which is 26 MeV.

The measured behavior of the dynamical dipole total yield as a function of the beam energy does not show a rise and fall behavior, as in [3], which is only reproduced if we use the Kelly parameterization for the pre-equilibrium energy loss. Instead, we observe a weak increase in the yield as the beam energy increases, in good agreement with the theoretical BNV model predictions. Since the DD yield depends on the symmetry term of the nuclear equation of state, different parameterizations were used as input for the BNV model, but all predictions fall within the error bars of the experimental data.

The BNV model was not used only to study the $^{16}O+^{116}Sn$ reaction, but also to predict the DD yield for the very asymmetric $^{132}Sn + ^{58}Ni$ reaction, which could be measured in a future facility with high-intensity exotic beams. In this case, a better sensitivity to the symmetry term of the nuclear equation of state can be achieved.

A detailed analysis of the model predictions also shows that the selection of small impact parameters (low angular momentum) can further enhance the sensitivity of the experiment to the equation of state, and that the theoretical results can be parameterized with a Fermi-like function with parameters which depend only the value of dipole moment and on the beam energy.

The second experiment studied in this thesis work aims to measure the isospin mixing of ^{80}Zr at the temperature of 2.4 MeV, and is a follow up of a previous experiment which measured the same quantity at the temperature of ~3 MeV. The final objective of the analysis is the extraction of the zero temperature value of the isospin mixing, which can be a constraint on the different parameterizations of the nuclear interaction. The ^{80}Zr nucleus was chosen as a case study because it is the heaviest N=Z isotope which can be studied using stable beams, and the isospin mixing effect increases with Z.

The experimental technique is based on the comparison between the high-energy γ-ray spectrum from a I=0 compound nucleus and the statistical model tuned on a reference fusion-evaporation reaction in which the isospin quantum number does not play a role (I ≠ 0: the GDR γ decay is forbidden by selection rules in the case of I=0 and the measured GDR decay is only allowed by the presence of mixed states. Therefore, two reactions were studied: $^{40}Ca + {}^{40}Ca = {}^{80}Zr$ to have an entrance channel with isospin I = 0, and $^{37}Cl + {}^{44}Ca = {}^{81}Rb$ as a reference, with I ≠ 0. The experiment was performed in may 2011 at LNL using the AGATA Demonstrator coupled to the HECTOR$^+$ array.

Neutrons interacting with γ detectors create a spurious increase of counts in the 8-10 MeV energy region, which can compromise the physical interpretation of the spectra. For this reason, neutron emission has to be identified and rejected. The evaporation residues populated in the two reactions were identified; in the $^{40}Ca + {}^{40}Ca$ reaction, the neutron emitting channels are negligible, whereas in the $^{37}Cl + {}^{44}Ca$ reaction only neutron emitting channels are populated. This implies that for the $^{37}Cl + {}^{44}Ca$ reaction only the HECTOR$^+$ data can be used at high energy, due to the good time resolution of $LaBr_3$:Ce detectors compared to HPGe detectors, while for the $^{40}Ca + {}^{40}Ca$ reaction the full efficiency of both the AGATA Demonstrator and HECTOR$^+$ can be used.

In the present work the high-energy γ-ray spectra were extracted for both reactions, showing the good performance of the HECTOR$^+$ array coupled to the AGATA Demonstrator. Future analysis will involve the statistical model calculation for the extraction of the isospin mixing parameter.

The isospin mixing experiment was the first in beam test of the HECTOR$^+$ array for the measurement of the γ decay of the GDR. In parallel, the performances of large volume $LaBr_3$:Ce detectors were investigated. In this thesis the conclusion of a series of test measurements, performed with standard sources at the Milano laboratories and with proton beams at Laboratori Nazionali di Catania (LNS) and at Institute of Nuclear Research of the Hungarian Academy of Sciences (ATOMKI) in Debrecen, are also reported.

A custom active voltage divider (VD) was developed by the electronics group of INFN of Milano to improve the performances of the detectors. The properties of signal (rise time and fall time) were measured and compared with the ones measured with a standard voltage divider. The non-linearity and the energy resolution were measured from 5.7 keV up to 22.6 MeV. Using the custom active voltage divider the non linearity is 2.2% at 22.6 MeV, while with a standard VD it is already ~10% at 9 MeV. The stability with the counting rate was also studied for both the active VD (centroid drift smaller than 1%) and the standard one (centroid drift about 5%).

The work presented in this thesis shows how $LaBr_3$:Ce detectors are particularly suited to the measurement of high-energy gamma rays. The HECTOR$^+$ array will be a powerful tool to investigate the collective properties of nuclear systems, especially in future measurements with exotic beams.

Bibliography

[1] P. F. Bortignon, A. Bracco, e R. A. Broglia, *Giant Resonances: Nuclear Structure at Finite Temperature*. Harwood Academic Publ., 1998.

[2] M. N. Harakeh e A. Woude, *Giant Resonances: Fundamental High-Frequency Modes of Nuclear Excitation*. Oxford University Press, 2001.

[3] D. Pierroutsakou, B. Martin, C. Agodi, R. Alba, V. Baran, A. Boiano, G. Cardella, M. Colonna, R. Coniglione, E. D. Filippo, A. D. Zoppo, M. D. Toro, G. Inglima, T. Glodariu, M. L. Commara, C. Maiolino, M. Mazzocco, A. Pagano, C. Parascandolo, P. Piattelli, S. Pirrone, C. Rizzo, M. Romoli, M. Sandoli, D. Santonocito, P. Sapienza, e C. Signorini, «Dynamical dipole mode in fusion reactions at 16 MeV/nucleon and beam energy dependence», *Phys. Rev. C*, vol 80, n° 2, pag 024612, 2009.

[4] D. Pierroutsakou, B. Martin, G. Inglima, A. Boiano, A. D. Rosa, M. D. Pietro, M. L. Commara, R. Mordente, M. Romoli, M. Sandoli, M. Trotta, E. Vardaci, T. Glodariu, M. Mazzocco, C. Signorini, L. Stroe, V. Baran, M. Colonna, M. D. Toro, e N. Pellegriti, «Evolution of the prompt dipole γ-ray emission with incident energy in fusion reactions», *Phys. Rev. C*, vol 71, n° 5, pag 054605, Mag 2005.

[5] B. Martin, D. Pierroutsakou, C. Agodi, R. Alba, V. Baran, A. Boiano, G. Cardella, M. Colonna, R. Coniglione, E. De Filippo, A. Del Zoppo, M. Di Toro, G. Inglima, T. Glodariu, M. La Commara, C. Maiolino, M. Mazzocco, A. Pagano, P. Piattelli, S. Pirrone, C. Rizzo, M. Romoli, M. Sandoli, D. Santonocito, P. Sapienza, e C. Signorini, «Prompt dipole radiation in fusion reactions», *Physics Letters B*, vol 664, n° 1–2, pagg 47–51, Giu 2008.

[6] A. Corsi, O. Wieland, V. L. Kravchuk, A. Bracco, F. Camera, G. Benzoni, N. Blasi, S. Brambilla, F. C. L. Crespi, A. Giussani, S. Leoni, B. Million, D. Montanari, A. Moroni, F. Gramegna, A. Lanchais, P. Mastinu, M. Brekiesz, M. Kmiecik, A. Maj, M. Bruno, M. D'Agostino, E. Geraci, G. Vannini, S. Barlini, G. Casini, M. Chiari, A. Nannini, A. Ordine, M. Di Toro, C. Rizzo, M. Colonna, e V. Baran, «Excitation of the dynamical dipole in the charge asymmetric reaction 16O + 116Sn», *Physics Letters B*, vol 679, n° 3, pagg 197–202, Ago 2009.

[7] V. Baran, D. M. Brink, M. Colonna, e M. Di Toro, «Collective Dipole Bremsstrahlung in Fusion Reactions», *Phys. Rev. Lett.*, vol 87, n° 18, pag 182501, Ott 2001.

[8] V. Baran, C. Rizzo, M. Colonna, M. D. Toro, e D. Pierroutsakou, «Dynamical dipole mode in fusion reactions with exotic nuclear beams», *Phys. Rev. C*, vol 79, n° 2, pag 021603, Feb 2009.

[9] W. Satuła, J. Dobaczewski, W. Nazarewicz, e M. Rafalski, «Isospin Mixing in Nuclei within the Nuclear Density Functional Theory», *Phys. Rev. Lett.*, vol 103, n° 1, pag 012502, Lug 2009.

[10] J. A. Behr, K. A. Snover, C. A. Gossett, M. Kicińska-Habior, J. H. Gundlach, Z. M. Drebi, M. S. Kaplan, e D. P. Wells, «Restoration of isospin symmetry in highly excited compound nuclei», *Phys. Rev. Lett.*, vol 70, n° 21, pagg 3201–3204, Mag 1993.

[11] M. N. Harakeh, D. H. Dowell, G. Feldman, E. F. Garman, R. Loveman, J. L. Osborne, e K. A. Snover, «Role of isospin in the statistical decay of the giant dipole resonance built on excited states», *Physics Letters B*, vol 176, n° 3–4, pagg 297–301, Ago 1986.

[12] R. Nicolini, F. Camera, N. Blasi, S. Brambilla, R. Bassini, C. Boiano, A. Bracco, F. C. L. Crespi, O. Wieland, G. Benzoni, S. Leoni, B. Million, D. Montanari, e A. Zalite, «Investigation of the properties of a 1″×1″ LaBr3:Ce scintillator», *Nuclear Instruments and Methods in Physics Research Section A: Accelerators, Spectrometers, Detectors and Associated Equipment*, vol 582, n° 2, pagg 554–561, Nov 2007.

[13] F. Quarati, A. J. J. Bos, S. Brandenburg, C. Dathy, P. Dorenbos, S. Kraft, R. W. Ostendorf, V. Ouspenski, e A. Owens, «X-ray and gamma-ray response of a 2″×2″ LaBr3:Ce scintillation detector», *Nuclear Instruments and Methods in Physics Research Section A: Accelerators, Spectrometers, Detectors and Associated Equipment*, vol 574, n° 1, pagg 115–120, Apr 2007.

[14] F. C. L. Crespi, F. Camera, N. Blasi, A. Bracco, S. Brambilla, B. Million, R. Nicolini, L. Pellegri, S. Riboldi, M. Sassi, O. Wieland, F. Quarati, e A. Owens, «Alpha–gamma discrimination by pulse shape in LaBr3:Ce and LaCl3:Ce», *Nuclear Instruments and Methods in Physics Research Section A: Accelerators, Spectrometers, Detectors and Associated Equipment*, vol 602, n° 2, pagg 520–524, Apr 2009.

[15] J. J. (Niels B. I. Gaardhøje, *The Dynamics of Nuclear Structure at High Excitation Energy*. New York, 1985.

[16] O. Wieland, A. Bracco, F. Camera, G. Benzoni, N. Blasi, S. Brambilla, F. Crespi, A. Giussani, S. Leoni, P. Mason, B. Million, A. Moroni, S. Barlini, V. L. Kravchuk, F. Gramegna, A. Lanchais, P. Mastinu, A. Maj, M. Brekiesz, M. Kmiecik, M. Bruno, E. Geraci, G. Vannini, G. Casini, M. Chiari, A. Nannini, A. Ordine, e E. Ormand, «Giant Dipole Resonance in the Hot and Thermalized ^{132}Ce Nucleus: Damping of Collective Modes at Finite Temperature», *Phys. Rev. Lett.*, vol 97, n° 1, pag 012501, Lug 2006.

[17] M. P. Kelly, K. A. Snover, J. P. S. van Schagen, M. Kicińska-Habior, e Z. Trznadel, «Giant Dipole Resonance in Highly Excited Nuclei: Does the Width Saturate?», *Phys. Rev. Lett.*, vol 82, n° 17, pagg 3404–3407, Apr 1999.

[18] M. Mattiuzzi, A. Bracco, F. Camera, W. E. Ormand, J. J. Gaardhøje, A. Maj, B. Million, M. Pignanelli, e T. Tveter, «Angular momentum dependence of the GDR width in Sn nuclei at fixed excitation energy», *Nuclear Physics A*, vol 612, n° 2, pagg 262–278, Gen 1997.

[19] P. Chomaz, «Influence of the compound-nucleus lifetime on the observed width of hot giant dipole resonances», *Physics Letters B*, vol 347, n° 1–2, pagg 1–5, Mar 1995.

[20] R. Bass, «Fusion of heavy nuclei in a classical model», *Nuclear Physics A*, vol 231, n° 1, pagg 45–63, Ott 1974.

[21] S. Cohen, F. Plasil, e W. J. Swiatecki, «Equilibrium configurations of rotating charged or gravitating liquid masses with surface tension. II», *Annals of Physics*, vol 82, n° 2, pagg 557–596, Feb 1974.

[22] V. Baran, M. Cabibbo, M. Colonna, M. Di Toro, e N. Tsoneva, «The dynamical dipole mode in dissipative heavy-ion collisions», *Nuclear Physics A*, vol 679, n° 3–4, pagg 373–392, Gen 2001.

[23] S. Flibotte, P. Chomaz, M. Colonna, M. Cromaz, J. DeGraaf, T. E. Drake, A. Galindo-Uribarri, V. P. Janzen, J. Jonkman, S. W. Marshall, S. M. Mullins, J. M. Nieminen, D. C. Radford, J. L. Rodriguez, J. C. Waddington, D. Ward, e J. N. Wilson, «Pre-Equilibrium Effects in the Population of Giant Dipole Resonances», *Phys. Rev. Lett.*, vol 77, n° 8, pagg 1448–1451, 1996.

[24] M. Cinausero, N. Gelli, G. Viesti, F. Lucarelli, D. Bazzacco, P. Bortignon, A. Brondi, D. Fabris, E. Farnea, E. Fiore, L. Fiore, E. Fioretto, B. Fornal, G. La Rana, M. Lunardon, D. Napoli, G. Nebbia, V. Paticchio, G. Prete, C. Rossi Alvarez, C. Ur, e E. Vardaci, «Giant dipole emission in N/Z asymmetric heavy-ion reactions», *Il Nuovo Cimento A (1971-1996)*, vol 111, n° 6, pagg 613–619, 1998.

[25] A. Carbone, G. Colò, A. Bracco, L.-G. Cao, P. F. Bortignon, F. Camera, e O. Wieland, «Constraints on the symmetry energy and neutron skins from pygmy resonances in ^{68}Ni and ^{132}Sn», *Phys. Rev. C*, vol 81, n° 4, pag 041301, Apr 2010.

[26] V. Baran, M. Colonna, V. Greco, e M. Di Toro, «Reaction dynamics with exotic nuclei», *Physics Reports*, vol 410, n° 5–6, pagg 335–466, Mag 2005.

[27] C. Rizzo, V. Baran, M. Colonna, A. Corsi, e M. Di Toro, «Symmetry energy effects on fusion cross sections», *Phys. Rev. C*, vol 83, n° 1, pag 014604, Gen 2011.

[28] C. Simenel, P. Chomaz, e G. de France, «Quantum Calculation of the Dipole Excitation in Fusion Reactions», *Phys. Rev. Lett.*, vol 86, n° 14, pagg 2971–2974, Apr 2001.

[29] C. Simenel, P. Chomaz, e G. de France, «Fusion process studied with a preequilibrium giant dipole resonance in time-dependent Hartree-Fock theory», *Phys. Rev. C*, vol 76, n° 2, pag 024609, 2007.

[30] G. F. Bertsch e S. Das Gupta, «A guide to microscopic models for intermediate energy heavy ion collisions», *Physics Reports*, vol 160, n° 4, pagg 189–233, Mar 1988.

[31] A. Maj, J. J. Gaardhøje, A. Ataç, S. Mitarai, J. Nyberg, A. Virtanen, A. Bracco, F. Camera, B. Million, e M. Pignanelli, «Angular distribution of photons from the delay of the GDR in hot and rotating light Yb nuclei from exclusive experiments», *Nuclear Physics A*, vol 571, n° 1, pagg 185–220, Apr 1994.

[32] F. Gramegna, U. Abbondanno, A. Andreano, R. Bassini, F. Bonutti, M. Bruno, G. Casini, M. D'Agostino, G. Manzin, G. V. Margagliotti, P. F. Mastinu, P. M. Milazzo, A. Moroni, M. Squarcini, F. Tonetto, G. Vannini, e L. Vannucci, «A telescope with microstrip gas chambers for the detection of charged products in heavy-ion reactions», *Nuclear Instruments and Methods in Physics Research Section A: Accelerators, Spectrometers, Detectors and Associated Equipment*, vol 389, n° 3, pagg 474–478, Apr 1997.

[33] M. Bini, G. Casini, A. Olmi, G. Poggi, A. A. Stefanini, L. Bardelli, A. Bartoli, L. Bidini, C. Coppi, P. Del Carmine, A. Mangiarotti, P. R. Maurenzig, G. Pasquali, S. Piantelli, S. Poggi, N. Taccetti, e E. Vanzi, «Fiasco: a multidetector optimized for semiperipheral heavy ion collisions at Fermi energies», *Nuclear Instruments and Methods in Physics Research Section A: Accelerators, Spectrometers, Detectors and Associated Equipment*, vol 515, n° 3, pagg 497–523, Dic 2003.

[34] L. Bardelli, M. Bini, G. Poggi, e N. Taccetti, «Application of digital sampling techniques to particle identification in scintillation detectors», *Nuclear Instruments and Methods in Physics Research Section A: Accelerators, Spectrometers, Detectors and Associated Equipment*, vol 491, n° 1–2, pagg 244–257, Set 2002.

[35] L. Bardelli, G. Poggi, M. Bini, e G. Pasquali, «An efficient method for timing synchronization between many digital sampling channels», *Nuclear Instruments and Methods in Physics Research Section A: Accelerators, Spectrometers, Detectors and Associated Equipment*, vol 572, n° 2, pagg 882–892, Mar 2007.

[36] G. Pasquali, R. Ciaranfi, L. Bardelli, M. Bini, A. Boiano, F. Giannelli, A. Ordine, e G. Poggi, «A DSP equipped digitizer for online analysis of nuclear detector signals», *Nuclear Instruments and Methods in Physics Research Section A: Accelerators, Spectrometers, Detectors and Associated Equipment*, vol 570, n° 1, pagg 126–132, Gen 2007.

[37] ROOT, «http://root.cern.ch/drupal/», 2012.

[38] S. Sambi, «Meccanismi di emissione di particelle leggere nella reazione nucleare 16O + 116Sn a 192 MeV». Master's thesis, University of Bologna, 2010.

[39] L. Morelli, M. Bruno, G. Baiocco, L. Bardelli, S. Barlini, M. Bini, G. Casini, M. D'Agostino, M. Degerlier, F. Gramegna, V. L. Kravchuk, T.

Marchi, G. Pasquali, e G. Poggi, «Automatic procedure for mass and charge identification of light isotopes detected in CsI(Tl) of the GARFIELD apparatus», *Nuclear Instruments and Methods in Physics Research Section A: Accelerators, Spectrometers, Detectors and Associated Equipment*, vol 620, n° 2–3, pagg 305–313, 11.

[40] U. Abbondanno, M. Bruno, G. Casini, R. Cavaletti, S. Cavallaro, M. Chiari, M. D'Agostino, F. Gramegna, A. Lanchais, G. . Margagliotti, P. . Mastinu, P. . Milazzo, A. Moroni, A. Nannini, A. Ordine, G. Vannini, e L. Vannucci, «Calibrating the CsI(Tl) detectors of the GARFIELD apparatus», *Nuclear Instruments and Methods in Physics Research Section A: Accelerators, Spectrometers, Detectors and Associated Equipment*, vol 488, n° 3, pagg 604–609, Ago 2002.

[41] O. V. Fotina, D. O. Eremenko, Y. L. Parfenova, S. Y. Platonov, O. A. Yuminov, V. L. Kravchuk, F. Gramegna, S. Barlini, G. Casini, M. Bruno, M. D'Agostino, O. Wieland, A. Bracco, e F. Camera, «PRE-EQUILIBRIUM EFFECTS IN THE SECONDARY PARTICLE SPECTRA IN THE REACTIONS WITH HEAVY IONS», *International Journal of Modern Physics E*, vol 19, n° 05n06, pagg 1134–1140, Giu 2010.

[42] J. Cabrera, T. Keutgen, Y. El Masri, C. Dufauquez, V. Roberfroid, I. Tilquin, J. Van Mol, R. Régimbart, R. J. Charity, J. B. Natowitz, K. Hagel, R. Wada, e D. J. Hinde, «Fusion-fission and fusion-evaporation processes in ^{20}Ne+^{159}Tb and ^{20}Ne+^{169}Tm interactions between E/A=8 and 16 MeV», *Phys. Rev. C*, vol 68, n° 3, pag 034613, Set 2003.

[43] R. Nicolini, *Peaks fitting manual*. 2008.

[44] F. Pühlhofer, «On the interpretation of evaporation residue mass distributions in heavy-ion induced fusion reactions», *Nuclear Physics A*, vol 280, n° 1, pagg 267–284, Apr 1977.

[45] W. Galster, *Hahn-Meitner-Institut Annual Report*, 1984.

[46] M. P. Kelly, J. F. Liang, A. A. Sonzogni, K. A. Snover, J. P. S. van Schagen, e J. P. Lestone, «Preequilibrium particle emission and the giant-dipole resonance in Sn nuclei», *Phys. Rev. C*, vol 56, n° 6, pagg 3201–3209, Dic 1997.

[47] F. Camera, A. Bracco, B. Million, M. Pignanelli, J. J. Gaardhøje, Z. Zelazny, T. Ramsøy, e A. Maj, «Large effects of orientation fluctuations in the angular distribution of the GDR photons», *Nuclear Physics A*, vol 572, n° 2, pagg 401–416, Mag 1994.

[48] K. Mazurek, M. Kmiecik, A. May, J. Dudek, e N. Schunck, «Effective GDR Width of 132Ce at high spins and temperatures from the LSD model_», Acta Physica Polonica B, pagg 1455–1461, and references therein-2007.

[49] K. Mazurek, *Private communication*.

[50] G. Q. Li e R. Machleidt, «Microscopic calculation of in-medium nucleon-nucleon cross sections», *Phys. Rev. C*, vol 48, n° 4, pagg 1702–1712, Ott 1993.

[51] G. Q. Li e R. Machleidt, «Microscopic calculation of in-medium proton-proton cross sections», *Phys. Rev. C*, vol 49, n° 1, pagg 566–569, Gen 1994.

[52] G. F. Knoll, *Radiation Detection and Measurement*, 3rd ed. Wiley, 2000.

[53] M. Ciemała, D. Balabanski, M. Csatlós, J. M. Daugas, G. Georgiev, J. Gulyás, M. Kmiecik, A. Krasznahorkay, S. Lalkovski, A. Lefebvre-Schuhl, R. Lozeva, A. Maj, e A. Vitez, «Measurements of high-energy - rays with detectors», *Nuclear Instruments and Methods in Physics Research Section A: Accelerators, Spectrometers, Detectors and Associated Equipment*, vol 608, n° 1, pagg 76–79, Set 2009.

[54] A. Corsi, O. Wieland, S. Barlini, A. Bracco, F. Camera, V. L. Kravchuk, G. Baiocco, L. Bardelli, G. Benzoni, M. Bini, N. Blasi, S. Brambilla, M. Bruno, G. Casini, M. Ciemala, M. Cinausero, F. C. L. Crespi, M. D'Agostino, M. Degerlier, A. Giaz, F. Gramegna, M. Kmiecik, S. Leoni, A. Maj, T. Marchi, K. Mazurek, W. Meczynski, B. Million, D. Montanari, L. Morelli, S. Myalski, A. Nannini, R. Nicolini, G. Pasquali, G. Poggi, V. Vandone, e G. Vannini, «Measurement of isospin mixing at a finite temperature in ^{80}Zr via giant dipole resonance decay», *Phys. Rev. C*, vol 84, n° 4, pag 041304, Ott 2011.

[55] W. Heisenberg, «Über den Bau der Atomkerne. I», *Zeitschrift für Physik A Hadrons and Nuclei*, vol 77, n° 1, pagg 1–11, 1932.

[56] D. H. Wilkinson, «XXXVII. Isotopic spin selection rules. VII: Breakdown of the rules and the situation in l6O», *Philosophical Magazine*, vol 1, n° 5, pagg 379–392, 1956.

[57] J. A. Behr, «Giant Dipole Radiation and Isospin Purity in Highgly Excited Compound Nuclei». PhD thesis, University of Washington, 1991.

[58] A. Bohr e B. R. Mottelson, *Nuclear Structure*. World Scientific Pub Co Inc, 1998.

[59] I. Hamamoto e H. Sagawa, «Gamow-Teller beta decay and isospin impurity in nuclei near the proton drip line», *Phys. Rev. C*, vol 48, n° 3, pagg R960–R963, Set 1993.

[60] J. Dobaczewski e I. Hamamoto, «Isospin impurities in ground states of N = Z nuclei near the proton-drip line», *Physics Letters B*, vol 345, n° 3, pagg 181–184, Feb 1995.

[61] G. Colò, M. A. Nagarajan, P. Van Isacker, e A. Vitturi, «Isospin mixing in proton-rich N≃Z nuclei», *Phys. Rev. C*, vol 52, n° 3, pagg R1175–R1178, Set 1995.

[62] H. Sagawa, P. . Bortignon, e G. Colò, «Restoration of isospin symmetry in highly excited nuclei», *Physics Letters B*, vol 444, n° 1–2, pagg 1–6, Dic 1998.

[63] H. L. Harney, A. Richter, e H. A. Weidenmüller, «Breaking of isospin symmetry in compound-nucleus reactions», *Rev. Mod. Phys.*, vol 58, n° 3, pagg 607–645, Lug 1986.

[64] T. Suzuki, H. Sagawa, e G. Colò, «Spreading width of the isobaric analog state and isospin mixing», *Phys. Rev. C*, vol 54, n° 6, pagg 2954–2958, Dic 1996.

[65] A. Corsi, «Nuclear colletive modes at finite temperature as a probe of nuclear structure and dynamics». PhD thesis, University of Milano, 2010.

[66] M. Kicinska-Habior, «Isospin Mixing at High Temperatures», *Acta Physica Polonica B*, pagg 1133–1144, 2005.

[67] E. Wojcik, M. Kicinska-Habior, O. Kijewska, M. Kowalczyk, M. Kisielinski, e J. Choinski, «Giant Dipole Radiation and Isospin Mixing in Hot Light Nuclei», *Acta Physica Polonica B*, pagg 207–212, 2006.

[68] M. Kicin´ska-Habior, E. Wo´jcik, O. Kijewska, M. Kisielin´ski, M. Kowalczyk, e J. Choin´ski, «Giant dipole radiation and isospin purity in highly excited32S nuclei», *Nuclear Physics A*, vol 731, n° 0, pagg 138–145, Feb 2004.

[69] E. Wojcik, M. Kicinska-Habior, O. Kijewska, M. Kowalczyk, M. Kisielinski, e J. Choinski, «Giant Dipole Radiation and Isospin Mixing in Hot Nuclei with A=32-60», *Acta Physica Polonica B*, pagg 1469–1472, 2007.

[70] S. Akkoyun, A. Algora, B. Alikhani, F. Ameil, G. de Angelis, L. Arnold, A. Astier, A. Ataç, Y. Aubert, C. Aufranc, A. Austin, S. Aydin, F. Azaiez, S. Badoer, D. L. Balabanski, D. Barrientos, G. Baulieu, R. Baumann, D. Bazzacco, F. A. Beck, T. Beck, P. Bednarczyk, M. Bellato, M. A. Bentley, G. Benzoni, R. Berthier, L. Berti, R. Beunard, G. Lo Bianco, B. Birkenbach, P. G. Bizzeti, A. M. Bizzeti-Sona, F. Le Blanc, J. M. Blasco, N. Blasi, D. Bloor, C. Boiano, M. Borsato, D. Bortolato, A. J. Boston, H. C. Boston, P. Bourgault, P. Boutachkov, A. Bouty, A. Bracco, S. Brambilla, I. P. Brawn, A. Brondi, S. Broussard, B. Bruyneel, D. Bucurescu, I. Burrows, A. Bürger, S. Cabaret, B. Cahan, E. Calore, F. Camera, A. Capsoni, F. Carrió, G. Casati, M. Castoldi, B. Cederwall, J.-L. Cercus, V. Chambert, M. El Chambit, R. Chapman, L. Charles, J. Chavas, E. Clément, P. Cocconi, S. Coelli, P. J. Coleman-Smith, A. Colombo, S. Colosimo, C. Commeaux, D. Conventi, R. J. Cooper, A. Corsi, A. Cortesi, L. Costa, F. C. L. Crespi, J. R. Cresswell, D. M. Cullen, D. Curien, A. Czermak, D. Delbourg, R. Depalo, T. Descombes, P. Désesquelles, P. Detistov, C. Diarra, F. Didierjean, M. R. Dimmock, Q. T. Doan, C. Domingo-Pardo, M. Doncel, F. Dorangeville, N. Dosme, Y. Drouen, G. Duchêne, B. Dulny, J. Eberth, P. Edelbruck, J. Egea, T. Engert, M. N. Erduran, S. Ertürk, C. Fanin, S. Fantinel, E. Farnea, T. Faul, M. Filliger, F. Filmer, C. Finck, G. de France, A. Gadea, W. Gast, A. Geraci, J. Gerl, R. Gernhäuser, A. Giannatiempo, A. Giaz, L. Gibelin,

A. Givechev, N. Goel, V. González, A. Gottardo, X. Grave, J. Gre˛bosz, R. Griffiths, A. N. Grint, P. Gros, L. Guevara, M. Gulmini, A. Görgen, H. T. M. Ha, T. Habermann, L. J. Harkness, H. Harroch, K. Hauschild, C. He, A. Hernández-Prieto, B. Hervieu, H. Hess, T. Hüyük, E. Ince, R. Isocrate, G. Jaworski, A. Johnson, J. Jolie, P. Jones, B. Jonson, P. Joshi, D. S. Judson, A. Jungclaus, M. Kaci, N. Karkour, M. Karolak, A. Kaşkaş, M. Kebbiri, R. S. Kempley, A. Khaplanov, S. Klupp, M. Kogimtzis, I. Kojouharov, A. Korichi, W. Korten, T. Kröll, R. Krücken, N. Kurz, B. Y. Ky, M. Labiche, X. Lafay, L. Lavergne, I. H. Lazarus, S. Leboutelier, F. Lefebvre, E. Legay, L. Legeard, F. Lelli, S. M. Lenzi, S. Leoni, A. Lermitage, D. Lersch, J. Leske, S. C. Letts, S. Lhenoret, R. M. Lieder, D. Linget, J. Ljungvall, A. Lopez-Martens, A. Lotodé, S. Lunardi, A. Maj, J. van der Marel, Y. Mariette, N. Marginean, R. Marginean, G. Maron, A. R. Mather, W. Me˛czyński, V. Mendéz, P. Medina, B. Melon, R. Menegazzo, D. Mengoni, E. Merchan, L. Mihailescu, C. Michelagnoli, J. Mierzejewski, L. Milechina, B. Million, K. Mitev, P. Molini, D. Montanari, S. Moon, F. Morbiducci, R. Moro, P. S. Morrall, O. Möller, A. Nannini, D. R. Napoli, L. Nelson, M. Nespolo, V. L. Ngo, M. Nicoletto, R. Nicolini, Y. Le Noa, P. J. Nolan, M. Norman, J. Nyberg, A. Obertelli, A. Olariu, R. Orlandi, D. C. Oxley, C. Özben, M. Ozille, C. Oziol, E. Pachoud, M. Palacz, J. Palin, J. Pancin, C. Parisel, P. Pariset, G. Pascovici, R. Peghin, L. Pellegri, A. Perego, S. Perrier, M. Petcu, P. Petkov, C. Petrache, E. Pierre, N. Pietralla, S. Pietri, M. Pignanelli, I. Piqueras, Z. Podolyak, P. Le Pouhalec, J. Pouthas, D. Pugnére, V. F. E. Pucknell, A. Pullia, B. Quintana, R. Raine, G. Rainovski, L. Ramina, G. Rampazzo, G. La Rana, M. Rebeschini, F. Recchia, N. Redon, M. Reese, P. Reiter, P. H. Regan, S. Riboldi, M. Richer, M. Rigato, S. Rigby, G. Ripamonti, A. P. Robinson, J. Robin, J. Roccaz, J.-A. Ropert, B. Rossé, C. Rossi Alvarez, D. Rosso, B. Rubio, D. Rudolph, F. Saillant, E. Şahin, F. Salomon, M.-D. Salsac, J. Salt, G. Salvato, J. Sampson, E. Sanchis, C. Santos, H. Schaffner, M. Schlarb, D. P. Scraggs, D. Seddon, M. Şenyiğit, M.-H. Sigward, G. Simpson, J. Simpson, M. Slee, J. F. Smith, P. Sona, B. Sowicki, P. Spolaore, C. Stahl, T. Stanios, E. Stefanova, O. Stézowski, J. Strachan, G. Suliman, P.-A. Söderström, J. L. Tain, S. Tanguy, S. Tashenov, C. Theisen, J. Thornhill, F. Tomasi, N. Toniolo, R. Touzery, B. Travers, A. Triossi, M. Tripon, K. M. M. Tun-Lanoë, M. Turcato, C. Unsworth, C. A. Ur, J. J. Valiente-Dobon, V. Vandone, E. Vardaci, R. Venturelli, F. Veronese, C. Veyssiere, E. Viscione, R. Wadsworth, P. M. Walker, N. Warr, C. Weber, D. Weisshaar, D. Wells, O. Wieland, A. Wiens, G. Wittwer, H. J. Wollersheim, F. Zocca, N. V. Zamfir, M. Zie˛bliński, e A. Zucchiatti, «AGATA—Advanced GAmma Tracking Array», *Nuclear Instruments and Methods in Physics Research Section A: Accelerators, Spectrometers, Detectors and Associated Equipment*, vol 668, n° 0, pagg 26–58, Mar 2012.

[71] D. Bazzacco, «The Advanced Gamma Ray Tracking Array AGATA», *Nuclear Physics A*, vol 746, n° 0, pagg 248–254, Dic 2004.

[72] Kmax, «http://www.sparrowcorp.com/products/software».

[73] X. Grave, R. Canedo, J.-F. Clavelin, S. Du, e E. Legay, «NARVAL a modular distributed data acquisition system with Ada 95 and RTAI», in *Real Time Conference, 2005. 14th IEEE-NPSS*, 2005, pag 5 pp.

[74] C. Boiano, R. Bassini, F. Camera, B. Million, O. Wieland, e A. Giaz, «A 16 channel NIM module for a complete processing of fast scintillator signals», in *IEEE Nuclear Science Symposium Conference Record, 2008. NSS '08*, 2008, pagg 2068 –2070.

[75] H. J. Wollersheim, D. E. Appelbe, A. Banu, R. Bassini, T. Beck, F. Becker, P. Bednarczyk, K.-H. Behr, M. A. Bentley, G. Benzoni, C. Boiano, U. Bonnes, A. Bracco, S. Brambilla, A. Brünle, A. Bürger, K. Burkard, P. A. Butler, F. Camera, D. Curien, J. Devin, P. Doornenbal, C. Fahlander, K. Fayz, H. Geissel, J. Gerl, M. Górska, H. Grawe, J. Gre˛bosz, R. Griffiths, G. Hammond, M. Hellström, J. Hoffmann, H. Hübel, J. Jolie, J. V. Kalben, M. Kmiecik, I. Kojouharov, R. Kulessa, N. Kurz, I. Lazarus, J. Li, J. Leske, R. Lozeva, A. Maj, S. Mandal, W. Me˛czyński, B. Million, G. Münzenberg, S. Muralithar, M. Mutterer, P. J. Nolan, G. Neyens, J. Nyberg, W. Prokopowicz, V. F. E. Pucknell, P. Reiter, D. Rudolph, N. Saito, T. R. Saito, D. Seddon, H. Schaffner, J. Simpson, K.-H. Speidel, J. Styczeń, K. Sümmerer, N. Warr, H. Weick, C. Wheldon, O. Wieland, M. Winkler, e M. Zie˛bliński, «Rare ISotopes INvestigation at GSI (RISING) using gamma-ray spectroscopy at relativistic energies», *Nuclear Instruments and Methods in Physics Research Section A: Accelerators, Spectrometers, Detectors and Associated Equipment*, vol 537, n° 3, pagg 637–657, Feb 2005.

Acknowledgments

Many people contributed to this thesis in innumerable ways, I am grateful to all of them and I apologize to anyone who may have been left out.

First and foremost I would like to thank to my advisor, Professor Franco Camera, for supporting me during these three years. I am very appreciative of his advice, time, useful and entertaining conversation, kindness and more importantly for the trust he accorded me; without his support, this thesis would not have been possible.

I gratefully acknowledge Professor Mauro Bruno for agreeing to referee this thesis, and for his careful reading and constructive comments. I would also like to thank the others committee members, Professors Angela Bracco and Giovanni La Rana.

I am indebted to Anna Corsi whom I have been working on the data analysis of the dynamical dipole experiment during my first year. She was fundamental for the data-taking and played a very active role in the early stages of the analysis. She provided insightful discussions and suggestions about this experiment, she gave me scientific advice and she enriched this analysis with her knowledge.

I thank all the members of the γ-spectroscopy group of Milano, with whom I shared many years of working, for the pleasant atmosphere and the company. I would especially like to thank Oliver Wieland, for his help during the first part of the DD data analysis. I also in debt to Simone Ceruti, who has been working with me on the data analysis of the isospin mixing experiment. He took a very active part in the analysis and was fundamental in obtaining most of the results reported in this work.

Many thanks also go to Sergio Brambilla, whose expertise was essential for all the experiments reported in this thesis. I am also grateful to Stefano Riboldi for his helpfulness and explanations concerning the $LaBr_3$:Ce detectors and their front-end electronics, and for the pleasant discussions.

I gratefully acknowledge the contribution that all the members of the GARFIELD collaboration gave before, during and after the experiment. I very much appreciated the nice atmosphere between members of the collaboration. In particular, I wish to thank Dr. Fabiana Gramegna for the long and fruitful discussions on the GARFIELD data analysis.

I am grateful to Dr. Maria Colonna and Dr. Carmelo Rizzo for their explanations on the BNV model: they both helped me to achieve a deeper understanding of the physics of the dynamical dipole mode.

I gratefully acknowledge the AGATA groups of Padova and Legnaro, who were very helpful both before the experiment for the preparations, and after the experiment for the preliminary steps of the analysis of the AGATA data.

I also would like to acknowledge all people that worked on the characterization of the $LaBr_3$:Ce detectors, and made possible to write a paper on this topic. The help of the group lead by Dr. Attila Krasznahorkay at the ATOMKI Laboratories in Debrecen was fundamental.

Finally, I thank my family for supporting me through all these years, and for being so proud of my PhD. I would like to thank my friends for all the good moments we shared and for their patience when they listen to me speaking about physics. My final, and most heartfelt, acknowledgment must go to Roberto Nicolini for the hardware and software support that he patiently supplies and for all the help that he gave me while writing this thesis. His support, encouragement, friendship and love made this experience much more pleasant.